Integrated Modeling and Design of Lightweight, Active Mirrors for Launch Survival and On-Orbit Performance

by

Lucy E. Cohan

B.S., Cornell University (2005)

S.M., Massachusetts Institute of Technology (2007)

Submitted to the Department of Aeronautics and Astronautics
in partial fulfillment of the requirements for the degree of

Doctor of Philosophy

at the

MASSACHUSETTS INSTITUTE OF TECHNOLOGY

June 2010

Author .....
Department of Aeronautics and Astronautics
February 12, 2010

Certified by .....
David W. Miller
Professor of Aeronautics and Astronautics
Thesis Committee Chair

Certified by .....
Karen Willcox
Associate Professor of Aeronautics and Astronautics

Certified by .....
Jonathan P. How
Professor of Aeronautics and Astronautics

Certified by .....
Howard A. MacEwen
Principal Scientist, Mantech International Corporation

Accepted by .....
Eytan Modiano
Associate Professor of Aeronautics and Astronautics
Chair, Committee on Graduate Students

Integrated Modeling and Design of Lightweight, Active Mirrors for Launch Survival and On-Orbit Performance

by

Lucy E. Cohan

Submitted to the Department of Aeronautics and Astronautics
on February 12, 2010, in partial fulfillment of the
requirements for the degree of
Doctor of Philosophy

Abstract

Lightweight, active mirrors are an enabling technology for large aperture, space-based optical systems. These mirrors have the potential to improve the optical resolution and sensitivity beyond what is currently possible. However, as with all technology development programs, there are remaining issues to be solved before such mirrors can be used in operational systems. As of yet, no efforts have been made to explore the design space or optimize the design of lightweight mirrors across operational environments and constraints. The extremely harsh launch environment is of particular concern because launch survival constraints could dictate aspects of the mirror design. Additionally, on-orbit optical performance, in terms of high spatial frequency wavefront error and low spatial frequency correctability, are extremely important aspects of mirror design.

Due to the lack of heritage systems, the best designs for lightweight, active mirrors are not immediately apparent. Therefore, an integrated modeling methodology for technology development programs is developed. This framework uses model-based design and evolutionary models to guide the technology development program. This methodology is applied to the lightweight, active mirror systems of interest.

The mirrors are modeled and analyzed in two distinct environments: on-orbit and during launch. The on-orbit model and analysis are presented, as well as the designs with the best optical performance, which tend to have many ribs and actuators. Additionally, a dynamic state-space model of the launch environment is developed. The designs that are most likely to survive launch have few ribs and actuators, directly in conflict with the best on-orbit designs. Launch load alleviation techniques, including techniques making use of the existing embedded actuators, are also implemented to increase the probability of launch survival. Finally, a fully integrated trade space analysis of designs is shown, along with families of designs that perform well with respect to different mission objectives.

The integrated modeling approach allows for the seamless combination of the two analyses, as well as a way in which to determine the best performing designs. By using this approach, the model can be updated to include any new insights and to

reflect the current state of the technology, making it useful throughout the life cycle of the program.

Thesis Committee Chair: David W. Miller
Title: Professor of Aeronautics and Astronautics

Thesis Committee Member: Karen Willcox
Title: Associate Professor of Aeronautics and Astronautics

Thesis Committee Member: Jonathan P. How
Title: Professor of Aeronautics and Astronautics

Thesis Committee Member: Howard A. MacEwen
Title: Principal Scientist, Mantech International Corporation

Acknowledgments

This work has been supported by the Department of Defense, the National Defense Science and Engineering Graduate Fellowship program, the National Science Foundation Graduate Research Fellowship program, and the Zonta International Amelia Earhart Fellowship. I am grateful to all of these institutions for their financial support throughout my graduate work.

I would like to thank my advisor, Prof. Dave Miller, for his guidance and support through my years here. I appreciate all of the technical advice, challenges, and happy hours. I would like to thank Prof Karen Willcox, Prof Jonathan How, and Dr Howard MacEwen for providing guidance and advice as a part of my thesis committee. Their ideas and insights have helped to shape this work. Also, thank you to Dr Lee Peterson for hosting me at JPL and giving me the chance to experience life there.

I would also like to thank the MOST team over the years, including Scott Uebelhart, Deborah Howell, Liz Jordan, Andrzej Stewart, Tom Gray, Joe Bogosian, and Matt Smith, for their ideas and collaboration. Thank you to the entire Space Systems Lab, who have made my time here more enjoyable. Also thank you to Sharon Brown and Marilyn Good, who have provided much needed assistance and always tried to make life easier.

Finally, thank you to my family and to all of my friends. I could not have done this alone. Special thanks to my parents, Mike and Sarah, for their love and support in everything that I have done.

Contents

List of Figures

List of Tables

Chapter 1

Introduction

The next generation of space-based imaging systems will push the limits of current technology and design methodologies, while achieving performance that has previously been impossible. Whether the goals are Earth imaging systems with better ground resolution and located in higher orbits, or astronomical telescopes looking back into time, the desired improvement in optical resolution and sensitivity can be obtained through the use of larger primary apertures. However, larger apertures bring about a number of design challenges including mass, volume, and flexibility. Mirrors larger than about three meters in diameter encounter packaging constraints due to the size and volume limits of the launch vehicle shroud. Also, mass-to-orbit is limited and extremely expensive, requiring the areal density, or mass per unit area, of the mirrors to decrease as the diameter increases in order to maintain an acceptable launch mass. Furthermore, the large size and the lower mass combine to significantly increase the flexibility of the mirrors, lowering flexible mode frequencies and making them more susceptible to static and dynamic distortion, so maintaining optical tolerances across the mirror surface becomes increasingly difficult. While these challenges are immense, they can be dealt with through the use of lightweight, actuated, segmented primary mirrors. Instead of the traditional monolithic design, the primary aperture is made up of multiple smaller mirror segments which are easier to manufacture and can deploy from a stowed configuration that will fit within a launch vehicle. Furthermore, the mirrors can be rib-stiffened to achieve low mass while maintaining

adequate stiffness, and the ribs can contain embedded actuators to control the shape of the mirror to optical tolerances. The size of the achievable apertures, and hence the potential imaging resolution, are very promising.

As with many promising new technology developments, lightweight, active mirror segments solve one problem (aperture size), but introduce a new set of challenges that must be addressed. One issue that arises is the ability to design the mirror to accommodate multiple environments and disturbance sources in an efficient way. For example, launch survival is a key challenge in the mirror design. Launch is an extremely harsh environment and silicon carbide, which is the selected material for this thesis, is a brittle material that could break at low areal densities when exposed to the vibrations and acoustics from launch. Yet it is imperative that these fragile optical components arrive on orbit undamaged. Once on orbit, the mirror design must also meet tight optical performance requirements, in the form of low wavefront error, in the face of static and dynamic disturbances during operation. However, designing a mirror to best survive launch would yield a mirror that is substantially different than one which provides a high degree of correctability on orbit. Therefore, the mirror structure and control system design must be carefully analyzed and optimized in an integrated fashion in order to advance the state of the art in active mirror design.

This thesis focuses on the design and optimization of lightweight mirrors, specifically with respect to the launch and operational environments, resulting in an integrated design methodology, which can in turn be used for technology optimization and advancement. This will ultimately lead to increased capabilities of space-based imaging systems.

1.1 Background

1.1.1 Space Based Imaging Systems

Space based imaging systems provide a number of benefits that cannot be gained from ground-based systems. Astronomical space telescopes have the potential to greatly

Figure 1-1: Hubble Space Telescope [130]

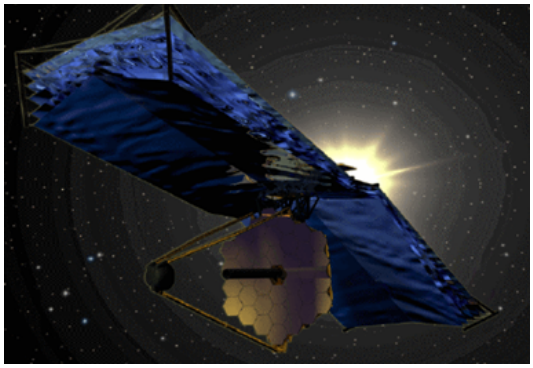

Figure 1-2: James Webb Space Telescope [99]

expand our knowledge of the universe, and have a view that is unobstructed by the distortions of the Earth's atmosphere and avoid atmospheric absorption. Earth imaging telescopes provide knowledge about our planet that is simply unattainable through ground-based systems.

Astronomical space telescopes contribute vastly to the understanding of the universe. The Hubble Space Telescope (Figure 1-1), launched in 1990, images from ultraviolet to near-infrared wavelengths and has provided an immense amount of scientific data. Hubble has helped to determine the age of the universe, improved understanding of planet formation, and discovered extra-solar organic matter, among numerous other accomplishments [130]. The James Webb Space Telescope (JWST) (Figure 1-2) will continue the tradition of large, orbiting observatories [99]. JWST is scheduled to launch in 2013 and will use infrared imaging to provide data that will help scientists understand the Big Bang theory. With its 6.5 m diameter segmented primary mirror, it provides greater mirror design challenges than Hubble, whose primary mirror measures 2.4 m in diameter.

Earth observation systems can be used for Earth imaging, climate change, national security, and other applications. A history of Earth observation can be found in Kramer [89]. For example, the LandSat program [142] has been running since 1972 and is a resource for global change research in fields such as geology and agriculture. Recently, commercial imaging systems such as IKONOS [8] have also been successful, with new commercial imaging satellites including DigitalGlobe's Worldview-1 [9] and

GeoEye's GeoEye-1 [7] having recently launched in September 2007 and September 2008, respectively. These new commercial systems have ground resolutions as fine as 40 cm, with the largest primary aperture being 1.1 m in diameter [85]. It is worth noting that, even with the increased capabilities of the new commercial systems, commercial imaging systems are generally significantly smaller than their government funded counterparts, particularly the large space observatories such as Hubble and JWST.

Since space-based optical systems have been very successful, it is desirable to determine and develop the capabilities and technologies that will enable the next generation of space-based imaging systems. The next logical steps are to continue to increase the aperture size to reap the benefits of the increased resolution capabilities [20]. However, the areal density, or mass per unit area of the primary mirror, must decrease to keep the mass and launch costs feasible. NASA has developed a capability road map to address the technologies that are necessary to enable the next generation of envisioned space telescopes and observatories [126]. These technologies include optics, wavefront sensing and control, distributed and advanced spacecraft systems, large precision structures, and cryogenic and thermal control systems. In the realm of optics, the following technology goal is stated: "Lightweight affordable optics is an enabling capability for future large-aperture space optical systems for Earth science, solar observations, and astronomy" [126]. This motivates the development of lightweight, active mirror segments as a potentially affordable approach to achieving larger aperture systems.

1.1.2 Lightweight Mirrors

Lightweight mirrors are necessary to be able to launch larger apertures. The Hubble mirror has an areal density of 180 kg/m^2, yielding a total mass of 720 kg for the 2.4 m diameter mirror. Mirrors this massive are expensive to launch, and scaling the high areal density to a larger diameter system is impractical. Therefore, mirrors must become lighter to increase their size. Light-weighting can be achieved by removing unnecessary material from the back of the mirror, resulting in a rib-stiffened back struc-

ture that can maintain structural stiffness at a lower mass. However, rib-stiffening has limitations and, as the areal density decreases, the flexible mode frequencies will decrease, making the mirrors more susceptible to deformations, leading to thermal, dynamic, and manufacturing distortions. To counteract these errors, actuation can be used to control the mirror surface to optical tolerances, increasing the possibilities in mirror design by allowing lower mass systems to meet performance requirements.

A number of material options exist for lightweight mirrors, including glass, beryllium, and silicon carbide, as discussed further in Section 2.1. Traditional mirrors have been made from glass, though glass is difficult to form and polish leading to long manufacturing times. Furthermore, glass mirrors can be manufactured with areal densities as low as about 15 kg/m^2, but cannot be decreased further. Beryllium has high stiffness, low mass, and is stable at cryogenic temperatures, which are good qualities in optical materials. However, beryllium is toxic and limited in supply. Actuated silicon carbide (SiC) mirrors provide a promising path for a number of reasons [44, 88]. Silicon carbide mirrors can be manufactured faster, and some of the lengthy polishing process can be replaced with actuation that reduces distortion. Furthermore, compared to glass, SiC's higher strength allows larger strains, simplifying actuation and making the mirror more correctable. SiC also has a high thermal conductivity, reducing thermal gradients that can be a significant source of deformation.

However, there are also a number of issues with actuated SiC mirrors that need to be resolved. First, there can be manufacturing errors from a number of sources, including print-through, which is a high spatial frequency error resulting from the non-uniformity of the stiffness and the polishing process, leading to errors in the mirror with the same spatial frequency as the rib structure. Dimpling is another source of error, and refers to uncontrollable, high spatial frequency error that is induced by actuating low spatial frequency shapes. Also, SiC has a high coefficient of thermal expansion (CTE), which causes deformations due to temperature changes which must be counteracted with actuation. Additionally, actuator channel count complexity becomes an issue as the number of actuators that are embedded in the

mirror increases. Finally, launch survival is of significant concern, especially as the areal density decreases. Each of these issues drive the mirror design in different directions, but a single mirror design must be used in all situations.

A great deal of work has been done on advancing the silicon carbide mirror technology, particularly in the areas of manufacturing and developing necessary supporting technologies, such as wavefront sensing. However, relatively little attention has been paid to the design implications of addressing multiple issues, such as low spatial frequency actuation, minimization of high spatial frequency errors, vibration suppression, thermal distortions, and launch stress. Designing a mirror to best accommodate the objectives of launch survival, correctability of focus, or minimization of high spatial frequency error would result in three different mirrors, which is clearly not possible, motivating an integrated design methodology for lightweight active mirrors that can be used to find one mirror design that accommodates all three objectives.

1.2 Problem Statement and Objectives

The use of lightweight, active, silicon carbide mirrors for space-based optical applications has clear benefits. However, it also introduces a number of challenges and issues. Therefore, it is essential to have the ability to analyze and optimize the mirrors for both survival during launch and performance on-orbit.

In order to advance the state of the art for the mirrors, it is preferable to explore the trade space and optimize the design, rather than choose point designs. Oftentimes, a promising point design is chosen early in the design process, but as the development progresses, problems emerge and workarounds or redesigns must be implemented. However, if an integrated model is retained, any issues that are found can be added to the model, and new, better performing designs can be quickly identified. Therefore, an integrated modeling framework is used to quickly create entirely new, distinct mirror models for analysis. With this methodology, the families of favorable designs, as well as the parameters to which the design is most sensitive, can be identified. Parameters can also be varied in support of uncertainty analysis, where uncertainty in the design

parameters can be propagated through the model to estimate the uncertainty in the system performance. Furthermore, test data and lessons learned can be incorporated into the model, so that the model acts as an archive of corporate knowledge as well as a tool for future system design.

There are a number of issues related to the mirror design. First, the ability of the mirror to survive launch can be greatly influenced by the design of the mirror. Survivability can be augmented by isolation or other methods, but the design of the mirror is a significant contributor. Additionally, the operational imaging performance, in terms of wavefront error, is largely dependent on the mirror design. Both of these areas contribute to the overall performance of the mirror, and are described in more detail below.

Launch Survivability Launch is an extremely harsh environment, and launch survival can dominate many aspects of design. Therefore, it is desirable to identify and understand the implications and limitations of design parameters (such as areal density and rib geometry) on launch survival. Furthermore, attenuating launch vibrations using isolation, as well as active and passive damping using the embedded actuators, is of significant interest. Therefore, one aspect of this thesis is to examine the mirror design from the launch perspective to ensure survival.

Operational Performance Requirements Once on-orbit, the primary objective of the mirror is imaging. Therefore, it is important to identify the optical performance resulting from design decisions. Due to thermal or dynamic disturbances, or manufacturing imperfections, one needs to be able to correct the surface figure of the mirror by changing the radius of curvature. However, the finite number and stroke of the actuators limits the achievable shape change. Thus the correctability, or the range of shapes than can be achieved with the embedded actuators, is the first metric for on-orbit performance. Furthermore, the applied correction induces uncontrollable high spatial frequency wavefront error due to the finite length and spacing of the actuators. Therefore, the residual wavefront error (WFE) after the control is applied

is the second on-orbit performance metric. This results in two correlated, yet distinct metrics for on-orbit performance: correctability and wavefront error.

While there has been previous work on modeling and multidisciplinary optimization, active mirror design involves challenges that make it a unique problem. First, the mirror must perform well, in terms of meeting performance requirements and constraints, under multiple types of disturbances. Next, it is a controlled structure, which increases complexity due to the interaction of the structural design and control systems. Additionally, it is an extremely high precision system, with error requirements on the order of nanometers. This type of precision over the large area of the mirror significantly increases complexity, making it necessary for models to have high spatial and temporal bandwidth, and requiring both high order model fidelity and accuracy. Also, the system is inherently multidisciplinary, including controls, structures, thermal, optics, sensing, disturbances, modeling, and uncertainty, which must all be considered simultaneously. Finally, the analysis requires high fidelity models to capture the characteristics of the system, but it is difficult to perform optimization with high order models due to computational expense. Therefore, the challenges involved in design and technology maturation of active, lightweight mirrors presents a rich and unique area of research.

1.2.1 Problem Statement

Given the benefits and challenges of lightweight, active mirror technology, the question becomes: how does one design a mirror that will *survive launch* and *perform well* on-orbit, in terms of wavefront error and correctability? Furthermore, how does one identify those designs in an efficient manner, with constrained amounts of money and time? The hypothesis is that this may be accomplished through the use of integrated modeling and trade space exploration, with models that will incorporate test data and other developmental experience. Consequently, the model will become a key component in guiding technology development as well as qualifying mirrors for flight and diagnosing in-flight anomalies. Moreover, the methodology developed herein will

prove useful for other precision opto-mechanical systems.

1.2.2 Thesis Objectives

The objective of this thesis is to develop and validate a methodology for modeling, optimizing, and thereby guiding the design of lightweight, active mirrors through the use of integrated models.

1. Build an integrated model for lightweight, active mirrors.
    - Create a model of both the launch and on-orbit environments, including structural design, control systems, optics, and disturbance sources.
2. Analyze the mirror response to vibroacoustic launch disturbances.
    - Create a dynamic, state-space model of launch vibrations and acoustics.
3. Analyze the feasibility and benefits of launch load alleviation techniques, including those making use of the existing embedded actuators.
    - Examine isolation, passive shunting circuits, and active damping.
4. Identify favorable mirror architectures, considering both launch and on-orbit performance, through trade space exploration and optimization
    - Characterize the limitations of lightweight, active, SiC mirrors.
5. Develop a parametric, integrated modeling methodology for use in complex, opto-mechanical technology development programs.
    - Illustrate a procedure for capturing developmental experience, including test data, over the life cycle of such a model, and show how to use the model and optimization to guide future development.
    - Demonstrate the chronological nature of the design process in technology development, and how the evolution of the model contributes to the design.
    - Show how to use the model to find families of strongly performing designs in order to guide development.

1.3 Thesis Scope

The technology development for lightweight, active mirrors is an extremely large topic. Therefore, the scope must be limited to ensure a problem with a feasible size. First, only issues pertaining to the *mirror design* will be considered. Therefore, any issues with manufacturing, telescope design, mission, etc. are outside of the scope of this work. It should be noted that these other issues are important and will need to be considered and addressed, though their impacts can be assessed through a secondary analysis. Also, manufacturing constraints such as minimum rib thickness will be imposed on the design as to not ignore manufacturing implications. Second, there are a number of different environments in which the mirror will operate, as well as various disturbance sources that could affect the mirror. Many of these disturbances either result in small errors compared to other sources or could be counteracted through other, more traditional techniques. For example, reaction wheel imbalance results in dynamic jitter of the telescope system. Rather than mitigating this vibration with the embedded actuators in the primary mirror, it is possible to use multi-stage isolation as in JWST and Chandra, as well as a fast steering mirror farther down in the optical train to correct for the jitter, resulting in a much less complex solution. Therefore, by applying these criteria to the various factors in the mirror design, the scope of this thesis is to model and analyze mirrors considering the following:

- Vibroacoustic launch load analysis and alleviation
- High spatial frequency residual wavefront error (errors with spatial frequencies above the spatial frequency of the actuators)
- Correctability (amount of low spatial frequency shape change that can be achieved through actuation)

This combination accounts for the major areas of mirror design, without introducing unnecessary scope to complicate the problem.

In considering these various objectives, a number of modeling techniques will be used. The error sources will be addressed using a set of tools, including structural

design, control systems, isolation, and damping augmentation. Therefore, the focus on control system design is not in the development of new algorithms, but rather in the use of controls to achieve the necessary performance in the presence of uncertainty and noise. Furthermore, existing modeling, reduction, numerical conditioning, and optimization techniques will be exploited and augmented with new approaches as necessary. By limiting the number of disturbance environments and performance outputs, and using existing control, modeling and optimization techniques when appropriate, the scope of the mirror design problem is limited to a reasonable size, while still providing valuable information about active mirror design and design methodologies for technology development programs and model-based flight qualification.

1.4 Contributions

The primary contributions of this thesis are summarized below. They will be discussed in greater detail in Chapter 7.

- Creation of an integrated model for lightweight, active mirrors in the launch and on-orbit environments.
- Development of a dynamic, state-space modeling technique for vibroacoustic launch disturbances to which control systems and alleviation techniques can be directly added.
- Formulation of launch load alleviation in mirrors using existing embedded actuators in conjunction with passive shunt circuits or active damping.
- Synthesis of design guidelines for lightweight, active mirrors specifying how to obtain Pareto optimal designs with good performance and advancing the design knowledge of such mirrors.
- Development of an integrated modeling framework to support technology development through evolutionary models and model-based design.

1.5 Thesis Outline

This thesis uses an integrated modeling methodology to analyze the design of lightweight, active mirrors. Figure 1-3 shows an overview block diagram illustrating the organization of the thesis. Chapter 2 presents an overview of literature that is relevant to the various aspects of this thesis. Chapter 3 presents the integrated modeling methodology used throughout the thesis, specifically applied to complex opto-mechanical technology development programs. Chapter 4 presents an overview of the mirror model, as well as on-orbit performance model and results. Chapter 5 continues with the launch analysis and results. Chapter 6 addresses the full, integrated design problem, considering both the launch and on-orbit environments, including the resulting families of favorable designs. Finally, Chapter 7 concludes the thesis with a summary and contributions.

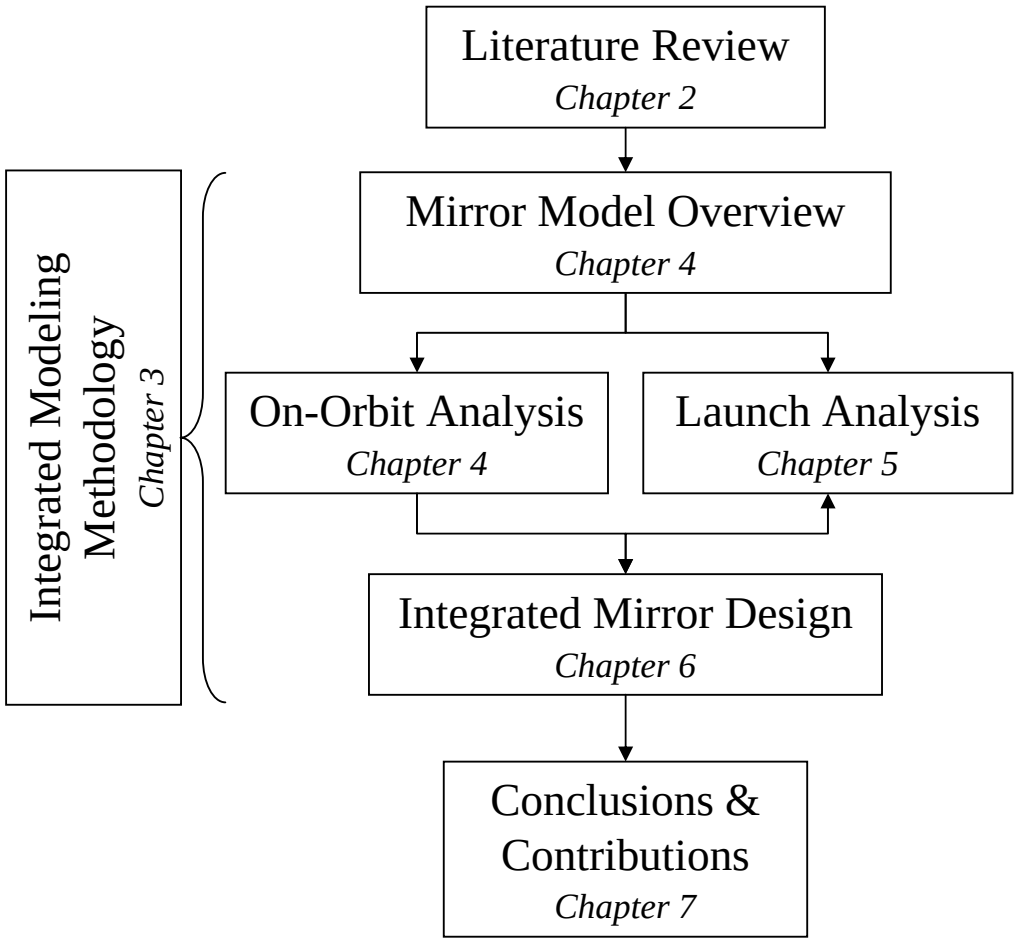

Figure 1-3: Thesis Outline

Chapter 2

Literature Review

The work proposed herein draws on a number of areas of literature. These can be assembled into a few major categories: telescopes and mirror design, modeling and optimization, controls and controlled structures, and launch analysis. These areas encompass the bulk of the material that is pertinent to this thesis, and include relevant portions of the fields of optics, structures, controls, structural dynamics, disturbance analysis, and optimization.

2.1 Telescopes and Mirrors

There is a large amount of literature concerning telescopes and mirror design. The applications are numerous and the scientific possibilities are abundant, as described briefly in Section 1.1.1. There exist capability road maps [126, 139] that discuss the technological advances necessary to make future concept missions a reality, including the development of large, lightweight optics. The scientific benefits of large aperture imaging systems, as well as the stated desire to develop lightweight optics capabilities to achieve large aperture systems clearly motivate this work.

Future space telescope concepts are trending toward utilizing more actuation to meet performance requirements. Lillie and Bronowicki [93] propose achieving optical performance requirements by using actuated mirror mounts and passive isolation. MacEwen [97] goes a step further and discusses using embedded actuation in the

mirror to similarly achieve optical performance at low areal densities. Ealey [45] proposes moving toward actuation in the entire telescope system for achieving the desired performance. As these future architectures trend toward increasing flexibility and control, more integrated modeling is required to ensure success. The current state-of-the-art in space telescope development is JWST. JWST uses seven degree-of-freedom actuation of the rigid body motion and radius of curvature of the mirror segments, and has an extensive modeling effort associated with its development [110]. Models for many subsystems, such as thermal, optics, and structures, are combined in order to calculate the performance of the system [74, 79]. However, the modeling is largely of the single chosen point design, with limited opportunities for changing design variables to explore alternate, potentially better performing architectures, due to the maturity of the design.

Large ground telescope systems also undergo significant modeling efforts. Ground telescopes face fundamentally different issues than space telescopes. Launch weight and volume are no longer restricted, and, instead, the mirror size constraint is due to manufacturability, gravity sag, diurnal thermal transients, wind buffeting, and the size of the enclosure. Furthermore, since mass is less expensive on the ground and the mirror weight must be supported, the mirrors use heavier surface-normal actuation, where the actuators are normal to the surface and push against a massive back structure to control the shape of the mirror. Despite these differences, large ground telescopes are precision, opto-mechanical systems, and space telescopes could use similar modeling efforts as these ground-based systems. Angeli et al. [12, 13] are developing an integrated modeling environment for cost and performance predictions for large, ground-based telescope systems. They advocate versatile models that can be used for design and can accurately predict relevant performance parameters under typical disturbances. The parametric modeling environment for design is a step toward using integrated modeling early in the design process as a way to determine the system architecture, as is proposed herein.

In addition to integrated modeling for telescopes, the development of lightweight mirrors and their corresponding actuation systems is pertinent to this work. Lightweight

mirrors are imperative to the ability to launch systems with larger apertures, and are most often built by eliminating mass from the back side of the mirror and creating a rib structure which maintains stiffness. The Hubble Space Telescope mirror has an areal density of approximately 180 kg/m^2 and is made of glass. The JWST mirror, as discussed in Stahl [125], will achieve an areal density of 26.5 kg/m^2 and is made of beryllium, which will be state-of-the-art for space-based systems. During the initial development of JWST, a number of potential mirror materials were examined as a part of the Advanced Mirror System Demonstrator (AMSD) program. The AMSD effort, described in more detail in Mayo [104], examined many materials in Phase 1, and eventually down-selected to three designs: Kodak's ultra-low expansion (ULE) glass mirror [103], Ball Aerospace's beryllium mirror [86], and Goodrich's fused silica mirror [53]. Ultimately, beryllium was chosen for JWST for its stiffness and ability to maintain optical stability in the cryogenic thermal environment in which JWST will operate. However, there are a number of issues with beryllium, such as limited availability and toxicity, that suggest continued investment in other mirror materials and technologies. Therefore, in general, glass is likely the best option for areal densities of 15 kg/m^2 or above, and silicon carbide and composite mirrors provide the most promise for attaining lower areal densities, as discussed in Matson and Mollenhauer [102] and Kasl and Crowe [84].

Burge, Angel, Miller et al. [26, 27, 107] have developed lightweight glass mirrors through the use of a glass membrane on an actuated support structure. These mirrors have been manufactured up to 2 m in diameter, and can theoretically be scaled to as large as 6-8 m in diameter, while achieving areal densities as low as 15 kg/m^2. However, they will require a great deal of active control to maintain optical tolerances and extremely large mirrors are difficult to manufacture and launch.

Ealey [46, 44] and Kowbel [88] both discuss the properties of silicon carbide (SiC) that make it an attractive material for large, very lightweight optics, such as high stiffness, high fracture toughness, and high thermal conductivity. Ealey goes on to discuss both the challenges and benefits involved in manufacturing SiC mirrors. SiC mirrors are often cast, which is a replication process that can save time and money

when multiple mirror segments are manufactured. The benefits of SiC will result in continued attention to it as an optical material; however, SiC mirrors will normally need to be actuated to achieve the optical performance requirements.

The actuation of SiC mirrors necessitates the field of active and adaptive optics. Active and adaptive optics refer to optical components whose characteristics are controlled during operation to modify the wavefront, with the difference being the bandwidth of the control. Adaptive optics typically refers to high bandwidth, and active optics generally refers to low bandwidth or quasi-static control, though the terms are occasionally used interchangeably. Adaptive optics has been used since the 1950s; Hardy [69] presents an overview of early developments in the field. Adaptive optic systems were first used on ground based systems to counteract the "twinkling" due to atmospheric turbulence [131], and were implemented using deformable mirrors in the optical train as tertiary, or further downstream mirrors. Freeman and Pearson [51] present a review of deformable mirror technology. Active optics can also be used in a segmented primary mirror to control the piston, tip, and tilt of each mirror segment, as well as to control the figure of the mirror surface, as proposed by Robertson [118] in 1970.

Quasi-static shape control has continued to receive attention over the years, and is generally accomplished through the use of influence functions, which are the measured effect of each actuator on the mirror surface figure. Furber et al. [52] developed a correctability model of a one-meter ULE glass mirror segment through the use of finite element modeling (FEM) for the purpose of investigating the effect of the number of actuators on correctability, and Shepherd et al. [121] have compared FEM results to test articles for achieving quasi-static shape control. Additionally, Jordan [81, 80] used integrated modeling to investigate athermalization of an actuated mirror through the use of embedded sensors, and Gray [62] investigated the residual high spatial frequency error due to shape control. The work proposed herein will directly build upon the initial work of Jordan and Gray.

A great deal of work has been done on telescope modeling, both for ground and space based systems. Also, lightweight mirrors and their active optics systems are

being developed and improved, with research focusing on optical material selection, manufacturing techniques, wavefront sensing and control, and actuator design. However, there are a few key areas of literature that are lacking from lightweight mirror design, including optimization of the lightweight mirror system and analysis of the effects of launch. This thesis will help to fill those gaps in the literature, advancing the field of lightweight, actuated mirror design.

2.2 Modeling and Optimization

Modeling, simulation, optimization, and the design process are critical to the development and design of any complex system. Specifically, literature pertaining to integrated modeling, multidisciplinary optimization, model reduction, and validation is related to this work and discussed below.

Parametric, integrated modeling refers to modeling of systems containing multiple disciplines in such a way that design variables are parameterized and can be easily changed to create new models. It has been shown to be useful for a number of different applications, particularly during the conceptual design phase of a program. A number of such applications are discussed in Uebelhart [133], and include the automotive and aircraft industries. The Modular Optical Space Telescope (MOST) project, upon which this work is built, has done significant work on parameterized, integrated modeling for trade space exploration, as summarized in References [135, 82, 134, 34]. Of particular interest, Uebelhart [133, 136] looks at the benefits of integrated modeling and uncertainty analysis early in the design process while using a modular software environment. There have also been a few instances of fully parameterized integrated modeling for space systems. Jilla [77] uses parametric integrated modeling for Terrestrial Planet Finder (TPF), but with less detail than is necessary for detailed mirror design. Lobosco [95] uses an integrated model of the TPF Structurally Connected Interferometer (SCI) with a few variable structural parameters, but again without the full set of structural and control parameters considered here. Similarly, Gutierrez [66] uses integrated modeling for the Space Interferometer Mission (SIM). Additionally,

as cited above, JWST extensively used integrated modeling [110, 74, 79, 41] in the design, though it is used on the chosen point design, rather than in a parameterized manner during conceptual design.

In addition to model development, there has also been progress in developing integrated modeling environments. The Disturbance, Optics, Controls, and Structures (DOCS) [22, 96] toolbox provides a way to combine different disciplines in a MATLAB environment. Similarly, Genberg et al. [54, 55] have combined optical modeling programs such as Code V with NASTRAN through a tool called Sigfit for integrated opto-mechanical modeling, and Lieber has developed an integrated telescope model based in Simulink [92]. Tools such as these simplify the modeling process by easing the integration of multiple types of models. DOCS will be used in this work. Parametric, integrated models and modeling environments are particularly useful in optimization and have been successful in other fields, though use has been thus far limited in space applications.

Multidisciplinary optimization (MDO) involves using optimization across disciplines and at the system level, rather than the subsystem level, and is a natural progression to maximize the benefits of integrated modeling. An overview of the field of MDO can be found in Sobieski and Haftka [124], which reviews modeling for MDO, approximation methods, sensitivity, as well as examples of MDO in aerodynamic/structural optimization and aerospace structural/control optimization. While the overall field of MDO is large and growing rapidly, MDO techniques as applied to opto-mechanical systems represents a significantly smaller set of literature. Haftka [67] and Onoda and Haftka [114] have used MDO techniques to simultaneously optimize structural and control parameters for space structures. Jilla [77] used multiple MDO techniques to optimize the conceptual design of a distributed satellite system. De Weck [42] used MDO to find Pareto-optimal points satisfying achievable iso-performance characteristics for precision opto-mechanical systems. Finally, Cullimore et al. [40] combined commercial structural, thermal, and optical software packages in order to use MDO for a space telescope design to demonstrate the benefits of such an option. These works represent progress toward using MDO in space

applications and provide a point from which to begin this work.

A potential difficulty with MDO in mirror systems is the computational expense, as the mirror models must be high fidelity to capture the intricacies of the design and control. Model reduction and approximation methods can be used to decrease the size of a model to make optimization possible. Model reduction can be done in a number of ways. A popular way is balanced truncation, as originally proposed in Moore [109] and further discussed in Pernebo and Silverman [115] and Uebelhart [132], among others. There are a number of difficulties that balanced truncation can encounter, such as a high computational cost and a limitation to linear systems. Therefore, a number of methods have subsequently been developed to make balanced truncation more widely applicable. One such method presented by Willcox and Peraire [141] uses proper orthogonal decomposition to approximate the dominant eigenvectors of the grammian matrices, which can be used to compute an approximate balanced truncation. In addition to reduction, Barthelemy and Haftka [18] provide a review and analysis of a number of approximation concepts, including local, medium range, and global approximation concepts for structural optimization applications. Robinson [119] discusses surrogate-based optimization where a low fidelity model is used for the majority of the optimization, with occasional checking of the high fidelity model for accuracy. Furthermore, the symmetry of the mirror system can be exploited to reduce the order of the model. Circulant symmetry can be used to block diagonalize the system such that it can be analyzed as a much smaller system, and is described in Wall [137], How [71], and Grocott [65]. Model reduction can be done in a variety of ways, and the type of model reduction to use depends heavily on the type of model being considered.

Model validation and verification (V&V) is an important aspect in any model-based design. According to AIAA [4], verification is the process of determining that a model implementation accurately represents the developer's conceptual description of the model and the solution to the model. Validation is the process of determining the degree to which a model is an accurate representation of the real world from the perspective of the intended uses of the model. Balci [17] presents an overview

of validation, verification, and testing techniques that are available for use. Space telescope and mirrors are extremely difficult to test on the ground, which limits the amount of model validation that is possible. To address this issue, a number of efforts have been undertaken to ensure that the system will function despite this difficulty in testing. Babuska, Carter, and Lane [15] discuss the Structural Vibration Modeling and Validation (SVMV) program with the goal of addressing exactly this issue, and suggest robust control methods, which are stable on uncertain systems, though they have performance set-backs as compared to optimal techniques. Robust control will be revisited in Section 2.3. Masterson and Miller [100, 101] use dynamic tuning to modify the system on-orbit. If the system is designed to be tuned after it is launched, then it can accept more uncertainty than an untunable system, eliminating some of the ill effects of uncertainty in the model. Finally, Kerley et al. [87] discusses the validation of the integrated model for the Thirty Meter Telescope (TMT), which is a complex, opto-mechanical simulation model with limited amount of data with which to validate. Kerley's method validates each component in the model to the furthest extent possible, and also uses the model under known conditions to verify that the model correctly predicts the results for those simple cases. This work will draw upon each of these methods, using robust design along with more traditional V&V to validate the mirror model. Unfortunately, there does not exist a suite of test data on the baseline mirror considered in this thesis that encompasses a modal survey, thermal deformation, launch vibrations, launch acoustics, and radius of curvature control. However, such data does exist across a variety of different mirrors, and the parametric modeling allows one to correlate this data with the model.

Modeling, simulation, and optimization represent a significant challenge in this thesis. There has been substantial work done in the realms of MDO, model reduction, and validation. These existing techniques will be used to the extent possible, and modified and built upon such that they are appropriate for the mirror system. There is a gap in the literature in using parametric, integrated modeling and optimization for lightweight mirror systems. This thesis will fill this gap and extend these methods for use in technology development for precision-controlled opto-mechanical systems.

2.3 Controlled Structures

A third major area of research from which this work will draw is controlled structures. According to Crawley, Campbell, and Hall [35], a controlled structure is: "one in which there are actuators, sensors and a feedback or feed forward architecture to allow the control of static shape or flexible dynamic behavior." Controlled structures introduce complications in design, but result in significantly improved performance when the structural and control systems are designed together. Crawley, Masters, and Hyde [37] present a methodology for conceptual design and reiterate the importance of considering the controlled structure early in the process.

The Middeck Active Controls Experiment (MACE) was a space shuttle flight experiment that flew in 1995 to investigate approaches to controls-structures interactions (CSI) in a 0-g environment. Research associated with MACE included FEM and measurement based modeling (Glaese [59]), system identification (Jacques [76] and Liu et al [94]), robust controls (How [70, 72] and Grocott [106]) and uncertainty analysis (Campbell [28, 29]), among others. Many of the achievements of MACE, as well as lists of the many published works can be found in *The Mace Summary Report* [105]. The MACE program produced a great deal of work on modeling of systems and robust control techniques to work with uncertain systems that will be built upon in this thesis. Additionally, robust control theory and applications are summarized in Zhou and Doyle [145], and Grocott [64] presents a number of robust control techniques for use in structural control of uncertain systems. Furthermore, Miller and Grocott [106] discuss why a controlled-structures approach is necessary for high bandwidth control of a flexible adaptive secondary mirror. The methods presented in this set of literature will be used and adapted to the mirror structural control problem.

There has also been significant work done on shape control of various systems, where shape control refers to a system where the control is being used to attempt to achieve a certain shape, for example focusing a mirror. Irschik [75] presents an overview of static and dynamic shape control, mostly through the use of piezoelectric

actuation. Shape control has been looked at in a variety of systems ranging from simple structures such as beams [11], to two-dimensional plates [113], to more complex structures [127]. The shape control work is primarily focused on actuator type and placement and analytical models for shape control. This will be used and expanded in this thesis to include mirror shape control, while accounting for design constraints.

Controlled structures can either be altered dynamically or quasi-statically. Dynamic controlled structures generally require robust control techniques to account for modeling uncertainties. Quasi-static control is simpler and usually relies upon measured influence functions. In both cases, there is previous literature available from which to draw. These methods will be expanded in this thesis for lightweight mirror control.

2.4 Launch Loads

The final major category of literature applicable to this thesis is launch. The harsh launch environment is the subject of a great deal of work, including analysis of systems in the launch environment and launch load alleviation techniques. Kabe [83] discusses the launch load analysis process and lessons learned from past systems, focusing on model validation and the types of loading encountered. However, Kabe approaches the launch load analysis as either doing a very simple analysis in preliminary design, or through a very detailed coupled loads analysis with the spacecraft and launch vehicle on the final design. The simple loads analysis is done with a Mass Acceleration Curve (MAC), as described in Trubert [129]. Neither the MAC, nor coupled loads analyses are conducive to conceptual design of a lightweight mirror system where controls will be involved. The MAC is too simplistic for a design where launch survival is of significant concern, and the coupled loads analysis is too time consuming, based on iterative analysis of detailed models, to be used for conceptual design. Also, neither method allows for the addition of control systems directly to the model. These shortfalls motivate the development of a dynamic, state-space launch load analysis technique.

In addition to launch load analysis, there has also been work on launch load alleviation. Bicos, Johnson, and Davis [21] discuss the need for, and benefits from, whole-spacecraft vibration isolation. They contend that isolation can reduce weight and cost as well an increase reliability. CSA Engineering has commercially developed isolation systems, known collectively as "SoftRide" [2], which can reduce axial and lateral vibration and shock. Acoustic control has also been investigated. Leo and Anderson [91] have modeled payload fairings to investigate the benefits of proof-mass actuator and piezoelectric acoustic control of the launch vehicle fairing. Similarly, Griffin et al [63] have also examined the use of proof mass actuators for active acoustic control of the fairing. Furthermore, Glaese [60] and Asari [14] discuss the use of active structural-acoustic control with Sensitivity Weighted Linear Quadratic Gaussian (SWLQG) and impedance matching robust control methods on the launch vehicle fairings to reduce the vibroacoustic loading. Though isolation and fairing control have been considered and analyzed, the literature lacks an assessment of the use of embedded actuators in the payload for launch load alleviation. This thesis will help to fill in this gap.

Additionally, shunted piezoelectrics are potentially of use as a form of passive damping during launch. Hagood and von Flotow [68] present the theory and modeling of piezoelectric materials used in a shunting circuit, and relate the results to mechanical vibration absorbers. Moheimani [108] presents a review of the research on vibration damping with shunted piezoelectrics in the decade following Hagood's work. This work can be built upon and adapted to piezoelectric damping of the mirror using embedded actuators.

The launch environment has been studied because of its harshness. Work has been done characterizing the environment and determining the loads and stresses that a system will see. Preliminary work has also been done on isolation and active acoustic control. Also, while it has not yet been applied to launch, there has been work using shunted piezoelectrics as vibration absorbers. These concepts will be built upon to expand the possibilities for launch load modeling and alleviation techniques for actuated mirrors.

2.5 Literature Summary

The previous four categories: telescopes and mirrors, modeling and optimization, controlled structures, and launch, encompass the bulk of the literature that is relevant to this work. This thesis will draw upon pieces of each of these areas to combine them into an integrated mirror design formulation. While each of the fields, on their own, contains a great deal of work (beyond what is discussed here), there are a few aspects lacking.

- **Lightweight, actuated, SiC mirror trade space analysis.** Significant work has been done in determining material properties and manufacturing techniques for lightweight mirrors, but there is no literature available on the effects of the structural and control system design on the mirror performance. Specifically, the effects of geometric design variables, such as rib structure, are lacking.

- **Design optimization and trade space exploration of a high-precision space system early in the design process.** Trade space exploration and MDO during conceptual design has been used in other industries and on very simple space system models. However, the process has not been applied to precision controlled space systems, such as lightweight mirrors, especially during technology development.

- **Lightweight mirror launch analysis.** There is no existing literature on the effects of launch loads on lightweight mirrors, or the constraints that launch load survivability requirements may impose on the design.

- **Launch analysis methodology for use with optimization, isolation, and control systems.** Launch analysis is typically done with a simple load factors or a very complex analysis. An approach to launch load analysis which provides sufficient detail to use in design and alleviation analysis, while still being general enough to use during the conceptual design, is lacking.

- **Launch load alleviation using embedded actuators.** Launch load alleviation has been examined using isolation or payload fairing control. Conversely,

the possibility of using the existing, embedded actuators for passive or active damping during launch has not been studied.

- **Lightweight mirror analysis and design considering operations and launch constraints.** A trade space exploration and analysis of the design of lightweight mirrors to meet operational performance requirements and launch survival constraints has not been performed.

The work proposed herein will fill in these gaps, and combine and expand upon the aforementioned literature to advance the state-of-the-art in lightweight mirror design and the design process for technology development programs.

Chapter 3

Integrated Modeling Methodology for Technology Development

Traditionally, the design of space-based opto-mechanical systems occurs by choosing a point design very early in the design process life cycle. This design is typically chosen based on heritage, engineering judgment, basic design principles, or very simple trade studies. The chosen point design is then developed further, and modeled in great detail as the program progresses. As more is learned about the design through the development of the program, this design strategy can result in many outcomes. These outcomes can be generalized into three categories: the design meets the program requirements, the design nearly meets the requirements, or the design does not meet the requirements. In the first case, where the chosen point design meets the requirements, the design can proceed as planned. A design that nearly meets the requirements is one in which minor design modifications will result in a design that does meet requirements. Alternatively, as more information is obtained about the design, minor requirement exceedances may be allowable, making those designs acceptable. In either situation, the design can be made to meet the requirements with minimal modifications, and the design can proceed. The third case occurs when the design does not meet the requirements, and minor changes will not suffice. In this case, the preliminary design must begin again from the beginning with a new point design. The process is then repeated in the hopes that the new design will satisfy all

requirements. This redesign is both costly and time consuming, and can cause the system to be over budget and over schedule.

When the design has a lot of heritage, there is engineering experience that can be used to guide the initial design. In this case, there are often engineers and designers who have worked with similar systems and understand the technology and challenges. Also, data and models from previous, similar programs can be leveraged to aide in the initial design. While the chosen point design is likely not optimal, it will most likely meet the system requirements and be successful. The point design methodology becomes an issue in systems that are not largely based on heritage designs. When there are major design changes or technology breakthroughs, the engineering experience and past data are lacking, and the probability of initially picking a point design that meets all of the requirements drastically decreases. This is particularly apparent in technology development programs where, by nature, there is very little knowledge about the performance of the system. When considering the complex systems of interest here, the technology development and ground test-beds are still extremely expensive, and thus the design decisions, even in the development phase, must be chosen carefully, such that the probability of success is maximized and the development continues.

Additionally, new designs and technologies represent risks and unknowns, resulting in initial scrutiny. Therefore, the likelihood that a new technology is developed into an expensive, operational system depends on the rewards outweighing the risks of using the new, unproven technology. As such, better performance of the new technology results in a greater probability that the technology development effort will continue and the technology will be implemented in a system. This motivates the desire to choose designs that are optimal, rather than designs that simply meet requirements. The nature of technology development is to expand the performance possibilities. Thus, choosing and developing systems in the highest performing areas of the design space will result in both continued development of the technology, and better performing future systems.

This chapter describes on a methodology for technology development that is based

on integrated modeling. While this could also be used for the design of a system, the focus here is on technology development, as those programs are in greatest need of such a methodology due to the aforementioned reasons. First, Section 3.1 discusses the integrated modeling philosophy and benefits. Then, Section 3.2 continues with how to used models to develop a technology and design. Finally, though this thesis applies this methodology to lightweight, active mirror systems, as discussed in Section 3.3, it could be used for many different complex technology development programs, and Section 3.4 discusses the extensions to other types of systems.

3.1 Parametric, Integrated Modeling

Parametric, integrated modeling is the process by which a system is modeled considering multiple disciplines and variable design parameters. Integrated modeling refers to using a single model for analysis of a system over multiple disciplines [133], while parametric modeling refers to keeping all of the system design parameters as variables, enabling exploration of the design space.

The parametric, integrated modeling method, which will be referred to henceforth as simply "integrated modeling", has a number of benefits. As an example, the parametric nature allow for the analysis of many different types of designs quickly such that they can be compared against one another. Also, by using the single model, the interactions between disciplines can be captured and the design can proceed without iterating between different disciplinary models to converge on a design. This section discusses the details, benefits, and implementation of integrated modeling.

3.1.1 Key Features of Integrated Modeling

The integrated modeling methodology has some key features that make it conducive to technology development, including parameterization, multidisciplinary models, autogenerating models, modularity, adaptability, and computational efficiency.

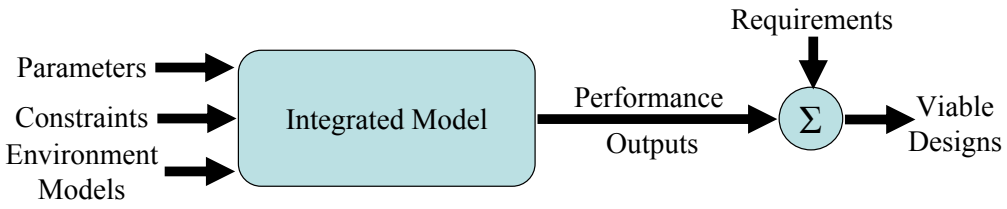

Figure 3-1: Integrated Modeling Schematic

Parameterization The first key feature of the integrated model is that it is parametric in nature, meaning that all relevant design parameters are kept as variables. These parameters are all defined within a single input file, which can then be used to create the model corresponding to those parameters. Consider Figure 3-1, which shows a top-level overview of the integrated modeling process. Here, the parametric inputs are all kept separate from the model, and used with the integrated model for each design instantiation. This allows the same model to be used to analyze many different designs.

The types of parametric inputs can range widely, and examples include geometries, material properties, and control systems, among others. Additionally, high level, architectural variables can be defined as parameters, allowing large design variations, such as the type of mirror in the telescope or the structural configuration of a mirror. For example, Figure 3-2 shows the back side of two different rib-stiffened mirror segments. These two mirror models are created using the same parametric model, with only a single input parameter, defining the number of ribs, changed. By maintaining many design parameters as variable, a wide variety of designs can be created and analyzed using the same integrated model.

Multidisciplinary Model The second important feature of the integrated model is that it combines multiple disciplines into a single model. Traditionally, subsystem models are analyzed separately for each discipline. For example, structural, optical, and thermal models of a telescope would all be created independently. However, when designing and optimizing a complex system, it is important to consider all of the relevant disciplines simultaneously, so that an overall high performing design can

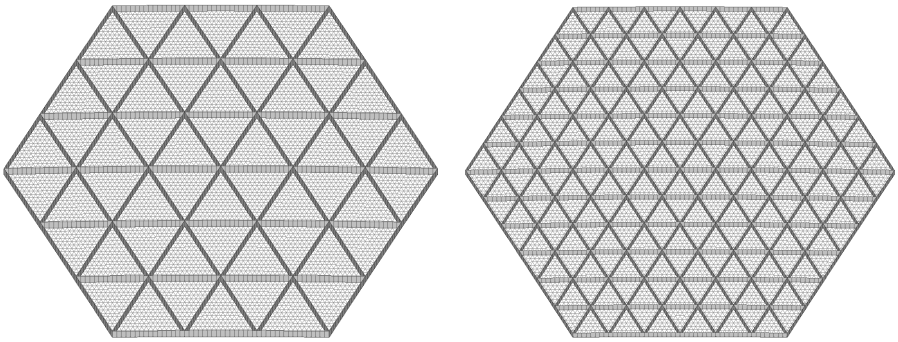

Figure 3-2: Two Mirror Models with Only a Single Parameter Changed

be found. Additionally, with certain types of complex systems, there are potential interactions between disciplines that must be captured. For example, the active mirror considered here necessitates considering the structural and control design simultaneously [37].

Another benefit of using a multidisciplinary model is that all of the analyses are performed on the same model, thereby providing configuration control. When using individual subsystem models, it is possible to have design parameters that are not the same or minor differences between the various subsystem models, resulting in different designs being analyzed. By using the single multidisciplinary model, these configuration management issues are solved, and all modeling information is kept in a single location.

As an example, the mirror model considered in this thesis captures the following disciplines:

- Structural finite element modeling
- Optics
- Control systems
- Vibroacoustic launch loads
- Disturbance analysis

Rather than using five distinct models, a single model is used, and interactions between disciplines are captured.

Auto-Generation The next important feature in the integrated modeling methodology is the use of auto-generation methods, in which models are automatically created and run given only a set of input parameters. For example, considering Figure 3-1, given specific input parameters, the integrated modeling block is entirely automatic and creates the performance outputs without any manual intervention.

Removing all manual intervention from a model can be a challenge. Specifically, when finite element models are necessary, as is the case herein, all of the finite element meshing must be completed automatically. This includes both the geometry of the system, as well as the finite element mesh layout and density. Typically, finite element meshes are generated using meshing software on a computer aided design (CAD) model, but this method involves manual intervention. Rather, finite element meshing capabilities, based on the parametric inputs, must be developed. Furthermore, input parameters can be used to define fidelity, mesh density, and other outputs associated with model accuracy and processing performance. More detail on the auto-meshing logic can be found in Reference [80].

Using auto-generation allows a variety of models, generated from a variety of inputs parameter, to be analyzed in batch. The auto-generation is necessary for any trade space exploration or optimization that may be desired.

Modular Modeling Environment The integrated model must also be adaptable so that it can be used to analyze many different types of designs, and also be adapted to changing expectations and information, as will be described in Section 3.2. This is best accomplished through the use of a modular modeling environment. By keeping all of the functions and routines in the model separate, they can be added to, or swapped in and out, without affecting other portions of the model. This can be manifested through the addition a new module within an existing type of analysis, such as adding an additional control system to an existing model, or through the addition of a new type of analysis to be run on the same model. In both cases, maximizing adaptability by utilizing the modular modeling framework allows the capabilities of the model to be easily expanded and adapted.

Again, consider the very basic model overview in Figure 3-1. The integrated modeling block can be further broken down into different modeling components, an example of which can be seen in Figure 3-3(a). Here, the integrated model is broken into finite element model creation, finite element model analysis, and state-space analysis, which includes the disturbances and control systems. Each of these modeling components can be further broken down. For example, consider the state-space analysis, which can be broken down into creation of the state-space model, the addition of control systems, the disturbance inputs, and the disturbance analysis, as seen in Figure 3-3(b). These modules could also be broken down further into their respective components. They can also be substituted in and out of the model, based on the specific input parameters. For example, there could be many different possible control systems; the inclusion or exclusion of each would be defined by the input parameters. Also, these control systems could be implemented simultaneously, resulting in multiple control systems, or they could represent different control algorithms acting on the same set of inputs and outputs, where only one is used and the algorithms are being compared against one another. In either circumstance, the modular environment provides the flexibility to alter the system without major changes to the model.

An additional benefit of the modular modeling environment is the ability to analyze the entire model or smaller parts of the model. For example, consider a full segmented mirror system, as described in Chapter 1, where one may want to analyze the entire primary aperture composed of many mirror segments, or focus on the design of a single segment. Or, one may want to analyze only the on-orbit performance or only the launch survival of the mirror, or consider both environments simultaneously. The modular environment makes these types of analyses possible without major modifications to the integrated model.

Computational Efficiency Finally, the level of detail is an important consideration in integrated modeling. The models considered here are physics-based, and must include a certain level of detail to accurately capture the response of the true

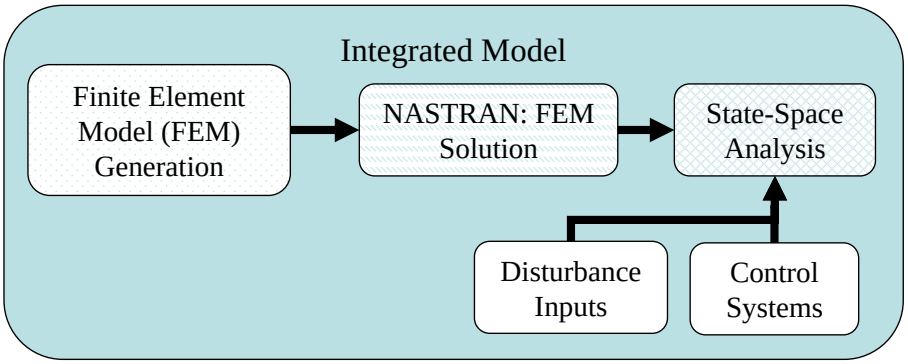

(a) First Level

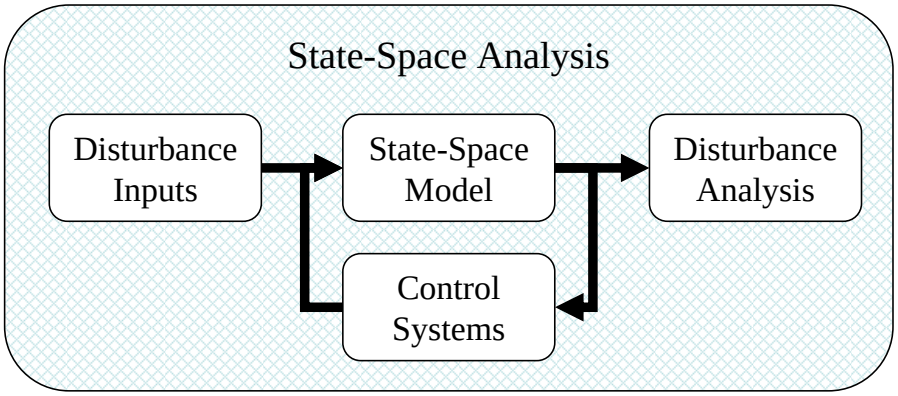

(b) Second Level

Figure 3-3: Integrated Model Breakdown

system. However, the level of detail must be kept low enough that the model runs relatively quickly, and many designs can be analyzed. Therefore, the models are not so detailed that they include very specific design aspects such as bolt patterns, but rather include enough detail to capture the salient effects of major design decisions. The details would then be added once a specific design is chosen and developed. Additionally, focusing on only the relevant portions of the system can eliminate some of the complexity of the model without compromising the integrity of the model of aspects of interest.

3.1.2 Integrated Modeling Benefits

Integrated modeling has a number of benefits that make it useful in the preliminary design phase and during technology development. As discussed above, the integrated modeling considered in this thesis uses auto-generating models based on parameterized inputs, considers multiple disciplines, and is adaptable and upgradeable due to the modular modeling environment.

The first benefit of this integrated modeling formulation is that it easily allows for trade space exploration or optimization. In trade space exploration, many different designs, defined by different values for the input parameters, can be analyzed with the integrated model to determine the desired performance outputs. These many different designs can be compared in terms of the performance metrics to determine which design or families of designs are best for the particular metric of interest, or to determine the trade-offs between performance metrics. For example, Figure 3-4 shows an example trade space. Each point in the plot represents a distinct design with a unique set of input parameter values, and the two axes represent two performance metrics (J_1 and J_2), where lower values for both metrics are better. By creating an integrated model, rather than a point design, many designs can be analyzed and compared against one another to determine those that are most promising. This is particularly useful when considering a system with conflicting performance metrics, where a design that performs best according to the first performance metric is ill-suited when considering the second performance metric, and vice-versa. This

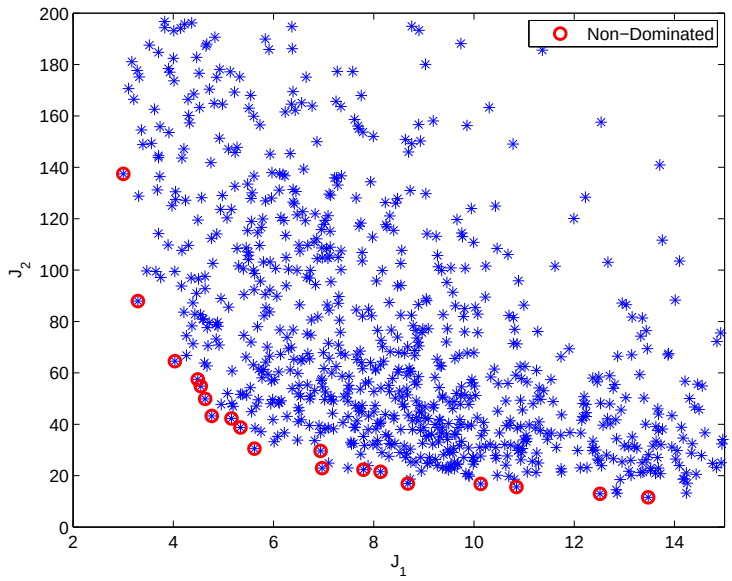

Figure 3-4: Example Trade Space

results in a concept known as Pareto optimality, where considering multiple performance metrics, there is no single optimal design. Rather, a design can be Pareto optimal if improving the performance with respect to one metric requires decreasing performance with respect to another metric, resulting in a set of Pareto optimal points defined by the front closest to the origin in Figure 3-4 that are circled in red. The trade space exploration can help find the designs that will perform best when considering both requirements or to strike the proper compromise.

In addition to the trade space exploration, it is possible to add optimization routines that connect the performance outputs to the parameter inputs and optimize over a certain objective function. Integrated modeling is becoming more prominent in many industries because of this ability to consider multiple disciplines and explore the design space, as was described in Section 2.2.

Additionally, the integrated modeling framework allows different aspects of a design to be examined or validated in isolation, or in combination with other aspects. For example, consider a system with two performance metrics from two types of analysis. By using the integrated modeling framework, the same model can be used to analyze and optimize the system with respect to either individual performance metric,

or to perform a trade space exploration or multi-objective optimization considering both performance metrics.

Another benefit of the integrated modeling framework is the adaptability and flexibility afforded by the modeling environment. As the technology is developed, test data becomes available, and other issues are discovered, the model can be continually updated and adapted to reflect the current state of the technology. Section 3.2 discusses the adaptable nature of the model, as specifically applied to model-based design.

3.2 Model-Based Design

As a result of recent increases in available computational power, integrated modeling can be used to analyze many different designs, rather than a single point design, as described in Section 3.1. By utilizing the adaptability available in the integrated modeling framework, this can be extended further to encompass the design process though model-based design, where model-based design refers to the process by which an integrated model is used to guide the development of a technology or the design of a system.

It is possible to obtain a great deal of data through the use of trade space exploration with an integrated model. Additionally, as a technology advances, test data is generated from prototypes or test set-ups. While it is desirable to have as much data as possible, from both analysis and test, it can become difficult to manage the data in an effective manner. Also, as more tests are run on various aspects of the technology that may be undergoing development at different contractors, it can become disjointed, and the data is not always captured in an efficient way, oftentimes resulting in repetition of work in the future. A model-based design, where the integrated model is central to the design process, can eliminate many of these difficulties and inefficiencies, ultimately resulting in a more successful program.

This section discusses model-based design, specifically using the integrated modeling philosophy described in Section 3.1. Then, the adaptability and evolutionary

aspects of the model are discussed, as applied to technology development programs. Finally, the use of the model as a source of corporate knowledge is proposed.

3.2.1 Model-Based Design Overview

Model-based design is the process by which one uses integrated models to guide designs, or technology development efforts, rather than choosing and developing a single point design. This has many benefits discussed in the beginning of this chapter, including finding optimal (or near optimal) designs to maximize performance and increase the probability of adopting a new technology in operational systems. In model-based design, the integrated model is central to the design process. The model is used to determine promising families of designs, where promising families of designs are designs with similar sets of parameter inputs and performance metric outputs that are in close proximity to the Pareto optimal front. Additionally, the model is used to determine areas where more data or information may be needed, including gaps in the test data necessary to validate the model, or areas with high sensitivity to uncertainty. This information from the model can then be used to develop tests and prototypes, which are in turn used to validate the model, as well as provide insights into other aspects of the technology that may be important. Those aspects can then be incorporated into the model, resulting in an iterative process of testing, archiving, analyzing, and optimizing the design, with the model at the center of the process.

In this framework, the model is the central component of the design; all other efforts are in support of the model. For example, a primary purpose of tests and prototypes are to validate the model. A validated model will assist in designing many systems using the technology, rather than a single test or prototype which is only valid for that particular instance. Also, the model is used to guide the tests and prototypes that are built, such that the best portions of the design space are fully explored. It also provides a central archive where lessons learned are captured in case vendors are lost or facilities are dismantled.

Consider Figure 3-5, which shows the relationship of the model to various other aspects of the development program. Notice that in this framework, the model is

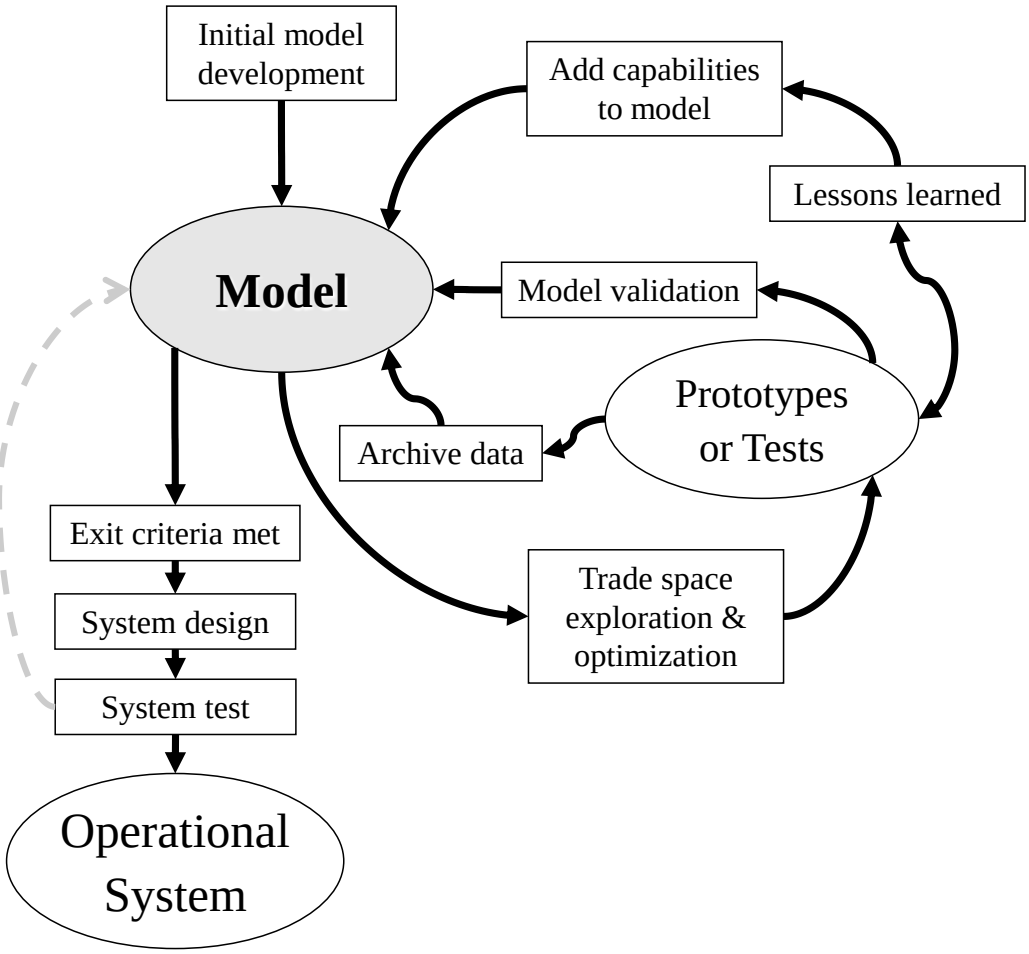

Figure 3-5: Model-Based Design Schematic

central. The initial model development serves as the foundation for the integrated model. The model is then used to explore the design space, from which tests and prototypes are derived. The tests and prototypes are chosen to validate the model and discover any missing components in the model. Also, the lessons learned, as will be described further in Section 3.2.2, are fed back into the model as new capabilities, requiring an update of the model. Additionally, the test data is archived directly within the model, such that all information pertaining to the development is kept in a single location. Note that this is an iterative process, and most technology development programs will use multiple tests or prototypes, either simultaneously or sequentially. The evolutionary nature of the model, as described in the next section, enables this iteration, and also allows the same model to be used throughout the development process, rather than for a single system or prototype. As designs change or as other programs develop similar prototypes, the model can adapt to absorb this data and track programmatic evolution. Eventually, the technology reaches a level of maturity as specified by exit criteria, which includes, but is not limited to, a validated model with test data matching the model and a set of designs that meets the system requirements. The validated model can then be used to design the operational system to the specifications, and the design will be modeled in greater detail, then built as an operational system. If desired, the model could also be used during operations. If it is continually updated using on-orbit data, it can be used to identify subtle changes due to changing properties to give advanced notice of impending problems. Note that the same model can be used for multiple systems due to the parametric nature of the model thereby leaving a knowledge and experience-based legacy to future programs.

3.2.2 Evolutionary Aspect of Modeling

A key aspect of the model-based design is the ability to update and adapt the model to accommodate test data, lessons learned, and new analyses. Section 3.1 discussed the use of a modular modeling environment in order to maximize the versatility and adaptability of the model, which is particularly important when considering evolving a model alongside a development program. In the iterative design process described

in Section 3.2.1, the model must be updated to include any insights obtained from testing.

Consider the temporal aspect of a technology development program. As time moves forward, the technology is modeled, analyzed, and tested, resulting in a greater knowledge of both the performance potential and limitations of the technology. These efforts can, and often do, lead to unforeseen insights. One may encounter a factor that affects the performance that was previously overlooked. Or, a disturbance source could have a significantly greater or smaller effect than initially thought, necessitating the addition of a disturbance analysis or source, or rendering a previous analysis unnecessary. Alternatively a certain design option could be found inferior to another option in all respects, changing the focus of the development to the superior designs. Regardless of the exact change, technology development programs have a strong temporal variation, and it is desirable to have a model that can adapt over time to include those variations as well as archive the lessons learned from abandoned development paths.

Not only should models be updated and evolved, but model uncertainty factors (MUFs) should also be updated over time based on the knowledge gained in the development process. MUFs are uncertainty factors applied to model results that account for the uncertainty in the model. A simple model without validation would have a very high MUF, indicating that the results from that model cannot be trusted to be accurate. However, as the model evolves to include validation from a number of prototypes, and the issues in the technology are better understood, the MUFs can be reduced, indicating that one trust the results of the model to be accurate within a smaller factor, thus reducing the amount of over design necessary.

In addition to encountering unforeseen changes in the technology development, it is also common to have multiple entities working on the same technology. Especially in complex system development programs where there are multiple aspects to the design, it is likely that multiple groups will be working on different aspects of the technology, resulting in multiple prototypes or test set-ups. In order to effectively manage all of the efforts and be certain that all interactions are captured, the model

must be able to adapt to each test. By using the integrated modeling philosophy, the model can be quickly and easily adapted to mimic each test and validate the model against that test.

Each of the issues enumerated above, which are typically encountered by technology development programs, can be solved through the use of an evolutionary model. This requires the up-front effort to create an integrated model in a modular environment, as described in Section 3.1. Additionally, someone must be responsible for the model and keep the model updated to reflect the current state of the technology. As mentioned above, this requires validating the model, adding analyses, and including test data, among other model maintenance responsibilities. However, this initial effort will save time, money, and repetition of work in the long run, as well as result in a higher performing system due to the ability to optimize the validated model and minimize programmatic amnesia.

3.2.3 Integrated Modeling as a Source of Knowledge

In addition to the evolutionary aspect of model-based design, which allows the model to change with time and additional information, it can also be used as a repository for knowledge about the technology development. In complex development programs, there is often a great deal of data generated, either through modeling or testing. Sometimes the same type of data is generated multiple times due to inaccessibility of the original data to the interested party. The model-centric framework provides a convenient location to store all data, such that all information, both from models and tests, are stored in a single location and are easily accessible and locatable. With this philosophy, the model then becomes the source of knowledge about a program, ensuring that work is not lost. Again, this requires someone to maintain the model, and to add the data generated through testing. However, after the initial investment in setting up the integrated model, the addition of data to the model is not difficult.

Additionally, using configuration management, the model provides an archive of the previous generations of the technology, as well as the lessons learned. The model is adapted and upgraded in response to any lessons learned, and thus the older ver-

sions of the model archive the history of those lessons. With this approach, a failed technology development pathway is not seen as a failure of the technology, but instead is seen as an education that facilitates identification of a better pathway.

3.2.4 Model-Based Design Summary

This section describes the model-based design methodology, in which the model is kept at the center of the technology development program. This has many benefits, including a model that evolves with time and captures all knowledge about the system, rather than a series of individual models for each test or prototype. This increases efficiency and ultimately results in a better performing system. The integrated modeling and model-based design framework is illustrated using the case of lightweight, active mirrors. Section 3.3 discusses the specific application of this philosophy to the mirrors, while Section 3.4 discusses the general applicability to other systems.

3.3 Application to Lightweight, Active Mirrors

The are clearly many benefits of using integrated modeling and model-based design for technology development programs. Lightweight, active mirrors are a good example of a technology development effort that can benefit greatly from such a methodology. First, lightweight, active mirrors represent a significant deviation from traditional telescope mirror designs. Traditional, monolithic, glass primary mirrors have heritage and are understood quite well. However, lightweight, SiC mirrors have very little heritage on which to base a new design. The high degree of actuation, and specifically surface-parallel actuation, is another substantial change. Traditional glass mirrors are passive, and most actuated mirrors that have been developed thus far are either for ground-based systems or very small deformable mirrors, in which surface-normal actuation is used. Surface-normal actuation requires a back structure of at least similar mass as the mirror to provide reaction forces. While this is possible with ground based systems, or very small mirrors, it is not the best option for a lightweight

mirror that will be launched into space. Therefore, there is very little on which to base the design of a lightweight, active mirror system to ensure that it performs well.

Furthermore, the potential performance improvements in telescopes with the advent of lightweight, active mirrors have caused them to be of significant interest to the community. Therefore, there are multiple entities that are working on various aspects of the technology development program, according to their specific expertise, such as manufacturing techniques, control strategies, and prototype development. Managing a variety of efforts working toward the same goal is always a challenge, and this case is no exception. Therefore, a central modeling effort, capturing the work of the various groups, would assemble the knowledge so that the efforts are cooperative and neither repetitive nor lacking in key areas.

Finally, lightweight, active mirrors are a good candidate for integrated modeling due to the complexity of the system. The mirrors considered here are extremely complex systems which must be accurate to optical tolerances (nanometers). This involves structural design, disturbance analysis, control systems, and optics, all combined within a single model in order to capture all of the effects of the design on the performance of the system. Therefore, the design of lightweight, active mirrors will be used to demonstrate the methodology described in Sections 3.1 and 3.2. The remainder of this section discusses the integrated model used throughout this thesis, as well as the evolution of the model over time and the use of it to design systems that perform well.

3.3.1 Lightweight, Active Mirror Integrated Model

The design of lightweight mirrors necessitates a number of disciplines and design areas. Some of the design aspects that must be addressed for lightweight mirrors to be utilized in operational systems are:

- Mirror structural design
- Optical design and performance
  - Primary mirror

  - Secondary, tertiary, fold mirrors, etc.

- Wavefront sensing
- Thermal design
- Control system design
- Launch survival
- Manufacturing

It is clear that the development of lightweight, active mirrors involves many different aspects, too many to be included in this thesis. Therefore, as discussed in Section 1.3, the scope is decreased to include only those issues that are directly affected by the primary mirror design. This includes the structural and control system design with regards to high spatial frequency wavefront error, low spatial frequency correctability, and launch survival. However, though they are not included here, the other aspects of the design of lightweight mirror systems could be added to the model within the modular framework in the future.

The design of the primary mirror requires the use of multiple disciplines. These include: structural finite element modeling, optical performance modeling, control system analysis, vibroacoustic disturbance analysis, and on-orbit disturbance and actuation analysis. Also, the model is physics-based, such that it includes enough detail to obtain the performance of the system without heritage-based, empirical models.

The mirror model used in this thesis is based in MATLAB. The modeling process is illustrated in Figure 3-6. MATLAB is used to define the input parameters, and create the mirror structural model, including geometry, mounting configuration, and material properties. This is formatted as a finite element model (FEM) that can be used with the MSC.NASTRAN finite element solver. Two different types of analyses are considered: a quasi-static analysis for on-orbit performance, and a dynamic analysis for launch. These analyses will be discussed in detail in Chapters 4 and 5. The NASTRAN results are brought back into MATLAB, where control systems are added and the analysis routines are run, including the optical performance and disturbance

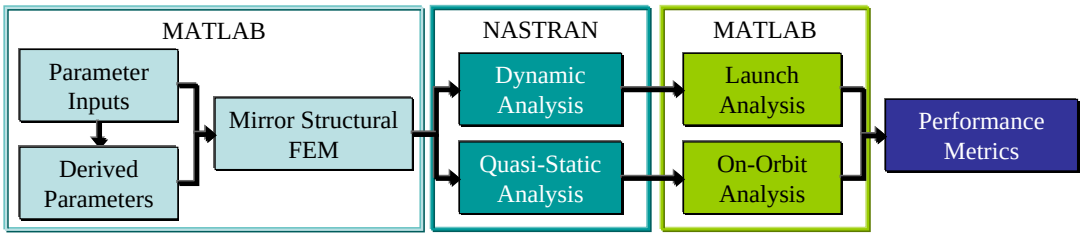

Figure 3-6: Lightweight, Active Mirror Model Overview Diagram

analysis. Notice that there are two distinct analyses routines: a quasi-static on-orbit analysis, and a dynamic launch analysis. These analysis routines necessitate different types of analyses, but are still based on the same input parameters and mirror structural model. In this manner, other, independent analyses could also be added.

Additionally, as discussed in Section 3.1, the model is completely modular, such that various components can be added, subtracted, or substituted, as long as the input/output structure of the functions are retained. This modularity is manifested throughout the model. One example is in the structural FEM. Figure 3-7 shows a schematic of the FEM. The geometry, mounting configuration, and material properties are all defined based on the inputs, and each block represents a function (note that the blocks may include more functions not shown at this level of detail). Notice that the geometry is broken down further to allow specification of the type of mirror as either monolithic, segmented, or single segment. Also, single segment code is the foundation for the segmented mirror, and the actuator code is used in all cases. By keeping the inputs and outputs consistent, this substitution is possible, and the rest of the model can continue, regardless of these parameter choices. Additionally, though it is not shown here, it is possible to have multiple types of mounting configurations. The modularity is also present in all other parts of the model not illustrated here.

The mirror model will be discussed in detail in Chapters 4 and 5, including the different components mentioned here, and will be used throughout this thesis. It is set up such that it follows the principles laid out in Section 3.1.

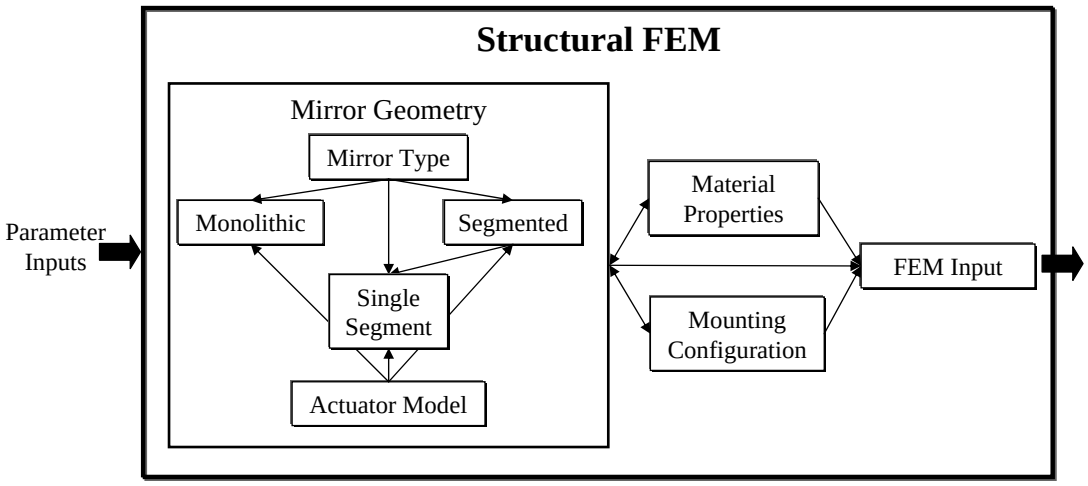

Figure 3-7: Mirror Structural Model Diagram

3.3.2 Mirror Model Evolution

The evolutionary aspect of model-based design can also be illustrated with the active mirror example. This section presents some of the history of modeling of lightweight mirrors for space telescopes.

Initially, the modeling effort for lightweight mirrors included the entire telescope, as opposed to only the primary mirror [134, 34, 82]. This included the bus, solar panels, primary mirror, secondary mirror, tertiary mirror, optical bench, secondary support structure, and mirror support system. One could model a monolithic or segmented primary mirror, and the segmented mirror contained a variable number of segments. Also, the secondary support structure, which supports the secondary mirror, could take multiple forms, including a tower, a tripod, and a hexapod. Figure 3-8 shows an example realization of the original telescope model. However, as time progressed, it became clear that the key difficulty in the lightweight telescope was the active, primary mirror; the other aspects of the system are more standard and based on heritage systems. Also, the primary mirror necessitated a higher fidelity model than the rest of the structure. This resulted in a model with varying fidelity, which is not ideal [73]. Therefore, the focus began to shift to include only the higher fidelity, primary mirror model.

The shift from the entire telescope system to only the primary mirror was possible

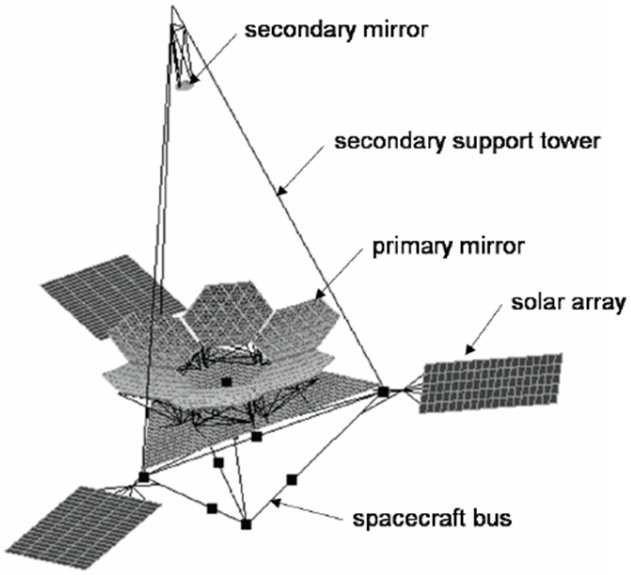

Figure 3-8: Example of Entire Telescope Model Instantiation

due to the modular nature of the model, as described above. The rest of the telescope could be eliminated, without affecting the mirror model, provided that the mounting, inputs, and outputs were consistent.

In addition to the shift from the telescope to the mirror, the types of disturbance analyses also changed over time. Initially, the model included the analysis of on-orbit dynamic control through layered control systems [31, 32]. Specifically, the embedded actuators in the mirror were used dynamically in a high-bandwidth control system to eliminate the jitter and wavefront error distortions resulting from dynamic disturbances, such as reaction wheel imbalance. While this did improve the results, the magnitudes of the initial (and final) errors due to the dynamic disturbances were small in comparison with other, quasi-static disturbance sources. Therefore, the added complexity of the higher bandwidth control system was deemed unnecessary and henceforth excluded since there were many other issues to solve first. In the future, this type of control may become warranted, and the control systems and analysis routines could once again be included in the model.

Also, as lightweight, active mirrors progressed, more disturbances and issues were discovered. First, traditional, monolithic glass mirrors are large, massive, and sturdy,

and hence survive launch without great difficulty. However, the lightweight, SiC mirrors are much less massive and have lower fundamental frequencies making them more susceptible to launch load-induced stress. This revelation was made after significant progress had been made into the development, and was then included in the integrated model. As will be seen in Chapter 5, this concern is warranted, and the design must take launch loads into consideration at the earliest phases so that launch survival is ensured.

Similarly, after a prototype mirror system was built, it was found that the radii of curvature between the mirror segments varied slightly due to manufacturing imperfections. In order to phase the mirror, the radii must be matched, which is accomplished using the embedded actuators. However, when the actuation was applied, the high spatial frequency residual error that was induced by the actuators was much greater than anticipated, and became a serious issue. Again, this phenomenon was added to the integrated model, and the results from the prototype were authentically represented in the model, so the design of future mirrors can account for the high frequency residual error.

Though there is more to this history, it is apparent from the examples above that the model has changed with time to reflect the current state of the technology. These changes have been both to eliminate unnecessary or extraneous portions of the model, and to add analysis routines to account for issues that were not previously considered. By evolving the model with time, the same model can be used throughout the life cycle, saving the time and effort of remodeling for every new analysis or prototype.

3.3.3 Integrated Modeling to Guide Mirror Design

As will be shown in this thesis, the integrated model can be used to discover portions of the design space that were previously unconsidered. By using trade space exploration and optimization, designs that perform better than the existing prototypes can be found. Also, by validating the model against all of the prototype data available, one can trust that the chosen designs will indeed perform as expected. The insights gained from the modeling effort are ideally used to determine the next prototype, which will

potentially reveal another issue, and the process will repeat until the technology converges and is sufficiently developed to be used in an operational system, as was described in Section 3.2.

In addition to using the model to find high performing designs, it can also be used to analyze the uncertainty in the designs. By propagating parametric uncertainties through the model, the performance can be bounded, which is extremely valuable in the design phase. Specifically, this can be used to refine MUFs, as was discussed in Section 3.2.2.

3.3.4 Summary of Mirror as an Integrated Model Example

This section has presented a brief overview of the integrated model for lightweight, active mirrors. By framing the model in an appropriate manner, it can evolve with time to reflect the current state of the technology. The remaining chapters in this thesis will use this model and approach to assist in the design of lightweight, active mirrors. Specifically, Chapter 4 discusses the structural model, and the quasi-static, on-orbit analysis, as well as results pertaining to the on-orbit environment. Chapter 5 continues with the vibroacoustic launch analysis, and illustrates how to use the model to design for launch. Finally, Chapter 6 illustrates the full benefits of the integrated modeling technique by simultaneously designing for on-orbit and launch.

3.4 Application to Other Systems

Though this thesis illustrates the integrated modeling methodology as applied to the development of lightweight, active mirror systems, the same methodology is useful for a variety of other systems. The design of any complex system requiring multiple disciplines could benefit. The types of structural, disturbance, control, and optical modeling contained herein is particularly applicable to other complex, opto-mechanical systems, and this method could be very easily adapted to systems such as those. However, it does not preclude using the same type of methodology, with different modeling techniques, on other types of systems.

Additionally, the lightweight, active mirror systems described herein can be considered a technology development program. That is, it is in the modeling, prototyping, and design stage. It is envisioned that this methodology will work best for programs in the development stage. Very early conceptual systems that are less developed can be difficult to model with enough detail due to the problem being ill-defined. In order to use physics-based modeling with sufficient detail, it is advisable that the basic concept is somewhat refined, though this could be adapted to be used with less detailed models for very early concepts as well. Also, when systems are no longer in the technology development phase, and are in the production phase, there usually exists a very detailed model of the system, and enough information to build systems that meet requirements without the full modeling effort presented here. That is not to say that the production systems would not benefit from the knowledge gained through the integrated modeling effort, but the time and budget necessary for such an effort may not be warranted for the performance gain beyond the requirements for a system that is in production. As touched about at the beginning of this chapter, systems that are in the development phase are often in a state of uncertainty. They represent risk to highly complex, expensive systems, so the performance gain reward must be worth the risk, motivating finding the best performing designs.

Therefore, though this thesis will focus on lightweight, active mirrors hereafter, the integrated modeling could be useful to many different systems, and ultimately result in technology development programs that achieve their full potential.

3.5 Integrated Modeling Summary

This chapter has presented an integrated modeling methodology for use in technology development programs, with specific application to opto-mechanical systems. By using a parametric integrated model built within a flexible modeling framework, one can use the model to identify high performing designs. Also, the model can evolve with time in order to remain relevant and useful over the life cycle of the program, and even be used to determine real-time fixes for malfunctioning systems. This methodol-

ogy is applied to the development of lightweight, active mirrors, in this thesis, as will be discussed in the proceeding chapters. However, it could also be applied to many other types of systems, provided they are multidisciplinary, complex, technology development programs.

Chapter 4

Mirror Model and On-Orbit Performance

As described in Section 1.1.2, lightweight, active mirrors have great potential for increasing the performance and decreasing the cost of space-based optical systems. The segmented, rib-stiffened, highly actuated construct addresses many of the issues associated with larger aperture systems, and can enable space-based optical systems with greater capabilities. However, there are a number of remaining design challenges with lightweight mirror technology. Two such challenges are on-orbit optical performance and launch survival, as discussed in Chapter 1.

The integrated modeling methodology described in Chapter 3 is used to guide the design of lightweight, active mirrors. This chapter details the mirror model, discussing the structural model and assumptions. Additionally, the on-orbit performance model and analysis is presented.

4.1 Model Overview

The mirror model combines a number of disciplines, including structures, controls, optics, and vibroacoustics. The mirror structural model is created using finite element modeling, described further in Section 4.3. The structural model is then used for two types of analysis: a quasi-static analysis for on-orbit performance, and a dynamic

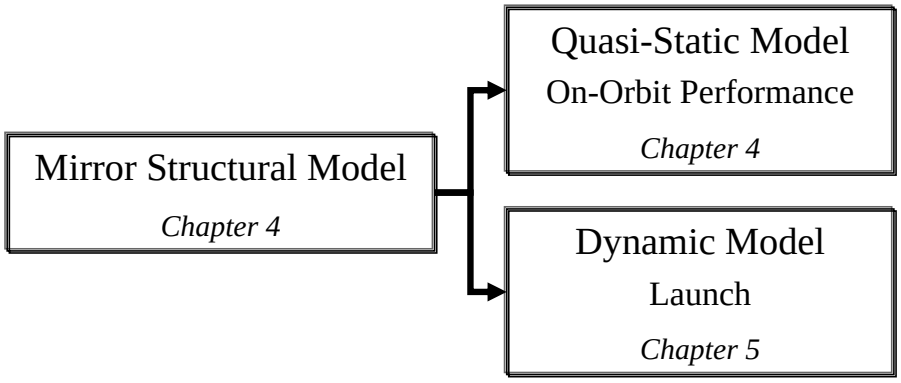

Figure 4-1: Mirror Modeling Diagram

analysis for launch.

The quasi-static analysis for on-orbit performance is described in detail in Section 4.4. The metrics for on-orbit performance considered here are low spatial frequency correctability of the mirror and high spatial frequency wavefront error resulting from low spatial frequency actuation. The time scales of the disturbances of interest in this analysis are very long and can be considered quasi-static. This allows the transient dynamics of the mirror system to be ignored, and the system and control to be considered quasi-static. The quasi-static assumption results in significantly simpler control algorithms and analysis. Section 4.4 discusses the quasi-static assumption and model in greater detail.

The second analysis is a dynamic analysis used in the launch simulations. Launch is a highly dynamic process, and any control systems used during launch need to consider the full dynamic system. Therefore, normal modes analysis and state-space modeling are used for the launch analysis, as is described in detail in Section 5.1.

The same parameters and structural mirror model are used for all environments and performance metrics. However, two different types of analyses are performed for the two different environments. The remainder of this chapter will discuss the mirror structural model and the quasi-static modeling for on-orbit performance. Chapter 5 will discuss the dynamic model for launch. The block diagram in Figure 4-1 overviews the modeling organization in this thesis.

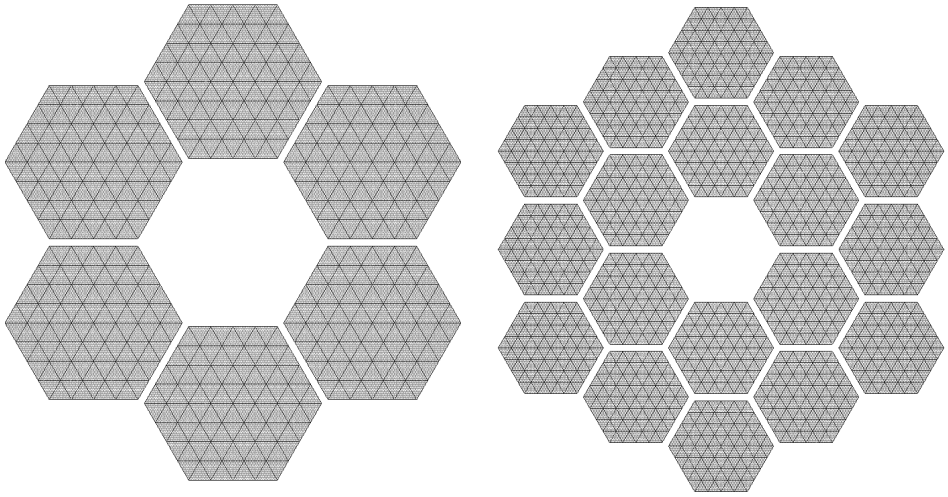

Figure 4-2: Primary Apertures Composed of Multiple Mirror Segments

4.2 Assumptions

As discussed in Chapter 3, it is important to keep the integrated model simple enough to run quickly, yet still capture the important aspects of the design. In keeping with this requirement, a number of assumptions are made about the lightweight, active mirror system. This section details those assumptions and their implications.

Section 1.1.2 suggests achieving large aperture systems through segmented apertures composed of multiple, smaller mirror segments. The mirror segments can be combined in a number of ways to obtain primary mirrors with varying overall diameters and numbers of mirror segments. As an example, Figure 4-2 shows primary mirrors made up of varying numbers of concentric rings of hexagonal mirror segments. The exact number and layout of segments will be mission specific.

However, in this thesis, only a single mirror segment is modeled. Using a single segment limits the size and the complexity of the model, as well as generalizes the result to be applicable regardless of the exact segment layout and support structure. Additionally, the design issues of interest in this thesis, namely on-orbit optical performance and launch survival, can be accurately analyzed on a single mirror segment. The mirror segment is mounted using three kinematic bipod mounts, which are connected to a rigid back structure. This implementation results in a worst-case

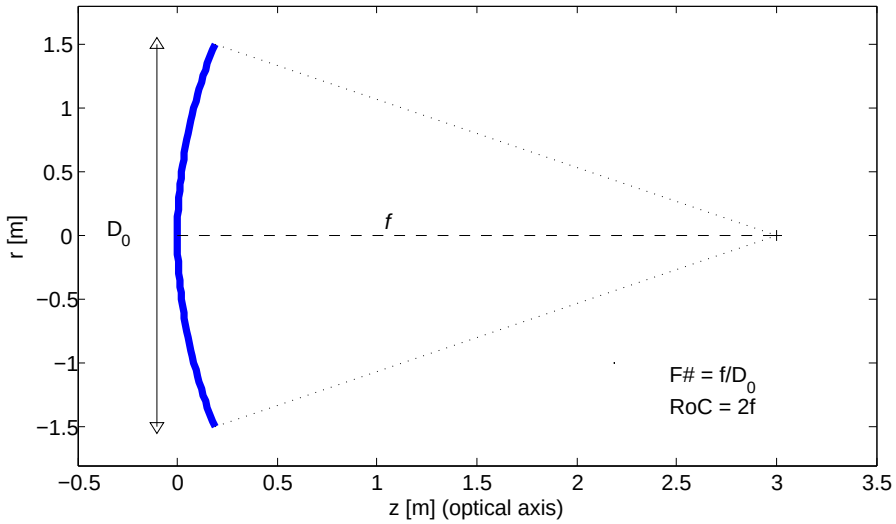

Figure 4-3: Schematic of Monolithic Mirror and Optical Definitions

scenario for the transmission of vibratory loads during launch. In reality, the spacecraft structure contains damping that would absorb some of the loads before they reach the mirror. However, without a detailed model of the spacecraft, it is difficult to accurately estimate the absorption of the loads. Therefore, since launch survival is critical, the worst case is assumed. The on-orbit performance metrics can be defined relative to a mirror segment, so they are unaffected by the single segment assumption. Therefore, a single mirror segment model is used throughout this thesis, while the other mirror segments and the spacecraft are excluded. By including only a single segment, the mirror can be modeled in adequately high detail to provide accurate results, while maintaining the computational expense at a level low enough to perform optimization and trade space analyses.

Modeling a single segment versus a primary aperture composed of multiple segments results in a few nuances in the optical definitions. The mirror curvature is assumed to be parabolic, and can be defined in terms of basic optical quantities. Consider first a monolithic mirror of diameter, D_0, and focal length, f, defined as the distance along the optical axis from the surface of the mirror to the point where the light will focus. Figure 4-3 shows this configuration in two dimensions for clarity. The $F\#$ of the mirror is defined as:

$$F\# = \frac{f}{D_0} \tag{4.1}$$

The $F\#$ describes the curvature, or, as it is often referred to, the "speed" of the mirror. A mirror with a low $F\#$ is a fast, highly curved mirror, while a high $F\#$ indicates a slower, flatter mirror. The mirror can also be described in terms of a radius of curvature (RoC). For a parabolic mirror, the RoC at the center of the mirror (on the optical axis) can be shown to be:

$$\text{RoC} = 2F\#D_0 = 2f \tag{4.2}$$

Now consider a mirror that is made up of multiple segments. Again, projecting this to two dimensions for clarity, Figure 4-4 shows a slice of a seven segment (or six segment mirror with a hole in the place of the center segment) system, as was shown in the left of Figure 4-2, with the same $F\#$ as in Figure 4-3. Since the $F\#$ depends on both the diameter and the focal length of the system, matching the $F\#$ of a single mirror segment to the $F\#$ of an entire primary aperture results in a very different focal length and radius of curvature. *Therefore, the $F\#$ of the mirror segment is specified assuming that the mirror is one segment in a seven segment mirror, and the focal length and RoC are calculated to match that assumption.*

As an example, if the same $F\#$ that is specified for the entire aperture in Figure 4-4 is instead specified for the individual mirror segment, and that mirror segment is a part of a segmented aperture, the resulting curvature would be as is shown in Figure 4-5. As is visible in the figures, the factor of three difference in the total diameter and segment diameter results in a factor of three difference in the focal length, and results in a different mirror curvature. Other definitions could have been chosen, all of which would result in similar variations of the mirror curvature, the only difference being the ranges of possible values. Since the segment will be used as a part of a larger, segmented aperture, this definition is used throughout the remainder of the thesis.

Another assumption is that the mirror is modeled as an on-axis segment. When a mirror segment is a part of a larger aperture, the center of curvature is in the center

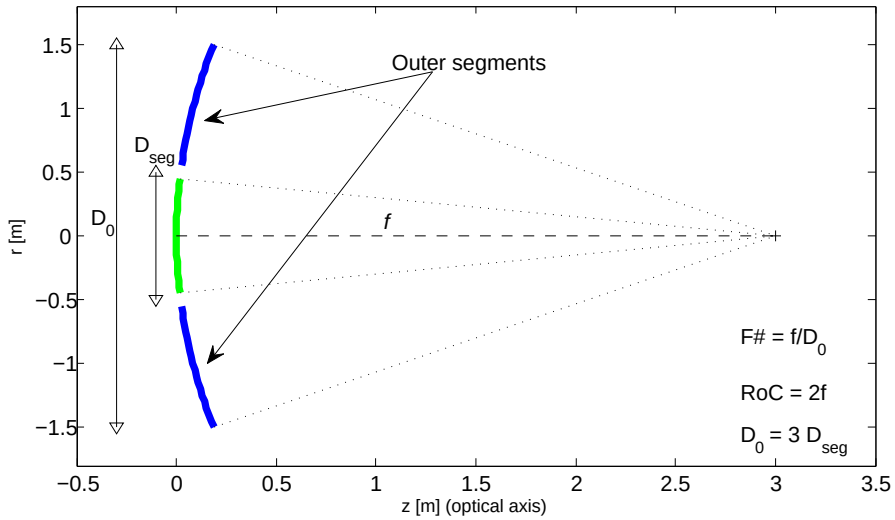

Figure 4-4: Schematic of Segmented Mirror and Optical Definitions

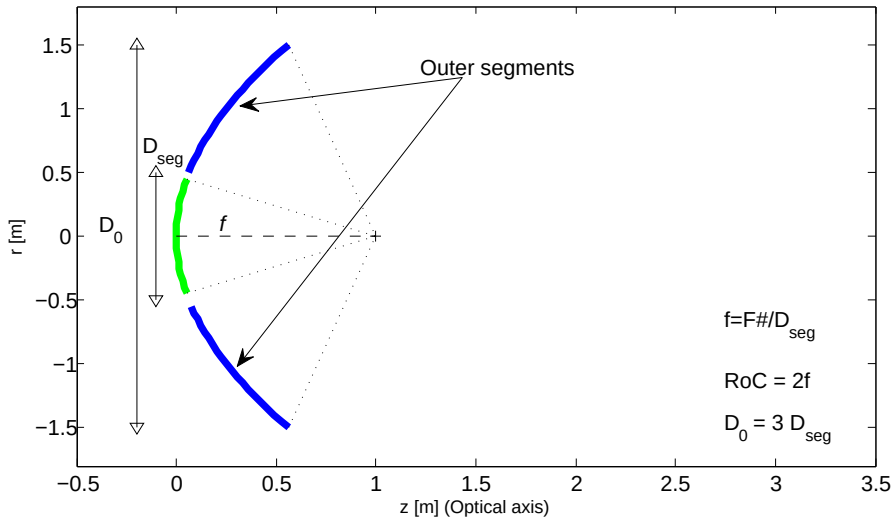

Figure 4-5: Schematic of Segmented Mirror with $F\#$ Defined for the Mirror Segment

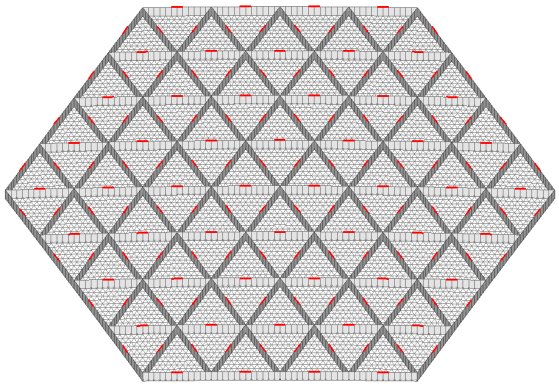

Figure 4-6: Mirror Finite Element Model

of the entire aperture, and each segment, with the exception of a possible middle segment, is off-axis. This is illustrated by the two outer segments in Figures 4-4 and 4-5. In these figures, the middle segment is an on-axis segment, and represents the model used in this thesis. The on-axis assumption allows the symmetry of the mirror to be exploited, greatly reducing computational expense. Additionally, it has been found that the variation in the results when the segment is assumed on or off-axis is extremely small. Therefore, the segment is assumed to be on-axis, leading to three-fold symmetry in the mirror and mirror mount system.

These assumptions simplify the mirror model such that its computational expense is kept low, while still retaining high-fidelity in the important features.

4.3 Mirror Structural Model

The basis of the mirror model is the structural finite element model, and this structural model is used for all of the analyses. This section presents the details of that model.

The mirror structural model is constructed using finite element modeling (FEM); a view of the back side of the mirror can be seen in Figure 4-6. The mirror is rib-stiffened with silicon carbide (SiC) material properties, and is made up of two-dimensional shell elements. The face sheet is made up of triangular elements (CTRIA3), and the ribs are made up of quadrilateral elements (CQUAD4). Additionally, there are

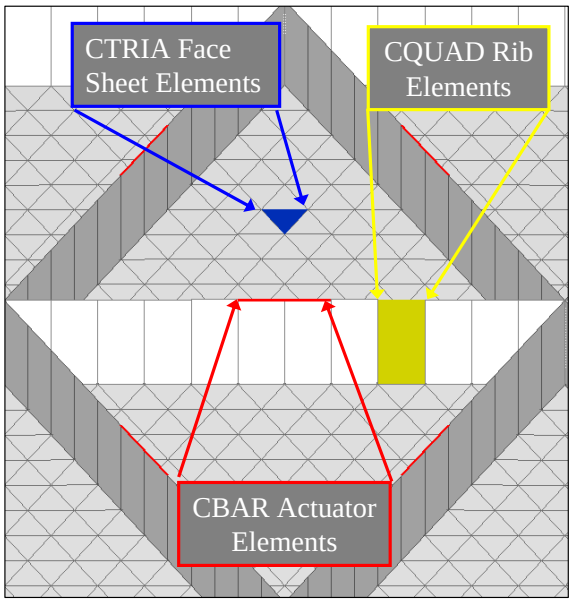

Figure 4-7: Close Up View of Element Types in the FEM

surface-parallel piezoelectric actuators embedded in the ribs, allowing for actuation of the mirror. The actuators are modeled as bar elements, which account for the mechanical mass and stiffness associated with the actuators. The full piezo modeling scheme will be discussed further in Sections 4.4.1 and 5.1.2. Figure 4-7 shows a close up view of a triangular cell formed from the ribs, highlighting the element types used in the FEM.

In addition to the primary ribs, cathedral ribs can be included if desired. Cathedral ribs are smaller ribs within each cell. These help support the face sheet more evenly, especially during polishing and grinding processes. Figure 4-8 shows an example of a mirror with cathedral ribs, including both a full mirror and a close-up of the cathedral ribs.

The mirror constraint configuration can be seen in Figure 4-9. In this configuration, the mirror is connected to three bipod mounts. The three bipod mounts are then connected to a rigid back structure, as discussed in Section 4.2. The connection between the rigid back structure and the mirror mimics that of a kinematic bipod flexure that helps to mitigate the transference of disturbance energy from the structure to the aperture. The bipod mounts locally constrain motion in the surface normal

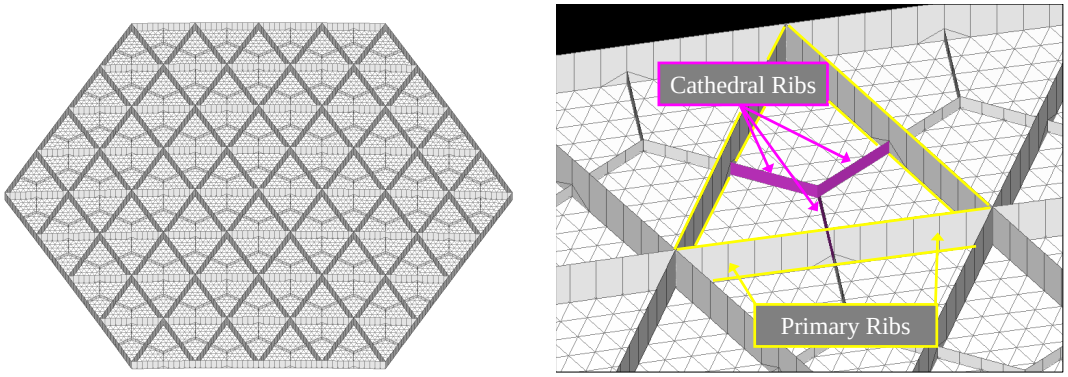

(a) Full Mirror (b) Close-Up

Figure 4-8: Mirror with Cathedral Ribs

(z) and circumferential directions. There is a soft spring connecting the radial and rotational degrees of freedom which connect, but do not rigidly constrain, the motion in these degrees of freedom. Specifically, the soft degrees of freedom of the bipods have very low stiffness, so deformation of the back structure creates constrained rigid body motion of the mirror segment.

The bipod connections to the mirror are created with a load-spreading technique to eliminate a large stress concentration resulting from a single node connection. This method connects the bipod to seven points on the mirror (the center point at the rib intersection, and the first node outwards on each rib), as seen in Figure 4-10, eliminating the stress concentration and more accurately representing a true mounting configuration. Additionally, the elements nearest the bipod connection are tapered to be thicker at the connection point for more support. The increase in thickness is a variable parameter in the model. Note that this thickness increase cannot be seen in the figures, which show only the element structure, and not the thicknesses, which are defined using NASTRAN property cards.

The mirror FEM, as discussed above, is created using the subsequently described input parameters. The mirror FEM mesh, defining the nodes, elements, and material properties, is automatically generated based on modal fidelity and input parameters [80]. Then, the finite element solver MSC.NASTRAN is used to determine the

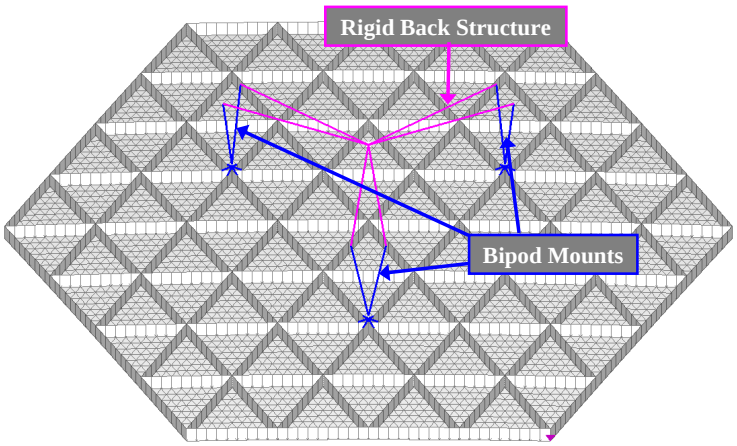

Figure 4-9: Mirror FEM Constraint Configuration

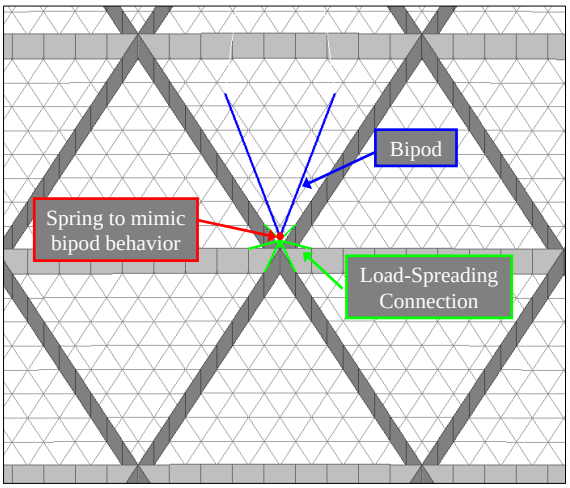

Figure 4-10: Bipod Mount with Load Spreading Configuration

mass and stiffness matrices for the system of nodes, elements, and material properties. NASTRAN can be used to for both quasi-static and dynamic analyses, as discussed in Sections 4.4 and 5.1, respectively. This process can be seen in Figure 4-11

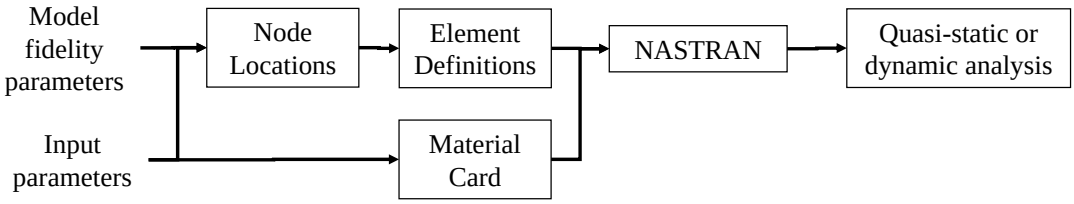

Figure 4-11: FEM Creation Process Overview

4.3.1 Mirror Parameters

The mirror model is completely parameterized. The key design parameters and their definitions are:

- **Segment Size**: vertex-to-vertex diameter of the hexagonal mirror segment.
- **F#**: focal length divided by the diameter; defines the curvature of the mirror. Computed assuming a seven segment mirror system (Section 4.2)
- **Areal Density**: mass per reflecting area of the silicon carbide substrate.
- **Number of Rib Rings**: number of concentric hexagonal rings of primary ribs in the segment. Ribs are filled in as defined by the number of rings (See Figure 4-12). This also defines the number of actuators as one per cell side, where the triangular rib pattern creates the cells.
- **Rib Aspect Ratio**: height perpendicular to the face sheet divided by thickness of the ribs.
- **Face Sheet Mass Fraction**: percentage of SiC mass in the face sheet. The remainder of the SiC mass is in the ribs.

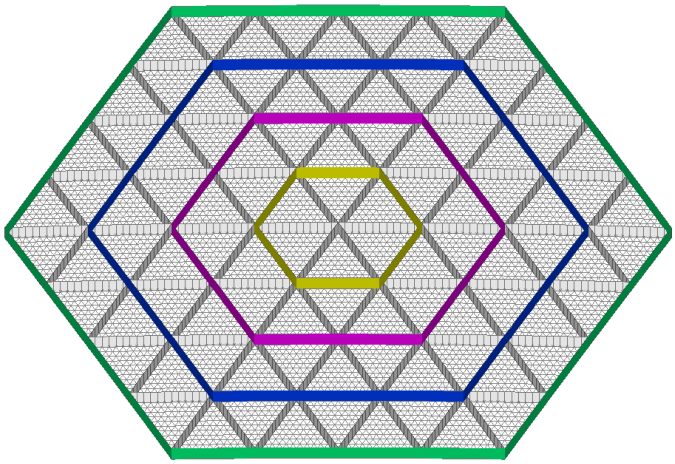

Figure 4-12: Rib Ring Definition: 4 Rib Rings Shown

- **Cathedral Rib Mass Fraction**: inclusion or exclusion of smaller, cathedral ribs by fraction of SiC mass in the cathedral ribs.

- **Actuator Length**: length of the actuator. Represents the distance between the moment on either side of the actuator, rather than the length of the piezoelectric material.

- **Bipod Reinforcement**: factor to taper ribs near reinforced bipod connection points.

- **Damping Ratio**: modal damping ratio

The baseline values and ranges of each of the parameters can be seen in Table 4.1. These values were chosen to represent an existing baseline prototype which is thought to have good performance. The baseline is used throughout the thesis as a design with which to compare performance variations.

The mirror and actuator material properties are also parameterized, though they are generally set to be those of silicon carbide and lead-magnesium-niobate respectively. The baseline material properties are defined in Table 4.2. These parameters are used throughout this thesis unless specified otherwise.

Table 4.1: Baseline Mirror Properties

Parameter	Units	Baseline Value	Range
Segment Size	m	1.2	0.5 - 2.5
F#	-	2.0	1.0 - 5.0
Areal Density	kg/m^2	7.5	2.5 - 15
Number of Rib Rings	-	4	3 - 6
Rib Aspect Ratio	-	25	10 - 80
Face Sheet Mass Fraction	-	0.63	0.3 - 0.9
Cathedral Rib Mass Fraction	-	0	0 - 0.05
Actuator Length	cm	2.5	1 - 10
Bipod Reinforcement	-	2	1 - 4
Damping Ratio	-	0.01	0.005 - 0.02

Table 4.2: Baseline Mirror Material Properties

	Units	Silicon Carbide	Actuator
Young's Modulus	GPa	375	93
Poisson ratio	-	0.17	0.3
Density	kg/m^3	3200	7650
Yield Stress	MPa	600	140
Coefficient of Thermal Expansion	m/deg	4.5 x10^{-6}	3.6 x10^{-10}

4.3.2 Validation

The FEM is an approximation to the mirror structure, so it is necessary to validate the FEM to ensure that it accurately represents reality. A standard FEM analysis, and the analysis used in the dynamic model, is a normal modes analysis, which determines the frequencies and mode shapes of the system from the mass and stiffness matrices. This validation step will be based on comparing FEM predicted fundamental frequency with that measured on an existing prototype. The second order equation of motion of the system is:

$$M\ddot{\eta} + K\eta = 0 \tag{4.3}$$

where M is the mass matrix, K is the stiffness matrix, and η are the nodal degrees of freedom. NASTRAN solves this eigenvalue problem for the natural frequencies and mode shapes of the system.

$$\left(K - \Omega^2 M\right) \Phi = 0 \tag{4.4}$$

where Ω are the modal frequencies and Φ are the mode shapes of the system. The modal frequencies, and particularly the fundamental, or lowest non-rigid body mode, frequency is often used for model validation.

Fundamental frequency information is available for a mirror similar to those modeled here. The pertinent mirror parameters can be seen in Table 4.3. The parametric nature of the model makes it easy to quickly match the model to the available structure. In this case, the model has a fundamental frequency of 155 Hz, while the actual system had a fundamental frequency near 158 Hz, as best measured. This is less than 2% error, which is quite accurate.

Table 4.3: Parameters for Mirror Frequency Validation

SiC areal density	8 kg/m^2
Number of rib rings	4
Number of actuators	156
Face sheet mass fraction	0.68
Rib aspect ratio	25.4
F#	1.0

Further validations and convergence analyses will be presented in Section 4.4.3 for the quasi-static model and in Section 5.2 for the dynamic launch model.

The mirror structural model described in the preceding sections will be used throughout the remainder of this thesis.

4.4 Quasi-Static Model for On-Orbit Performance

On-orbit, optical performance is the principal function of the primary mirror. The mirror must reflect light, and perform well optically. On-orbit performance can be described in a variety of ways. Here, only metrics that are directly influenced by the primary mirror design will be considered. Therefore, issues such as spacecraft jitter, that will affect the optical performance regardless of the primary mirror type,

are ignored. The main on-orbit performance metrics of interest are correctability and high spatial frequency wavefront error. Correctability refers to the size of the achievable shape change with the embedded actuators, while wavefront error refers to the distortion of the corrected mirror surface with reference to the ideal shape.

Low order shape correctability is desirable for a number of reasons, including thermal, manufacturing, and optical prescription change. Due to the high coefficient of thermal expansion (CTE) and high thermal conductivity of silicon carbide, thermal variations result in low order deformations in the mirror. Therefore, either tight thermal control or the ability to correct for the thermally induced shape changes are necessary. Also, issues in the manufacturing process result in variations in the radii of curvature between segments. In order to use multiple mirror segments as a single primary aperture, the curvatures of the segments must be matched using a low order correction. Third, there is a desire to have the ability to change the optical prescription of the mirror while on-orbit or from mission to mission so that it can be used for multiple missions or instruments. A large range of correctability improves all of these issues, and allows the mirror to be more functional. However, there are a limited number of actuators with finite stroke lengths, so there is a limit to the achievable shape change.

Additionally, the low order shape change is accomplished through the use of discrete embedded piezoelectric actuators. The discrete nature of the actuators, acting to induce a continuous shape, results in a high spatial frequency dimpling on the surface, as seen in Figure 4-13. This dimpling is above the spatial frequency of the actuators, and is thus uncorrectable. The dimpling causes distortions of the mirror surface, which are quantified as wavefront error.

All of these disturbances act on a long time scale and can be considered quasi-static. In other words, the control inputs change, but at long intervals that do not require active control systems. This results in much simpler control algorithms and no stability concerns.

The structural mirror model is as described in Section 4.3, and the quasi-static finite element analysis and control is built upon the work of Gray [62] and Jordan [80].

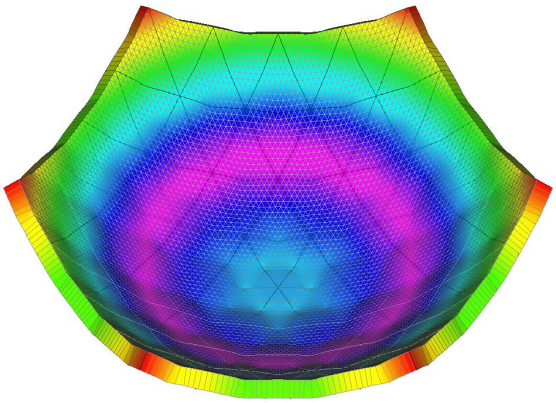

Figure 4-13: High Spatial Frequency Error Induced by Low Order Shape Changes

The following sections describe the control analysis, performance metrics, and validation, followed by a brief analysis of the best mirrors considering only the optical performance metrics.

4.4.1 Control

As mentioned above, the disturbances of interest act on a very long time scale, thus the control is computed in a quasi-static manner. In other words, the control inputs are computed, then applied to the mirror, without regard for the transient, dynamic behavior due to the actuation. This results in the telescope being non-operational at the time that the control is applied and for a brief period of time after. The control voltage is then held constant until the next update, which could be anywhere from minutes to days later. The following sections discuss how the quasi-static control is implemented through actuator influence functions, as well as the computation of the control commands.

Actuator Influence Functions

The quasi-static control is implemented through the use of actuator influence functions, which describe the effect of each actuator on the mirror surface. The actuator influence functions are created using the MSC.NASTAN finite element solver. Each actuator is given a unit actuation command, and the surface normal (z) displace-

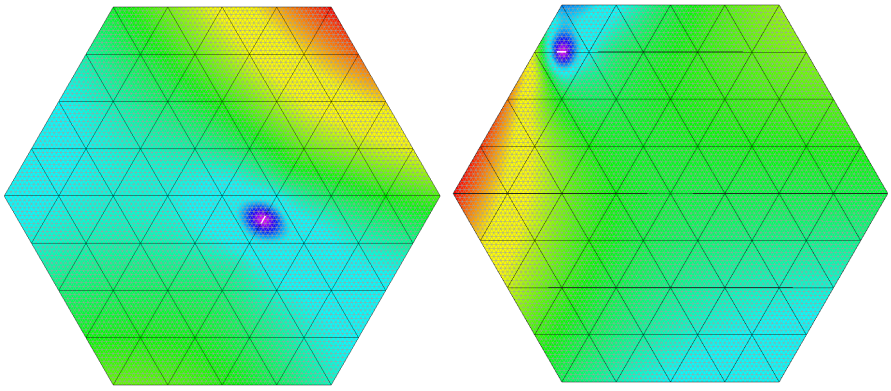

Figure 4-14: Influence Function Examples

ments of all nodes on the surface of the mirror are computed. The influence function for each actuator is then stored in a column of the influence function matrix, Σ. The symmetry of the mirror segment is exploited in order to minimize the computational burden of computing the actuator influence functions. More details on the actuator influence function and computation can be found in Gray [62]. Two example influence functions can be seen in Figure 4-14. Here, the actuator location is shown in white, and the contour represents the influence function across the mirror. The shape and size of the influence function depend on both the location within the mirror and the mirror parameters.

In reality, the actuation is induced through a voltage command. The piezoelectric equation in the along-axis direction is given in Equation 4.5 [36, 68, 3].

$$S = d_{33}\frac{V}{L} + s_{33}^{E}T \tag{4.5}$$

where S is the mechanical strain, d_{33} is the piezoelectric constant, V is the voltage, L is the length of the piezo, s_{33}^{E} is the compliance at short circuit, T is the vector of material stress, and 3 corresponds to the along-axis direction. Applying a voltage to the piezo induces both stress and strain in the system. Therefore, the actuator cannot be considered as a displacement actuator, which induces only strain, or a force actuator, which induces only stress. NASTRAN does not directly support piezoelectric elements and actuation. Instead, the actuation is achieved in NASTRAN through the use of

temperature changes [50]. The actuators are thermally isolated from the structure in the finite element model through the use of rigid elements. By applying a temperature change to the actuator, the coefficient of thermal expansion causes it to change length. However, the SiC structure resists the expansion of the actuator, mimicking the true behavior of piezoelectrics by balancing the stress in the actuator due to its inability to achieve free strain and the stress in the SiC due to the deformation from the actuator [62, 80]. The temperatures can then be mapped back to voltages to ensure that limits are not exceeded.

Control Algorithm

The influence function-based control uses a constrained least squares approach to minimize the error between the desired and actual shape [80, 143]. Without voltage limitations on the actuators, the equation dictating the actuator commands is:

$$\Sigma u + z = 0 \tag{4.6}$$

where Σ is the matrix of nodal influence functions, u are the actuator commands, and z are the nodal displacements of the mirror surface with reference to the desired final shape, as discussed in the next section. The solution to Equation 4.6 that minimizes the error uses a Moore-Penrose pseudoinverse to compute the control commands:

$$u = -(\Sigma^T \Sigma)^{-1} \Sigma^T z \tag{4.7}$$

The voltage limitation in the actuators results in a constrained least squares problem, with bounds on the values of u. In this case, the problem can be stated as:

$$\begin{gathered} \min_u \frac{1}{2} \left\| \Sigma u - z \right\|^2 \\ \text{such that: } Au \leq b \end{gathered} \tag{4.8}$$

where A and b describe the voltage limitations and are defined as:

$$A = C_v \begin{bmatrix} I \\ -I \end{bmatrix} \tag{4.9}$$

$$b = \begin{bmatrix} V_{ub} \\ -V_{lb} \end{bmatrix} \tag{4.10}$$

where C_v is the constant relating the CTE to the voltage, I is the identity matrix of the size $[n_p \times n_p]$, V_{ub} is the voltage upper bound in a matrix of size $[n_p \times 1]$, V_{lb} is the similar matrix consisting of the voltage lower bound, and n_p is the number of piezoelectric actuators.

Equation 4.8 is solved using the MATLAB constrained least squares function, *lsqlin.m*. If there are no saturated actuators, then this solution reduces to the simple, unconstrained least squares solution of Equation 4.7. If the bounds are reached, the algorithm uses a quadratic programming projection method to minimize the least squares residual [57].

The calculated u actuator commands are applied to the mirror using NASTRAN. The displacements of the surface grid points are determined and used to calculate the post-corrected surface.

Radius of Curvature Change Commands

The typical desired shape change, specified through z, is to change the radius of curvature (RoC) of the mirror. The curvature of the mirror can be described using the equation for conic sections:

$$z_{des} = \frac{\frac{r^2}{\text{RoC}}}{1 + \sqrt{1 - \frac{(k+1)r^2}{\text{RoC}^2}}} \tag{4.11}$$

where z_{des} is the desired surface height at a node, r is the radius of that node, RoC is the radius of curvature at the center of the mirror, and k is the conic constant. For a parabolic mirror, $k = -1$, reducing Equation 4.11 to:

$$z_{des} = \frac{r^2}{2\text{RoC}} \tag{4.12}$$

The shape change of the surface, z, is calculated by computing the surface shape of a mirror with the new radius of curvature ($\text{RoC}_0 + \Delta$ RoC), defined as $z_{desired}$. Then, the change between the initial surface (z_0) and desired surface defines the shape change.

$$z = z_0 - z_{desired} \tag{4.13}$$

4.4.2 Performance Outputs

As mentioned previously, there are two primary performance outputs associated with the on-orbit mirror control. The first is the wavefront error of the post-corrected surface, and the second is the maximum achievable radius of curvature change. Both metrics are described below.

Wavefront Error

The first performance metric is the residual wavefront error (WFE). After an applied curvature change, there is a high spatial frequency residual surface error that remains. This is above the spatial frequency of the actuators, and thus is uncorrectable. The goal is to minimize this uncorrectable error.

For each mirror, a specified change in the radius of curvature is commanded. The appropriate z deflections are determined, and the control is applied as described above. Then, the surface error is determined by taking the root-mean-square (RMS) of the difference between the desired and actual position of each node on the mirror surface. The wavefront error is then twice the surface error because the light is reflected, causing a surface error of a given length to result in an optical path length error of twice the surface error.

Maximum Achievable Radius of Curvature Change

The second metric for on-orbit performance is the maximum change in radius of curvature, which is defined as the maximum achievable RoC change within the saturation limits of the actuators. This is calculated by increasing the commanded radius of curvature change until the achieved RoC change assymptotes to a maximum value, and the actuators are saturated. The achieved radius of curvature change is calculated using a least squares solution of the post corrected surface shape with the maximum RoC change.

As seen in Figure 4-13, this shape change also results in a dimpling wavefront error that is typically higher than that calculated for the prescribed change in RoC used in the wavefront error calculation. Therefore, this metric represents the capability of the actuators, rather than the RoC change permitted by optical wavefront limitations. However, the maximum RoC change subject to wavefront error limitations will be explored in Chapter 6.

4.4.3 Validation

The quasi-static mirror model was compared with an experimental test. A given radius of curvature change was applied to the mirror, and the resulting high spatial frequency wavefront error was calculated. The model was within about 7% of the test data, indicating that the model is performing quite well.

4.4.4 Mirror Design for On-Orbit Performance

The effects of the mirror parameters on the optical performance metrics are examined. First, single-axis trades are performed, in which a single parameter is varied while all others are held constant, helping to identify the effects of each parameter and the sensitivities of the performance metrics to the parameters. Next, a trade space is shown, illustrating the effects of the interactions between parameters, and suggesting families of designs that perform well, with reference to the aforementioned performance metrics.

Single-Axis Trades

Single-axis trades can be used to determine to which parameters the performance metrics are most sensitive. One shortcoming is that it does not include any of the interactions between parameters. In each trade, all of the parameters are held at their baseline values with the exception of the parameter of interest, which is varied within the range of possible values. The single-axis trades here consider two primary performance metrics: dimpling when subjected to a prescribed radius of curvature change, and the maximum achievable radius of curvature change. Note that the maximum achievable curvature represents the maximum capability of the actuators due to saturation, and does not include limitations on the dimpling wavefront error of the resulting surface.

There are eight parameters of interest: diameter, mirror F#, silicon carbide areal density, number of rib rings, cathedral rib inclusion, rib aspect ratio, face sheet mass fraction, and actuator length. Figure 4-15 shows the resulting dimpling from a 5 mm change in radius of curvature, and Figure 4-16 shows the maximum achievable change in RoC.

Figure 4-15 shows that in order to minimize dimpling, the mirror should have a small diameter, a large F#, high areal density, many ribs, no cathedral ribs, and long actuators. Figure 4-16 shows that in order to maximize the achievable RoC change, the mirror should have a small diameter, a large F#, low areal density, many ribs, and long actuators. Notice that many parameters result in both lower dimpling and higher achievable RoC changes. For example, adding more ribs, and therefore more actuators, or increasing the length of the actuators positively impacts both performance metrics. However, consider the areal density, where increasing areal density decreases the dimpling, yet also results in a lower maximum RoC change. Increasing the areal density helps to widen the influence functions, so that the actuators create a more global shape change, and dimpling is minimized. However, the higher mass also necessitates more force to manipulate the mirror surface, which results in the

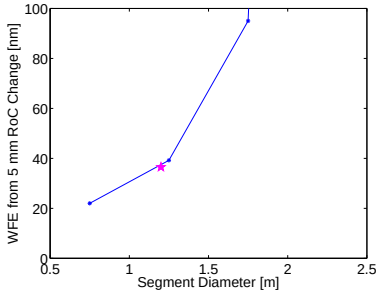

(a) Diameter

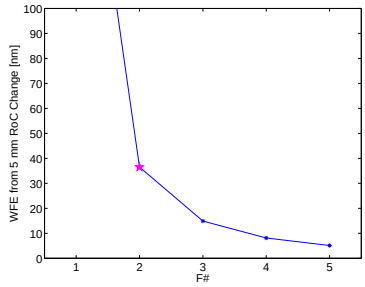

(b) F#

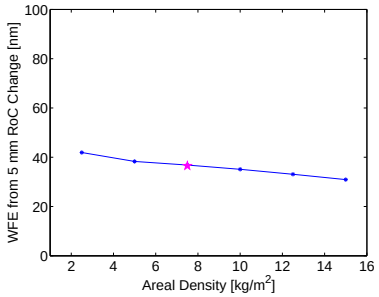

(c) SiC Areal Density

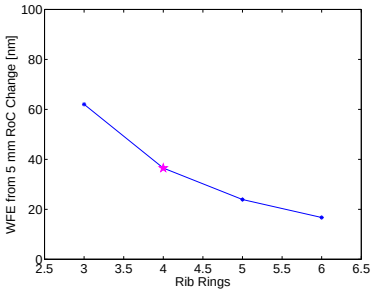

(d) Number of Rib Rings

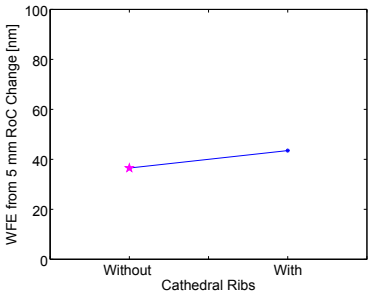

(e) Cathedral Ribs

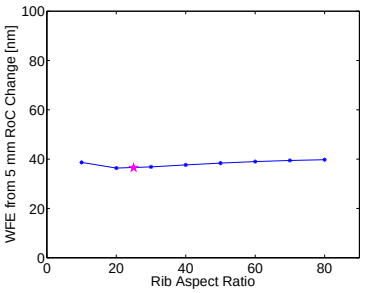

(f) Rib Aspect Ratio

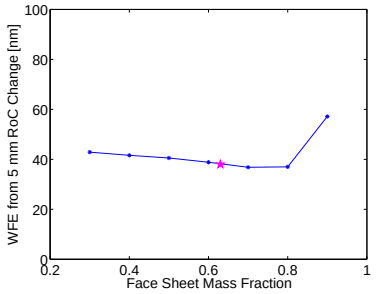

(g) Face Sheet Mass Fraction

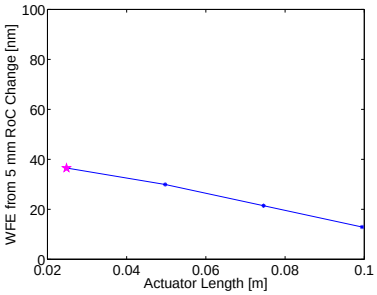

(h) Actuator Length

Figure 4-15: Single-Axis Trade Studies: Dimpling Resulting from a 5 mm RoC Change

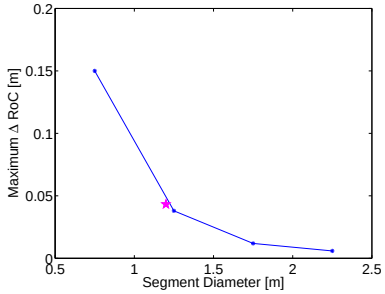

(a) Diameter

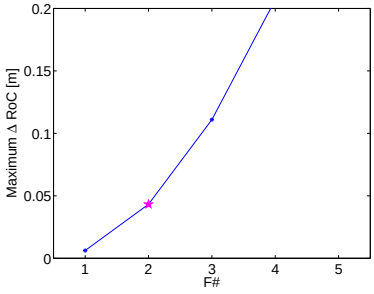

(b) F#

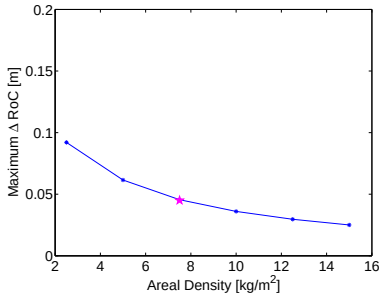

(c) SiC Areal Density

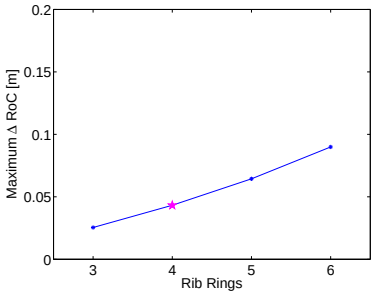

(d) Number of Rib Rings

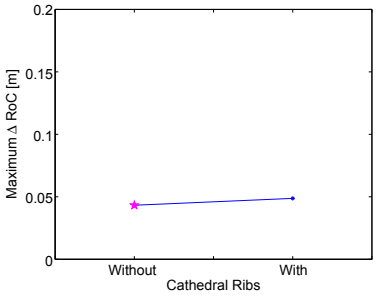

(e) Cathedral Ribs

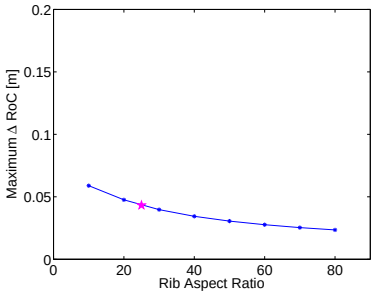

(f) Rib Aspect Ratio

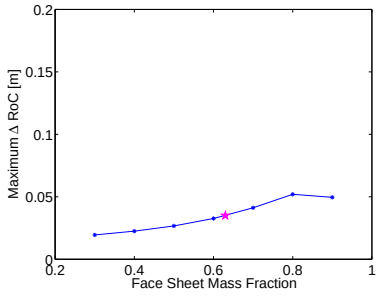

(g) Face Sheet Mass Fraction

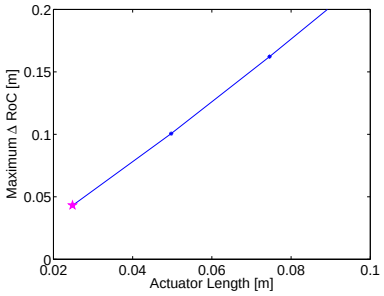

(h) Actuator Length

Figure 4-16: Single-Axis Trade Studies: Maximum Change in RoC

actuators saturating more quickly, and limiting the achievable shape change.

Notice that both the diameter and the F# appear to have large effects on both the wavefront error and on the achievable radius of curvature change. While this is true, it is also misleading. The actuation is prescribed as a change in the radius of curvature. However, that radius of curvature depends on both the diameter and the F#, as described in Section 4.2. For example, consider the baseline mirror that has an F# of 2, a segment diameter of 1.2, and an initial RoC of 12.4 m. A 5 mm RoC change results in a maximum z-displacement of 5.8 μm. A mirror with the same diameter, but an $F\#$ of 5 subjected to the same 5 mm RoC change results in a maximum z-displacement of 0.9 μm. In order to match the maximum z-displacement between two mirrors with different F#s, the command must be scaled by:

$$\Delta RoC_{new} = \left(\frac{F\#_{new}}{F\#_i}\right)^2 \Delta RoC_i \tag{4.14}$$

where ΔRoC_{new} is the new RoC command, ΔROC_i is the initial RoC Command, and $F\#_{new}$ and $F\#_i$ are the new and initial F#s, respectively. Using these scaled commands, the dimpling as a function of $F\#$ can be seen in Figure 4-17. Here, one can see that while a higher F# (flatter mirror) does reduce dimpling, the effect is not as extreme as it appeared when the commands simply were equivalent changes in RoC as in Figure 4-15(b).

Optical Performance Trade Space

The single-axis trades help identify the important parameters to include in the trade space analysis. In an effort to compare similar systems, the diameter and F# are held constant. Changing the diameter or the F# significantly alters the optical system, making direct comparison difficult. Also, the trends found in the trade space exploration will hold for each combination of diameter and F#, making this analysis applicable to other combinations. Additionally, cathedral ribs are not included, since in all cases, adding cathedral ribs slightly detracts from the performance. Since this trend is constant, it can be extrapolated that a good design with cathedral ribs will

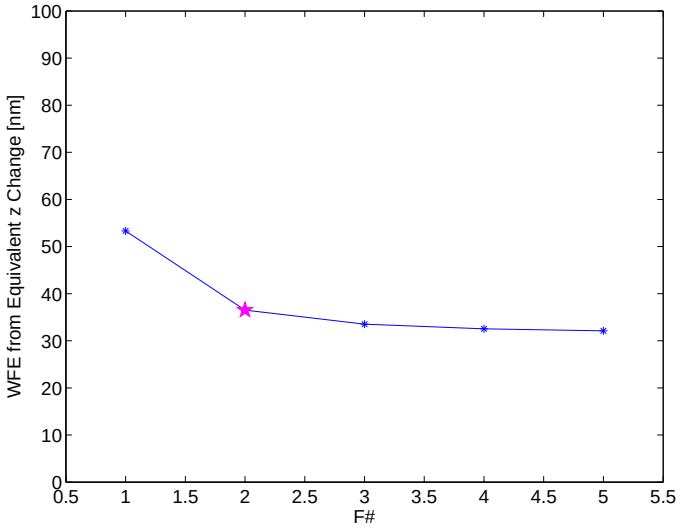

Figure 4-17: Dimpling as a Function of F# with Scaled Δ RoC Commands

be the same as a good design without cathedral ribs, and the performance will be slightly degraded. The trade space analysis includes the other five parameters: SiC areal density, number of ribs, rib aspect ratio, face sheet mass fraction, and actuator length. While it appears that the rib aspect ratio and face sheet mass fraction have small effects in Figures 4-15 and 4-16, they interact with one another, making it important to include them in the trade space analysis.

A design of experiments technique is used to explore the trade space. While multi-objective optimization could be used to find the optimal designs, a trade space exploration technique is chosen in order to visualize the trade space and the effects of the parameters for this particular analysis.

Latin Hypercube sampling (LHS) is used to efficiently explore the design space. Latin Hypercube sampling is a Design of Experiments sampling technique that ensures uniform coverage of the parameter space. The parameter ranges are divided into bins, and the samples are chosen such that there is exactly one sample in each row or column of the n-dimensional hypercube, where n is the number of the parameters [30]. Though LHS sampling provides uniform coverage of the parameter space, it does not ensure full coverage of the trade space. It is possible to miss portions of the design space. However, the large number of samples relative to the number of parameters

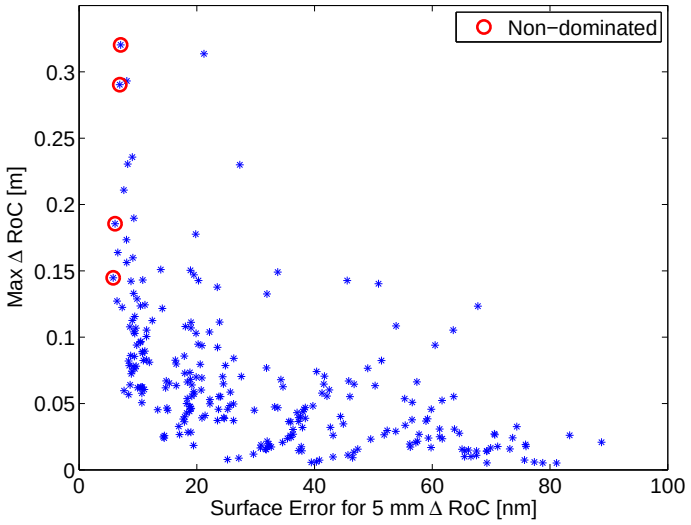

Figure 4-18: Design Space for On-Orbit Performance

helps to more fully cover the design space, while maintaining computational efficiency. Full factorial sampling would give more complete coverage of the design space, but it is extremely computationally expensive. As an example, five parameters with 10 levels in each parameter would result in 100,000 designs. Therefore, despite its limitations, LHS provides a way to sample and visualize the trade space for this portion of the design.

In this analysis, 1000 designs are analyzed. For each design, the dimpling is calculated with respect to a 5 mm change in radius of curvature. Also, the maximum change in RoC is calculated.

Figure 4-18 shows the trade space of designs; each point in the plot represents a distinct design. The x-axis shows the surface error resulting from the prescribed radius of curvature change, while the y-axis shows the maximum achievable RoC change. The goal is to minimize the surface error from the prescribed RoC change and to maximize the achievable RoC change, so the best designs are in the top, left corner of the plot. Since these two performance metrics are cooperative and not necessarily opposing, there is not a Pareto front. Instead, many of the designs that perform best with respect to one metric also perform best with respect to the other metric.

In order to identify which parameters contribute most to the performance metrics, the designs in Figure 4-18 can be differentiated by the various design parameters so that the resulting trends can be visualized. Figure 4-19 shows the same designs points as in Figure 4-18, but each subplot shows the designs differentiated by a different design parameter. Figure 4-19(a) shows the designs differentiated by the number of rib rings. The number of rib rings dictates the number of actuators in the system, so it is no surprise that increasing the number of rib rings results in better performance in both the dimpling surface error and achievable RoC change. Figures 4-19(b) and 4-19(c) show that neither the rib aspect ratio nor the face sheet mass fraction have a global effect. Rather, the interaction between the two parameters, along with the variation in the number of ribs, influence the rib design and thus the on-orbit performance. Figure 4-19(d) shows the designs differentiated by areal density. Here, notice that higher areal densities result in lower dimpling but lower RoC changes, as was seen in Figures 4-15(c) and 4-16(c). However, this effect is not nearly as extreme as in the single-axis cases, because other parameters have a greater effect on the outputs. Finally, Figure 4-19(e) shows the designs differentiated by actuator length. Longer actuators do result in generally better performance with respect to both metrics, but again, the effect is not as dominant as the number of actuators.

Consider the two parameters with the most significant effects on the outputs: the number of rib rings and the actuator length. Both metrics contribute to the total length of actuator in the mirror. Therefore, the derived parameter, total actuator length, is created. The total actuator length is determined by multiplying the actuator length by the total number of actuators (which is determined through the number of rib rings). Figure 4-20 shows the same trade space, but differentiated by the total actuator length. Here, it is clear that the total actuator length is the dominant parameter in the design space; a longer total actuator length results in better performance. Intuitively, it is reasonable that greater actuator coverage of the surface results in better performance when actuating continuous shapes.

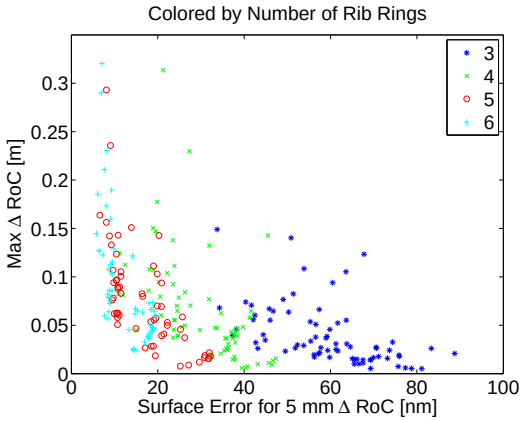

(a) Differentiated by Number of Rib Rings

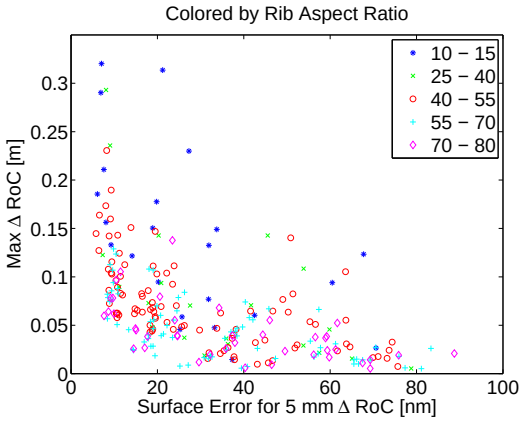

(b) Differentiated by Rib Aspect Ratio

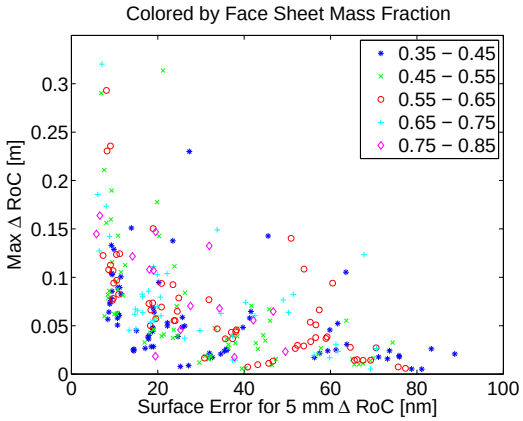

(c) Differentiated by Face Sheet Mass Fraction

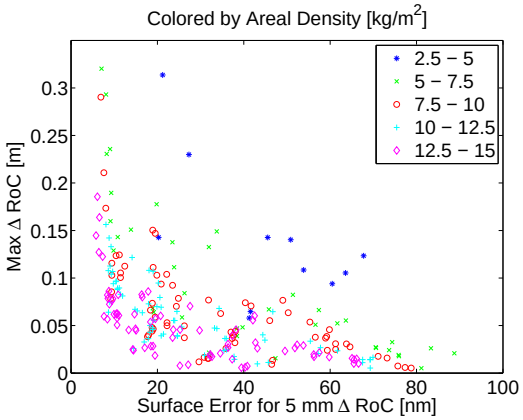

(d) Differentiated by SiC Areal Density

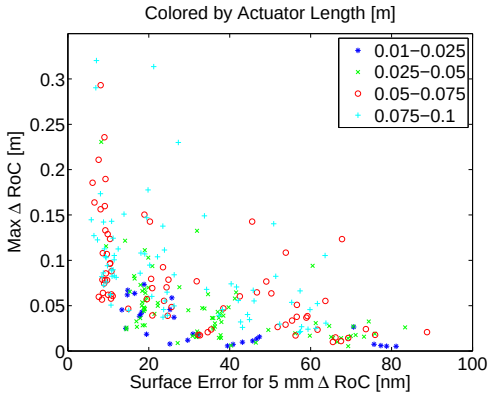

(e) Differentiated by Actuator Length

Figure 4-19: On-Orbit Trade Space with Design Parameter Differentiation

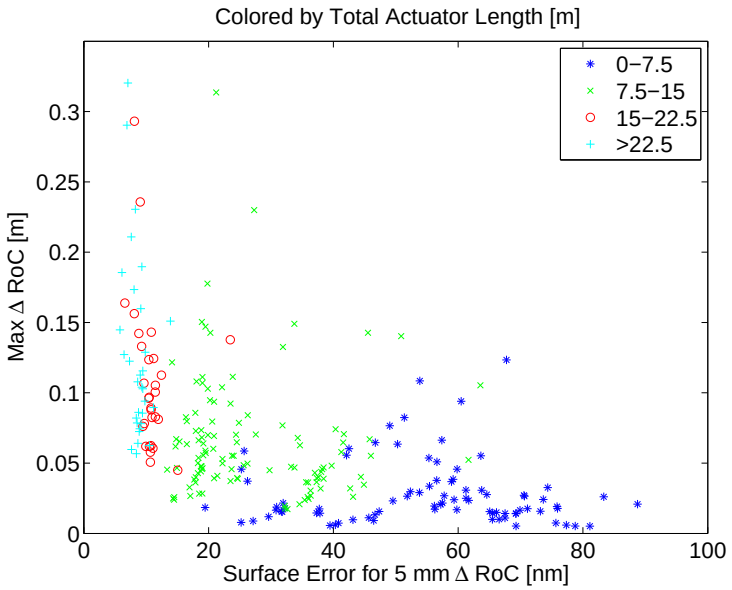

Figure 4-20: Design Space for On-Orbit Performance Differentiated by Total Actuator Length

4.4.5 On-Orbit Performance Summary

Designing a mirror for on-orbit performance, considering the dimpling wavefront error and the maximum achievable RoC change, results in a design that maximizes the total actuator length, where the total actuator length is a combination of the number and length of the actuators in the mirror. Also, a more correctable mirror, in terms of achievable shape change, can be achieved through using lower areal densities. However, the locality of the influence functions in low areal density systems results in large dimpling wavefront error, leading to a trade-off between the two metrics. The rib structure, as defined by the rib aspect ratio, face sheet mass fraction, and number of ribs, also influences the performance output, though the effects are more subtle, and depend on the combinations, rather than a single parameter. Also, given the cooperative nature of the two metrics here, optimal designs that satisfy both metrics can be obtained. These optimal designs will be explored further in Chapter 6, which discusses the integrated mirror design and optimization.

4.5 Mirror Model Summary

This chapter discusses the mirror model that is used to analyze lightweight, active mirrors, including the assumptions and simplifications that make it possible to use the model in conjunction with integrated modeling and trade space exploration techniques. In addition to the structural model and baseline mirror, the methodology for analyzing the on-orbit performance is presented. The on-orbit performance, characterized by the maximum achievable radius of curvature change before actuator saturation and the high spatial frequency wavefront error of the post-corrected surface due to a curvature change, is modeled using a quasi-static model and control. It is found that the best designs for on-orbit performance maximize both the number and length of the actuators. The mirror response to launch will be explored in Chapter 5, while the integrated mirror design, considering both the on-orbit and launch environments, is discussed in Chapter 6.

Chapter 5

Launch Survival

Launch survival is a key concern for very lightweight mirrors. As will be shown, many mirror designs are quite close to launch stress limits. Therefore, it is important to verify that the mirror designs will survive launch and to understand the launch stress implications of various design choices.

Traditional launch load modeling is performed either with a very simple quasi-static model, or with a full coupled loads analysis on the spacecraft-launch vehicle system [83]. However, given the proximity of the launch stresses to limitations, it is desirable to have the ability to include launch load alleviation techniques directly in the model. Therefore, a dynamic, state-space model of the mirror subjected to vibroacoustic launch loads is developed. While it is a deviation from traditional launch analysis methods, this method allows the addition of launch load alleviation techniques, as well as trade space exploration due to improvements in the computational expense.

This chapter presents a dynamic model that can be used to analyze the response of the mirror to the launch environment. It begins with a detailed description of the launch model and modeling methodology, followed by analysis of a baseline mirror and parameter sensitivities. A trade space considering the design of a mirror specifically for launch survival is presented in Section 5.4. Additionally, launch load alleviation techniques, designed to increase the chance of launch survival by decreasing the launch stresses, are included, as well as an analysis of the additional designs that would

survive launch with the addition of the launch load alleviation.

5.1 Launch Model

As discussed in Section 4.1, launch is an environment that necessitates a dynamic model. The model used here is a state-space model derived from a finite element normal modes analysis. The mirror structural FEM (Section 4.3) defines the nodes, elements, and materials that are used to create the mass and stiffness matrices for the system. MSC.NASTRAN is used to solve for the frequencies and mode shapes of the system, as described in Section 4.3.2. The frequency and mode shapes, in conjunction with the desired inputs and outputs, are used to form a state-space model of the system. The state-space model of the mirror system is of the following form:

$$\begin{aligned}
\begin{bmatrix} \dot{q} \\ \ddot{q} \end{bmatrix} &= \begin{bmatrix} 0 & I \\ -\Omega^2 & -2\zeta\Omega \end{bmatrix} \begin{bmatrix} q \\ \dot{q} \end{bmatrix} + B_w w + B_u u \\
y &= C_y \begin{bmatrix} q \\ \dot{q} \end{bmatrix} + D_{yu} u + D_{yw} w \\
z &= C_z \begin{bmatrix} q \\ \dot{q} \end{bmatrix} + D_{zu} u
\end{aligned} \tag{5.1}$$

where q are the modal degrees of freedom, Ω are the modal frequencies, ζ is the prescribed modal damping, w are the disturbance inputs, u is the vector of control inputs, y are the control sensors (when applicable), and z are the performance outputs. The FEM defines the dynamics of the system (Ω, Φ), leaving the inputs and outputs to be defined. In this system, there are a number of inputs and outputs that are considered. State-space modeling allows one to easily add or subtract inputs or outputs by adding columns (inputs) or rows (outputs) to the appropriate B, C, or D matrices.

The remainder of this section details the state-space model. First, the performance

outputs, z, are discussed. Next, the piezoelectric control inputs, u, are described. The finite element model accounts for the mechanical properties of the piezos, but the electrical properties must be added using the piezoelectric equations. Next, the disturbance inputs, w, are discussed. In this case, the disturbances are the random vibrations and acoustics due to launch. The control sensors, y, are not discussed in this section, as they are not necessary to analyze the mirror. Rather, they are only included when certain types of alleviation techniques (Section 5.5) are used, and will be discussed in the appropriate sections corresponding to each alleviation technique. Note that the control sensors in the state-space model in this chapter are control sensors for use during launch, and do not refer to the wavefront sensor that is used on-orbit. Finally, the disturbance analysis is briefly discussed, followed by a convergence analysis to ensure that the model is functioning correctly.

5.1.1 Launch Performance Outputs

The goal of the launch analysis is to determine the response of the mirrors to the launch loads and ascertain whether or not the mirror will survive launch. This is best determined through the stress distribution in the mirror and by comparison of peak stresses to stress limits. Therefore, the performance outputs of the state-space model, z, are the elemental stresses.

There are multiple types of stresses to consider. In the silicon carbide substrate, in-plane stresses and out-of-plane bending stresses are of concern, while the axial stress is of concern in the actuators. Each of these stresses are calculated by computing the strain, and using Hooke's law to determine the stress. The three formulations, corresponding to the three types of stresses, are all described below.

SiC In-Plane Stress The in-plane stress in the SiC is the most complex computation. The natural outputs of a model built using normal modes analysis are nodal displacements and rotations and their derivatives. In order to determine elemental stresses, the nodal displacements must be transformed into strains. This is accomplished using finite element theory and interpolation functions. The process by which

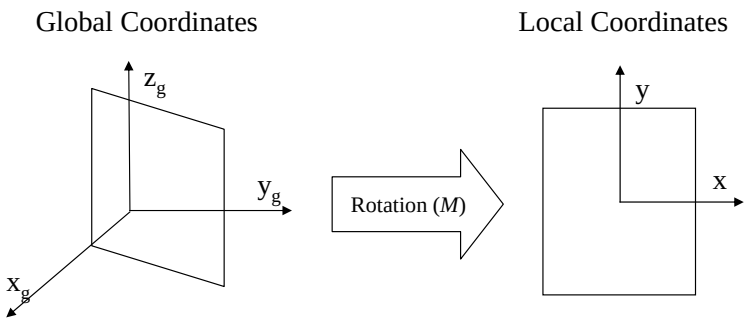

Figure 5-1: Local to Global Coordinate Transformation through Projection Matrix

this is achieved is outlined below.

In order to determine the in-plane stress in the elements, the three-dimensional nodal displacements of the grid points defining that element must be transformed into a local, two-dimensional coordinate system in the plane of the element. This is accomplished by creating a $[2 \times 3]$ projection matrix (M) for each element which rotates the coordinates from the global coordinate system into the local system, transforming each three-dimensional global coordinate to a two-dimensional, in-plane, local coordinate, as seen in Figure 5-1. Note that each element will have its own projection matrix.

Once the nodal displacements are converted into local, two-dimensional space, a strain transformation matrix is created to transform the nodal displacements into elemental strains. The strain transformation is taken from finite element theory, and uses interpolation functions to relate displacements to strains [19]. The local, in-plane strain in each element is described as:

$$\begin{aligned} \epsilon &= \begin{bmatrix} \epsilon_{xx} \\ \epsilon_{yy} \\ 2\epsilon_{xy} \end{bmatrix} \\ &= \begin{bmatrix} \frac{\partial u_x}{\partial x} \\ \frac{\partial u_y}{\partial y} \\ \frac{\partial u_x}{\partial y} + \frac{\partial u_y}{\partial x} \end{bmatrix} \end{aligned} \tag{5.2}$$

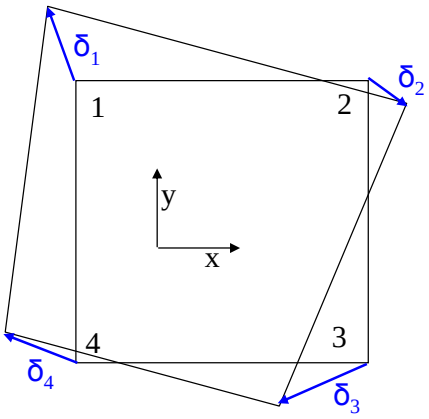

Figure 5-2: Element Deformation used in Stress Calculation

where ϵ is the strain, u is displacement, and x and y describe the local, two-dimensional coordinate system. The strain transformation matrix, B_ϵ, will convert the nodal displacements to strain as follows:

$$\epsilon = B_\epsilon \hat{u} \tag{5.3}$$

where $\hat{u}$ is the vector of nodal displacements, as seen in Figure 5-2, and defined as:

$$\hat{u} = \begin{bmatrix} \delta_{x_1} & \delta_{y_1} & \delta_{x_2} & \delta_{y_2} & \delta_{x_3} & \delta_{y_3} & \delta_{x_4} & \delta_{y_4} \end{bmatrix}^T \tag{5.4}$$

where δ_{x_i} and δ_{y_i} are the x and y direction displacements of the i^{th} grid point in the element. Once the B_ϵ matrix is determined, it can be used with the projection matrix to determine the strain, and hence the stress, in the element. The challenge arises in computing the B_ϵ matrix. Note that the formulations for quadrilateral elements and triangular elements are slightly different because of the differing number of nodes. The slightly more complex quadrilateral case is described here.

The first step in creating the B_ϵ matrix is to define interpolation functions for the element. The interpolation functions must sum to one, be equal to one at the node of interest, and be equal to zero at all other nodes with respect to the internal coordinates, r and s, where the nodes are located at $(r, s) = (1, 1)$, $(-1, 1)$, $(-1, -1)$, and $(1, -1)$. In this case, the interpolation functions are defined as:

$$
\begin{aligned}
h_1 &= 0.25(1+r)(1+s) \\
h_2 &= 0.25(1-r)(1+s) \\
h_3 &= 0.25(1-r)(1-s) \\
h_4 &= 0.25(1+r)(1-s)
\end{aligned}
\tag{5.5}
$$

where h_i are the interpolation functions. The next step is to determine the derivatives of the interpolation functions with respect to x and y. This can be accomplished using the chain rule:

$$
\begin{bmatrix}
\frac{\partial h_1}{\partial x} & \frac{\partial h_2}{\partial x} & \frac{\partial h_3}{\partial x} & \frac{\partial h_4}{\partial x} \\
\frac{\partial h_1}{\partial y} & \frac{\partial h_2}{\partial y} & \frac{\partial h_3}{\partial y} & \frac{\partial h_4}{\partial y}
\end{bmatrix}
=
\begin{bmatrix}
\frac{\partial r}{\partial x} & \frac{\partial s}{\partial x} \\
\frac{\partial r}{\partial y} & \frac{\partial s}{\partial y}
\end{bmatrix}
\begin{bmatrix}
\frac{\partial h_1}{\partial r} & \frac{\partial h_2}{\partial r} & \frac{\partial h_3}{\partial r} & \frac{\partial h_4}{\partial r} \\
\frac{\partial h_1}{\partial s} & \frac{\partial h_2}{\partial s} & \frac{\partial h_3}{\partial s} & \frac{\partial h_4}{\partial s}
\end{bmatrix}
\tag{5.6}
$$

Equation 5.6 can be solved through defining the Jacobian as:

$$
\begin{aligned}
J &= \begin{bmatrix}
\frac{\partial x}{\partial r} & \frac{\partial x}{\partial s} \\
\frac{\partial y}{\partial r} & \frac{\partial y}{\partial s}
\end{bmatrix} \\
&= 0.25 \begin{bmatrix}
(1+s) & -(1+s) & -(1-s) & (1-s) \\
(1+r) & (1-r) & -(1-r) & -(1+r)
\end{bmatrix}
\begin{bmatrix}
x_1 & y_1 \\
x_2 & y_2 \\
x_3 & y_3 \\
x_4 & y_4
\end{bmatrix}
\end{aligned}
\tag{5.7}
$$

The Jacobian, J, is invertible, and the inverse of the Jacobian, along with the derivatives of h_i with respect to r and s, can be used to determine the derivatives of the interpolation functions with respect to x and y through Equation 5.6. These derivatives can be substituted into the appropriate locations in Equation 5.8, thus defining the strain interpolation matrix.

$$B_\epsilon = \begin{bmatrix} h_{1,x} & 0 & h_{2,x} & 0 & h_{3,x} & 0 & h_{4,x} & 0 \\ 0 & h_{1,y} & 0 & h_{2,y} & 0 & h_{3,y} & 0 & h_{4,y} \\ h_{1,y} & h_{1,x} & h_{2,y} & h_{2,x} & h_{3,y} & h_{3,x} & h_{4,y} & h_{4,x} \end{bmatrix} \tag{5.8}$$

where $h_{i,x}$ is the partial derivative of h_i with respect to x.

The strain interpolation matrix converts the nodal displacement outputs of the normal modes analysis to elemental strains. These strains can then be converted to stresses using Hooke's law for plane stress [56]:

$$\begin{bmatrix} \sigma_x \\ \sigma_y \\ \sigma_{xy} \end{bmatrix} = \frac{E}{1-\nu^2} \begin{bmatrix} 1 & \nu & 0 \\ \nu & 1 & 0 \\ 0 & 0 & \frac{1-\nu}{2} \end{bmatrix} \begin{bmatrix} \epsilon_x \\ \epsilon_y \\ 2\epsilon_{xy} \end{bmatrix} \tag{5.9}$$

where E is the Young's modulus and ν is the poisson ratio. Equation 5.9 can also be written as simply:

$$\sigma = C_\epsilon \epsilon \tag{5.10}$$

where C_ϵ is the compliance matrix relating the vector of strains to the vector of stresses.

The preceding steps allow for the calculation of a series of matrices that convert the three-dimensional nodal displacements of the grid points in an element to the elemental stresses. For each element, the full transformation from global, three-dimensional coordinates to stress can be described as:

$$\sigma = C_\epsilon B_\epsilon M \delta \tag{5.11}$$

where δ are the nodal displacements in the global, three-dimensional coordinates. These matrices can be automatically calculated, combined, and formatted to be the C_z matrix in the state-space model (Equation 5.1) for as many elements as desired.

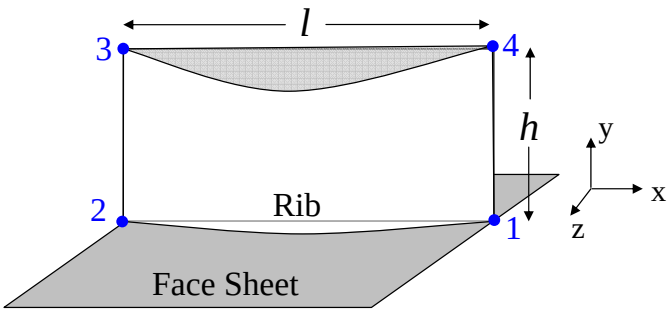

Figure 5-3: Bending Stress Schematic

SiC Out-of-Plane Bending Stress The second source of stress in the SiC plate elements is out-of-plane bending stress. Though it is typically much smaller than the in-plane stress, it is computed for thoroughness. The bending stresses are calculated using curvature. The bending strain can be defined as:

$$\begin{aligned} \epsilon_b &= -\kappa z \\ &= -\frac{d\theta}{dx} z \end{aligned} \tag{5.12}$$

where ϵ_b is the strain from the bending, κ is the curvature, z is the distance from the neutral axis, and θ is the rotation, with respect to the coordinate system in Figure 5-3, which shows a greatly exaggerated out-of-plane bending. If the elements are sufficiently small, the strain, and hence the stress due to bending can be approximated as:

$$\epsilon_b \approx \frac{(\theta_{y_3} - \theta_{y_4})}{l} \frac{t}{2} \tag{5.13}$$

where θ_{y_3} and θ_{y_4} are the rotations about the local y-axis of grid points 3 and 4, respectively, l is the distance between grid points 3 and 4, and t is the element thickness, again referring to the grid point numbering and coordinate system in Figure 5-3. The local rotations are obtained from transforming the rotations of the grid points to the local element coordinate system with the projection matrix (described in the plane stress case). The strain from bending can then be transformed to stress using

the Young's modulus and Hooke's law. Note that the bending stress in the local y direction dominates the bending stress in the local x direction in the rib elements. However, both the x and y bending stresses must be calculated for the face sheet elements.

Actuator Stress The final type of stress considered is the axial stress in the actuators, which can be calculated as:

$$\begin{aligned} \sigma_{act} &= E\epsilon_{act} \\ &= E\frac{\Delta L_{act}}{L_{act}} \end{aligned} \tag{5.14}$$

where σ_{act} is the actuator stress, E is the Young's modulus, ϵ_{act} is the actuator strain, ΔL_{act} is the change in length of the actuator, and L_{act} is the original length of the actuator. This simple calculation determines the tension or compression stresses experienced by the actuators.

Stress Calculation Summary The elemental stress outputs of the model are created through the three types of stress transformations, as described above. Both in-plane and out-of-plane stresses are calculated for the SiC plate elements, while axial stresses are calculated for the actuators. In all cases, the nodal displacements or rotations of the grid points describing the element, which are readily available from the normal modes analysis, are transformed such that the output of the state-space model is stress that can be used to determine launch survival.

5.1.2 Piezoelectric Actuator Model

The control actuator inputs to the mirror system are the embedded piezoelectric posts. In the structural model, the piezos are included as bar elements. The FEM bar elements account for the mass and stiffness, but the full electromechanical effects of the piezo must be included in the mirror system model. In the quasi-static case (Section 4.4.1), the electromechanical effects of the piezo are implemented using a

temperature analog. While that implementation works well for the quasi-static model, it is not a feasible method for the dynamic model. Instead, the piezoelectric equations are used to derive an expression that is implementable in the state-space model. This section will derive the full electromechanical model of the piezo through a simple, two degree-of-freedom system, then describe how that is used to include the piezo actuation in the state-space model.

A simple spring-mass system is used to illustrate the piezo implementation in the mirror model; consider the system shown in Figure 5-4. The finite element model can be considered as a series of lumped masses and springs, as described by the mass and stiffness matrices. Therefore, though this model is extremely simple, it is easily transferable to the larger mirror system.

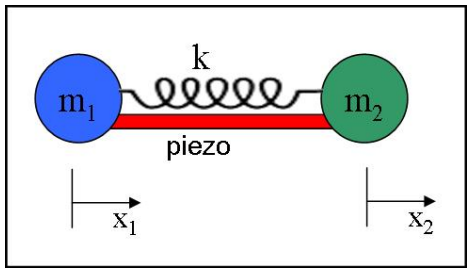

Figure 5-4: Simple Spring-Mass System for Piezo Equation Derivation

Assuming that the piezo acts as a force, the equations of motion for the system in Figure 5-4 can be written as follows:

$$m_1\ddot{x_1} = k(x_2 - x_1) + F_p \tag{5.15a}$$

$$m_2\ddot{x_2} = -k(x_2 - x_1) - F_p \tag{5.15b}$$

where m_1 and m_2 are the masses, k is the spring stiffness, and F_p is the piezo force.

The piezo force can be obtained through the use of the piezoelectric equations [36, 68, 3]:

$$\begin{bmatrix} D \\ S \end{bmatrix} = \begin{bmatrix} \epsilon^T & d \\ d_t & s^E \end{bmatrix} \begin{bmatrix} E \\ T \end{bmatrix} \tag{5.16}$$

where, using standard piezoelectric nomenclature, D is the vector of electrical displacements, E is the vector of electrical field in the material, S is the vector of mechanical strain, T is the vector of material stress, ϵ^T is the dielectric constant in a free condition, d is the piezoelectric constant, s^E is the compliance at short circuit, and the subscript $()_t$ denotes a transpose. In a piezo post, only the 3 direction is of concern, where the 3 direction corresponds to extension along the piezo post axis. The force can be obtained by considering the second part of Equation 5.16:

$$S = d_{33}E_3 + s_{33}^E T \tag{5.17}$$

Additionally, the following definitions are of use:

$$E = \frac{V}{L} \tag{5.18a}$$
$$S = \frac{\Delta L}{L} \tag{5.18b}$$
$$T = \frac{F_p}{A} \tag{5.18c}$$
$$D = \frac{Q}{A} \tag{5.18d}$$

where V is the voltage, L is the length of the piezo, A is the cross sectional area of the piezo, $\Delta L = x_2 - x_1$ is the change in length of the piezo, Q is the charge, and F_p is the piezo force. Using Equations 5.17 and 5.18, an expression for the piezo force is found:

$$F_p = \frac{A}{s_{33}^E L}(x_2 - x_1) - \frac{d_{33}A}{s_{33}^E L}V \tag{5.19}$$

For simplicity, the following variables are defined:

$$k_{pm} \equiv \frac{A}{s_{33}^E L} \tag{5.20a}$$

$$k_{pe} \equiv \frac{d_{33} A}{s_{33}^E L} \tag{5.20b}$$

Substituting Equations 5.19 and 5.20 into Equation 5.15 yields:

$$m_1 \ddot{x_1} = -kx_1 + kx_2 - k_{pm}x_1 + k_{pm}x_2 - k_{pe}V \tag{5.21a}$$

$$m_2 \ddot{x_2} = kx_1 - kx_2 + k_{pm}x_1 - k_{pm}x_2 + k_{pe}V \tag{5.21b}$$

This represents a system containing mechanical stiffness due to the spring and due to the piezo (k, and k_{pm}, respectively). Also, it contains the electrical properties of the piezo (k_{pe}), and the voltage input. The formulation can be used with the full mirror system to model the piezos.

When considering the larger, more complex mirror system, the FEM defines the spring-mass structure of the mirror. The FEM accounts for the mass and stiffness of the mirror structure, and the mechanical stiffness of the piezos (k and k_{pm}). However, the electrical aspects of the piezos (k_{pe}) must be added. For the piezo, the voltage is considered the control input ($u = V$). Therefore, the B_u matrix in Equation 5.1 is defined using the electrical properties of the piezo (k_{pe}) and Equation 5.21. By considering the appropriate degrees of freedom of the system and transforming to modal coordinates, the piezo implementation is complete and can be added to the full state-space model.

5.1.3 Disturbance Sources

The final aspects of the state-space model discussed in this section are the disturbance inputs. The primary disturbance sources of concern for the mirrors during launch are

random vibrations and acoustics. Acoustics are particularly problematic given the large surface area and low mass of the mirror. This section outlines the modeling methodology for both disturbance sources, as well as typical input spectra.

Vibrations

Random vibrations enter the spacecraft at the interface between the spacecraft and the launch vehicle. Since there is no spacecraft in this model, the vibrations enter through the rigid back structure, as described in Section 4.2. Again, this translates into a worst case scenario as the spacecraft structure would actually absorb some of the vibrations before they reach the mirror.

Random vibrations are generally described in terms of acceleration power spectral density functions. To apply the acceleration power spectral density to the model, the "big M" method is used [111, 122]. In this method, a large concentrated mass is placed on a base structure of the finite element model. The acceleration spectral density is scaled by the square of the magnitude of the large mass, and the resulting scaled spectrum is applied as a force. Through Newton's second law ($F = ma$), the scaled force PSD produces the desired acceleration in the mirror system.

The vibrations are applied in all three directions. One axis is considered translational, while the other two are considered transverse. Though the model allows for any axis to be the translational axis, the analysis herein assumes a stowed configuration in which the x axis is the translational axis, as seen in Figure 5-5. The transverse PSD is then applied to the y and z axes.

The vibration spectrum is a parametric variable in the model, and thus can be easily changed. Vibration spectra are available for a variety of launch vehicles, a few of which can be seen in Figure 5-6. The spectrum used in this thesis is taken from acceptance levels of the Shuttle, and is representative of typical launch vehicles. It is chosen because it is in the middle of the range of available spectra, and the rigid back structure implementation already assumes a worst case scenario. The g-loads of both the translational and transverse acceleration spectra that are utilized are summarized in, Table 5.1.3, and the spectra can be seen in Figure 5-7.

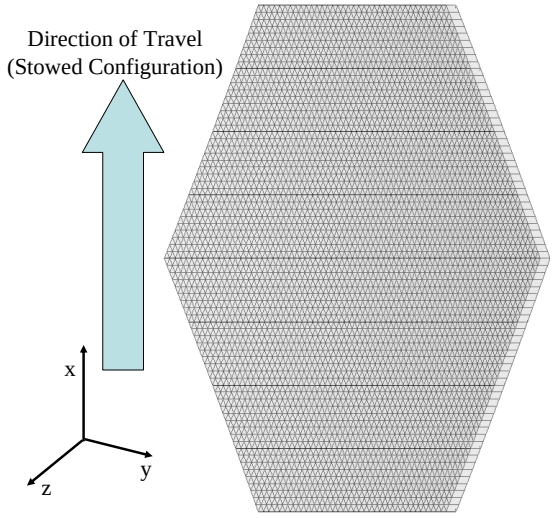

Figure 5-5: Launch Configuration

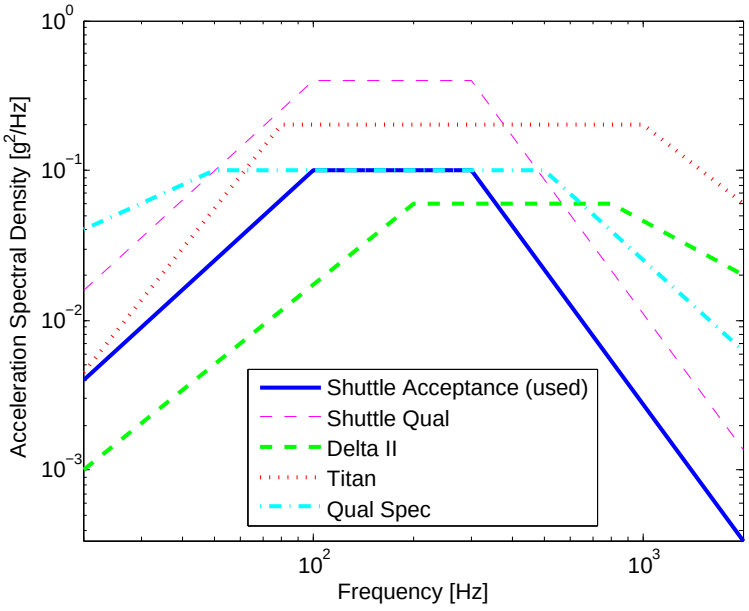

Figure 5-6: Random Vibration Spectra for Various Launch Vehicles [6, 5, 138]

Table 5.1: Launch PSD Data

Translational (Thrust) Axis		Transverse Axis	
Frequency (Hz)	PSD (g^2/Hz)	Frequency (Hz)	PSD (g^2/Hz)
20	0.004	20	0.001
20-100	+6 dB/Octave	20-100	+5 dB/Octave
100-300	0.1	100-300	0.01
300-2000	-9 dB/Octave	300-2000	-9 dB/Octave
2000	0.00034	2000	0.00001
Total	6.1 g RMS	Total	1.9 g RMS

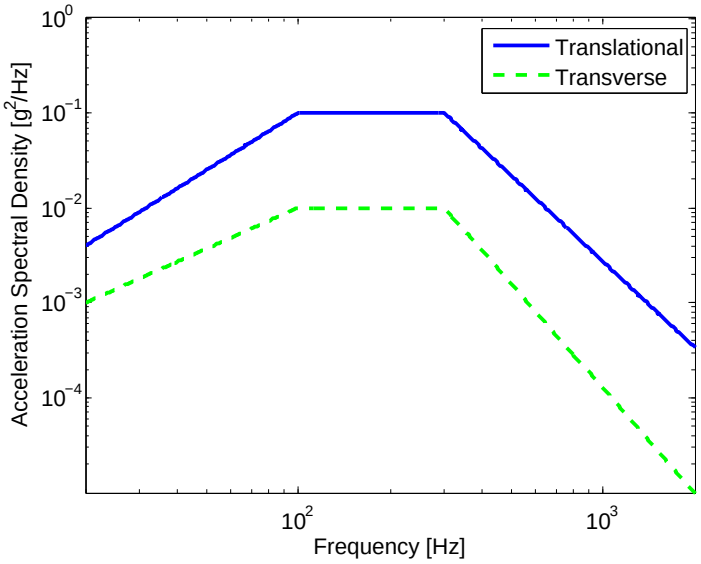

Figure 5-7: Chosen Random Vibration Spectra

Acoustics

The second disturbance source is acoustic loading, where the acoustic waves in the launch fairing apply pressure to the surface of the mirror. The acoustic pressure is analyzed using the patch method [120, 23]. In this method, a pressure force is applied to the surface of the mirror in patches. The pressure is correlated over each patch and uncorrelated to other patches.

There are a number of assumptions that must be made in the patch method. The first is angle of the pressure force application. Here, the pressure is applied normal to the mirror surface, which is the worst case angle, as shown below. The critical angle for acoustic pressure waves is that where the wave number of the acoustic wave projected on the mirror surface equals that of the structural bending mode, causing the spatial variation of the pressure to align with the structural mode shape.

$$k_{str} = k_{ac} sin\left(\theta_{cr}\right) \tag{5.22}$$

where k_{str} is the structural wave number, k_{ac} is the acoustic wave number, and θ_{cr} is the critical angle. The structural and acoustic wave numbers can be described in terms of basic quantities as follows:

$$k_{ac}^2 = \alpha^2 \omega^2 \qquad \alpha^2 = \frac{1}{\gamma R T} \tag{5.23a}$$

$$k_{str}^4 = \beta^4 \omega^2 \qquad \beta^4 = \frac{\rho A}{EI} \tag{5.23b}$$

where ω is frequency, $\frac{1}{\alpha}$ is the speed of sound, γ is the adiabatic index, R is the gas constant, T is temperature, ρ is density, A is area, E is Young's modulus, and I is the area moment of inertia. Equations 5.22 and 5.23 can be combined to yield:

$$\beta\sqrt{\omega} = \alpha\omega sin\left(\theta_{cr}\right) \tag{5.24a}$$

$$sin\left(\theta_{cr}\right) = \frac{\beta}{\alpha\sqrt{\omega}} \tag{5.24b}$$

The maximum of $sin\left(\theta_{cr}\right)$ is 1, yielding a cut-off frequency for critical angles (ω_c) of:

$$\omega_c = \left(\frac{\beta}{\alpha}\right)^2 \tag{5.25}$$

The cut-off frequency is calculated using a circular plate approximation for the mirror and the numerical values in Table 5.2. This yields a frequency cut-off of 211.6 rad/s, or approximately 33 Hz. The critical angle for all frequencies above ω_c is surface normal. Since the acoustic disturbance spectrum in this analysis begins at a frequency of approximately 25 Hz, the worst-case angle is assumed to be surface normal for all frequencies, and the pressures are all applied normal to the mirror surface.

Table 5.2: Numerical Values for Critical Angle Frequency Calculation

ρ	3200	kg/m^2
A	0.866	m^2
E	375×10^9	Pa
I	0.0871	m^4
β	0.0171	$\frac{\sqrt{s}}{m}$
α	0.0029	$\frac{s}{m}$

The second major assumption in the patch method is the number of patches on the mirror. Typically, a small number of patches is used [23], thereby saving computation. In this case, the patches are formed through a simple gridding of the surface, resulting in 1, 4, 9, 16, etc patches. The number of patches does have an effect on the output, as can be seen in Figure 5-8. Figure 5-8 shows the peak stress in the mirror as a function of the number of patches in the analysis. Four patches, which is the worst case, is chosen for this analysis.

The patch method is a commonly used approximation for acoustic analysis, and is convenient because it can be implemented with a finite element model, and without

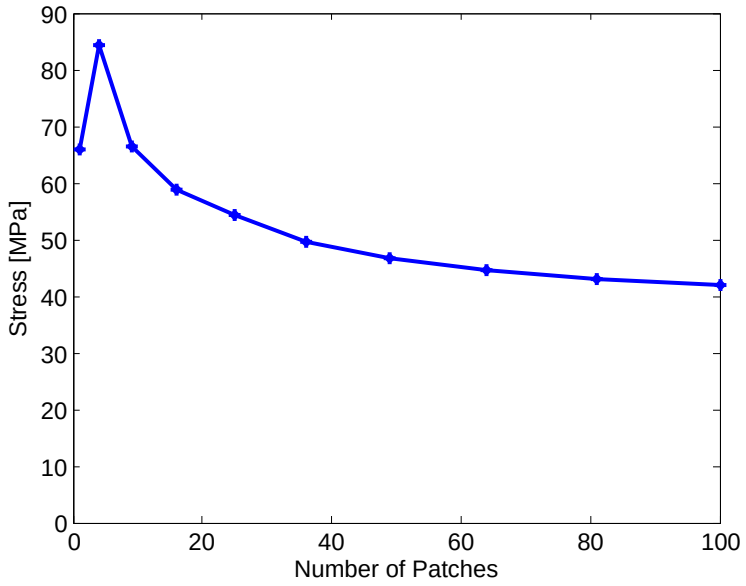

Figure 5-8: Effect of Number of Acoustic Patches on Stress

detailed knowledge of the launch fairing cavity. However, it does not actually model the acoustic waves or their reverberations (which can lead to amplification due to cavity resonance), so there is significant uncertainty involved in the analysis, as is seen in the variations due to the number of patches chosen. The uncertainty involved in the acoustic analysis will be discussed further in Section 5.3 and in Appendix A.

The acoustic input spectrum is specified in terms of sound pressure levels (SPLs). Again, this varies significantly between launch vehicles, as seen in Figure 5-9. The qualification specification, which is similar to the Delta IV spectrum, is used to ensure survival in any launch vehicle.

In order to apply the acoustic pressure to the model, it must be converted to a pressure power spectral density. For one-third octave bands and a reference pressure of $P_{ref} = 20\mu$Pa, the following steps convert the SPL to the pressure spectral density.

$$P(f) = P_{ref} 10^{\frac{SPL(f)}{20}} \tag{5.26a}$$

$$\Delta_f(f) = \left(2^{1/6} - 2^{-1/6}\right) = 0.2316f \tag{5.26b}$$

$$PSD(f) = \frac{P(f)^2}{\Delta_f(f)} \tag{5.26c}$$

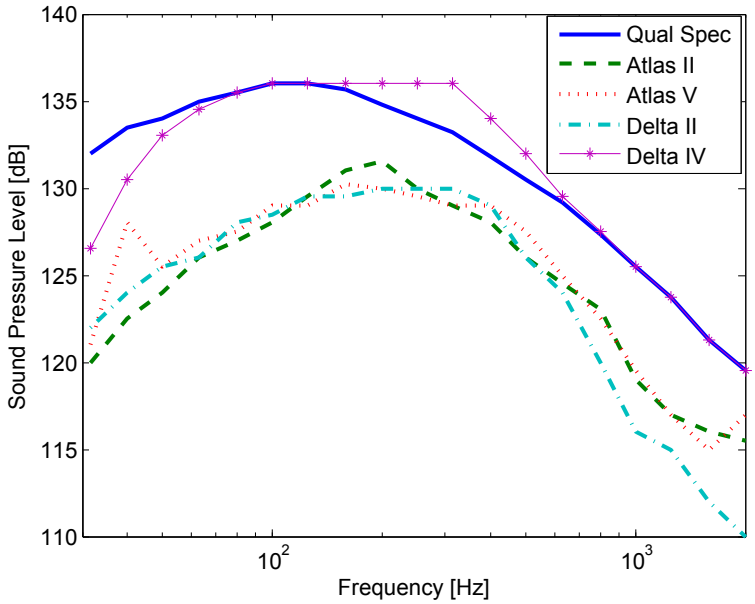

Figure 5-9: Sound Pressure Levels for Various Launch Vehicles [6, 5]

where P_{ref} is the reference pressure, $SPL(f)$ is the given sound pressure level curve (Figure 5-10(a)), $\Delta_f(f)$ is the frequency band size, and $PSD(f)$ is the desired pressure spectral density (Figure 5-10(b)).

5.1.4 Disturbance Analysis

With the state-space model of the plant and the launch load power spectral densities fully defined, a disturbance analysis can be performed to determine the stresses in the mirror when it is subjected to the prescribed disturbances. A frequency domain, steady state, dynamic disturbance analysis is performed. First, the integrated state-space model (Equation 5.1) is transformed into a frequency domain transfer function matrix as follows:

$$G_{zw} = C_z(sI - A)^{-1}B_w \tag{5.27}$$

The PSD of the output can then be found using:

$$S_{zz} = G_{zw} \cdot S_{ww} \cdot G_{zw}^H \tag{5.28}$$

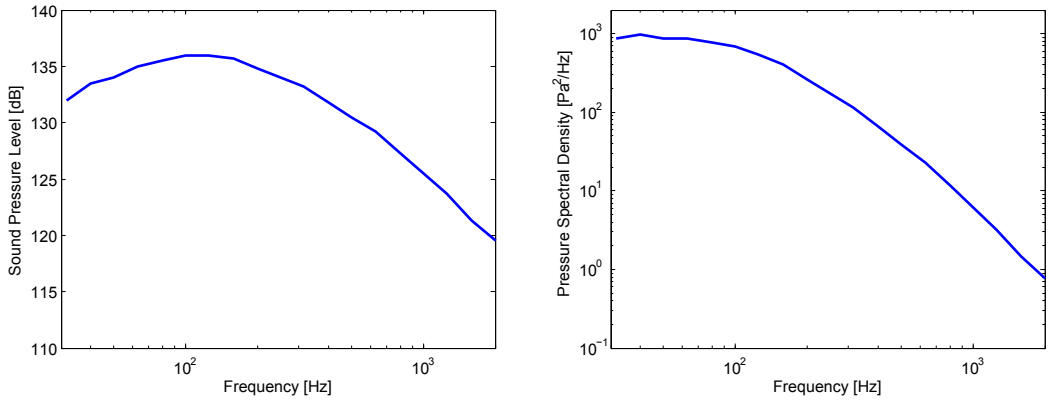

(a) Sound Pressure Levels

(b) Pressure Spectral Density

Figure 5-10: Acoustic Input Spectrum

where S_{zz} is the PSD of the output, S_{ww} is the PSD of the disturbance input (Figures 5-7 and 5-10(b)), G_{zw} is the system transfer function matrix (Equation 5.27), and $()^H$ is the hermitian operator. The mean squared value of the outputs can then be computed [24]:

$$\bar{z_i^2} = \frac{1}{2\pi}\int_{-\infty}^{+\infty} S_{zz}(j\omega)_{i,i}d\omega = \frac{1}{\pi}\int_{0}^{+\infty} S_{zz}(j\omega)_{i,i}d\omega \tag{5.29}$$

The square root of $\bar{z_i^2}$ yields the root-mean-square value of the output. The resulting stress output is a 1-σ value, meaning that the stress is expected to be below that value 68.2% of the time. In order to have greater confidence, 3 or 6-σ values will be used to ensure greater than 99% launch survival confidence.

5.1.5 Launch Model Summary

The preceding sections describe the dynamic model used for launch analysis, including the performance outputs and disturbance and control inputs. Additionally, the vibroacoustic input spectra are defined. This model formulation allows the computation of the stress distribution in the mirror, and will be used throughout the remainder of this thesis.

5.2 Baseline Mirror Results and Validation

The baseline mirror, which was defined in Chapter 4, and is reiterated here in Table 5.3, is analyzed using the launch model and analysis described in Section 5.1. This baseline is used to validate the model, and as a reference point in single-axis trade studies. This section presents the baseline mirror and corresponding stress distribution, as well as model validation and convergence analyses

Table 5.3: Parameters for Baseline Mirror

Segment diameter	1.2 m
SiC areal density	7.5 kg/m^2
Number of rib rings	4
Number of actuators	156
Face sheet mass fraction	0.63
Rib aspect ratio	25.4
Bipod reinforcement	2
Damping ratio	1 %

5.2.1 Stress Distribution in the Baseline Mirror

The peak stresses in both the silicon carbide substrate and in the actuators for the baseline mirror (as defined in Table 5.3) can be seen in Table 5.4. Note that these stresses are 1-σ values, which will be further discussed in Section 5.3. The stress resulting from only vibration and only acoustic disturbances are shown in addition to the combination of both disturbance sources. The acousticly induced stresses are significantly higher than the vibration induced stresses because it is a lightweight, large surface area system. The stress distribution over the mirror due to both the vibration and acoustic disturbances can be seen in Figure 5-11.

5.2.2 Validation

The stress outputs from this baseline model are validated to the extent possible. They are compared to available data from two similar systems, and match within 10% in all cases. The only parameter that was tuned was the bipod reinforcement parameter,

Table 5.4: Baseline Mirror Peak Stresses

	SiC Stress [MPa]	**Actuator Stress [MPa]**
Vibration Only	36	3
Acoustic Only	76	6
Vibration and Acoustic	83	12

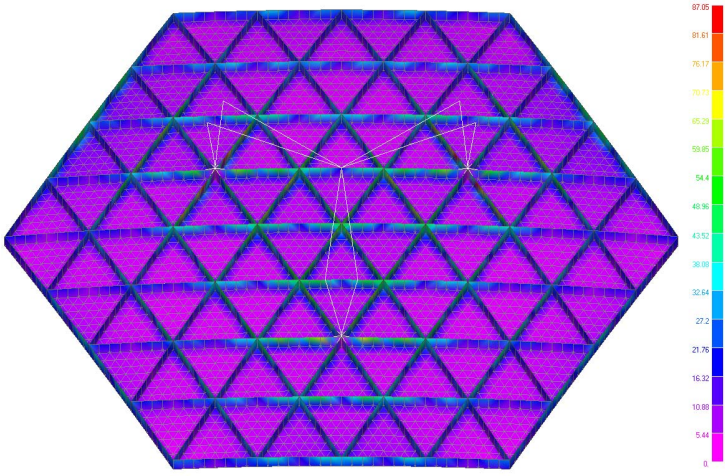

Figure 5-11: Stress Distribution in the Baseline Mirror

as it was unknown in the systems with available data. This adjustment was small, and within the range one would expect. The parametric nature of the model allows it to be validated against multiple sets of test data since the model can easily be made to represent the test setup.

5.2.3 Convergence Analyses

The launch model is created using finite element modeling, which is a discrete approximation to a continuous structure. Therefore, convergence analyses must be run to ensure that the model contains enough nodes, elements, and modes to approximate the true, continuous structure.

First, it is imperative that the system contains enough nodes and elements to approximate the continuous nature of the structure. More nodes and elements result in a closer approximation to the continuous structure, but also significantly increase

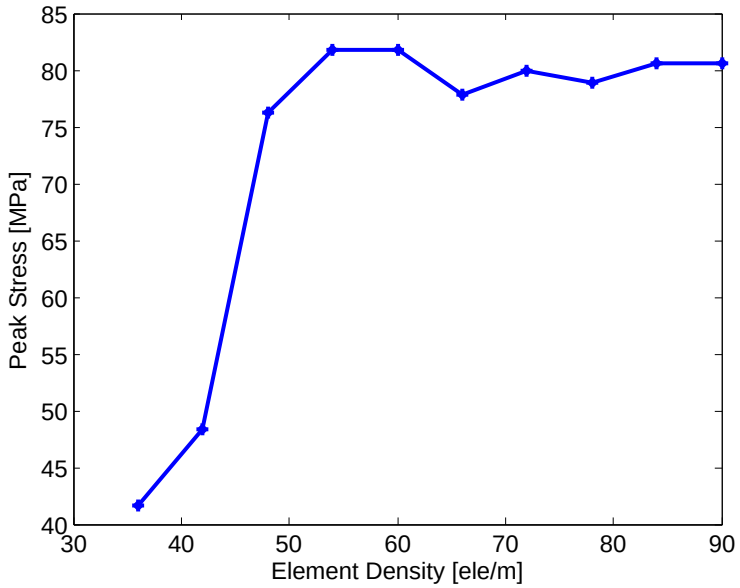

Figure 5-12: Convergence Analysis for Element Density

the computational expense of the model. The element density is defined as the number of elements per meter, and is plotted against peak stress in Figure 5-12. An element density of 80 elements per meter is chosen for use in the model, since, at that point, the output has converged.

Additionally, real structures have an infinite number of modes, but finite element modeling requires truncating high frequency modes. The FEM solver only computes the first n modes, where n is variable. In order to ensure that a sufficient number of modes remain in the system to accurately describe the response, a modal convergence is run. Figure 5-13 shows the peak stress plotted as a function of the number of modes retained in the model. Again, it is desirable to use the minimum number of modes that accurately describes the system, because adding modes significantly increases the size and computational expense of the model. As is visible in the plot, the system response can be accurately captured with the inclusion of approximately 25 modes. Therefore, 30 modes are used as the baseline without control.

One can eliminate the high frequency modes because both the system and the disturbance will roll-off at high frequencies. Consider Figure 5-14, which shows the stress PSD for the system containing 30 modes, along with the acoustic and vibration

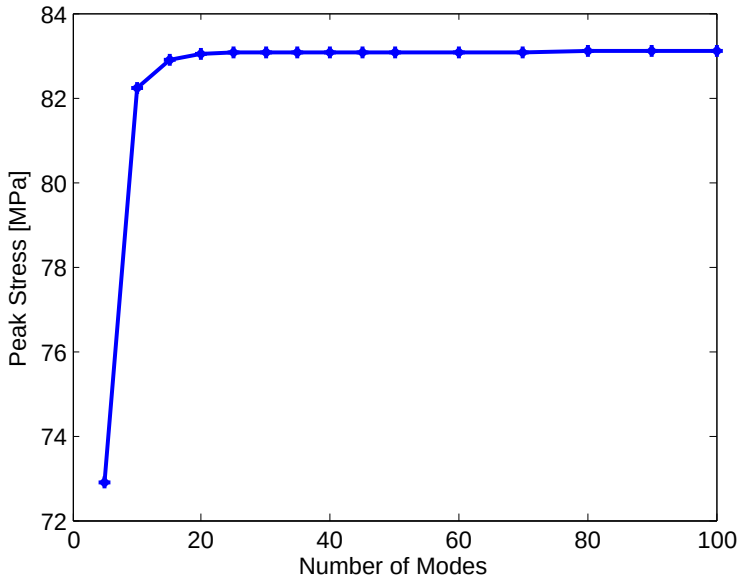

Figure 5-13: Convergence Analysis for Number of Modes

disturbance PSDs. The PSDs are normalized by their values at low frequency so that they can be compared against one another. Therefore, the magnitudes are irrelevant, and only the frequency content is of interest. Notice that the system contains modes as high as 1000 Hz, and, at that frequency, both disturbance spectra have significantly rolled-off. Therefore, it is unsurprising that the stress result is accurately captured using 30 modes. Also notice that in Figure 5-13, most of the stress is captured in only the first 10 modes, which is due to the fact that most of the energy in the system and in the disturbance spectra lie in the range of the first 3 modal frequencies, which encompasses the first nine modes.

An issue arises when shunt circuits or active damping, which will be described in Section 5.5, are added. The piezos interact with higher frequency modes, making it necessary to include more high frequency modes in the analysis. Figure 5-15 presents a similar plot to Figure 5-13, showing the number of modes versus the peak stress for a mirror with shunted piezos (as will be described in Section 5.5.2). In this case, the stress increases through approximately 100 modes. Therefore, 120 modes are used in systems in which there are shunt circuits or active damping.

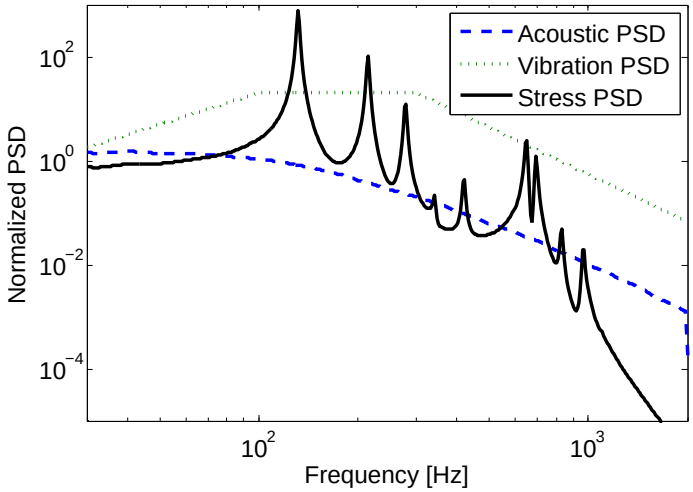

Figure 5-14: System Stress PSD Compared with Disturbance PSDs

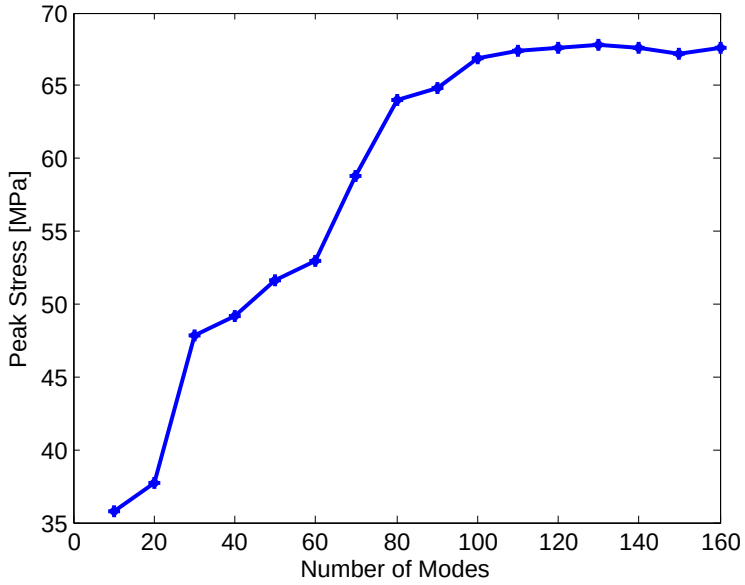

Figure 5-15: Convergence Analysis for Number of Modes with a Shunt Circuit

5.2.4 Baseline Mirror Summary

This section presents the baseline mirror and stress distribution. As expected, the acoustic disturbance is the driving factor in the stress output. The resulting stresses are validated against those for multiple other mirrors, and convergence analyses is performed on the finite element model to ensure fully converged results.

5.3 Stress Limits and Uncertainty Analysis

Launch survival is clearly necessary, and silicon carbide is a very brittle material. Therefore, the yield stresses are used as stress limitations for both the silicon carbide substrate and the actuators, which are approximately 600 MPa and 140 MPa, respectively. Also, a standard factor of safety of two is applied to the yield stresses.

The launch model calculates a value for stress that is a one standard deviation, or 1-σ, value. In other words, the stress will be at or below the calculated value about 68% of the time, assuming normal distributions. If a higher probability of launch survival is needed, then a higher standard deviation level should be used. Table 5.5 shows the confidence intervals associated with various standard deviation levels.

Table 5.5: Confidence Levels and Standard Deviation

Standard Deviation	**Confidence Interval**
1-σ	0.6826895
2-σ	0.9544997
3-σ	0.9973002
4-σ	0.9999366
5-σ	0.9999994
6-σ	0.999999998

Therefore, in order to have a 99.7% probability that the stress will be below a certain level, a 3-σ value should be used. This involves multiplying the value from the model by a factor of three, or alternatively, decreasing the stress limit level by a factor of three. The second method will be used here, where the output of the model is compared with an adjusted stress limit value. The 1-σ stress value, which

is obtained directly from the model, is compared to the adjusted limit levels, and if the 1-σ value from the model is below the calculated 3-σ limit (Table 5.6), then the mirror will survive with 3-σ certainty. This allows the mirror to be easily compared against multiple certainty level limits. Therefore, the stress limits shown in Table 5.6 are obtained, where the mirror will survive with the given certainty level as long as the model output is below the limit value.

Table 5.6: Stress Limits for 3 and 6-σ Confidence Levels

	Silicon Carbide	**Actuators**
3-σ (0.9973002)	100 MPa	23 MPa
6-σ (0.999999998)	50 MPa	11.5 MPa

There is significant disagreement in the community about the certainty level that is necessary. An overly conservative value will result in significant over design. However, a probability level that is too low and results in a high stress event causing the mirror to break would be catastrophic.

An uncertainty analysis on a flat plate sample problem is used to examine the necessary probability level. A model of acoustic loads acting on a flat plate is compared to test data, and a detailed uncertainty analysis is performed. The acoustic analysis is chosen because it is both the significant stress driver and more uncertain in nature compared with the vibrations. The analysis examines accelerometer outputs on a flat plate under acoustic loading. Uncertainty in material properties, geometry, damping, and the analysis method are all included. A full description and details of the model and uncertainty analysis can be found in Appendix A.

The uncertainty can be expressed as a cumulative distribution function (CDF), which shows the probability that the accelerometer output is less than a certain value. This is useful for launch survival analysis because it shows the probability that the mirror response will be below various output levels, which can be related to survivability limits. The CDF for the accelerometer on the flat plate can be seen in Figure 5-16. Additionally a CDF of a Gaussian distribution with the same mean and standard deviation are shown. Note that while the two plots have the same mean,

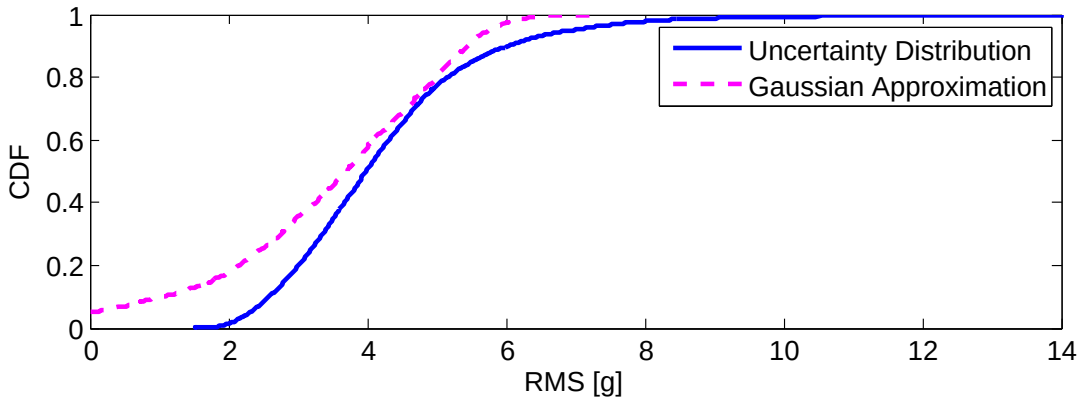

Figure 5-16: CDF for Acoustic Uncertainty Analysis on a Flat Plate

the uncertainty analysis results in a non-Gaussian distribution that is skewed upward toward higher acceleration levels. This can be seen by examining the upper tail and noticing that there is significant probability of high acceleration events, motivating the use of a 5 or 6-σ certainty level to ensure survival. The non-Gaussian nature of the output yields a 3-σ probability below the 99.7% probability level one would assume for a true Gaussian output. Though this analysis is performed using acceleration outputs, rather than stress, the uncertainty will manifest itself in the same way.

5.4 Mirror Design for Launch without Alleviation

With the completed model and stress limitations, the mirror design can be analyzed under launch disturbances. This section focuses on the design of the mirror, with no additional components, while Sections 5.5 and 5.6 discuss the addition of launch load alleviation techniques and design of the mirror for launch considering such techniques.

Section 5.4.1 presents a number of single-axis trades for the mirror. These single-axis trades can help determine the most sensitive and important parameters for launch. Next, Section 5.4.2 presents a design of experiments trade space for the launch model, which is used to determine the best families of designs considering launch.

5.4.1 Parameter Sensitivity for Launch

Single-axis trades are used to determine the effects and sensitivity of individual parameters. Here, all parameters are held constant at their baseline values (Table 5.3) except for the one being investigated. Single-axis trade plots for diameter, SiC areal density, rib aspect ratio, face sheet mass fraction, mirror F#, number of ribs, bipod reinforcement, and actuator length can be seen in Figure 5-17. Each plot shows the variation of stress with the parameter of interest.

In each plot, the baseline mirror is marked with a star. Also, the dotted lines mark the 100 and 50 MPa stress lines, which correspond to 3 and 6-σ certainty levels for SiC, respectively, as discussed in Section 5.3. All designs with are at or below the 3 or 6-σ certainty lines will survive with at least that level of certainty. As the diameter increases, the mirror becomes more flexible, and the stress increases, as expected. Similarly, as the areal density of the silicon carbide decreases, the stress also increases. The F#, which corresponds to the mirror curvature, has very little effect on the stress output. The stress is highest near the mounting points, which are unaffected by mirror curvature. Figure 5-17(d) shows that increasing the number of ribs causes an increase in stress. Under constant areal density, adding ribs means that the mass has to be spread between more ribs, so they are smaller, and thus provide less stiffness, causing the stress to increase. An increase in the rib aspect ratio results in taller, thinner ribs, and therefore causes a decrease in the stress. However, there is a limit as to how thin the ribs can become before they are too thin to manufacture. Figure 5-17(f) shows the variation in stress due to changing the face sheet mass fraction, or percentage of mass in the face sheet. Decreasing the mass in the face sheet results in having more mass in the ribs, which decreases the stress. However, there is again a limit to the manufacturing thickness. Additionally, a face sheet with too little mass cannot support the ribs, and face sheet drum head modes will dominate at very low face sheet mass fractions, leading to high stress. However, this is only manifested in infeasible designs where the face sheet thickness is below the manufacturing limit, and is thus not a driving factor. Reinforcing the bipod

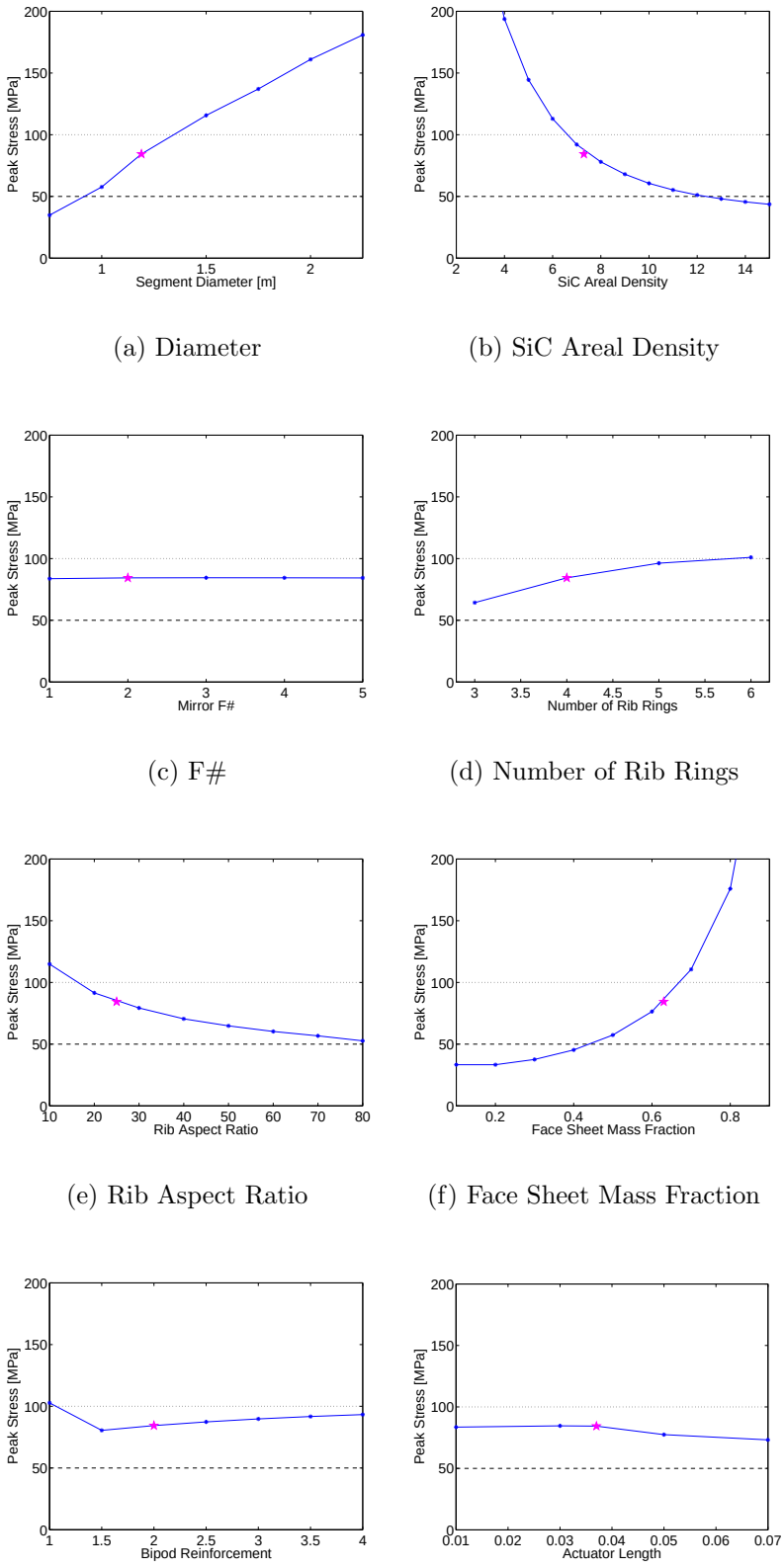

(a) Diameter

(b) SiC Areal Density

(c) F#

(d) Number of Rib Rings

(e) Rib Aspect Ratio

(f) Face Sheet Mass Fraction

(g) Bipod Reinforcement

(h) Actuator Length

Figure 5-17: Single-Axis Trade Studies and Parameter Sensitivities

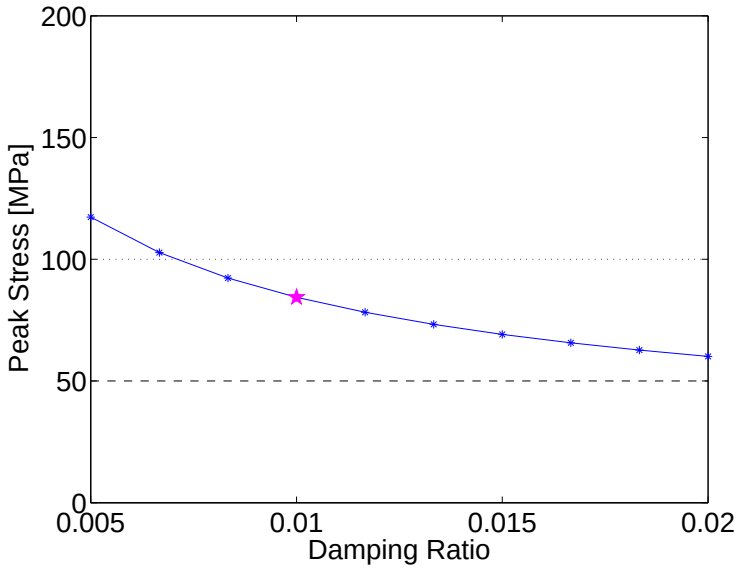

Figure 5-18: Single-Axis Damping Trade Study

connection points tends to decrease the stress in the elements nearest the mounting points. However, as the reinforcement continues to increase, the high stress points move farther out into the ribs, away from the connection points, and the peak stress increases. This is visible in Figure 5-17(g), where the discontinuity occurs when the peak stress moves to elements farther away from the bipod mount. Finally, Figure 5-17(h) shows the actuator length, which has very little effect on the stress output.

In addition to the structural parameters above, the modal damping ratio is also important. The effect of the damping on the peak stress can be seen in Figure 5-18. Adding damping always corresponds to a decrease in stress. However, without specifically adding damping through a launch load alleviation technique, as is discussed in Section 5.5, damping is outside of the control of the designer, and cannot be easily altered. Nonetheless, it is important to remember that damping has a significant effect, and thus the stress limits should account for any uncertainty in the damping ratio.

The single-axis trade results show to which parameters the stress is most sensitive, and can be used to choose the most important parameters for launch. The F# and actuator length clearly have minimal effects, and are thus unimportant in terms of finding a good design for launch and can be eliminated from the list. As mentioned

previously, though damping is very important, it lies outside the control of the designer, thus it is also eliminated from the list of launch design parameters. In an effort to compare similar mirrors, diameter is also eliminated. Changing the segment diameter significantly alters the characteristics of the system. Therefore, despite the importance of diameter, it is assumed that the mirror is being designed to be the best at a specific diameter. This leaves five parameters: silicon carbide areal density, number of ribs, rib aspect ratio, face sheet mass fraction, and bipod reinforcement. These five parameters are varied in the passive mirror trade space exploration in Section 5.4.2.

5.4.2 Launch Trade Space Analysis

The single-axis trades are used to determine the five parameters in the trade space analysis. In order to visualize the entire trade space of design options, a design of experiments sampling technique is used to explore the design space. Specifically, Latin Hypercube sampling (LHS) [30] is used to define 1000 designs, as was described for the on-orbit case in Section 4.4.4. The responses of each design are computed using the launch model. Again, though optimization could provide better results as to the actual set of non-dominated designs, the visualization of the design trade space would be lost. Therefore, for this preliminary analysis, LHS is used to efficiently examine the trade space.

For each design, the peak stresses are computed in both the silicon carbide and in the actuators. Additionally, the full mass of the system is calculated. In almost all cases, the silicon carbide has a peak stress that is closer to yield than the actuators, and, in the cases where the actuators are closer to yield, neither the peak stress in the actuator or in the SiC are near the stress limits. Therefore, the peak stress in the silicon carbide will be plotted against the mass. The entire trade space of designs can be seen in Figure 5-19. However, this does not exclude infeasible designs. There are manufacturing limits on the minimum rib thicknesses. Current manufacturing can achieve rib thicknesses of 0.7 mm. Figure 5-20 shows the designs that are eliminated (infeasible) due to the thickness constraint (Figure 5-20(a)) and the remaining,

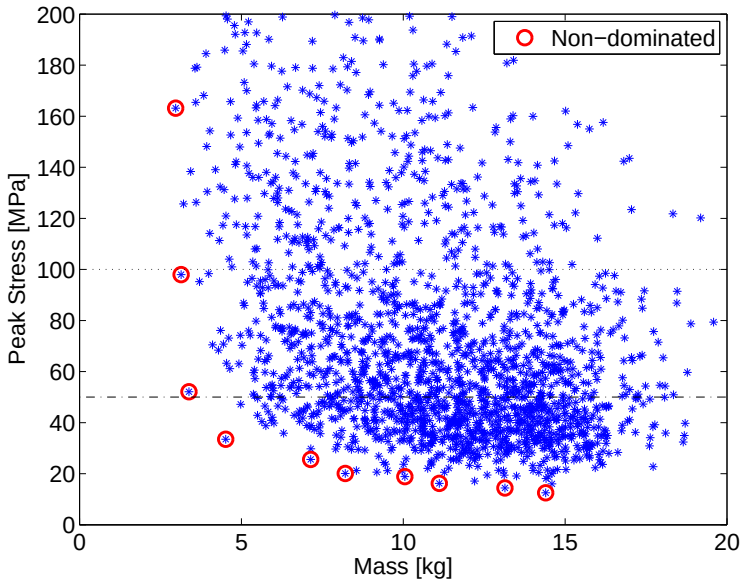

Figure 5-19: LHS Trade Space

feasible designs (Figure 5-20(b)).

Additionally, In Figures 5-19 and 5-20(b), the non-dominated designs are circled. These are the sets of designs for which there is no other design that has both lower mass and lower stress, so, within the set of non-dominated designs, one must sacrifice one objective to gain better performance in the other. The set of non-dominated designs approximates the Pareto front. In this case, since sampling was used and the design space is not entirely covered, the Pareto approximation is rough, and one can imagine it being filled in further if all possible designs were explored.

The trade space designs can also be differentiated and visualized by the different design parameters. Figure 5-21 shows the mass versus the peak stress for the feasible designs. Each of the plots shows the exact same designs, only the symbols are different to illustrate trends in the design parameters.

The first plot (Figure 5-21(a)) shows the trade space distinguished by the number of rib rings. Notice that the designs on the Pareto front tend to have a low number of rib rings. This is particularly apparent in the low mass designs. Figure 5-21(b) shows the designs differentiated by the rib aspect ratio. Here, it is clear that higher rib aspect ratios result in lower stress. Figure 5-21(c) differentiates the designs by the

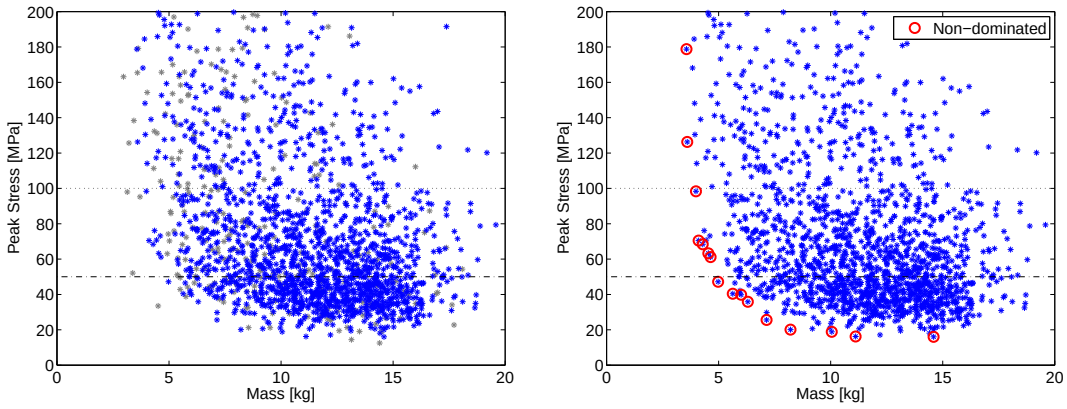

(a) Infeasible Designs Shaded

(b) Feasible Designs Only

Figure 5-20: Feasible Trade Space with Thickness Limit Applied

face sheet mass fraction, and designs with low face sheet mass fractions tend to be closer to the Pareto front. Figure 5-21(d) shows the designs distinguished by bipod reinforcement. The pattern here is not strong, but bipod reinforcement generally results in lower stress. Finally, Figure 5-21(e) shows the designs differentiated by areal density, which obviously has a very large effect on the mass. Also, notice that there are very few designs in the lowest range of 2.5 - 5 kg/m^2; most of these designs were either infeasible due to thickness limits, or have stresses well above the limits, indicating the difficulty of creating a low areal density mirror that will survive launch.

Table 5.7 summarizes the non-dominated designs, including the design parameters that make up each design, as well as the mass and peak stress. Notice that, by the definition of non-dominated designs, as the mass increases, the stress decreases. If one wants to move along the Pareto front, the primary parameter to vary is the areal density. Also, notice that the number of ribs tends to be low in most of the non-dominated designs. Most of the Pareto optimal designs have the minimum number of ribs. However, there are a few designs with more than three rib rings. This is a product of the LHS design search. In areas of the design space, there are many designs with very similar performances, and achieving the perfect balance of rib aspect ratio, face sheet mass fraction, and bipod reinforcement is difficult. If all information was available, as in a detailed full factorial search, or an optimization was performed,

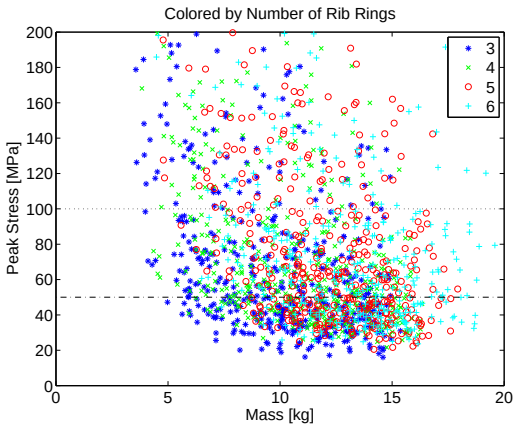

(a) Differentiated by Number of Rib Rings

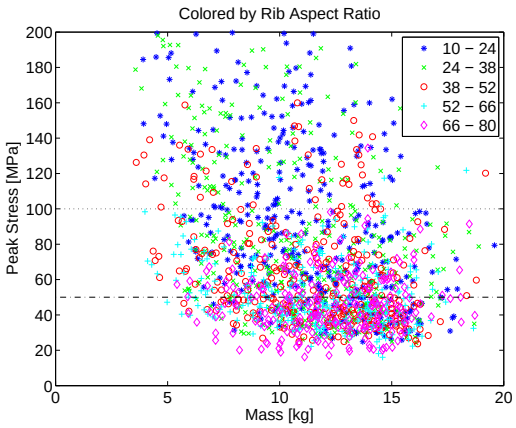

(b) Differentiated by Rib Aspect Ratio

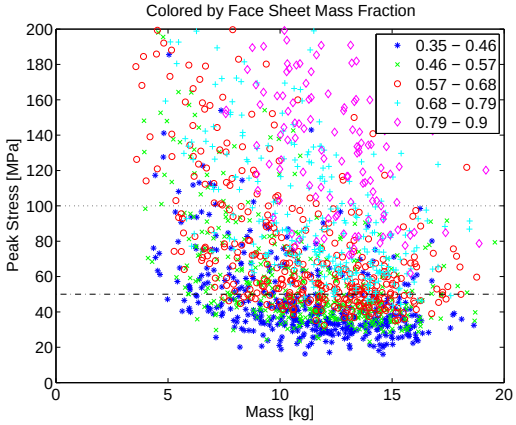

(c) Differentiated by Face Sheet Mass Fraction

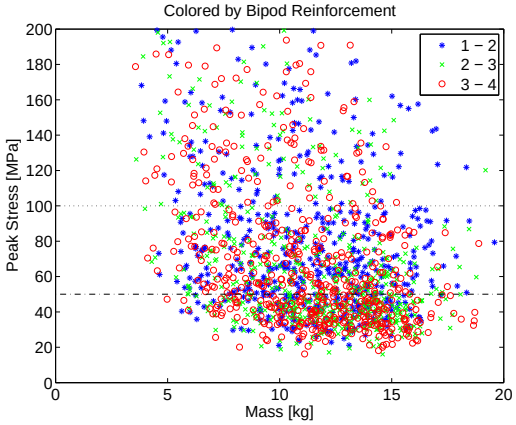

(d) Differentiated by Bipod Reinforcement

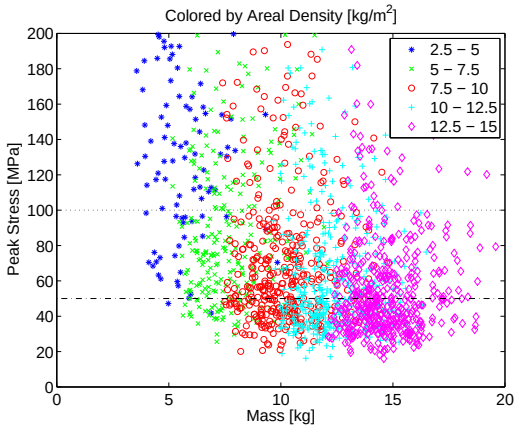

(e) Differentiated by SiC Areal Density

Figure 5-21: Trade Space with Design Parameter Differentiation

Table 5.7: Non-dominated designs in Launch Analysis

Design	Number of Ribs	Rib Aspect Ratio	Face Sheet Mass Fraction	Bipod Reinforcement	Areal Density [kg/m^2]	Mass [kg]	Peak Stress [MPa]
1	4	14	0.66	2.5	3.1	3.4	398
2	3	30	0.58	3.7	3.1	3.6	179
3	3	42	0.58	2.9	3.5	3.6	126
4	3	52	0.55	2.6	3.6	4.0	98
5	3	63	0.53	3.3	4.1	4.1	70
6	3	52	0.50	2.1	4.1	4.3	68
7	4	56	0.38	3.6	4.5	4.5	63
8	4	52	0.37	1.8	4.4	4.6	61
9	3	65	0.43	3.9	4.8	5.0	47
10	3	62	0.46	1.8	5.7	5.6	40
11	3	53	0.41	1.4	5.7	6.0	40
12	3	76	0.48	1.8	6.4	6.3	36
13	3	75	0.39	3.6	6.5	7.1	26
14	3	68	0.37	3.6	7.7	8.2	20
15	3	72	0.41	2.6	10.1	10.1	19
16	3	71	0.36	3.5	11.7	11.1	16
17	3	65	0.36	2.8	14.8	14.6	16

one would expect all of the designs on the Pareto front to have three rib rings. However, the similarity of the performance in conjunction with the incomplete trade space results in some of the non-dominated designs having more than the minimum number of rib rings. Also, the rib aspect ratio tends to be high and the face sheet mass fraction tends to be low, leading to taller ribs. This is especially apparent at higher areal densities where there is enough mass in the ribs to ensure that the thickness constraint is not violated, whereas the lowest areal density designs have slightly lower aspect ratios in order to meet the constraints.

The difficulty achieving the stress limits in both low areal density mirrors and mirrors with many rib rings, which are best for on-orbit performance, motivates the use of launch load alleviation techniques, as discussed in the following section.

5.5 Launch Load Alleviation

Though it is certainly possible to design mirrors that survive launch, the stresses due to launch loads are near the limits. Additionally, the mirrors that survive launch may not be optimally designed for on-orbit performance. In fact, designing mirrors for low launch stress or correctability drive the mirrors toward different ends of the design spectrum. This motivates using launch load alleviation to increase the number of designs that survive launch. Launch load alleviation techniques reduce the stresses in the mirror during launch, increasing the feasible design space and the probability of launch survival.

Three launch load alleviation techniques are considered: isolation, passive shunt circuits, and active damping. Isolation uses commercial isolation technology to separate the fragile spacecraft from the noisy launch vehicle, effectively reducing the magnitude of the vibration seen by the mirror. The other two techniques use the existing embedded actuators in the mirror to damp the structure. Shunt circuits provide damping through a passive circuit, while active damping involves a full active control system. The following sections elaborate on the implementation and effectiveness of each technique.

5.5.1 Isolation

One launch load alleviation option is isolation. Whole spacecraft isolation has the potential to reduce the vibratory loads seen by the spacecraft, thus increasing the survivability of the system. Currently, CSA Engineering [2] is a major contributor to whole-spacecraft isolation; they have developed a system called SoftRide which is placed between the spacecraft and the launch vehicle to provide vibration and shock isolation. Details of the SoftRide isolation system can be found in References [43, 140, 78, 98]. A model of the isolation resulting from a system such as SoftRide is created.

The isolator in the mirror model is based on a low-pass filter; the isolator is not modeled physically, but rather its effect on the system is modeled. The isolator filter

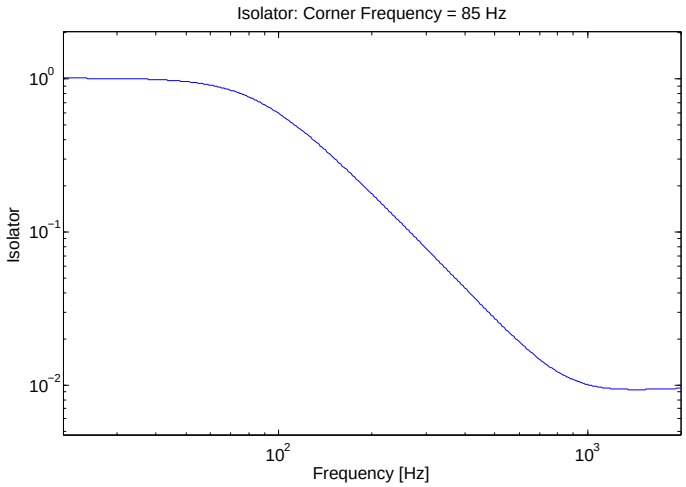

Figure 5-22: Baseline Isolator

has variable damping and corner frequencies and levels out at higher frequencies to represent the limitations of physical isolators. The baseline isolator parameters can be seen in Table 5.8, and the isolator filter can be seen in Figure 5-22. The corner frequency is based on the achieved isolation frequency of the CASPAR SoftRide isolator [98].

Table 5.8: Baseline Isolator Parameters

Corner frequency	85 Hz
Damping ratio	0.7
Decades of roll-off	2
Roll-off slope	-40 dB/decade

The isolator is implemented at the interface of the back structure mirror mount, where the vibrational force enters the mirror. This is also the point where the disturbance enters the model, and thus the vibration is attenuated before it reaches the mirror. In reality, the SoftRide isolation systems are implemented at the interface between the spacecraft and the launch vehicle, which is also where the vibrational loads enter the system. However, this model does not include the spacecraft structure. Therefore, though the structure would ideally be included, this placement of the isolator is consistent with the previous omission of the structure and load application as a worst-case scenario.

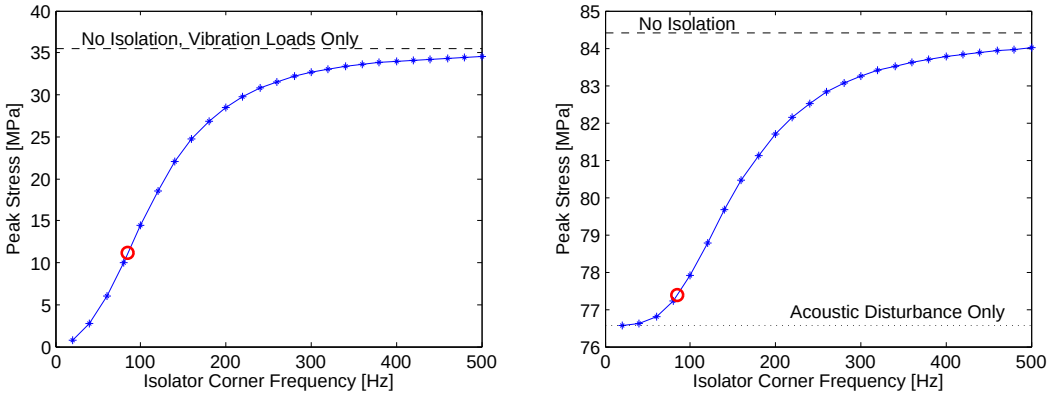

(a) Vibration Loads Only

(b) Vibration and Acoustic Loads

Figure 5-23: Stress as a Function of Isolator Corner Frequency (85 Hz Case Circled)

The isolator reduces the stress in the mirror. The isolator corner frequency is varied to illustrate its effect on the stress reduction. A lower corner frequency results in more of the disturbance being filtered and reduced, leading to lower stresses. Also, the effect of isolation is examined using vibration loads only, and a combination of vibration and acoustic loads. The results for both cases can be seen in Figure 5-23.

As is visible in the plots, the isolation has a large effect on the stress due to the vibration. However, it does not attenuate the acousticly induced stresses. This is as expected; the isolator filters the vibrations, but the acoustic loads act on the surface of the mirror, and are thus unaffected by the isolator. Note that the combined vibroacoustic analysis is not simply the summation of stresses due to the vibrations and acoustics, rather it is a coupled problem. Therefore, the reduction in stress in the vibration-only case is unequal to the stress reduction in the combined analysis.

The corner frequency must be chosen carefully. The spacecraft couples with the launch vehicle through the isolator, and thus that isolator must not be of such a low frequency as to induce undesirable resonances of the coupled system. Also, the isolator has a certain stroke, which must be maintained under the g-load of launch. In other words, the isolator is compressed, similar to a spring, as the vehicle undergoes acceleration. There is a limited stroke in that compression, and if the isolator is too soft, it reaches its stoke limit and no longer functions as an isolator. Therefore, the

frequency must be carefully chosen, and is assumed to be 85 Hz, as in the demonstrated SoftRide case. This results in a 65% reduction in stress in the vibration-only case, and a 5% reduction in stress when both vibration and acoustic disturbances are included. Both cases are marked by circles in Figure 5-23.

Additionally, adding an isolator adds mass to the system. The number of SoftRide isolator flexures necessary for a spacecraft is mission specific; a minimum of three are needed to isolate the spacecraft from the launch vehicle, and more can be added to improve performance. Each isolator component has a mass of 20 to 35 lbs [10]. For this case, it is assumed that three isolators would be used in the overall system, and that system would contain six mirror segments. This attributes the additional mass of half of one isolator component to a single mirror segment. Each isolator is approximated as 30 lbs, or 13.6 kg, so an additional 6.8 kg is added to the mass of the mirror segment when isolation is used. The number of mirrors and isolator components, as well as the exact mass of each isolator component, will vary with every mission. However, this approximation is a realistic estimate that will help define the mass penalty of including isolation.

In summary, isolation is implemented in the mirror model as a low pass filter that levels off at high frequencies to replicate the limitation of physically realizable isolators. The isolator greatly reduces the stress due to vibrations, but does not reduce stress from acoustic loading, which is the more detrimental load case for the mirror. However, the isolator does provide some level of stress reduction, which could be enough to ensure survival. Additionally, though the isolation may not be the appropriate solution when considering only mirror survival, it may also contribute to the launch survival of other fragile components on the spacecraft that are not considered here.

5.5.2 Shunted Piezos

The second launch load alleviation technique considered is passive shunting of the embedded piezos. The actuated mirrors under consideration contain many piezoelectric actuators for shape control of the mirror surface during operations. By applying

a voltage, the piezo converts the electrical energy to mechanical strain energy, and the piezo expands or contracts. This creates a moment that can be used to change the shape of the mirror surface in a desired way, as described in Chapter 4. One key element of piezoelectric actuators is that they can be used in either direction: electrical energy can be converted to mechanical energy, as in the actuator case, or mechanical energy can be converted to electrical energy. With this in mind, a passive shunting circuit can be added to the piezo, and mechanical energy can be converted to electrical energy and be dissipated through the circuit, providing additional damping. This additional damping can reduce the mirror response to the vibroacoustic launch disturbances, and increase the chance of survival.

Shunt Circuit Implementation

Shunt circuits are passive circuits that can be implemented using a number of configurations. In order to implement the circuits in the mirror model, a control system analog is used. The input to the system is the voltage, as described in Section 5.1.2, and the output is the charge, which can be obtained using the piezoelectric equation [36, 68, 3]:

$$D = \epsilon_3^T E + d_{33} T \tag{5.30}$$

where, using standard piezoelectric nomenclature, D is the vector of electrical displacements, E is the vector of electrical field in the material, T is the vector of material stress, ϵ_3^T is the dielectric constant in a free condition, and d_{33} is the piezoelectric constant. Considering Equation 5.30 and the same implementation method as was discussed in Section 5.1.2, the charge, Q, can be expressed as:

$$Q = k_{pe}(x_2 - x_1) + C_p V - d_{33} k_{pe} V \tag{5.31}$$

where k_{pe} was defined in Section 5.1.2 and contains the electrical aspects of the piezo, V is the voltage, and C_p is the piezo capacitance, and is equal to:

$$C_p = \frac{A\epsilon_3^T}{L} \tag{5.32}$$

where A is the cross-sectional area and L is the length of the piezo.

Equation 5.31 for the charge can be implemented in the state-space model as the control sensor, y. This formulation allows the creation of the piezo control input and output equations in the state-space model. Then, the shunt circuit can be implemented as a state-space control system and used to close the loop. Though the set-up is consistent with that of a control system, it is still a passive circuit. The control formulation simply provides a convenient implementation method. Currently, two types of shunts are considered: a purely resistive shunt and a tuned resonant shunt, involving a resistor and an inductor in series. In the tuned resonant shunt, the circuit is tuned to a specific, problematic frequency, and the additional damping is targeted at that frequency. Additionally, the tuned shunt can be used with multiple modes, tuning different piezos to different modal frequencies. Furthermore, the implementation of the shunt circuit as a control system allows for the possible future addition of other shunting circuit realizations.

Resistive Shunt

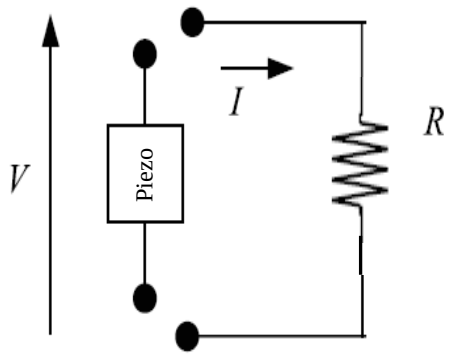

Figure 5-24: Resistive Shunt

The resistive shunt simply uses a resistor to dissipate energy, as seen in Figure 5-24. The equation for the resistive shunt is:

$$V + R\dot{Q} = 0 \tag{5.33}$$

where R is the resistance. This can be implemented as a state-space controller, though high-frequency roll-off poles must be included to make the system strictly proper.

$$\begin{aligned} \begin{bmatrix} \dot{x_c} \\ \ddot{x_c} \end{bmatrix} &= \begin{bmatrix} 0 & 1 \\ -\omega_c^2 & -2\zeta\omega_c \end{bmatrix} \begin{bmatrix} x_c \\ \dot{x_c} \end{bmatrix} + \begin{bmatrix} 0 \\ \omega_c^2 \end{bmatrix} Q \\ V &= \begin{bmatrix} 0 & -R \end{bmatrix} \begin{bmatrix} x_c \\ \dot{x_c} \end{bmatrix} \end{aligned} \tag{5.34}$$

where ω_c is the roll-off frequency, which is chosen above the frequency range of interest, and ζ is the damping ratio of the controller roll-off poles, and is chosen to be 0.7071, which is critically damped.

The optimal shunt circuit parameters can be calculated analytically, following the derivations in Hagood [68]. First, the electrical damping ratio of the resistant shunt can be shown to be:

$$r = RC_p^s\omega_n = \rho|_{\omega=\omega_n} \tag{5.35}$$

where

$$\rho = \sqrt{1 - k_{33}^2} \tag{5.36}$$

where r is the electrical damping ratio, ω_n is the natural frequency of the system, ρ is the non-dimensional frequency corresponding to the maximum loss factor of the shunted piezo, k_{33} is the coupling coefficient, and C_p^s is the inherent capacitance at constant strain (clamped). The square of the coupling coefficient represents the percentage of mechanical strain energy that can be converted to electrical energy and vice versa. It is defined as:

$$k_{33} = \frac{d_{33}}{\sqrt{s^E \epsilon_3^T}} \tag{5.37}$$

Also, the constant strain capacitance can be related to the constant stress capacitance (free condition) through the following relationship:

$$C_p^s = C_p(1 - k_{33}^2) \tag{5.38}$$

Therefore, the optimal resistance value, R, can be calculated from the system natural frequency and the properties of the piezos.

Tuned Resonant Shunt

The tuned resonant shunt circuit uses a resistor and an inductor in series to dissipate energy at a specific mode, as seen in Figure 5-25.

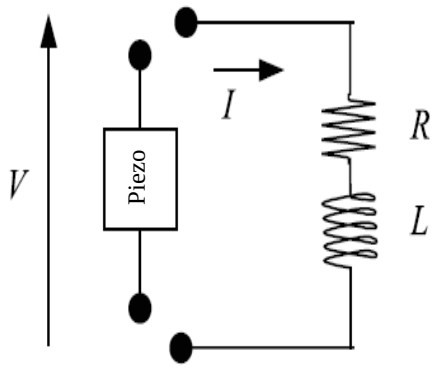

Figure 5-25: Tuned RL Shunt

The equation for the RL-shunt is:

$$L\ddot{Q} + R\dot{Q} + V = 0 \tag{5.39}$$

where L is the inductance. Equation 5.40 shows the state-space implementation, including high frequency roll-off poles.

$$\begin{bmatrix} \dot{x_c} \\ \ddot{x_c} \\ \dddot{x_c} \end{bmatrix} = \begin{bmatrix} 0 & 1 & 0 \\ 0 & 0 & 1 \\ -\omega_c^3 & -\omega_c^2(1+2\zeta) & -\omega_c(1+2\zeta) \end{bmatrix} \begin{bmatrix} x_c \\ \dot{x_c} \\ \ddot{x_c} \end{bmatrix} + \begin{bmatrix} 0 \\ 0 \\ \omega_c^3 \end{bmatrix} Q$$
$$V = \begin{bmatrix} 0 & -R & -L \end{bmatrix} \begin{bmatrix} x_c \\ \dot{x_c} \\ \ddot{x_c} \end{bmatrix} \tag{5.40}$$

As in the case of the resistive shunt, ω_c is the frequency of the controller roll-off poles used to make the system strictly proper, and ζ is the damping ratio chosen to be critically damped.

In order to maximize the damping at a certain resonance frequency, the electrical resonant frequency is set equal to the natural frequency modified by a tuning parameter.

$$\omega_e = \frac{1}{\sqrt{LC_p^s}} \tag{5.41a}$$
$$\delta = \frac{\omega_e}{\omega_n} \tag{5.41b}$$

where ω_e is the electrical resonant frequency and δ is the non-dimensional tuning parameter. Similar to the resistive shunt case, the resistance can be calculated using the electrical damping ratio, r.

$$r = RC_p^s\omega_n \tag{5.42}$$

However, in this case, the calculation of the electrical damping ratio, r, and tuning parameter, δ are not as simple. There are multiple ways to approximate the optimal parameters, two of which are outlined in Reference [68]. Using the transfer function optimization:

$$\delta_{opt} = \sqrt{1 + K_{ij}^2} \tag{5.43a}$$

$$r_{opt} \simeq \frac{\sqrt{2}K_{ij}}{1 + K_{ij}^2} \tag{5.43b}$$

where K_{ij} is the generalized electromechanical coupling coefficient, and can be calculated with the open circuit and short circuit natural frequencies:

$$K_{ij}^2 = \frac{\{(\omega_n^D)^2 - (\omega_n^E)^2\}}{(\omega_n^E)^2} \tag{5.44}$$

where ω_n^E is the natural frequency at short circuit (referred to as ω_n above), and ω_n^D is the natural frequency at open circuit. These relationships can be used to calculate the optimal values of L and R to be used with the shunt circuit set-up in Equation 5.40.

One potential issue with RL-shunt circuits is that they require high inductor values when trying to damp low frequencies. Traditional inductors with high inductance values are extremely massive. However, this issue can be counteracted through the use of a Riordan gyrator circuit [117] to achieve the desired inductance. Additionally, Fleming et al. [49] have demonstrated synthetic impedances for creating RL shunt circuits. Therefore, the issue of high inductances has been addressed and can be overcome through these means, making the resonant shunt a viable option.

Multi-Mode Resonant Shunt

The tuned resonant shunt formulation is derived for a single piezo and a single mode, and it is assumed that all of the piezos in the mirror are tuned to that mode. However, there may be multiple modes that significantly contribute to the mirror stress. Since the mirror system has many piezos, it is possible to tune some piezos to one mode, other piezos to a second mode, and so forth in order to minimize the stress in the mirror by targeting the set of modes that contribute most to the stress. This has the benefit of targeted damping of problematic modes, offered by the resonant shunt, but with the ability to address multiple significant modes.

The multi-mode case uses the same resonant shunt derivation technique described in the previous section. However, the optimal parameters (δ, r, R, L) are computed for each mode of interest. Then, each piezo uses the corresponding R and L values for the mode that it is assigned to damp. The difficulty involved with this case is in determining which piezos should damp which modes. Some piezos are in locations where a certain mode is unobservable or uncontrollable, making that shunt ineffective, and it is desirable to use the piezos in a capacity in which maximizes the damping. Therefore, one would like each piezo to be tuned to a mode over which that piezo is effective and that significantly contributes to the stress.

In order to determine which piezos should be tuned to which modes, a modal influence parameter is devised. First, the number of modes to be shunted and the corresponding modal frequencies must be determined. In the case of the mirror model, the first three modal frequencies typically have the most influence on the stress outputs. Next, the degrees of freedom corresponding to the the piezos' 3-direction are extracted from the mode shape matrix (Φ), and converted to a relative displacement (similar to the stress calculations), resulting in a single relative modal influence value for each piezo for each mode of interest. Then, the modes are weighted as to how important they are in the performance of the system. Finally, for each piezo, the mode with the highest weighted relative modal influence value is assigned to that piezo, and the RL circuit associated with that piezo is tuned accordingly.

Shunt Circuit Results

The shunted piezos are implemented in the mirror model. All piezos are assumed to be shunted, and the baseline mirror and piezo parameters are used. The PSD of the mirror system (stress output) subjected to the vibroacoustic launch loads can be seen in Figure 5-26. In addition to the output PSD, the cumulative mean squared output is shown in Figure 5-26. The cumulative output shows the integral of the PSD up to the frequency in the plot, so rises in the cumulative output illustrate which frequencies contribute most to the total RMS output. From the cumulative mean square stress distribution, it is clear that the first three modal frequencies contribute most to the

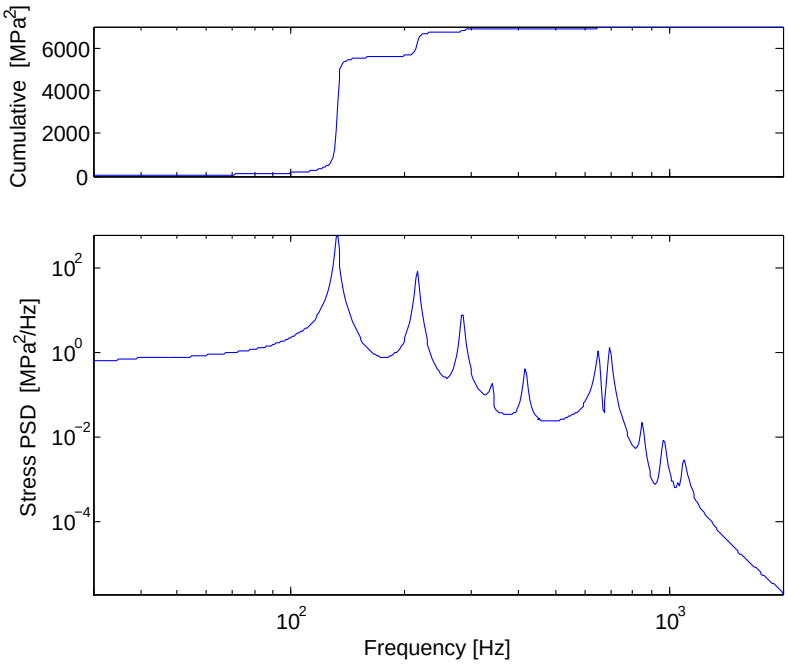

Figure 5-26: Mirror PSD (including cumulative)

resulting stress.

The optimal values for the resistive and resonant shunt circuits are calculated, and PSDs of the shunted system, focused around the first three modes, can be seen in Figure 5-27. The numbers in parentheses represent the total stress in each case (for the single element being considered).

Notice that the resistive shunt (R-Shunt) damps all modes a small amount. There are two different resonant shunts; one corresponds to all of the piezos being tuned to the first modal frequency, and the second corresponds to all of the piezos being tuned to the second modal frequency. The resonant shunt tuned to the first frequency (RL-Shunt ω_1) almost damps out the first mode, but the response for the second and third modes remains high. Similarly, the resonant shunt tuned to the second mode (RL-Shunt ω_2) damps the second mode, but not the first or third modes. The multi-mode shunt tunes each of the piezos to either the first, second, or third modal frequency. This case provides targeted damping at each of the three modes, and outperforms all other options.

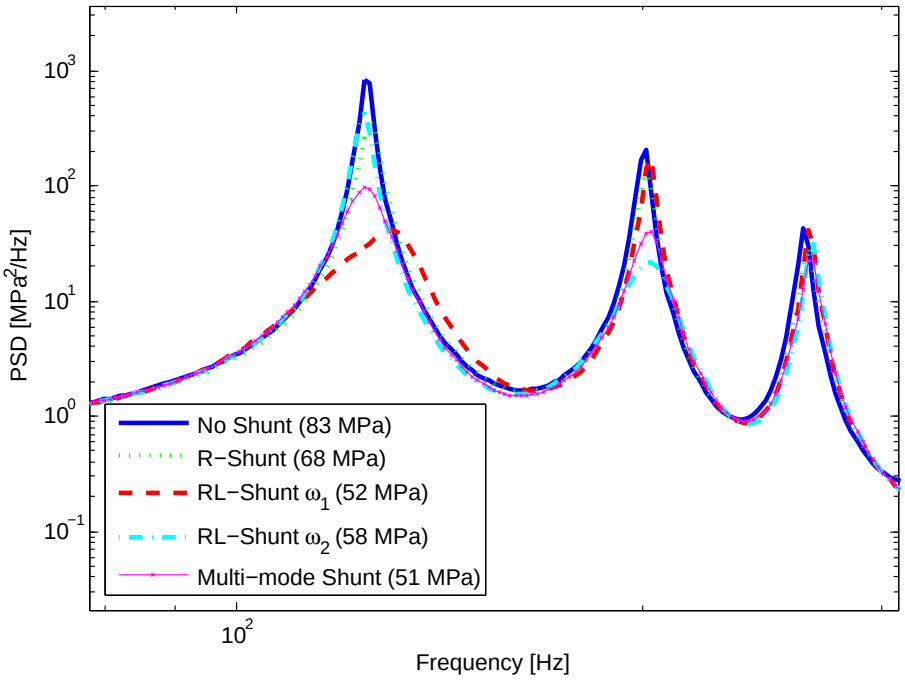

Figure 5-27: Mirror PSD with Multi-Mode Shunting Circuit

Model Reduction

The shunt circuit adds damping to the system and significantly decreases the response. However, the implementation increases the size of the model. The resistive shunt adds two states per piezo, and the resonant shunt adds three states per piezo. For the 156 piezo mirror, this amounts to an extra 312 and 462 states for the resistive and resonant shunts, respectively. The initial model contains 120 modes to capture the response of the system, resulting in a model with 240 states, so the piezo states increase the size of the model about three-fold. However, many of these states can be reduced out of the aggregate model. In implementing the shunt circuit, the extra states were necessary to make the control system strictly proper. When combined with the plant model, the aggregate model has enough poles that many of those additional states can be removed through model reduction.

The reduction method for this portion of the model is balanced truncation. The model is first balanced through a transformation that results in the observability and controllability grammians being equal. Details about balancing can be found in Ref-

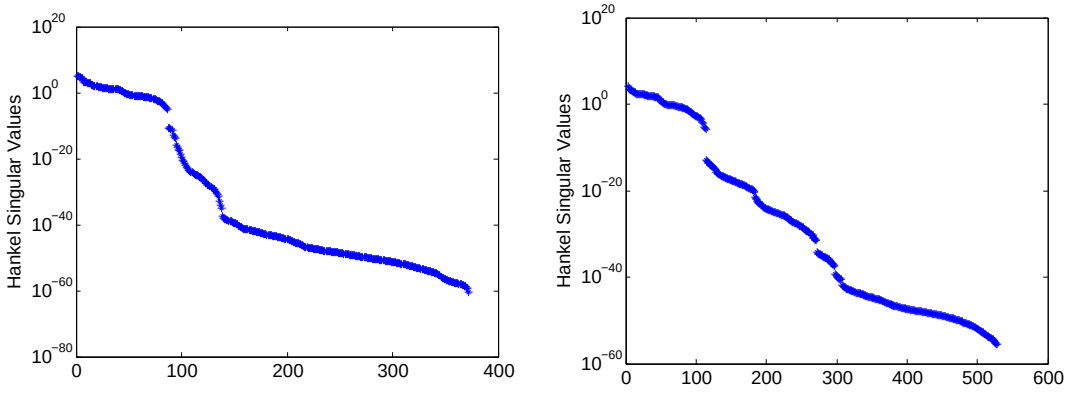

(a) Resistive Shunt

(b) Resonant Shunt

Figure 5-28: Hankel Singular Values of the Mirror System

erences [109, 115, 132]. The hankel singular values (HSVs) represent the amount that a state can be observed (or influences the performance) and controlled (or disturbed), and thus, states with low hankel singular values can be truncated. The HSVs for mirrors including resistive and resonant shunt can be seen in Figures 5-28(a) and 5-28(b) respectively. In both cases, the models are truncated to include only the 120 states with the largest HSVs, significantly reducing the size of the model. The PSDs of the full model and the 120-state model are shown in Figures 5-29(a) and 5-29(a). The reduced model represents the system well, and can be used in the analysis.

Mass and Complexity Implications

Though shunt circuits are passive circuits, they still add mass and complexity to the mirror. The mass of the circuit elements is small. However, all of the electrical energy from the shunt circuit must be dissipated as heat, requiring mass for heat sink elements. Therefore, the mass associated with each shunt circuit is broken into two pieces: the component mass for the circuit elements and the mass associated with the heat dissipation. The heat dissipation mass is determined based on the power dissipated in the circuit. The power is calculated for each type of circuit using the voltage output from the state-space model. Then, an empirical relationship between dissipated power and mass is used to determine the approximate mass needed.

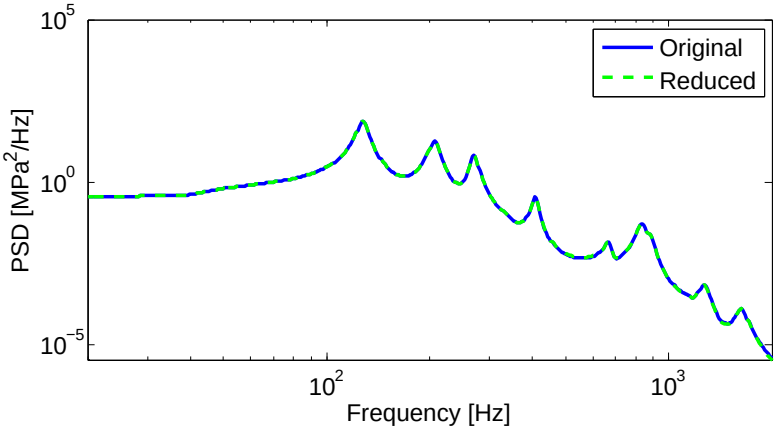

(a) Resistive Shunt

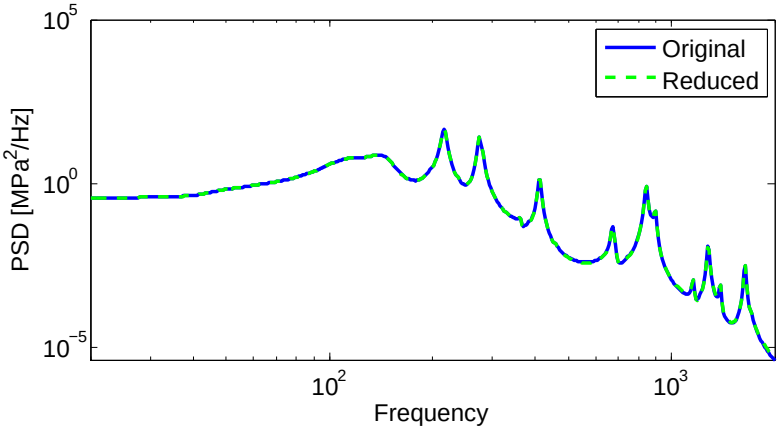

(b) Resonant Shunt

Figure 5-29: PSD of the Reduced Model

Shunt Circuit Summary

The piezoelectric shunt circuit can provide significant damping and stress reduction under launch loads using the existing piezos and a passive shunting circuit. Both a resistive and a resonant shunting circuit are considered, and the theoretically optimal values for the resistance and inductance that provide the maximum amount of additional damping are calculated. Furthermore, a multi-mode resonant shunt methodology has been created so that multiple modes can undergo targeted damping. The state-space implementation of the shunt-circuit requires the use of high-frequency states in order to make the systems strictly proper. This significantly increases the size of the model. However, once the shunt system is combined with the plant, many of these extra states can be reduced out of the model without performance implications. The shunt circuit is implemented within the context of vibroacoustic launch loads on a mirror, and is a viable solution for launch load alleviation.

5.5.3 Active Damping

The final launch load alleviation technique considered here is active damping. Active damping involves using an active control system to increase the amount of damping and decrease the system response to the disturbance. This necessitates a sensor, control algorithm, and control scheme in addition to the embedded actuators.

Given the large number of actuators, a multi-input, multi-output (MIMO) control scheme is possible. Modern control theory offers a variety of MIMO control algorithms, including optimal techniques [25, 90]. However, since these techniques are based on models, they can be extremely sensitive to the accuracy of the models. Model discrepancies can cause instabilities in the system, which would be devastating for the mirror. Steps have been taken to improve the robustness of optimal control algorithms [145, 70, 106], which have resulted in controllers that are more reliable and less prone to instabilities. However, given the uncertainties in the model, structural control is still a difficult task. Additionally, MIMO controllers are generally large and complex.

Therefore, given these issues and the reluctance of the community to allow any systems to be powered on during launch, a lower performing, yet simpler and more stable single-input, single-output (SISO) control scheme is used. In this formulation, each piezo actuator has its own SISO control loop and collocated sensor. Collocated control refers to a system where the sensor and actuator are placed at the same location, are aligned, and are energetically conjugated. This results in alternating poles and zeros, and can guarantee stability in many SISO control algorithms due to its phase-bounded behavior. Also, the SISO control implementation may not be model-dependent, so inherent uncertainties in the modal frequencies will not cause the system to become unstable if the control is implemented correctly with sufficient margins. Therefore, the stability guarantees and simpler implementation make this an ideal control scheme for active damping during launch.

As mentioned above, active damping requires a sensor, and the collocated SISO control requires a sensor at each actuator location. Active damping with piezo actuators is best accomplished through piezo sensors [116]. The piezoelectric strain sensor provides a true collocated sensor/actuator pair with the piezo actuator, and the associated stability guarantees.

Active Damping Algorithms

There are a variety of control algorithms that could be used for SISO collocated active damping. One common method is direct velocity feedback (DVFB) [16]. In a simple spring-mass system with a force input, damping is best achieved through velocity feedback to the force actuator, so it is unsurprising that velocity feedback is a good method for active damping. DVFB involves multiplying the output of velocity sensors by gains, and directly feeding them into collocated force actuators. DVFB is simple to implement, and has theoretical guarantees that spillover into high frequency modes will not destabilize the system. However, implementation issues such as lag and actuator and sensor dynamics can lead to unstable systems [61].

Also, DVFB necessitates velocity sensors and force actuators to function correctly. However, the piezo actuators are not purely force actuators. Furthermore, a velocity

sensor that could be used with the mirror system during launch is not immediately apparent. One could attempt to differentiate relative displacement sensors, such as strain gages, to obtain appropriate sensor outputs, but the noise introduced in the differentiation coupled with the implementation issues of DVFB result in a non ideal situation that could lead to an unstable system.

Therefore, for this particular problem, another control method, known as Positive Position Feedback (PPF), is used [61, 48]. PPF uses generalized displacement measurements, and works well with strain-based sensing. Furthermore, it is particularly well suited for a structure with piezo actuators and piezo sensors [116], making it appropriate for the mirror system. In addition, spillover dynamics into high frequency modes are stabilizing, as in DVFB, and PPF is also stable in the presence of finite actuator dynamics, which threaten to destabilize other methods. Finally, though it is not unconditionally stable, a non-dynamic stability condition can be derived for the system. Therefore, PPF is a good option for the damping of the mirror.

The PPF controller is a second order filter with the same form as a single degree-of-freedom (DOF) modal equation, but with much higher damping. The position term from the structure is positively fed into the filter, hence the name PPF. This is best illustrated through a single degree of freedom system [48]:

$$\text{structure: } \ddot{x} + 2\zeta\omega\dot{x} + \omega^2 x = g\omega^2 x_f \tag{5.45a}$$

$$\text{compensator: } \ddot{x_f} + 2\zeta_f\omega_f\dot{x_f} + \omega_f^2 x_f = \omega_f^2 x \tag{5.45b}$$

where x is the structural modal coordinate, ω is the modal frequency, ζ is the modal damping, x_f is the filter coordinate, ω_f is the filter frequency, ζ_f is the filter damping, and g is a scalar gain. It can be shown [61] that the system is stable for $0 < g < 1$. Reference [48] extends this stability criteria to multivariable systems. The state-space form of the PPF filter implemented here is:

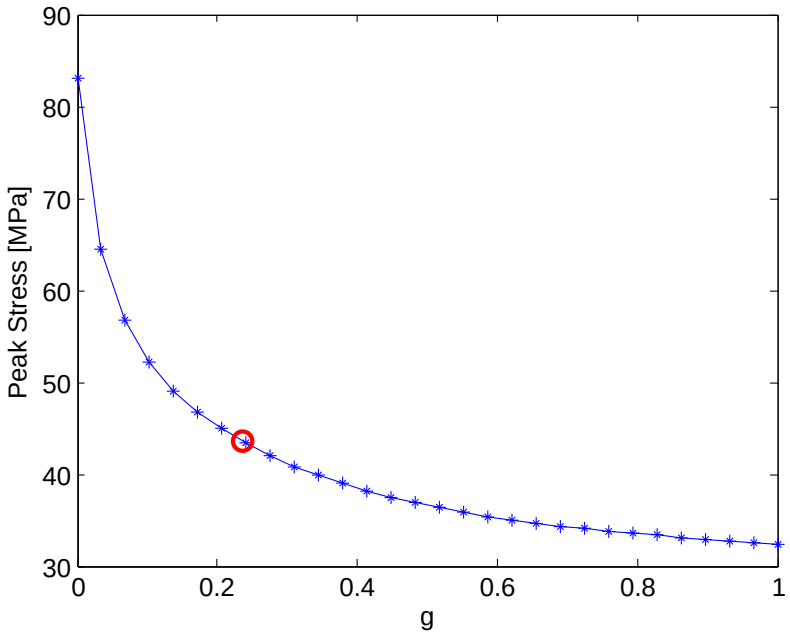

Figure 5-30: Peak Stress as a function of Active Damping

$$\begin{bmatrix} \dot{x_f} \\ \ddot{x_f} \end{bmatrix} = \begin{bmatrix} 0 & 1 \\ -\omega_f^2 & -2\zeta_f\omega_f \end{bmatrix} \begin{bmatrix} x_f \\ \dot{x_f} \end{bmatrix} + \begin{bmatrix} 0 \\ \omega_f^2 \end{bmatrix} y$$
$$u = \begin{bmatrix} g\omega^2 & 0 \end{bmatrix} \begin{bmatrix} x_c \\ \dot{x_c} \end{bmatrix} \tag{5.46}$$

Active Damping Results

The PPF control is implemented on the mirror using the collocated piezo sensor/actuator pairs. Figure 5-30 shows the stress as a function of the control parameter, g. The baseline value of g is marked with a circle, which results in a 47% stress reduction from the initial stress. This value is chosen using the multivariable stability criteria (Reference [48]), while maintaining adequate margin for variations in the design. Additionally, the stress reduction can be seen by looking at the PSD of the stress output. Figure 5-31 compares the PSD of the original system and the PSD with active damping applied. Figure 5-31(b) shows the PSD zoomed in around the first three modes. The additional damping is clearly visible from the reduction in the peaks in

the PSD.

The addition of the active damping also requires control voltages. This average voltage as a function of the amount of control can be seen in Figure 5-32. Again, the baseline value is demarcated with a circle. As expected, additional control requires an increase in voltage, though the baseline value is within the voltage saturation limitations of the actuators.

Mass and Complexity Implications

The active damping system effectively reduces stress, though one must also account for mass and complexity. Like in the shunted piezo case, the extra mass included consists of two parts: the mass of the components and mass to account for the energy dissipation, mainly heat sinks. The mass of the components is a simple function of the number of piezos and control loops. The mass for the energy dissipation is calculated by considering the power of the system, and using an empirical relationship between power and heat sink mass. The power is calculated using the bandwidth, voltage, and piezoelectric capacitance [1]. The power is then used to determine the mass of the heat sinks required.

Comparison to Optimal Techniques

As mentioned previously, optimal, multi-input, multi-output (MIMO) algorithms can theoretically provide better results than the SISO implementation used here. However, the optimal MIMO algorithms rely on accurate models and result in large controller sizes, making them inappropriate for this application. Nonetheless, the MIMO implementation can bound the performance of active damping with the embedded actuators. By allowing a large controller, assuming that the model perfectly describes the system, and assuming perfect measurements, the optimal algorithms can effectively provide the theoretical upper bound on the amount of stress reduction that is possible with the existing mirror system and actuators.

The optimal Linear Quadratic Regulator (LQR) implementation, which can be found in many optimal control texts [25, 90, 123], is implemented with the mirror

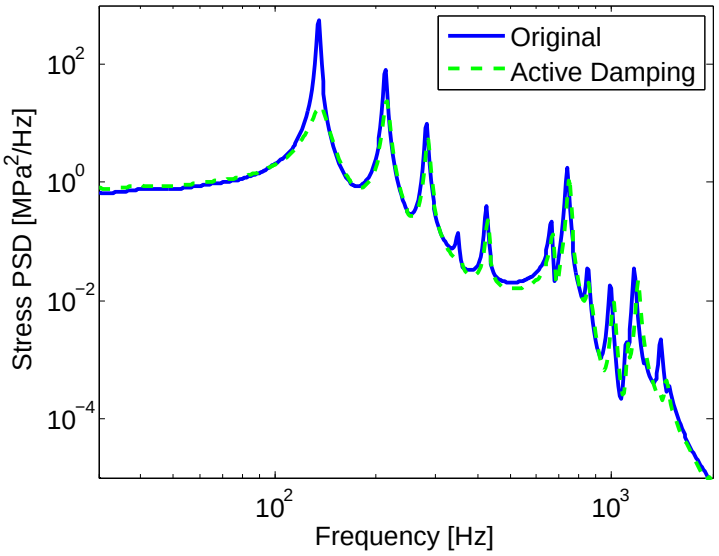

(a) Entire PSD

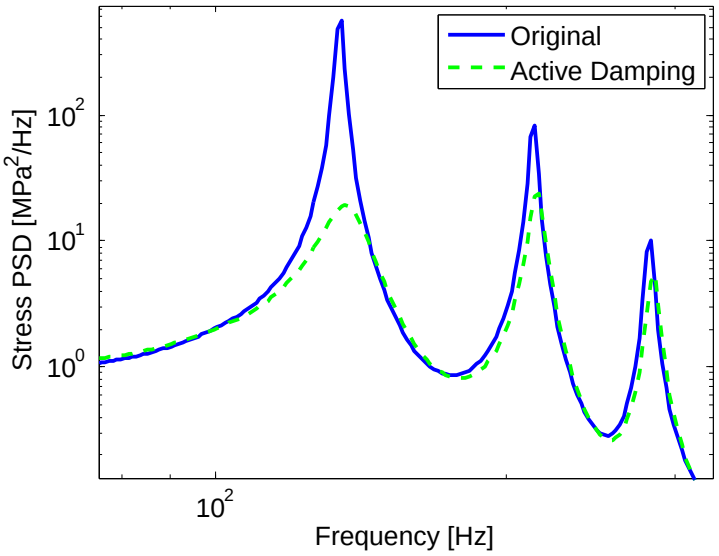

(b) First 3 Modes

Figure 5-31: PSD of the Stress with and without Active Damping

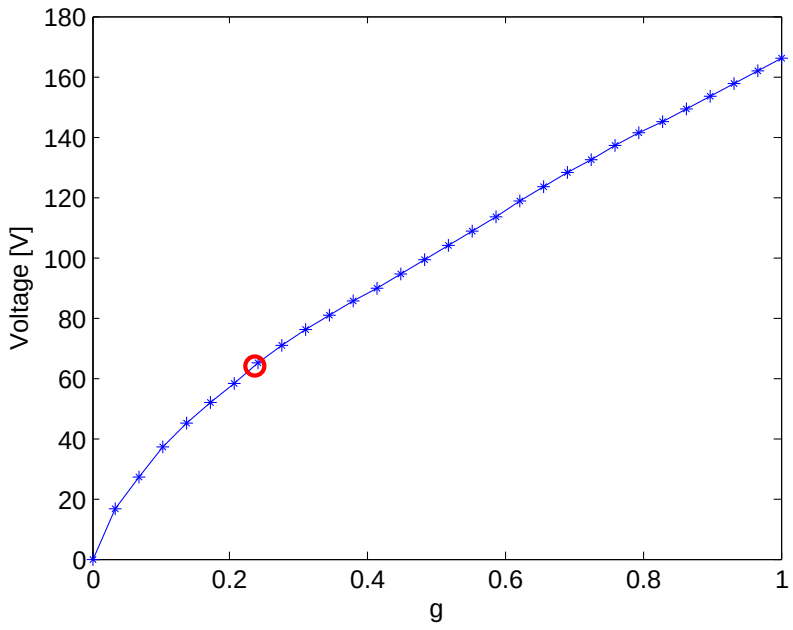

Figure 5-32: Average Voltage as a function of Active Damping

model. Assuming a state-space system of the form:

$$\begin{aligned} \dot{x} &= Ax + Bu \\ u &= -Kx \end{aligned} \tag{5.47}$$

where x is the state, u are the control inputs, and K is the controller. The mirror state-space system (Equation 5.1) is of this form. The LQR controller (K) is then determined by minimizing the quadratic cost function:

$$J = \int_0^\infty \left(x^T Q x + u^T R u\right) dt \tag{5.48}$$

where J is the cost functional, and Q and R are matrices weighting the state and control respectively. This can be solved using the algebraic Ricatti equation, and the weighting matrices are tuned to obtain good performance under the voltage constraints. One note is that the control assumes full state feedback. In other words, this formulation assumes full modal sensing knowledge. Though this would not actually be the case when using real sensors, it continues the ideal formulation.

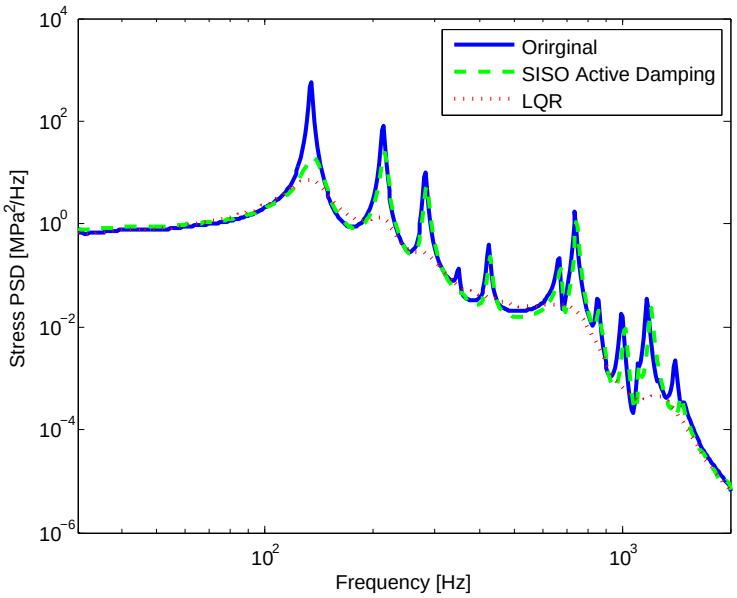

Figure 5-33: Stress PSD for SISO and Optimal MIMO Control

Figure 5-33 shows the stress PSD for the baseline mirror without alleviation, the mirror with SISO active damping, and the mirror with ideal LQR damping. The RMS peak stress values can be seen in Table 5.9. The LQR case clearly gives the best results, with about a 62% stress reduction, while the PPF control provides about 48% reduction. However, the LQR assumes perfect, complete sensing knowlege and perfect modeling. Given that a 62% reduction is the theoretical optimum, the achievable and implementable SISO system performs well, making it an appropriate choice for this system.

Table 5.9: Peak Stress With Active Damping

Original (passive) Mirror	83 MPa
SISO Active Damping with PPF	44 MPa
MIMO Active Damping with ideal LQR	32 MPa

Active Damping Summary

Active damping is implemented with the existing embedded piezo actuators. In order to ensure stability, individual collocated sensor/actuator pairs are used with simple,

SISO control loops. Though it is theoretically possible to achieve better performance through optimal MIMO techniques, the full state estimation, instability potential resulting from model uncertainties, and large computational burden outweigh the benefits, so the SISO implementation is chosen. The control is performed using a PPF filter, with gains chosen to maximize the stress reduction while ensuring that the voltage is within an acceptable range and the stability criterion are satisfied. This results in close to a 50% reduction in stress, which, as expected, outperforms the shunted piezo techniques.

5.5.4 Launch Load Alleviation Summary

Three launch load alleviation techniques are presented in this section: isolation, shunt circuits, and active damping. Additionally, three different types of shunting circuits are used: resistive, tuned resonant, and tuned resonant for multiple modes. All of these techniques reduce the stress in the system, but at the expense of extra mass and complexity. For comparison, the stress and mass of the baseline mirror are shown for each type of alleviation technique in Figure 5-34. Additionally, the PSD of the stress, zoomed in around the first three modes, can be seen in Figure 5-35. As one adds alleviation, moving from isolation, to resistive shunting, to resonant shunting, to active damping, the stress decreases. However, the mass increases, and the system becomes more complex.

5.6 Design for Launch Including Alleviation

A similar trade space analysis as in Section 5.4 is run to include the launch load alleviation techniques. In this case, 3000 LHS samples are considered. There are six parameters: the five considered previously (Section 4.3.1), and the launch load alleviation level. The launch load alleviation level parameter is defined as a discrete value with six possible levels corresponding to the numbers one through six: no alleviation, isolation, resistive shunting, resonant shunting of the first flexible mode, resonant multi-mode shunting, and active damping. All of the parameters for the

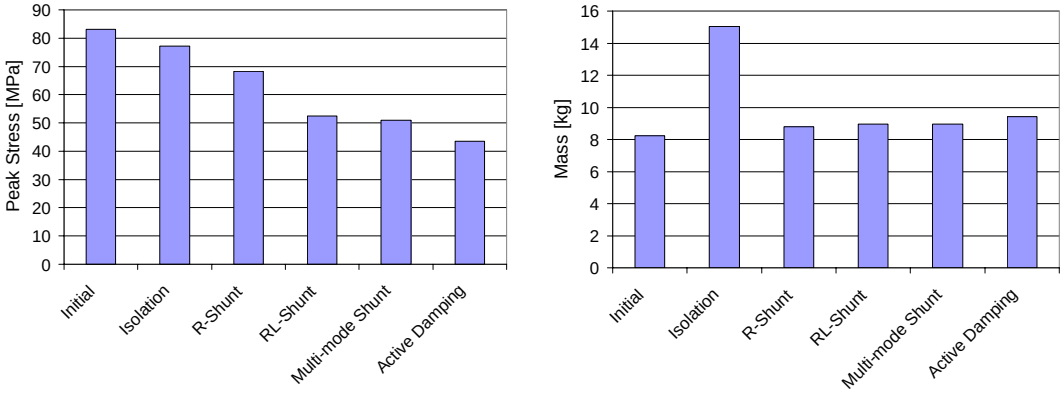

(a) Peak Stress

(b) Mass

Figure 5-34: Comparison of Launch Load Alleviation Techniques

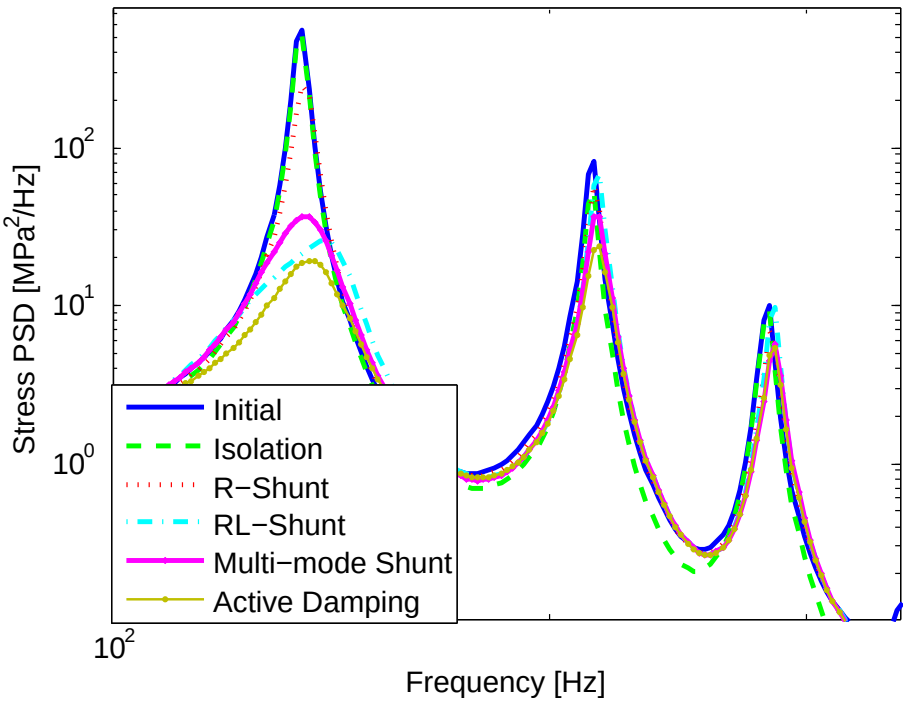

Figure 5-35: Stress PSD Comparing Launch Load Alleviation Techniques

Table 5.10: Parameters for Active Mirror Trade Space

Parameter	Range
Number of Rib Rings	3 - 6
Rib Aspect Ratio	10 - 80
Face Sheet Mass Fraction	0.3 - 0.9
Bipod Reinforcement	1 - 4
SiC Areal Density [kg/m^2]	2.5 - 15
Launch Load Alleviation Level	1 - 6

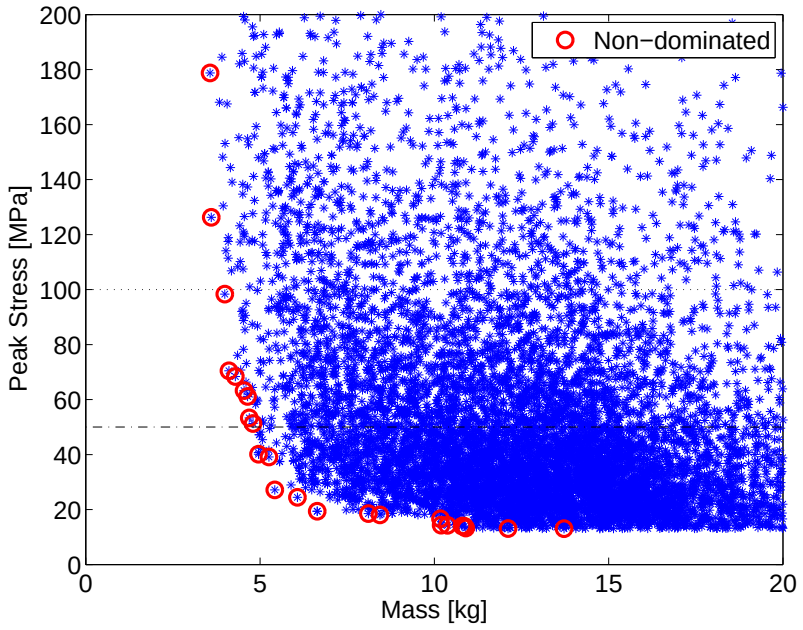

Figure 5-36: Feasible Launch Trade Space with Alleviation

analysis are summarized in Table 5.10.

The median run time of the simulation is 277 seconds, though this varies with the parameters of the given run. The number of actuators and launch load alleviation level particularly affect the run time. However, the run time of the simulation necessitates the efficient LHS sampling, rather than a full factorial exploration.

Figure 5-36 shows the feasible designs considering the thickness limits, as described in Section 5.4, along with the 3 and 6-σ limit lines. Additionally, the non-dominated designs, in terms of mass and stress, are circled. Notice that the designs tend to have lower stresses than the similar plot for passive mirrors (Figure 5-20). However, the masses do not decrease. The launch load alleviation techniques reduce the peak

stresses, but at the expense of adding mass to implement those techniques.

As in the mirror design without alleviation, the different design points can be distinguished and visualized by their parameters. Figure 5-37 shows the feasible designs differentiated by each of the six parameters. The first figure shows the designs differentiated by the number of rib rings. While the Pareto front designs still tend to be those with low numbers of rib rings, more designs with many ribs lie beneath the two stress limit lines than in the case without alleviation. This indicates that launch load alleviation can enable the use of designs that are good for on-orbit correction, but might not otherwise survive launch. Figures 5-37(b), 5-37(c), and 5-37(d) show the designs differentiated by rib aspect ratio, face sheet mass fraction, and bipod reinforcement, respectively. These three plots all show the same trends as in the case without alleviation: high rib aspect ratios, low face sheet mass fractions, and high bipod reinforcements lead to the low mass, low stress designs on the Pareto front. Figure 5-37(e) shows the designs distinguished by the SiC areal density. Here, more low areal density designs (2.5-5 kg/m^2) are beneath the stress limits than in the case without alleviation. Also, notice that the clear delineation between the areal density bands is gone; the additional mass from the launch load alleviation smears the vertical bands of areal densities together. Finally, Figure 5-37(f) shows the designs differentiated by the launch load alleviation level. Here, it is visible that while the lowest mass designs tend to be without alleviation, the lowest stress designs all use shunt circuits or active damping, with active damping designs achieving the lowest stresses. Also, as discussed in Section 5.5.1, while isolation does reduce stress, the increase in mass and relatively small stress reduction make it ill-suited for this particular problem, as is visible by noticing that all of the isolation designs in Figure 5-37(f) are away from the Pareto front.

Again, the Pareto optimal designs can be examined, and are shown in Table 5.11. As was visible in Figure 5-37(f), the lowest mass designs do not use alleviation, while the lowest stress designs utilize shunt circuits or active damping. Also notice that, unlike in the case without alleviation (Table 5.7), many of the Pareto designs have more than three rib rings. The lower stress afforded by utilizing the embedded

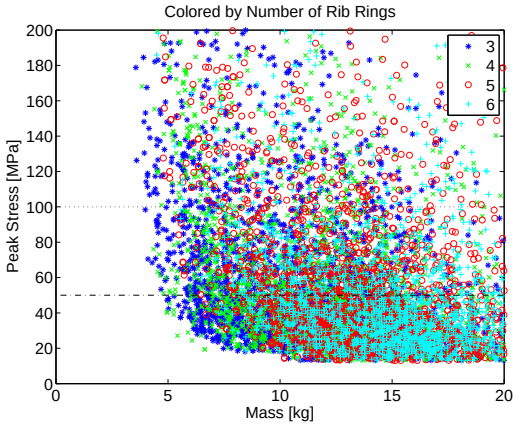

(a) Differentiated by Number of Rib Rings

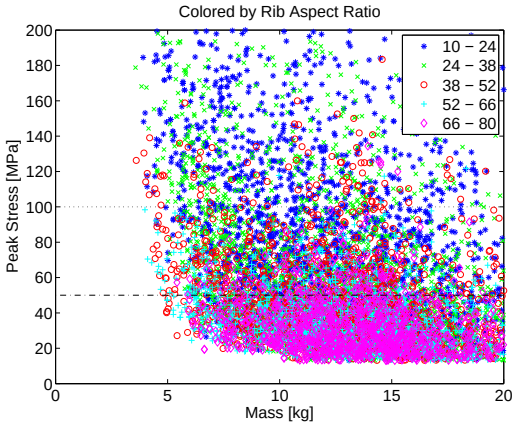

(b) Differentiated by Rib Aspect Ratio

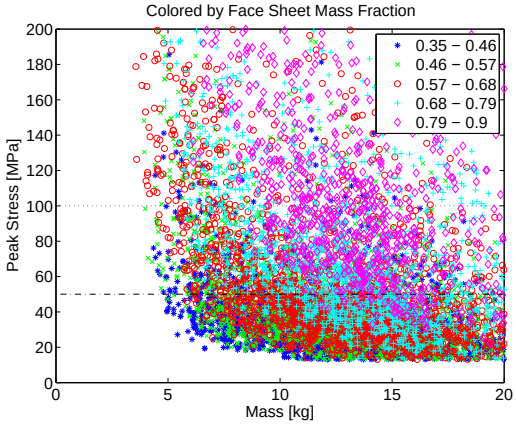

(c) Differentiated by Face Sheet Mass Fraction

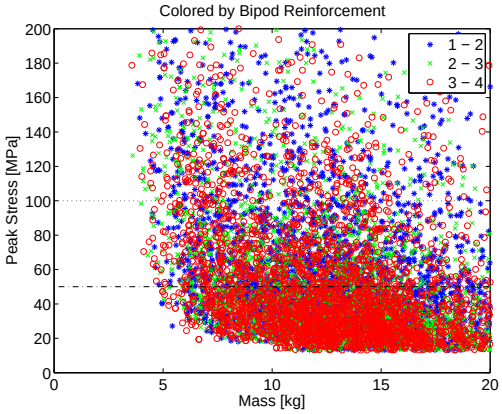

(d) Differentiated by Bipod Reinforcement

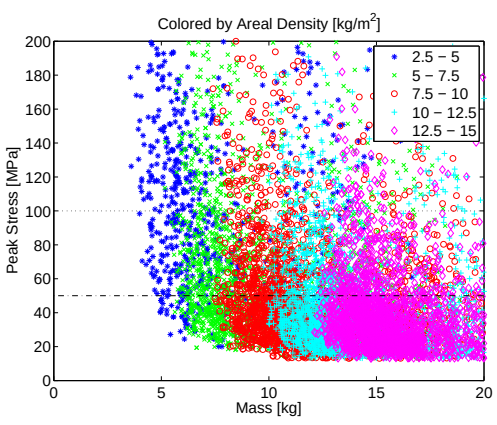

(e) Differentiated by SiC Areal Density

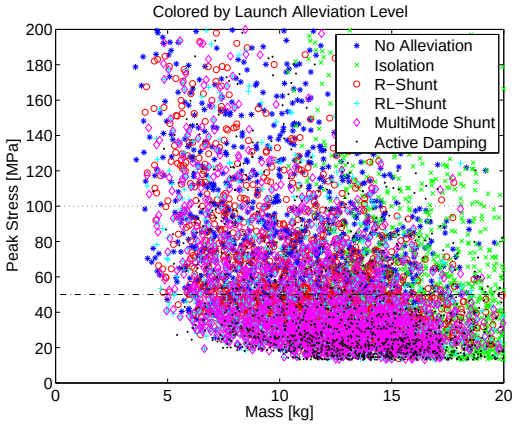

(f) Differentiated by Alleviation Level

Figure 5-37: Active Mirror Trade Space with Design Parameter Differentiation

actuators to add damping allows designs with more ribs to be on the Pareto front.

Table 5.11: Non-dominated designs in Launch Analysis Including Alleviation

	Number of Ribs	Rib Aspect Ratio	Face Sheet Mass Fraction	Bipod Rein-forcement	Areal Density [kg/m^2]	Allevi-ation	Mass [kg]	Peak Stress [MPa]
1	4	14	0.66	2.5	3.1	None	3.4	398
2	3	30	0.58	3.7	3.1	None	3.6	179
3	3	42	0.58	2.9	3.5	None	3.6	126
4	3	52	0.55	2.6	3.6	None	4.0	98
5	3	63	0.53	3.3	4.1	None	4.1	70
6	3	52	0.50	2.1	4.1	None	4.3	68
7	4	56	0.38	3.6	4.5	None	4.5	63
8	4	52	0.37	1.8	4.4	None	4.6	61
9	3	63	0.53	3.3	4.1	RL-Shunt	4.7	53
10	4	52	0.37	1.8	4.4	R-Shunt	4.8	51
11	4	52	0.37	1.8	4.4	RL-Shunt	5.0	40
12	4	56	0.38	3.6	4.5	RL-Shunt	5.3	39
13	4	52	0.37	1.8	4.4	Active	5.4	27
14	4	56	0.38	3.6	4.5	Active	6.1	24
15	4	80	0.35	3.3	5.5	Mult Shunt	6.6	19
16	3	63	0.44	1.3	6.0	Active	8.1	19
17	3	54	0.49	1.4	6.3	Active	8.4	18
18	3	57	0.37	2.2	9.1	Active	10.2	17
19	5	69	0.39	3.0	7.6	Mult Shunt	10.2	14
20	3	31	0.39	3.2	8.1	Active	10.4	14
21	6	71	0.35	2.7	7.5	RL-Shunt	10.8	14
22	4	43	0.43	3.0	8.9	Active	10.9	14
23	3	70	0.56	2.7	9.9	Active	10.9	13
24	4	36	0.40	2.9	6.4	Active	12.1	13
25	4	38	0.41	1.7	9.4	Active	13.7	13

5.6.1 Comparison with Mirrors without Alleviation

A direct comparison between the mirror trade spaces with and without launch load alleviation can be easily visualized by looking at the set of non-dominated designs. Figure 5-38 shows the combined set of non-dominated designs, distinguished by whether or not each design contains alleviation. Notice that the mirrors with alleviation domi-

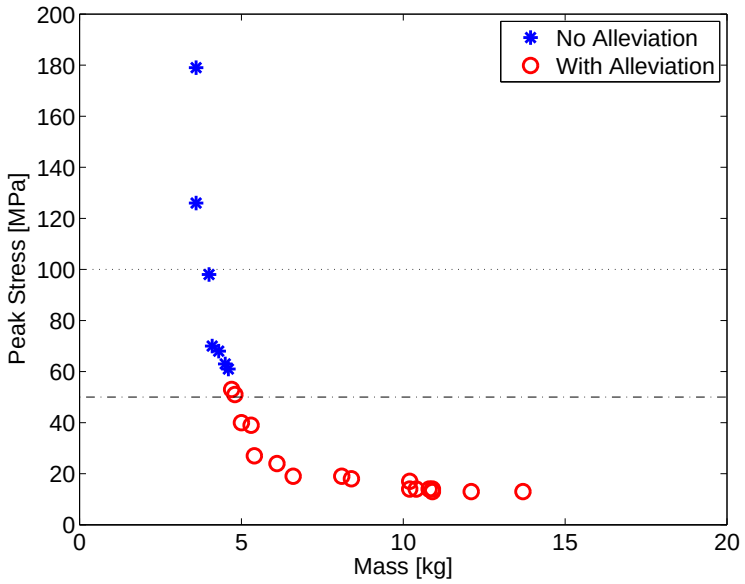

Figure 5-38: Non-Dominated Designs for Launch

nate in the low stress portion of the design space. However, the very low mass designs with slightly higher stresses do not use alleviation.

Another way to compare the designs with and without alleviation is through examining the percentage of designs that meet the stress limits. The percentage of feasible designs that meet the 50 MPa stress limit are compared for designs with and without alleviation, and for each parameter, as seen in the bar charts in Figure 5-39. In all cases, a higher percentage of designs meet the stress limit with launch load alleviation. The increase in percentage is particularly visible with many rib rings (Figure 5-39(a)), low rib aspect ratios (Figure 5-39(b)), and low areal densities (Figure 5-39(e)).

5.7 Summary of Launch Survival

This chapter presents a dynamic, state-space methodology for modeling and analyzing the disturbances encountered during launch. It computes the peak stress in the SiC substrate and in the actuators resulting from the vibroacoustic disturbances. While the baseline mirrors will likely survive launch, there are many design which are better suited for on-orbit wavefront correction, but are not likely to survive launch. The best

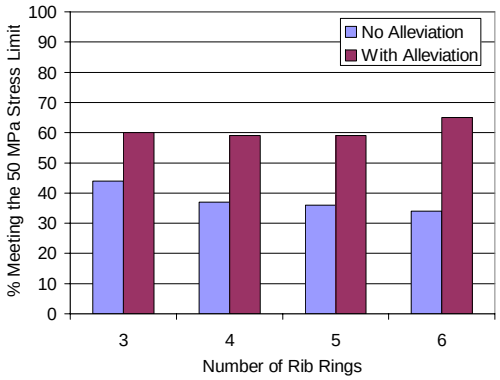

(a) Differentiated by Number of Rib Rings

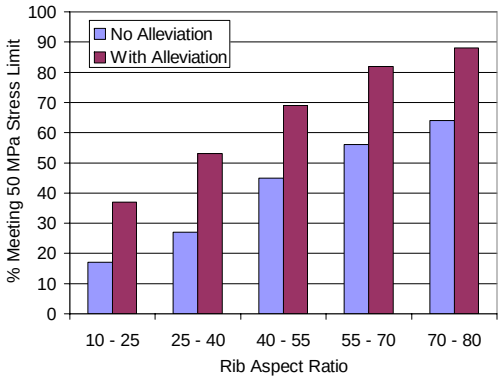

(b) Differentiated by Rib Aspect Ratio

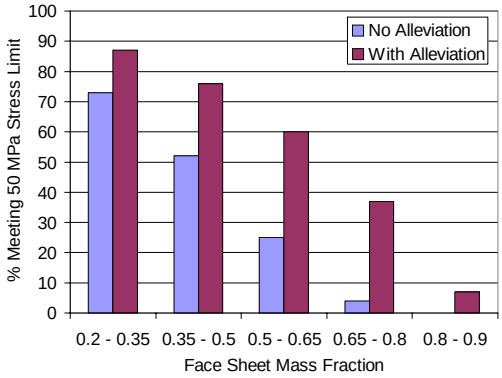

(c) Differentiated by Face Sheet Mass Fraction

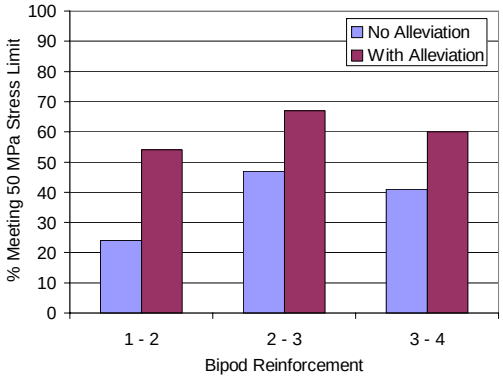

(d) Differentiated by Bipod Reinforcement

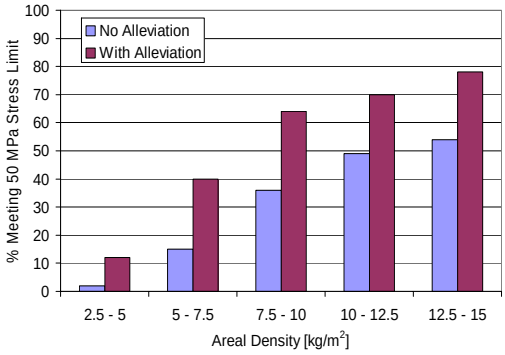

(e) Differentiated by SiC Areal Density

Figure 5-39: Percentage of Designs Meeting 50 MPa Stress Limit

mirror designs, with regard to launch, have very few ribs, and therefore few actuators, and high rib aspect ratios. Additionally, the mirror response is dominated (2-to-1) by the acoustic disturbance, which is highly uncertain by nature. Therefore, it may be desirable to add launch load alleviation techniques to increase the probability of survival, as well as allow the use of mirrors that may be otherwise unable to survive launch.

Three launch load alleviation techniques are explored, including isolation, passive shunting circuits using the existing embedded piezos, and active damping also using the piezos. These techniques can reduce the peak stress and increase the feasible design space, however this comes at the expense of mass and complexity. The designs making use of shunting circuits or active damping achieve the lowest stresses.

Given that the on-orbit correctability and launch environments drive the mirror design toward different ends of the design space, it is important to consider both environments during the mirror design. Chapter 6 discusses the combination of the two models, and designs that satisfy both sets of requirements.

Chapter 6

Integrated Mirror Design

The previous two chapters have examined the mirror design with respect to on-orbit performance and launch survival independently. However, the same mirror must perform well in both environments, and the two independent analyses lead to vastly different designs. The parameter with which this dichotomy is most apparent is the number of rib rings in the mirror. All of the best performing designs for on-orbit performance have many rib rings, and hence many actuators. However, the best designs for launch survival have very few rib rings. This conflicting desire necessitates integrated design, considering both environments simultaneously.

Within the integrated design framework, it is possible to perform a single analysis, as was shown in the previous chapters, or to perform both analyses together, as will be shown henceforth. This chapter presents the fully integrated model, beginning with model reduction efforts to decrease the computational expense of the full model. Next, results from the integrated trade space are shown and guidelines for the design of lightweight, active mirrors are presented.

6.1 Model Reduction and Approximations

While it is possible to simply run both sets of analyses on the mirror model, it is computationally expensive. The integrated mirror model, including both the on-orbit and launch environments, is quite complex. This section examines the computational ex-

pense of the model, and takes steps to reduce that computation, including symmetry exploitation, model reduction, and model approximations, all of which are discussed below.

6.1.1 Quasi-Static Analysis Computation

The computation time for the quasi-static model for on-orbit correction is quite long. The computation times quoted below are obtained from running the analysis on a single 3.6 GHz, Pentium 4 Processor. The baseline mirror quasi-static analysis, with no reduction efforts, takes approximately 4500 s, or about an hour and 15 minutes. This is quite long, and makes running many designs, as in the trade space exploration, infeasible. However, there are a number of steps that can be taken to reduce the computation, which will be subsequently described.

The quasi-static analysis consists of three major components. The three components and their corresponding initial computation times are as follows:

Table 6.1: Original Computation Time for Quasi-Static Analysis

Creation of the structural finite element model	6 s
Influence function calculation	4366 s
Control application	154 s

Clearly, the influence function calculation is the largest computational expense, and needs to be reduced. Two different methods are used to speed up the influence function calculation. First, writing of the input and output files between MATLAB and NASTRAN is greatly sped up by only overwriting the necessary lines in the input and output files, rather than the entire file. Second, the symmetry of the mirror is exploited. By using the symmetry, only a fraction of the influence functions need to be computed with NASTRAN, and the others can be computed through symmetry and appropriate rotations [62]. Figure 6-1 compares the influence function computation time with and without these reduction steps. Here, the first portions of each bar represent the amount of computation time spent directly computing influence functions in NASTRAN, and the second part of the computation time is due to exploiting the

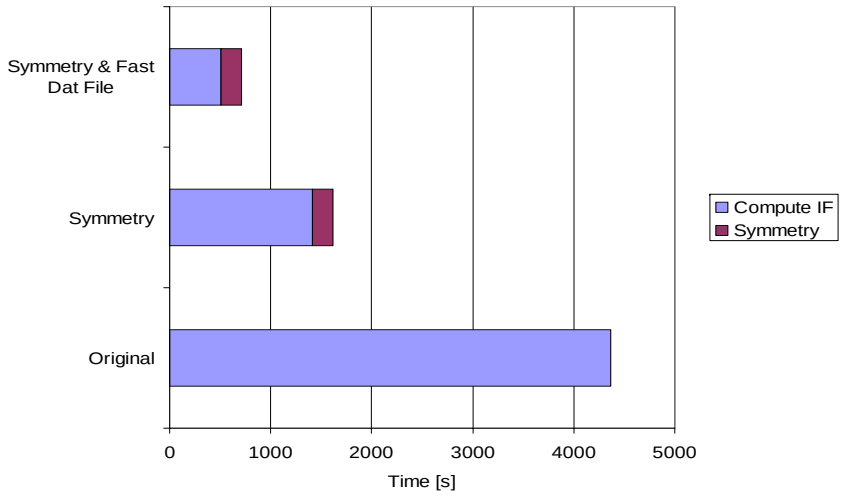

Figure 6-1: Influence Function Computational Expense

symmetry to calculate the remaining influence functions that are not computed with NASTRAN. The original method computes all influence functions with NASTRAN, so the symmetry computation time is zero. Notice that exploiting the symmetry reduces the computational expense by about 65%, and the more efficient input and output dat files results in another 50% reduction, resulting in a total computation time reduction of over 80%.

A computation reduction can also be realized in the control application through using a similar, more efficient method of writing the input and output files. This reduces the control computation by about 40%, from 154 s to 96 s. While this is a significant reduction for this portion of the model, it is a small fraction of the total computation.

With all of the reductions above, the total computation time for the baseline quasi-static analysis is reduced from over an hour to 814 s, which is an 82% total reduction. Though this is much quicker, each simulation run still takes around 13 minutes. This is acceptable for an effiecient trade space technique, and was used to obtain the LHS trade space from Section 4.4.4. However, the next section uses approximation methods to further reduce the computation time.

6.1.2 Response Surface Model

Due to the significant computation involved with a single run of the quasi-static model, a surrogate model is also developed. A surrogate model is a computationally inexpensive approximate model that captures the salient features of an expensive, high-fidelity model, such as the quasi-static mirror model. While there are multiple approaches to creating surrogate models, including model reduction, or physics-based approximations, the type of surrogate model considered here is a data-fit method, where the surrogate model is constructed using data generated from the high-fidelity "truth" model.

Data-fit models are non-physics-based approximations that typically involve interpolation or regression of the data obtained from the "truth" model. There are many types of data-fit approximation models available, and creating accurate surrogate models is an area of ongoing research. Some common types of data-fit methods include Taylor series approximations, polynomial response surfaces, and kriging interpolation [47].

A Taylor series approximation model is a local method, meaning that it provides trends in the vicinity of a single data point [47]. While this can be useful for uncertainty quantification where there is a single point around which one is interested in the variations, the local method is not particularly useful for the trade space exploration across a large parameter range, as is desired here.

The next approximation method is polynomial response surfaces, which model the system response with a polynomial expansion of the variables [112]. A least squares regression approach is used to determine the polynomial. This method is useful when the trends in the data are smooth, and resemble polynomial functions.

A third method is kriging spatial interpolation [38, 39, 58]. Like the polynomial response surface, kriging interpolation creates a smooth response surface from the set of data points. Unlike the polynomial response surface method, it does not assume any underlying trends in the data. This is useful for functions that are not smooth, have local minima or maxima, or do not resemble polynomials. Another key aspect

of kriging interpolation is that it is guaranteed to pass through all of the data points used to construct the model, while the polynomial response surface uses regression to minimize the difference between the model and data points. While exactly matching the data points can be a desirable feature, it can become problematic when there is noise or outliers in the data.

A global response surface model is necessary for the quasi-static mirror analysis due to the large parameter variations, so either a polynomial response surface or kriging interpolation can be used. While both methods have positive and negative aspects, the polynomial response surface method is chosen. The regression allows the model to be created using many data points from the original model, while the kriging model is prone to numerical ill-conditioning when data points used to construct it are in close proximity to one another. Additionally, the trends in the data with respect to each parameter are smooth, making the polynomial method an acceptable choice.

A quadratic polynomial response surface model of the quasi-static analysis is constructed, for both the dimpling and the maximum change in radius of curvature metrics. The values from the response surface model are compared to the results from the full model from Section 4.4.4. Figure 6-2 shows the results for each of the two performance metrics, where Figure 6-2(a) shows the dimpling in the full model versus the response surface model, and Figure 6-2(b) shows the maximum RoC change in the full and response surface models. Ideally, all designs would lie exactly on the diagonal line, meaning that the results from the response surface model exactly equal the full model results. Though it is obviously not perfect, most designs are very close to the line, indicating that the response surface model does perform well.

Both response surfaces necessitate fitting 28 coefficients using 260 samples. The fit of the response surface can be described by the R^2 value, which in statistics is the square of the correlation coefficient between the response surface predicted values and the actual sample values. The R^2 value for the dimpling response surface (Figure 6-2(a)) is 0.991, and the R^2 value for the maximum RoC change response surface (Figure 6-2(b)) is 0.960. While, as is visible with both the R^2 value and the plots in Figure 6-2, the dimpling has a slightly better fit. However, both response surfaces

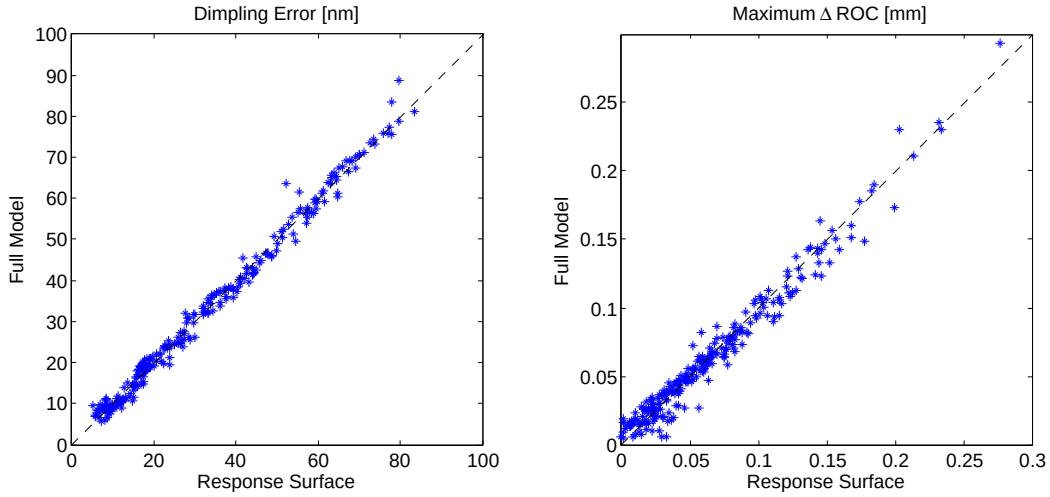

(a) Dimpling Error

(b) Maximum Change in RoC

Figure 6-2: Response Surface Model Results Compared to Full Model Results

have strong correlations and can be used to estimate the output of the full on-orbit model.

The response surface model can then be used for optimization, or to more fully explore the trade space, both of which would be difficult with the computational expense of the original model. However, the response surface model does need to be checked against the full model periodically, particularly for the best-performing cases, to ensure its accuracy.

6.1.3 Dynamic Analysis Computation

The dynamic launch analysis is not as initially computationally expensive as the quasi-static analysis. The initial computation time, when calculating all stress components across all elements in the mirror, is 945 s, or about 15 minutes. However, the peak stresses can be isolated in a subset of elements in the ribs. By calculating only the stresses in those elements, the computation time is reduced to 114 s, which is a substantial savings.

Additionally, the dynamic analysis already has computational savings built into the model. For example, the element density and number of modes are determined

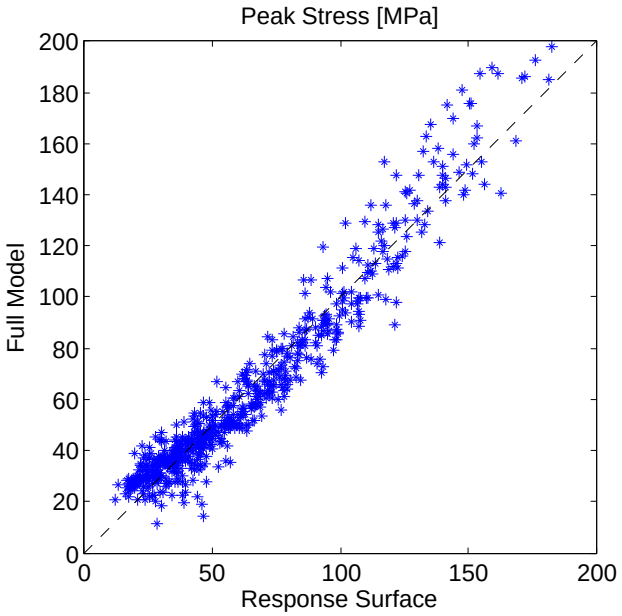

Figure 6-3: Response Surface Model for Launch Stress

based on the convergence analyses in Section 5.2.3 such that they are as small as possible, yet still accurate. Additionally, there is model reduction included in the launch load alleviation model, as was discussed in Section 5.5. The reduction in the launch load alleviation uses balanced truncation to reduce the number of states in the model, without affecting the output values.

Though it would be convenient to also use a response surface model for the launch analysis, the launch analysis is more complex than the on-orbit analysis, and the approximation is not as accurate. A response surface model, considering only the designs without alleviation, can be seen in Figure 6-3. Notice that these designs are not as closely clustered around the line as in the quasi-static cases (Figure 6-2), indicating that this model is not as good a fit. Additionally, when the launch load alleviation techniques are added, the system becomes more complex, the output trends become less smooth, and the accuracy of the response surface further decreases. Therefore, given that the the response surface is unable to accurately approximate the launch stress and that the computation time for the full model is manageable, the full launch model is used throughout the remainder of this work.

6.1.4 Model Reduction Summary

The mirror model is quite complex, resulting in large computation times. The quasi-static analysis computation is dominated by the calculation of influence functions. This was reduced by 80% by exploiting symmetry and changing the way in which the data files were transfered between NASTRAN and MATLAB. Additionally, a polynomial response surface model is created to approximate the on-orbit response very quickly. The launch model is more complex, and cannot be reduced to a response surface model. However, steps were taken to isolate the stresses and reduce the computation time of the launch analysis by 85%. With these reduction strategies, a large integrated trade space is computationally feasible.

6.2 Integrated Trade Space

In order to address the full mirror design problem, including both the on-orbit and launch environments, a large trade space is run. Like in the previous chapters, the trade space is a Latin Hypercube design of experiments trade space. The trade space includes 4000 distinct designs in order to adequately cover the design space. The parameters that are varied are the combined set from the on-orbit and launch trade spaces, namely:

- Number of rib rings
- Rib aspect ratio
- Face sheet mass fraction
- Bipod reinforcement
- Actuator length
- Areal density
- Launch load alleviation

In each case, the mass, peak stress, dimpling, and maximum change of radius of curvature are calculated. The peak stresses are calculated using the full launch model,

as described above, while the on-orbit performance is calculated using the response surface models.

As mentioned previously, in addition to this trade space exploration, it would also be possible to run multi-objective optimizations to find the true Pareto optimal points. However, this optimization involves weighting the performance metrics in terms of their relative value to the mission, or setting limits on them as constraints. While this is of use when a specific mission is involved and there are precise objectives, it is less useful when the exact performance requirements are not yet defined. Rather, more knowledge is gained by examining the trade-offs and interactions between the variables with a trade space. Additionally, by using a trade space, rather than an optimization, constraint limits can be imposed after the trade space is run by filtering out any results that do not meet the requirements. With the post-processed constraints, rather than built-in constraints, those limits can be changed, and the effects of changing requirements can be visualized. Given these benefits, the integrated mirror design is presented as a trade space, rather than an optimization. Additionally, a few targeted optimizations are run for specific cases, illustrating the benefits of optimization when requirements are expressly specified.

6.2.1 Integrated Trade Space Results

This section presents the results from the full, integrated trade space. The initial results shown do not include launch load alleviation, as it complicates the design. Designs with launch load alleviation will be shown later in this section to illustrate the benefits of adding alleviation. There are four primary performance metrics: one would like to minimize the mass, peak stress, and dimpling, and maximize the maximum change in radius of curvature. As it is difficult to visualize the four-dimensional trade space, the results will be shown in a variety of ways.

First, Figure 6-4 shows two dimensional plots of each combination of two performance metrics. In each plot in Figure 6-4, the two-dimensional Pareto optimal designs for the two metrics in each plot are circled. Also, there are limit lines marking the 3 and 6-σ stress limits at 100 MPa and 50 MPa, respectively. Also, there are lines

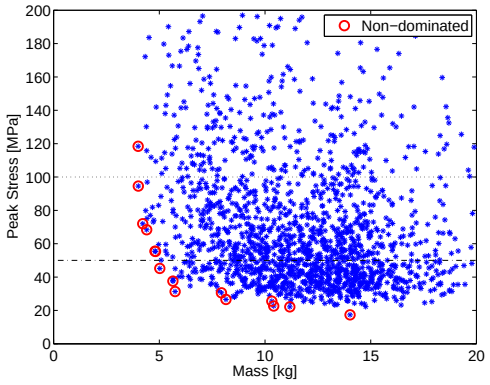

(a) Mass versus Peak Stress

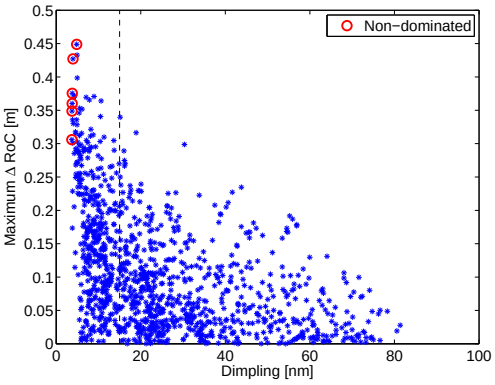

(b) Dimpling Error versus Maximum ΔRoC

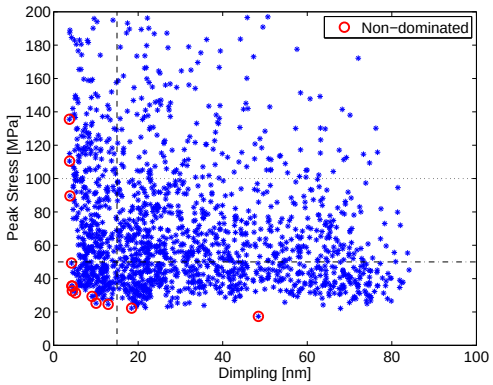

(c) Dimpling Error versus Peak Stress

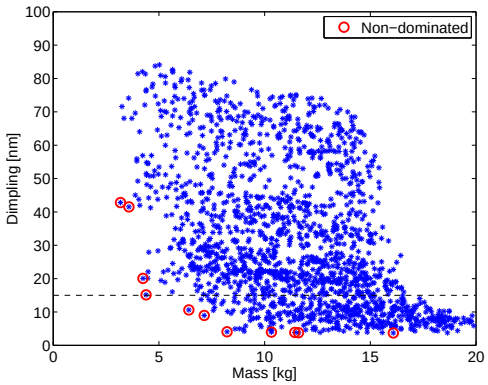

(d) Mass versus Dimpling Error

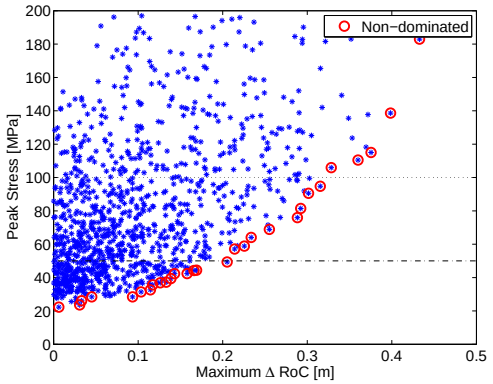

(e) Maximum ΔRoC versus Peak Stress

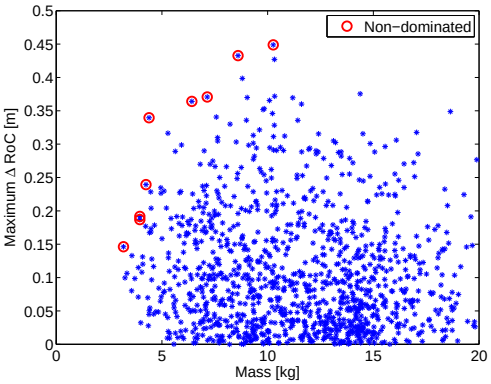

(f) Mass versus Maximum ΔRoC

Figure 6-4: Integrated Trade Space without Launch Alleviation

marking the 15 nm dimpling error, which is equal to 30 nm wavefront error, which, as will be discussed shortly, is a common optical limit.

First, Figure 6-4(a) shows the peak stress versus the mass. This is the same trade-off as in Chapter 5, and the same Pareto front can be seen. Figure 6-4(b) shows the dimpling versus the maximum change in RoC, which was also shown in Chapter 4. Again, since the two on-orbit performance metrics are largely cooperative, it is possible to find designs that perform very well with respect to both metrics. Figure 6-4(c) shows the peak stress versus the dimpling. Here, there is a trade-off between the two metrics, but it is subtle. More importantly, note that there are very few designs meeting both the marked dimpling and stress limits. Next, Figure 6-4(d) shows the mass versus the dimpling error; obtaining designs with low dimpling requires higher masses. Figure 6-4(e) shows a very clear trade off between peak stress and maximum change in RoC, where improving one metric involves sacrificing the performance of the other. Finally, Figure 6-4(f) shows the mass versus maximum change in RoC. The interaction between these two metrics is not strong, and designs with a range of masses can achieve a large change in RoC.

While the two-dimensional plots in Figure 6-4 can provide some interesting insights into the trade offs involved in mirror design, they do not include the important interactions of the full, four-dimensional space. Therefore, alternative views of the results are also shown.

The first modification made to the plots is to limit the optical performance, in terms of the wavefront error. A common optical limit is $\lambda/20$, where λ is the wavelength of light. Assuming visible wavelengths, $\lambda \approx 600$ nm, leading to a 30 nm wavefront error limit, and hence a 15 nm surface dimpling error limit. While this was shown in Figure 6-4 as a limit line, the radius of curvature change did not take this into account. The dimpling shown in the preceding plots is for a prescribed 5 mm change in radius of curvature, and the maximum radius of curvature change represents the maximum capability of the actuators, without regard to the induced wavefront error. It is possible to instead look at the maximum change in radius of curvature while maintaining the surface error within the 15 nm dimpling error limit.

The maximum change in radius of curvature while maintaining a wavefront error less than 30 nm will be referred to as correctability. For clarity, the previous maximum change of radius of curvature, regardless of surface error, is referred to as the actuator capability RoC change. Figure 6-5 shows the correctability versus the mass, peak stress, and the actuator capability radius of curvature change. First, Figure 6-5(a) shows the mass versus the correctability. Notice that there is a significant trade-off between the mass and curvature change; the more massive systems have influence functions that act more globally, allowing smoother actuation, and hence a larger change in curvature before reaching the dimpling limit. Figure 6-5(b) shows the stress versus the correctability, where systems with smaller peak stresses also tend to be less correctable. Finally, Figure 6-5(c) shows the correctability versus the actuator capability curvature change. As expected, designs with high curvature changes under the dimpling limit also tend to have high achievable curvature changes. However, this is not always the case, and there is some variation due to the conflicting effect of some of the design parameters on the two performance metrics, an example being areal density. Note that while these figures were obtained using the 15 nm dimpling limit, the limit could be easily altered to find designs meeting any limit.

As was done in the previous chapters, it is also possible to visualize any of the plots in Figure 6-4 or 6-5 by the parameters used to create the design. Due to the very large number of possible plots, they will not all be shown. Figure 6-6 shows the three plots from Figure 6-5, each differentiated by the number of rib rings and the areal density, as those are the most influential parameters over the three performance metrics.

Notice that in Figure 6-6(a), comparing mass and correctability, the designs are horizontally stratified by the number of ribs, and in Figure 6-6(b), they are vertically stratified by the areal density. This is largely as expected; the areal density contributes significantly to the mass, while increasing the number of ribs, and hence the number of actuators, significantly improves the on-orbit performance. Next, Figures 6-6(c) and 6-6(d) show the stress versus correctability. Here, it is clear that adding ribs again significantly improves the optical performance, though stress lim-

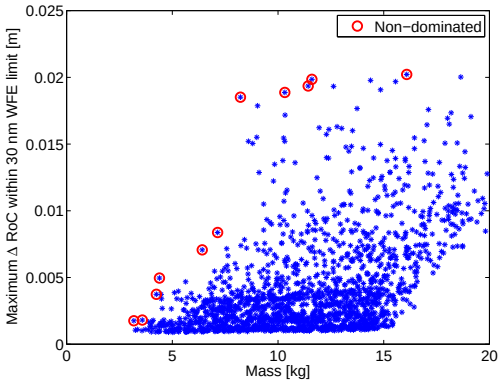

(a) Mass versus Correctability

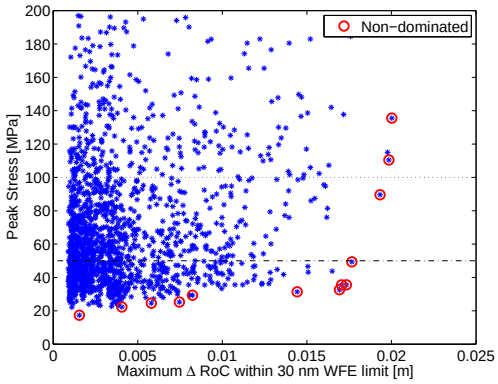

(b) Peak Stress versus Correctability

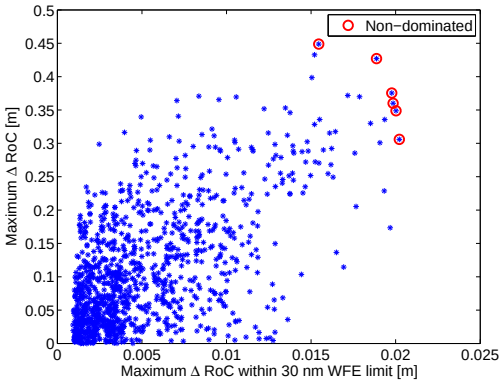

(c) Maximum Actuator Capability ΔRoC versus Correctability

Figure 6-5: Trade Space with Dimpling Limit Applied

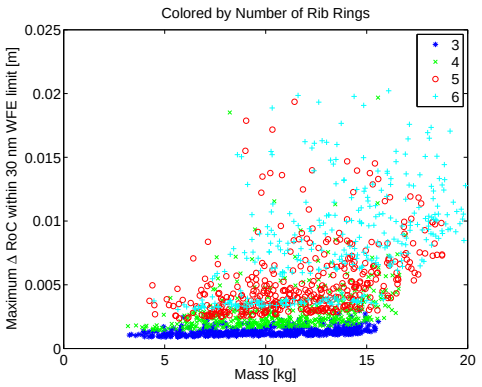

(a) Mass versus Correctability, Differentiated by Number of Ribs

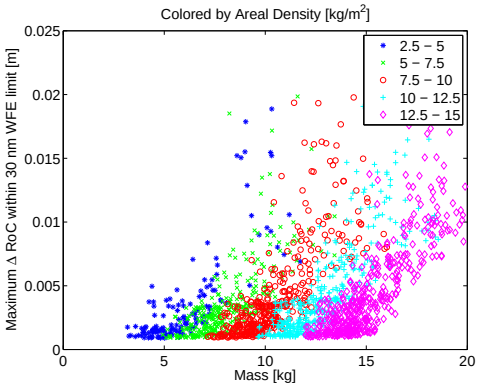

(b) Mass versus Correctability, Differentiated by Areal Density

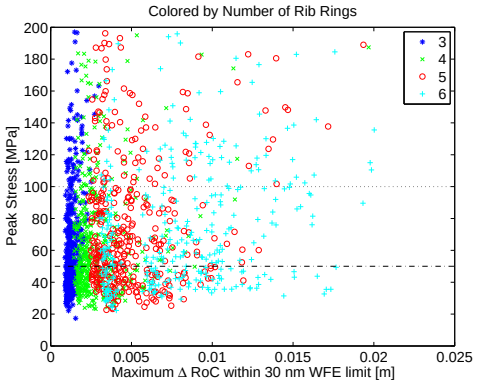

(c) Stress versus Correctability, Differentiated by Number of Ribs

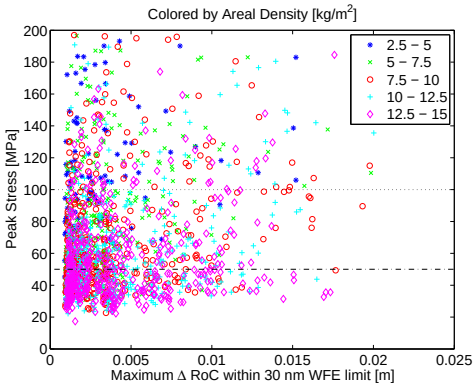

(d) Stress versus Correctability, Differentiated by Areal Density

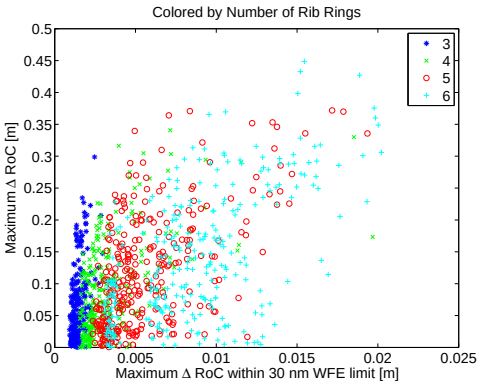

(e) Max Actuator Capability versus Correctability, Differentiated by Number of Ribs

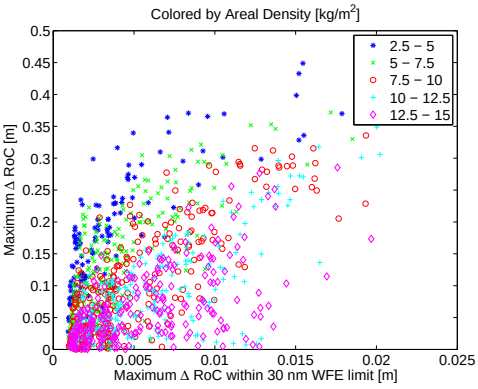

(f) Max Actuator Capability versus Correctability, Differentiated by Areal Density

Figure 6-6: Trade Space Considering Correctability with Parameter Differentiation

its will likely eliminate the best performing designs. Also, Figure 6-6(d) shows that the Pareto front with respect to stress and correctability is largely made up of high areal density designs, the same designs which were far from the Pareto front in Figure 6-6(b), indicating the limitations of the two dimensional representations. Finally, Figures 6-6(e) and 6-6(f) shows the correctability versus the maximum capability of the actuators. As before, the curvature change considering dimpling is dominated by the number of ribs. However, though the best designs for correctability under the dimpling limit are high areal density, the lowest areal density designs perform best with respect to the maximum capability of the actuators.

The differing designs on the two-dimensional Pareto fronts indicate the importance of considering all of the performance metrics together. Dimpling has been eliminated as a specific performance metric through applying the optical limits. Similarly, launch stress limits can be applied, and the stress can also be eliminated as a performance metric. Figure 6-7 shows the correctability versus the mass with both the 15 nm dimpling error limit and 50 MPa peak stress limit applied. This is the more conservative, 6-σ stress limit, as was discussed in Section 5.3. There is a definitive Pareto front, defined by the circled designs, indicating that there is a trade off between the correctability and the mass.

Figure 6-8 shows the correctability versus mass, with the 15 nm dimpling and 6-σ stress limits, differentiated by the design parameters. Figure 6-8(a) differentiates the designs by the number of ribs. While utilizing more ribs improves correctability, it also necessitates higher mass, primarily in order to meet the stress limits. Figure 6-8(b) shows the designs distinguished by areal density. Notice that as areal density decreases, fewer designs meet the limits and remain feasible. Figure 6-8(c) shows the effect of rib aspect ratio. Though the effect is not dominate, the Pareto designs with low mass tend to have high aspect ratios, while the Pareto designs with high mass tend to have lower aspect ratios. The high aspect ratio is necessary for the low mass designs to meet the stress requirement, while the lower aspect ratio allows for higher face sheet mass fractions, and more global influence functions, increasing correctability in the higher mass designs. While clear trends are difficult to decipher,

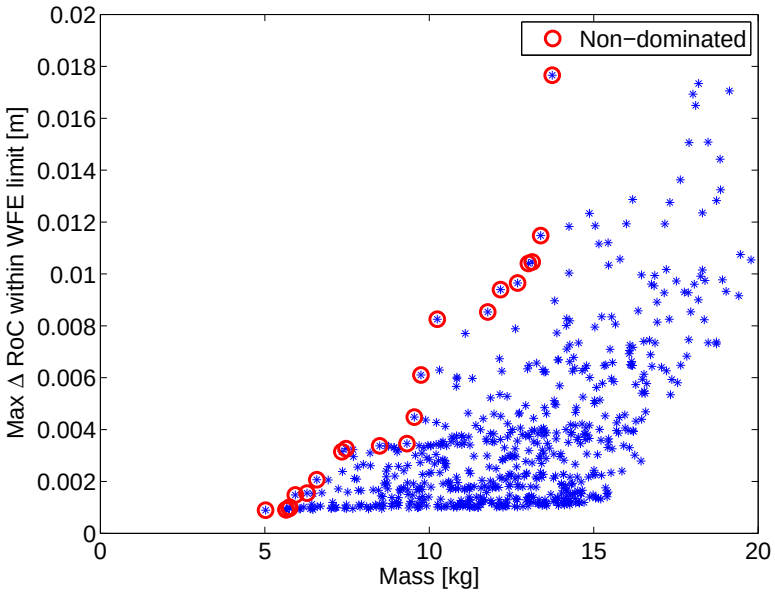

Figure 6-7: Mass versus Correctability with Dimpling and 6-σ Stress Limits

Figure 6-8(d) shows that designs with lower face sheet mass fractions are on the Pareto front in the area corresponding to low mass, due to the increased stiffness attainable through allocating more mass to the ribs. Figure 6-8(e) differentiates the designs by the bipod reinforcement, which tends to improve performance by allowing better performing designs, in terms of mass and correctability, to meet the stress limits. Finally, Figure 6-8(f) shows the designs distinguished by actuator length. Here, the improvement in correctability due to actuator length can be seen by noticing that the lower mass designs use short actuators, while the higher correctability designs use long actuators. This is because longer actuators increase the mass. However, this trend is not as strong as others. The actuator length is limited by the size of the rib cell, meaning that designs with fewer ribs can have longer actuators than designs with many ribs, and, designs with shorter actuators and many ribs still perform better than designs with long actuators and few ribs.

The previous plots were generated using the 6-σ stress limit. As mentioned above, this can easily be altered, and designs meeting other limits can also be viewed. For example, Figure 6-9 shows the same mass versus correctability plot for the 3-σ stress limit, and Figure 6-10 shows those designs differentiated by the number of ribs and

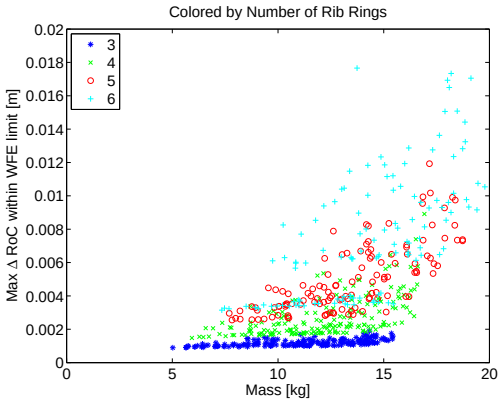

(a) Differentiated by Number of Rib Rings

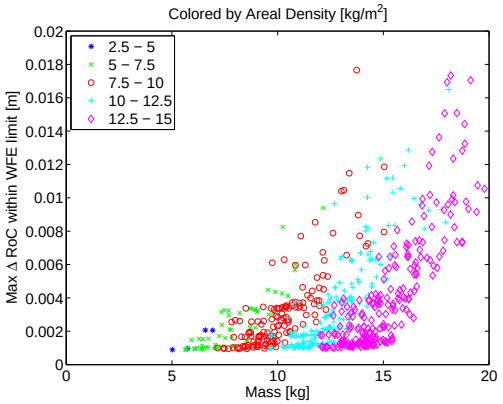

(b) Differentiated by Areal Density

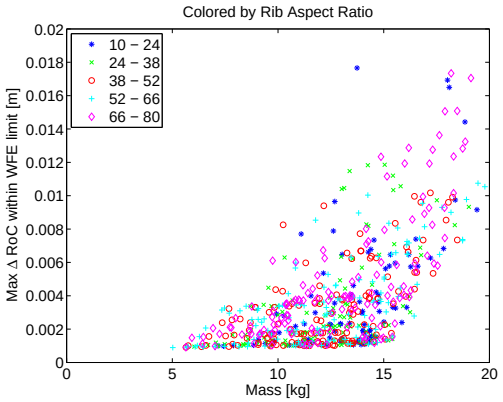

(c) Differentiated by Rib Aspect Ratio

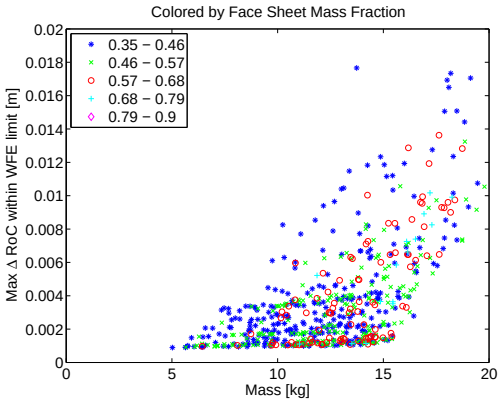

(d) Differentiated by Face Sheet Mass Fraction

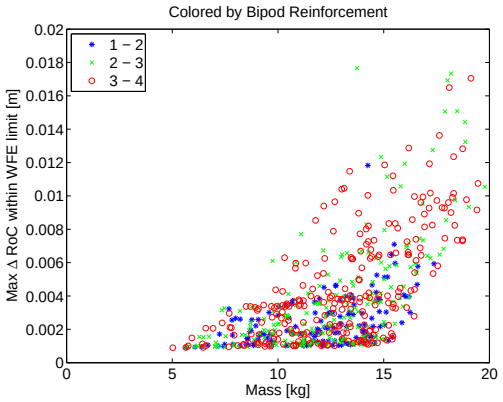

(e) Differentiated by Bipod Reinforcement

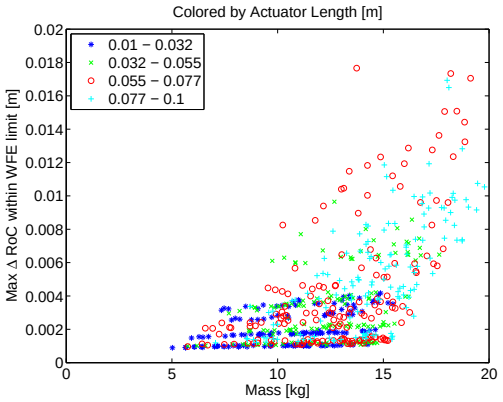

(f) Differentiated by Actuator Length

Figure 6-8: Mass versus Correctability with Dimpling and 6-σ Stress Limits, Differentiated by Design Parameters

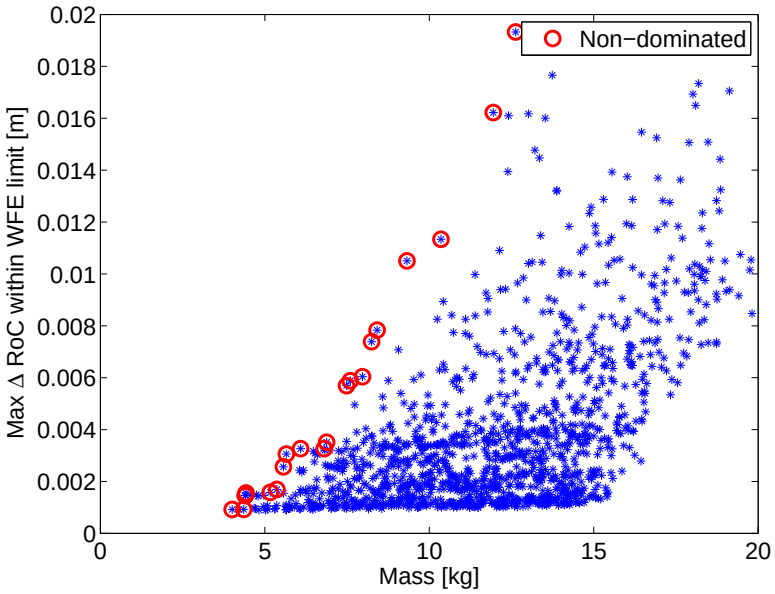

Figure 6-9: Mass versus Correctability with Dimpling and 3-σ Stress Limits Applied

areal density. Notice that many more designs are feasible due to the relaxed stress requirement. Overall, the parameter trends are the same as in the case with stricter limits, but many more designs with many ribs and low areal densities are now feasible, and many of them are on the Pareto front, indicating that the stress limit affects the location of the Pareto front and the optimal performance.

Figure 6-11 shows the Pareto designs for both the 6-σ and 3-σ stress limits. Relaxing the stress constraint shifts the Pareto front toward the upper left corner, offering improvements in both mass and correctability. This is particularly apparent in the designs with mid-range masses.

Figures 6-7 and 6-9 showed the mass versus the correctability, subject to dimpling and stress limitations. However, one can imagine situations, such as imaging at alternate wavelengths, in which the mirror would need to undergo larger deformations, despite the wavefront error. Thus, it is still useful to understand the effect of the design on the maximum achievable radius of curvature change, which indicates the capability of the actuators. Figure 6-12 again shows the mass versus the correctability for both the 6 and 3-σ stress limit cases, but the size of the points in the figure indicates the maximum achievable radius of curvature change, regardless of dimpling.

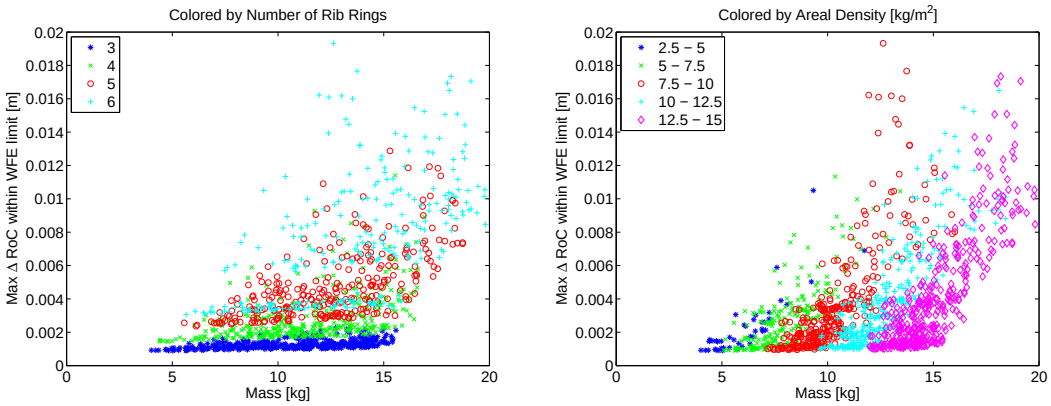

(a) Differentiated by Number of Rib Rings

(b) Differentiated by Areal Density

Figure 6-10: Mass versus Correctability with Dimpling and 3-σ Stress Limits and Parameter Differentiation

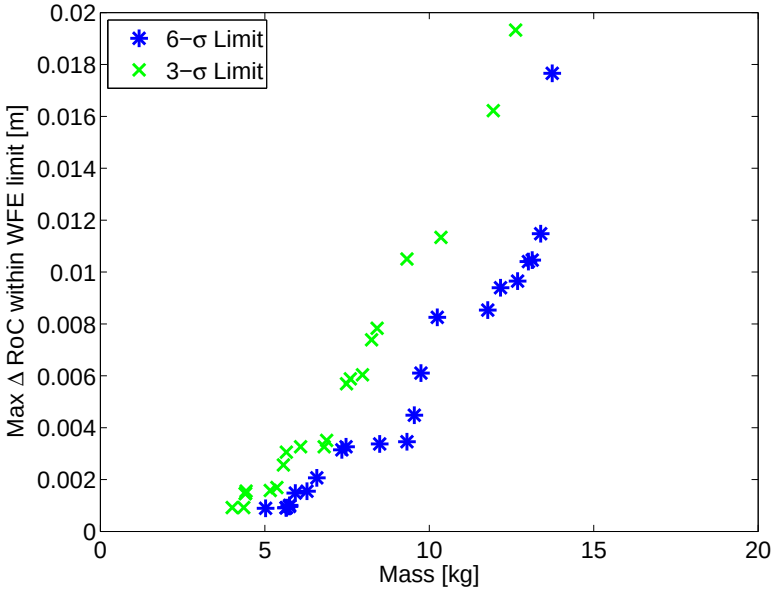

Figure 6-11: Mass versus Correctability Pareto Front Comparison

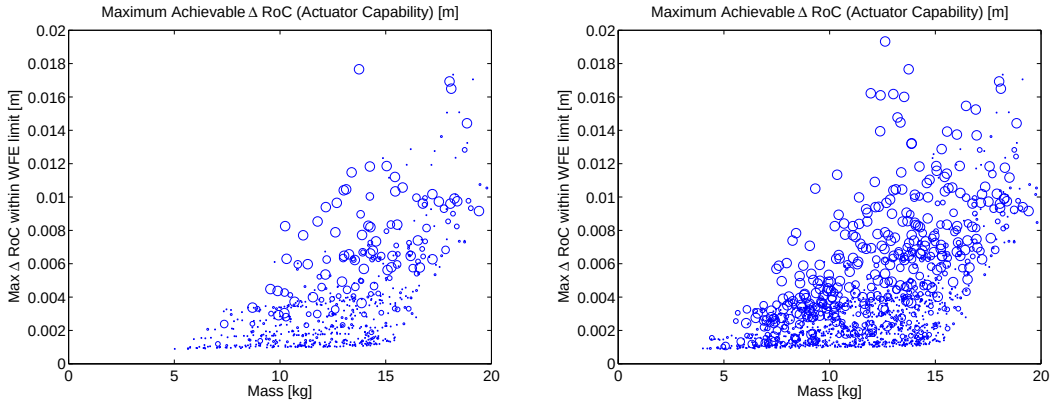

(a) 6-σ Stress Limits

(b) 3-σ Stress Limits

Figure 6-12: Mass versus Correctability with Limits, Large Dots Indicate Larger Achievable Shape Changes

Larger circles indicate larger achievable shape changes. The designs on the Pareto front tend to have larger achievable shape changes, indicating that the Pareto designs are also high performing in that respect.

All of the results in this section thus far have been for designs without launch load alleviation. The increase in the number of feasible designs due to relaxing the stress limit (seen in the change between Figure 6-7 and Figure 6-9), as well as the improved performance of the Pareto designs (Figure 6-11), indicates that the launch stress limit eliminates many otherwise good designs. Therefore, the launch load alleviation is added to the trade space. While all of the previous plots could be recreated for the trade space with launch load alleviation, only the mass versus correctability plots with the dimpling and 6-σ stress limits are shown for brevity.

Figure 6-13 shows the mass versus correctability trade space with the 15 nm dimpling error and 6-σ stress limits applied, including launch load alleviation. Notice that there are many more feasible designs with higher correctability, as compared to the case without alleviation (Figure 6-7), due to the addition of launch load alleviation. Also, Figure 6-14 shows the designs differentiated by number of ribs, areal density, and launch load alleviation. All of the designs with high correctability, which were infeasible without launch load alleviation, have many ribs. However, these designs all

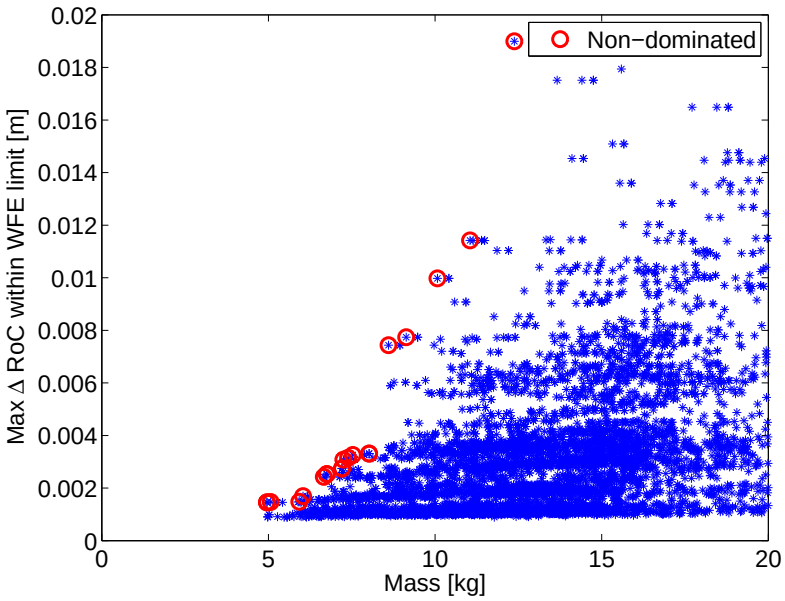

Figure 6-13: Mass versus Correctability with Dimpling and 6-σ Stress Limits, Including Launch Alleviation

have higher masses due to the increase in mass from the alleviation. The additional mass required in order to include shunt circuits and active damping is dependent on the number of actuators, so designs with many actuators and alleviation necessitate substantial mass increases. Also, Figure 6-14(c) shows that many of the Pareto designs utilize either shunt circuits or active damping. These methods allow designs that have high correctability to meet the stress requirements and become feasible design options.

This section shows the full, integrated trade space both with and without launch load alleviation. Additionally, by applying limits to the dimpling and the stress, the correctability and mass can be compared, showing the best performing designs that meet requirements. The next sections will focus on more specific areas of the trade space, and the best designs under various circumstances.

6.2.2 High Performing Designs

The previous section presented the results from the integrated trade space analysis. This section will focus on specific areas of the design space, and present possible

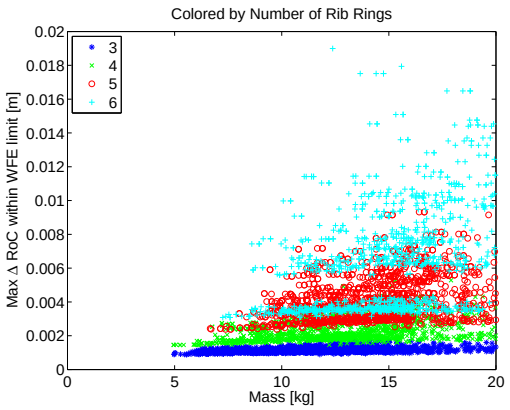

(a) Differentiated by Number of Rib Rings

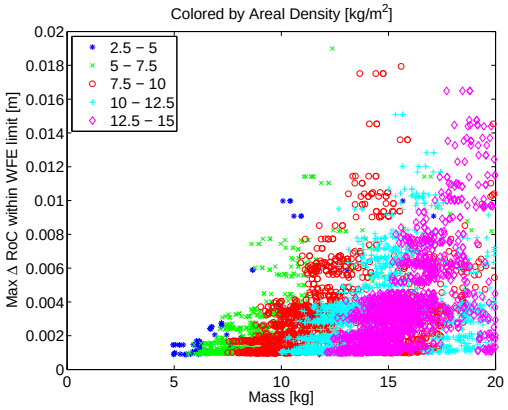

(b) Differentiated by Areal Density

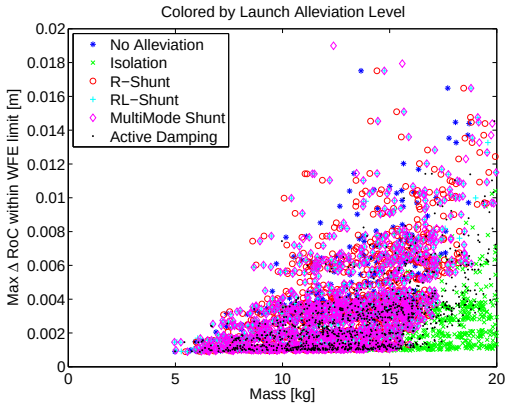

(c) Differentiated by Launch Load Alleviation

Figure 6-14: Mass versus Correctability, Including Launch Alleviation, Differentiated by Parameters

designs that one might want to use under various circumstances. First, an optimal design considering only on-orbit performance is shown. Similarly, very low mass designs are also shown. Then, the Pareto optimal front considering both mass and correctability is discussed, since there is a clear trade off between the two metrics.

Optimal Design for On-Orbit Performance

Conventional practice might suggest designing a mirror specifically for on-orbit correction, as optical performance is the primary function of the mirror. Launch would then be considered as an afterthought, and one would hope that the chosen mirror design meets the launch stress limits. If it does not, one would modify the design in order to obtain a design that does survive launch. This can be illustrated here by optimizing the mirror design for on-orbit correctability.

An optimization is performed on the response surface model that was discussed in Section 6.1.2. The objective is to maximize the correctability while keeping the wavefront error due to dimpling below 30 nm. Since the response surface is a continuous function of the design parameters, gradient based optimization can be used with relative ease. Gradient based sequential quadratic programming optimization is performed using the MATLAB optimization function, "fmincon.m". The optimization is set up to maximize the correctability subject to the following constraints:

- Dimpling error less than 15 nm (wavefront error less than 30 nm)
- Lower and upper bounds of the design parameters
- Thicknesses greater than manufacturing limits
- Actuator length less than the length of the cell side

With these constraints, the optimization is run with 50 different randomly generated initial conditions, to ensure that the global optimum is found. Also, the performance is verified using the full on-orbit model to ensure that it matches the response surface approximation. The parameters for the optimal design for on-orbit correctability under a dimpling limit can be seen in Table 6.2. Table 6.2 also shows the dimpling

when subjected to the prescribed 5 mm radius of curvature change and the maximum achievable radius of curvature, which were the two initial on-orbit performance metrics.

Table 6.2: Optimal Design for On-Orbit Correctability

Diameter	1.2 m
Number of Rib Rings	6
Rib Aspect Ratio	25
Face Sheet Mass Fraction	0.81
Areal Density	15 kg/m^2
Actuator Length	0.075 m
Maximum ΔRoC with WFE $<$ 30 nm	0.02 m
Dimpling under 5 mm ΔRoC	3.7 nm
Maximum achievable ΔRoC (actuator capability)	0.26 m

This design performs well in terms of the on-orbit correctability; however, launch survival must also be examined. The peak stress in the mirror is 93 MPa, when using the optimal bipod reinforcement for that design. This design does meet the 3-σ stress limit, but it does not meet the 6-σ limit. Therefore, if greater launch survival certainty is desired, launch load alleviation techniques can be employed to reduce the peak stress. Each launch load alleviation technique is added, and the resulting stresses and masses can be seen in Table 6.3. Resistive shunting performs quite well since there are so many actuators with which to add damping, increasing the survival probability from 3.3-σ to 4.9-σ. Resistive shunting is passive, and works across a broad frequency range, leading to a system that is not overly complex, making it a good option. If there is a desire to decrease the stress below the 6-σ limit, then active damping should be used, as it is the only option that meets the 6-σ limit. However, the multi-mode resonant shunt is also quite close to the limit, and, when considering uncertainty, it is statistically equivalent to the active damping solution. Therefore, multi-mode shunting could also be used if a passive system during launch is desired.

Given the addition of the launch load alleviation techniques, the optimal design for on-orbit performance can survive launch, making it a feasible design choice. However, notice that the mass is very large. Therefore, though it is possible to make the design

Table 6.3: Launch Alleviation Options for Optimal On-Orbit Design

Alleviation Option	Peak Stress] [MPa]	Launch Survival Certainty (σ)	Mass [kg]
None	93	3.3	19.4
Isolation	70	4.3	26.2
Resistive Shunt	61	4.9	20.4
Resonant Shunt	57	5.3	20.9
Multi-mode Shunt	53	5.7	21.0
Active Damping	49	6.1	22.7

survive launch with sufficient certainty, purely optimizing for on-orbit performance ignores other important aspects of the design. The integrated trade space, considering multiple metrics, can provide better overall results for the system by simultaneously considering all aspects, rather than designing for one and subsequently looking at the other metrics.

Low Mass Designs

Though the design with optimal on-orbit performance above performs well on-orbit and can meet the launch survival limits, it is quite massive, with high areal density and a large number of long actuators contributing to the large mass. Mass-to-orbit is extremely expensive, so low mass designs are also presented.

The parameters for the lowest mass design meeting the 3-σ launch stress limits can be seen in Table 6.4. Notice that this design has only 3 rib rings and short actuators, both of which contribute to the low correctability value. Furthermore, though the rib aspect ratio is not extremely high, both the rib and face sheet thicknesses are very near the constraint limits, and thus the aspect ratio cannot be increased without adding additional mass. Though this design is exceptionally lightweight, it likely does not perform well enough, in terms of the other performance metrics, to warrant its use in an operational system.

Similarly, one can examine the lowest mass design meeting the stricter, 6-σ launch stress limits. This design can be seen in Table 6.5. Here, the design has a higher rib aspect ratio than in the first low mass design (Table 6.4), made possible by the

Table 6.4: Parameters for Low Mass Design Meeting 3-σ Stress Limit

Number of Rib Rings	3
Rib Aspect Ratio	52
Face Sheet Mass Fraction	0.55
Bipod Reinforcement	2.6
Actuator Length	0.03 m
Areal Density	3.6 kg/m^2
Mass	4.0 kg
Correctability	0.9 nm
Peak Stress	98 MPa

slightly higher areal density, and resulting in much lower stress. Note that in the very low mass designs, the thickness constraints are limiting, as they preclude tall ribs, making it difficult for the low areal density systems to meet the stress limits.

Table 6.5: Parameters for Low Mass Design Meeting 6-σ Stress Limit

Number of Rib Rings	3
Rib Aspect Ratio	65
Face Sheet Mass Fraction	0.43
Bipod Reinforcement	3.9
Actuator Length	0.03 m
Areal Density	4.8 kg/m^2
Mass	5.0 kg
Correctability	0.9 mm
Peak Stress	47 MPa

Furthermore, one could add launch load alleviation techniques in order to make designs with lower areal densities feasible. However, for the lowest mass cases, the additional mass necessary to implement a launch load alleviation technique will offset any mass savings from reducing the areal density, as was discussed in Chapter 5.

Pareto Optimal Designs

As was seen in the trade space plots in Section 6.2.1, and is reiterated in this section, there is a clear trade off between mass and correctability. The optimal designs for on-orbit correctability have very high masses, while the lowest mass designs have

low correctabilities. The conflicting performance metrics motivate the use of the trade space, rather than simply designing for one metric. By considering all metrics simultaneously, one can find a Pareto optimal design that best balances the metrics, based on the requirements for the specific mission.

The Pareto optimal designs for the 6-σ certainty limits (Figure 6-7) can be seen in Table 6.6. As the mass increases and the correctability improves, the Pareto designs transition from having few ribs to having many ribs. The designs in the middle of the Pareto front have alternating numbers of ribs, and one can obtain similar performance from designs with differing numbers of ribs. Areal density is another metric to move along the Pareto front; increasing areal density increases both correctability and mass. Together, the rib aspect ratio and face sheet mass fraction determine the height and thickness of the ribs and the thickness of the face sheet, which must be optimized at each point in the design space. This makes it difficult to determine a clear trend with respect to the two variables, especially with the strict stress limits and no alleviation. The strict stress limits require there to be a significant amount of mass in the ribs, thus keeping the face sheet mass fraction at a moderate value. With less stringent stress limits, the face sheet mass fraction will be low in the low mass designs, maximizing the mass in the ribs, and it will be higher in the very correctable designs, resulting in broader influence functions. Similarly, the rib aspect ratio tends to be high in the lower mass designs, as the taller ribs are necessary to meet the stress requirements.

In examining the Pareto front designs, it is desirable to understand how to move along the Pareto front, particularly whether movement along the Pareto front is dictated by a single variable made up of a linear combination of design parameters, or a more complex relationship, necessitating the full integrated modeling effort. In order to determine the complexity of the relationships, a singular value decomposition (SVD) is utilized.

SVD involves factoring a matrix into three matrices as follows:

$$M = U\Sigma V' \tag{6.1}$$

Table 6.6: Mass versus Correctability Non-dominated Designs with 6-σ Stress Limit

	Number of Ribs	Rib Aspect Ratio	Face Sheet Mass Fraction	Actuator Length [cm]	Areal Density [kg/m^2]	Mass [kg]	Correct-abiity [mm]
1	3	65	0.43	3.0	4.8	5.0	0.9
2	3	72	0.45	2.2	5.6	5.6	0.9
3	3	62	0.46	2.0	5.7	5.7	0.9
4	3	64	0.38	5.9	5.0	5.8	1.0
5	3	41	0.39	3.9	5.4	5.8	1.0
6	4	80	0.35	2.5	5.5	5.9	1.5
7	4	53	0.46	1.9	6.1	6.3	1.6
8	4	60	0.41	6.9	4.6	6.6	2.1
9	6	60	0.40	2.3	6.1	7.3	3.1
10	6	53	0.38	1.3	7.0	7.5	3.3
11	6	63	0.38	1.7	7.8	8.5	3.4
12	5	68	0.52	3.7	7.4	8.7	3.4
13	6	31	0.41	2.1	8.4	9.3	3.5
14	5	36	0.36	6.1	6.9	9.5	4.5
15	6	71	0.35	3.8	7.5	9.7	6.1
16	6	47	0.40	6.1	6.2	10.2	8.3
17	6	52	0.44	6.3	7.7	11.8	8.5
18	6	46	0.35	7.3	7.4	12.2	9.4
19	6	10	0.36	3.9	10.6	12.7	9.6
20	6	32	0.44	6.8	8.6	13.0	10.4
21	6	34	0.40	7.5	8.2	13.1	10.5
22	6	34	0.37	6.6	9.2	13.4	11.5
23	6	13	0.41	7.2	9.1	13.7	17.7

where M is the original $[m \times n]$ matrix, Σ is the $[m \times n]$ diagonal matrix with the singular values on the diagonal, U is an $[m \times m]$ unitary matrix, and V is a $[n \times n]$ unitary matrix. The columns of V form an orthonormal basis for the inputs of M, and the singular values can be thought of as scalar gains. Furthermore, the number of non-zero singular values, which is equal to the rank of M, determines the number of linearly independent columns of M.

Consider the set of parameters from Table 6.6 that make up the Pareto front designs. There are 23 Pareto designs and six design parameters, resulting in a $[23 \times 6]$ matrix. One can perform an SVD on the normalized matrix of Pareto parameters, which can then be used to determine linear independence of those parameters. The

singular value matrix is:

$$\Sigma = \begin{bmatrix} 7.86 & 0 & 0 & 0 & 0 & 0 \\ 0 & 1.44 & 0 & 0 & 0 & 0 \\ 0 & 0 & 0.99 & 0 & 0 & 0 \\ 0 & 0 & 0 & 0.65 & 0 & 0 \\ 0 & 0 & 0 & 0 & 0.54 & 0 \\ 0 & 0 & 0 & 0 & 0 & 0.27 \\ 0 & 0 & 0 & 0 & 0 & 0 \\ \vdots & \vdots & \vdots & \vdots & \vdots & \vdots \\ 0 & 0 & 0 & 0 & 0 & 0 \end{bmatrix} \tag{6.2}$$

Notice that there are six non-zero singular values, indicating that moving along the Pareto front does not involve a linear combinations of parameters. Though none of the singular values are negligible, the first one is significantly greater than the others, and will be used to determine a linear combination of parameters that best approximates movement along the Pareto front.

As mentioned previously, the columns of the V matrix make up an orthonormal basis for the design parameters. Therefore, the first column of V (v_1), which corresponds to the largest singular value, can be used as a basis vector to move along the direction of the maximum singular value. One can start at any point on the Pareto front, and use v_1 to move along the front. A single variable, corresponding to the direction of v_1 and changing all design parameters, is varied in even increments with respect to the initial point. Therefore, the designs chosen are dependent on the starting location.

Figure 6-15 shows the Pareto front, along with the newly calculated designs, for six cases. Each case starts at a different Pareto point, indicated by the circle. The new designs which are feasible are marked with a +, while the new designs that violate the constraints are marked by an $\times$. From Figure 6-15, it is clear that moving along the direction corresponding to the largest singular value does roughly follow the Pareto front. However, in many cases, such as in Figures 6-15(b) and 6-15(e), the designs

near the initial point are close to the Pareto front, but as one moves farther from the initial point, the designs veer away from the Pareto front and are suboptimal. In other cases, many of the designs are infeasible due to either the stress or thickness constraints.

Therefore, while it may be desirable to determine a single linear combination of parameters that allows one to move along with Pareto front, thus minimizing the amount of necessary computation, the complexity involved in this case makes it unlikely. The linear combination corresponding to the direction of the maximum singular value would be extremely difficult to determine without an integrated model and trade space. However, even if this were possible due to past experience or engineering judgment, utilizing a single parameter to approximate the Pareto front will result in suboptimal or infeasible designs, thus necessitating the integrated model and full trade space exploration to determine the actual Pareto front.

One can also examine the change in the Pareto front as the stress limits change, or as launch load alleviation is added. Figure 6-16 shows three sets of Pareto designs: designs meeting the 6-σ stress limit without alleviation, designs meeting the 3-σ stress limits without alleviation, and designs meeting the 6-σ stress limits with alleviation. As was shown before, either adding launch load alleviation or relaxing the stress constraint improves the performance of the Pareto designs. Notice that there appear to be steps in the Pareto fronts, rather than smooth, continuous lines. The jumps in correctability are due to adding more ribs. Since the number of rib rings is a discrete geometric parameter with a great deal of influence on the performance, it causes the discontinuities in the Pareto fronts. Also notice that all three fronts undergo these jumps at similar values of correctability, and the masses at which the jumps occur varies. This is due to the feasibility of lower areal density designs with similar optical performance made possible through the constraint relaxation or addition of launch load alleviation.

By using the integrated model and trade space, it is possible to determine the trade offs involved between metrics and make educated decisions as to which designs will best satisfy all performance metrics and constraints. This results in a better

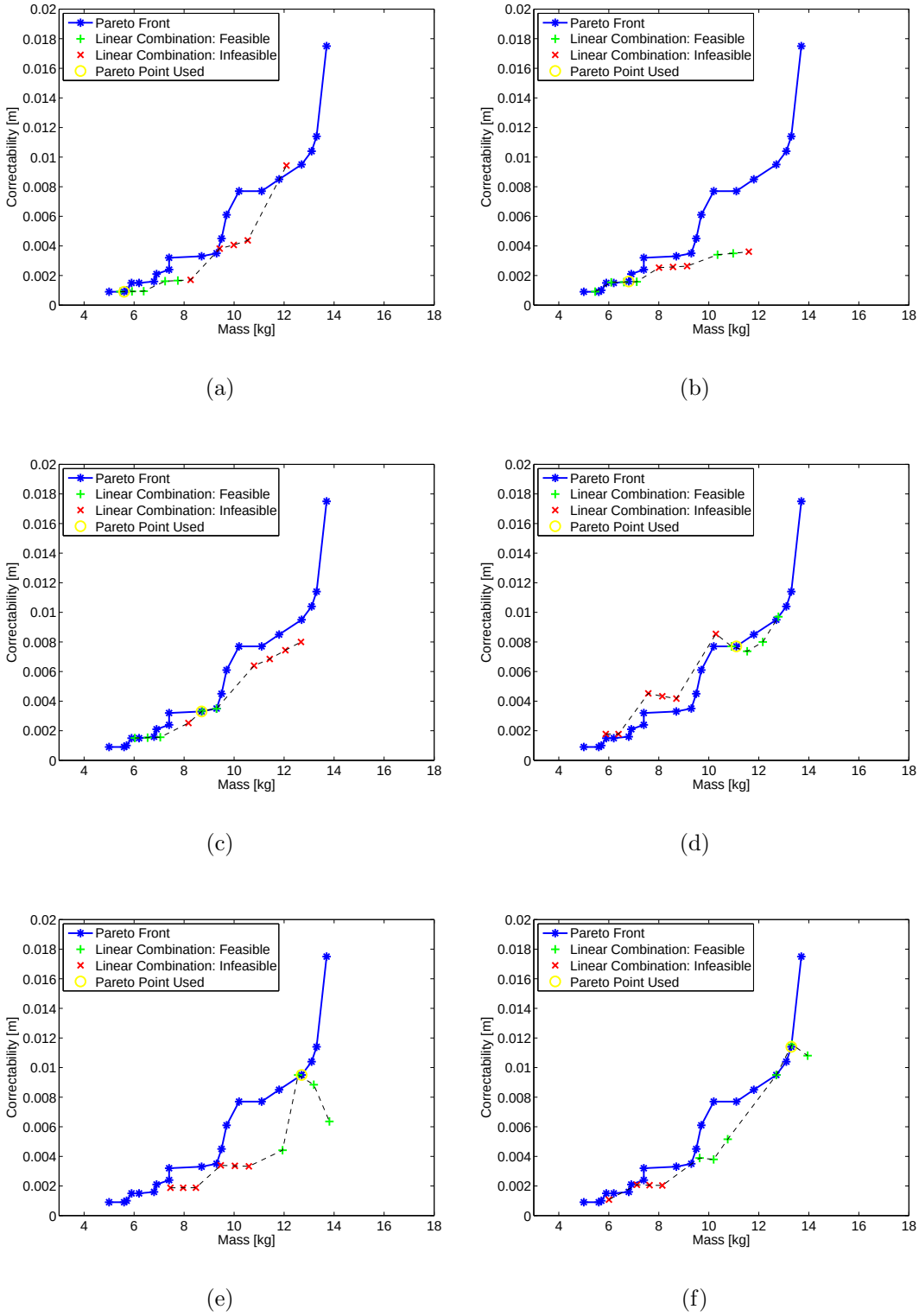

Figure 6-15: Pareto Comparison

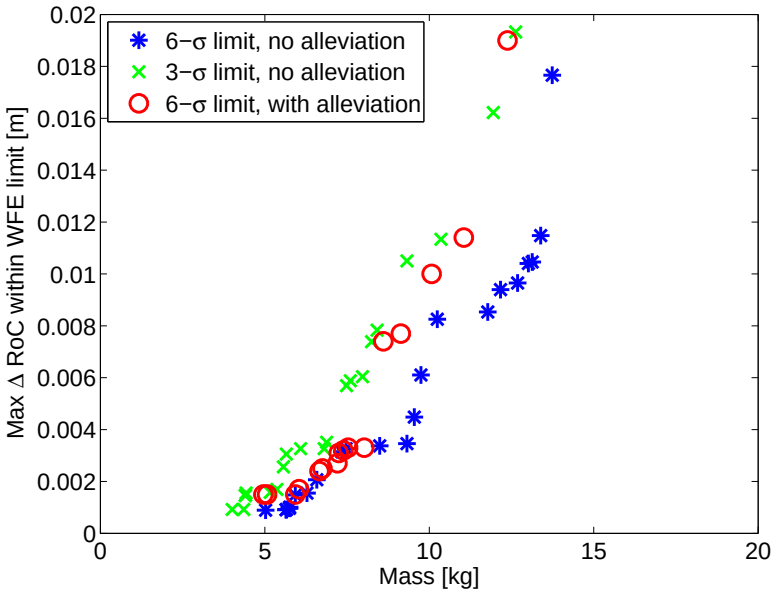

Figure 6-16: Comparison of Pareto Designs

performing design than sequentially designing for either correctability or mass.

6.2.3 Complexity

Another dimension of the design that has not yet been discussed is complexity. In general, systems that are less complex are less risky and less expensive to develop. While complexity is not formally defined for the mirrors, one can consider two design aspects that significantly contribute to the complexity of the system: number of actuators and launch load alleviation.

The number of actuators, as defined by the number of rib rings, has a considerable effect on the complexity of the system. Using more actuators involves more driver electronics, more wires, more influence functions, and more potential failure locations. While actuation generally improves optical performance, it also detracts from the simplicity, and the complexity grows as more actuators are added.

Launch load alleviation techniques also add to the complexity of the system, and despite the significant improvement in survival probability one can obtain when using alleviation techniques, it is far simpler to launch a mirror without any additional components. Furthermore, it is possible that the failure of a launch load alleviation

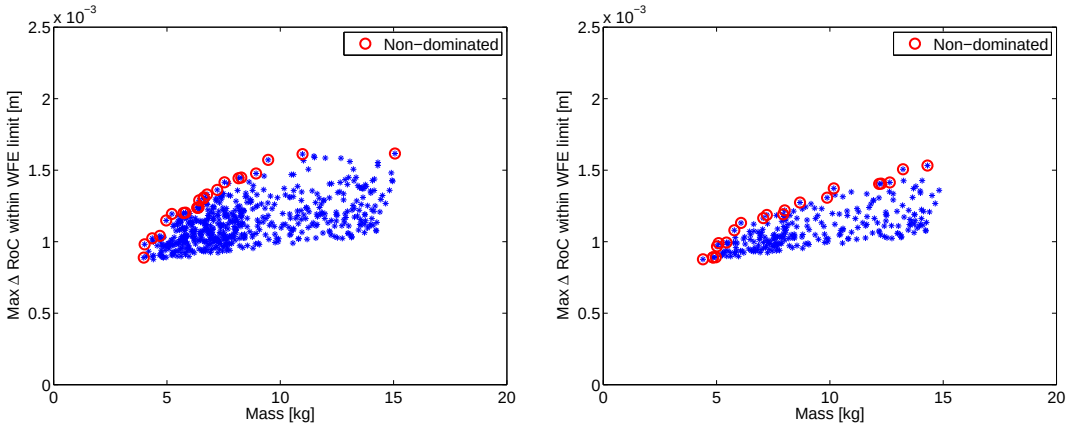

(a) 3-σ Stress Limit

(b) 6-σ Stress Limit

Figure 6-17: Mass versus Correctability for the Least Complex Systems

technique could result in breaking the mirror. Consider a mirror with an initial low probability of launch survival. One could add a launch load alleviation technique to increase the probability of survival, but the failure of that added alleviation technique would result in the equivalent of not having any alleviation, and, again, a low probability of survival. Therefore, adding launch load alleviation adds another potential point of failure, adding risk.

Given these observances, one can extrapolate that the least complex mirrors considered in this thesis are those that have only three rib rings and no launch load alleviation. Figure 6-17 shows the low complexity designs comparing mass and correctability, where Figure 6-17(a) shows the designs meeting the 3-σ stress limit and Figure 6-17(b) shows the designs meeting the 6-σ stress limit. Notice that the scale of the achievable shape change, under the 30 nm WFE requirement, is significantly lower than in the previous cases. Using so few actuators greatly limits the shape change that is achievable. Also, notice that applying the stricter stress limit results in eliminating the many of the Pareto optimal designs.

An example design is taken from the Pareto front of the 3-σ stress limit case (Figure 6-17(a)). The design parameters are shown in Table 6.7. The peak stress is very close to the 3-σ limit. If one desired a higher probability of launch survival, an

alternative, design with lower peak stress, on the Pareto front in Figure 6-17(b) can be seen in Table 6.8.

Table 6.7: Parameters for a Low Complexity Design Meeting 3-σ Stress Limit

Rib Aspect Ratio	58
Face Sheet Mass Fraction	0.71
Bipod Reinforcement	1.5
Actuator Length	0.07 m
Areal Density	6.2 kg/m^2
Mass	7.2 kg
Correctability	1.4 mm
Peak Stress	98 MPa

Table 6.8: Parameters for a Low Complexity Design Meeting 6-σ Stress Limit

Rib Aspect Ratio	26
Face Sheet Mass Fraction	0.49
Bipod Reinforcement	1.3
Actuator Length	0.05 m
Areal Density	7.8 kg/m^2
Mass	8.3 kg
Correctability	1.1 mm
Peak Stress	45 MPa

Though neither of these designs push the performance limits, they are the least complex of the designs considered here that meet the requirements. They could potentially be used as a lower budget system with less stringent performance requirements, or as a way to mitigate risk in an initial technology demonstration.

6.2.4 Uncertainty

In any modeling effort, it is important to consider the uncertainty involved in each design, especially as design decisions are made. Therefore, a parametric uncertainty analysis is run on three key designs to illustrate the effects of uncertainty on the performance metrics. Uncertainty distributions are defined for each parameter of interest, and a sampling-based uncertainty analysis is run to determine the mean and

standard deviation of the performance outputs. This uncertainty analysis addresses the parametric uncertainties that are captured with the model, so any uncertainties that are not included in the model are not accounted for in this analysis.

Three designs are chosen on which to perform the uncertainty analysis: the optimal on-orbit design, a low complexity design, and a Pareto optimal design balancing the mass and correctability performance metrics. The design parameters for each design are specified in Table 6.9.

Table 6.9: Designs Used for Uncertainty Analysis

Parameter	Design 1	Design 2	Design 3
Number of Ribs	6	3	5
Rib Aspect Ratio	25	58	68
Face Sheet Mass Fraction	0.81	0.71	0.52
Bipod Reinforcement	2.1	1.7	2.5
Actuator Length [cm]	7.5	7.0	3.7
Areal Density	15	6.2	7.4

Uncertainty distributions are defined for the design parameters, as well as for the material properties, piezoelectric properties, damping ratio, and diameter. The parameter uncertainties are specified as normal distributions with standard deviations approximately equal to 1% of the nominal values. The means and standard deviation of the performance metrics resulting from the uncertainty analysis can be seen in Table 6.10.

Table 6.10: Uncertainty Results

	Mass [kg]		Stress [MPa]		Correctability [mm]	
	Mean	Standard Dev.	Mean	Standard Dev.	Mean	Standard Dev.
Design 1	19.4	0.18	93	3.5	20.4	0.095
Design 2	7.2	0.10	98	5.8	1.5	0.007
Design 3	8.7	0.13	50	3.0	3.4	0.027

From Table 6.10, one can see that the relative standard deviations for both the correctability and the mass are low, with the standard deviations being approximately

equal to 0.3% and 1% of the nominal value, respectively. In other words, parameter variations within the expected ranges do not have a significant effect on the outputs. However, the stress has a slightly higher standard deviation, indicating that it is more susceptable to parametric uncertainty. This is largely due to the effect of the uncertainty in the modal damping ratio, as was discussed in Section 5.4.1. The damping ratio has no effect on the mass or the on-orbit performance, and only affects the dynamic launch analysis. This slightly larger uncertainty range in the stress means that designs with peak stresses within a few MPa of each other are statistically equivalent, and, if two designs have stresses close to one another, one cannot actually determine which will perform better.

From this analysis, one can see that the uncertainty resulting from parametric variations is relatively small. However, this analysis only includes the uncertainty due to the propagation of design parameter uncertainty through the model, and does not account for any sources of uncertainty external to the model. As the development proceeds and more data is gathered, any other uncertainty sources that are encountered and affect the results should be added to the model, as was discussed in Chapter 3.

6.2.5 Trade Space Summary

This section presents the integrated trade space considering the launch and on-orbit environments. The launch results are obtained using the dynamic launch model, while the on-orbit performance is obtained using a combination of the full, on-orbit model and the response surface approximation model. The four primary performance metrics are mass, peak stress, dimpling under a prescribed radius of curvature change, and maximum achievable radius of curvature change given the capability of the actuators. It is convenient to subject the on-orbit performance to an optical requirement of 30 nm wavefront error (15 nm dimpling error), and then maximize the radius of curvature change maintaining the dimpling error within that limit, referred to as correctability. This eliminates one performance metric. Also, the peak stress can be limited using either 3 or 6-σ launch survival certainty limits. By imposing the dimpling and stress

limits, the trade space can be shown in terms of the two remaining performance metrics: mass and correctability. There is a clear trade off between the two metrics, so the best design will be mission specific. Also, the imposed requirement limits do affect Pareto front outcome, but the trade space implementation allows those to be changed as a post processing step in order to see the differences.

Additionally, one can design a mirror to meet certain performance desires. For example, Section 6.2.2 optimizes the mirror correctability, and then discusses how launch load alleviation techniques can be used to ensure survival. Similarly, low mass designs, as well as the spectrum of Pareto designs are also shown. Furthermore, Section 6.2.3 examines low complexity designs, focusing only on those designs with the fewest actuators and no launch alleviation. Finally, Section 6.2.4 discusses the parametric uncertainty involved in the model. While parametric changes, within the expected bounds, have small effects on on-orbit performance and mass, they can potentially have larger effects on the launch stress, with the largest deviations being the result of damping variations. Finally, though only a few specific designs were discussed here, similar analyses could be run to determine the best designs given specific performance requirements and objectives, as was done in the low mass, low complexity, and high on-orbit performance cases. Given the data and insights available here, the next section will make specific recommendations on how best to proceed with lightweight, active mirror design.

6.3 Mirror Design Guidelines

While there is no optimal mirror design satisfying all performance metrics, recommendations can be made as to how to best proceed with the design of lightweight, active mirrors. First, specific attributes of high performing (Pareto optimal) designs are presented for various mission scenarios. Next, the areas of the design space in which technology demonstration and prototyping should focus in order to best support the development effort are discussed.

6.3.1 Characteristics of High Performing Mirror Designs

Given the trade space discussed in Section 6.2, it is clear that high performing designs, in the context of this thesis, have either low mass or high correctability. Since both objectives cannot be met simultaneously, there is a range of Pareto optimal designs with various combinations of low mass and high correctability. This section suggests promising areas of the design space, as well as methods by which one may choose a good design for a specific mission.

Low Mass Designs If one wishes to design a mirror with extremely low mass, the design attributes in Table 6.11 should be used. Utilizing fewer ribs at a given areal density allows the mass allocated to the ribs to be spread amongst fewer ribs, making those ribs taller than if the mass was spread amongst many ribs. This results in a stiffer mirror, and hence lower launch stress, allowing mirrors with lower areal densities to meet the stress requirements. Furthermore, rib height, not thickness, increases stiffness, so the rib mass should be allocated such that the ribs are tall and thin, thus maximizing the amount of stiffness obtained for a given amount of mass. To this end, the rib aspect ratio should be maximized. However, in the lowest areal density systems, only mid-range aspect ratios are feasible, as the highest aspect ratios violate the rib thickness constraint. Similarly, the face sheet mass fraction should be low, to increase the amount of mass in the ribs. Also, the lowest mass designs use short actuators, since longer actuators contain more mass then shorter actuators. Since launch load alleviation adds mass, the lowest mass designs will not use alleviation. However, one may desire a low areal density system with lower launch stresses, in which case launch load alleviation is useful, and while the system will be more massive than a similar one without alleviation, it can still achieve masses that are quite low.

Highly Correctable Designs A highly correctable mirror may also be desired; the design attributes of the most correctable systems can be seen in Table 6.12. As discussed previously, the total actuator length improves optical performance, so many,

Table 6.11: Properties of Low Mass Designs

Few rib rings and actuators
Tall, thin ribs
Low areal density
Short actuators
No launch load alleviation

long actuators provide the best performance. Also, broader influence functions allow for smoother actuation, and a larger curvature change before the wavefront error limit is met. Both high areal density and thick face sheets contribute to broader influence functions, making both parameters high in the most correctable systems. Furthermore, many of the best performing designs in terms of correctability do not meet the launch stress requirements. Therefore, many of the most correctable designs require shunt circuits or active damping to meet the stress requirements and become feasible design options.

Table 6.12: Properties of Highly Correctable Designs

Many rib rings and actuators
Thick face sheets
High areal density
Long actuators
Shunt circuits or active damping

Designs with a Large Achievable Radius of Curvature Change The attributes contributing to the best on-orbit designs, as discussed above, are specifically applicable to the visible spectrum and 30 nm wavefront error requirement. One can imagine using a lightweight, active mirror at alternate wavelengths. For example, consider near infrared, with a wavelength of approximately 3 μm. Using the same $\lambda/20$ requirement, the wavefront error limit is 150 nm. This allows a much greater range of actuation before the dimpling limit is reached, and the actuators will begin to reach saturation. If the actuators saturate before the wavefront error limit is reached, then the areal density should be reduced to increase the achievable RoC

change, and the actuator capability metric becomes the driving metric, rather than the correctability subject to dimpling constraints.

Use of Launch Load Alleviation Though launch load alleviation adds mass and complexity to the system, it enables a large portion of the trade space to become feasible, especially if the stricter, 6-σ launch stress limit is required. The reduction in stress due to the launch load alleviation moves the Pareto front, so that many design with mid-range masses have higher correctability than would be possible without alleviation. Specifically, the shunt circuits make use of the existing actuators, and can significantly decrease the stress without a lot of additional components or an active system, making it a good option for this situation.

Moving Along the Pareto Front One likely requires a mirror that is both low in mass and has high correctability, necessitating balancing the two metrics. This can be best accomplished by moving along the Pareto front. Figure 6-18 demonstrates the design knobs that allow one to move along the pareto front, where the utopia point refers to the best portion of the design space where the designs have both low mass and high correctability. The other performance metrics (rib aspect ratio and bipod reinforcement) work in conjunction with these parameters to ensure a feasible and Pareto optimal design.

Once a specific mission objective is chosen, then a design can be chosen from the Pareto front using these guidelines. However, it is important to ensure that the correct balance of parameters is determined so that the design is on the Pareto front and is not dominated. The wrong combinations of parameters can result in a design that performs poorly with respect to both mass and correctability. For example, a mirror with a high areal density and few actuators performs poorly with respect to both metrics. Similarly, a design with many rib rings but a low face sheet mass fraction has very localized influence functions, so the high spatial frequency error dominates and the design is far from the Pareto front. Therefore, the trade space results should be used to find a design with good performance, since single-axis trades

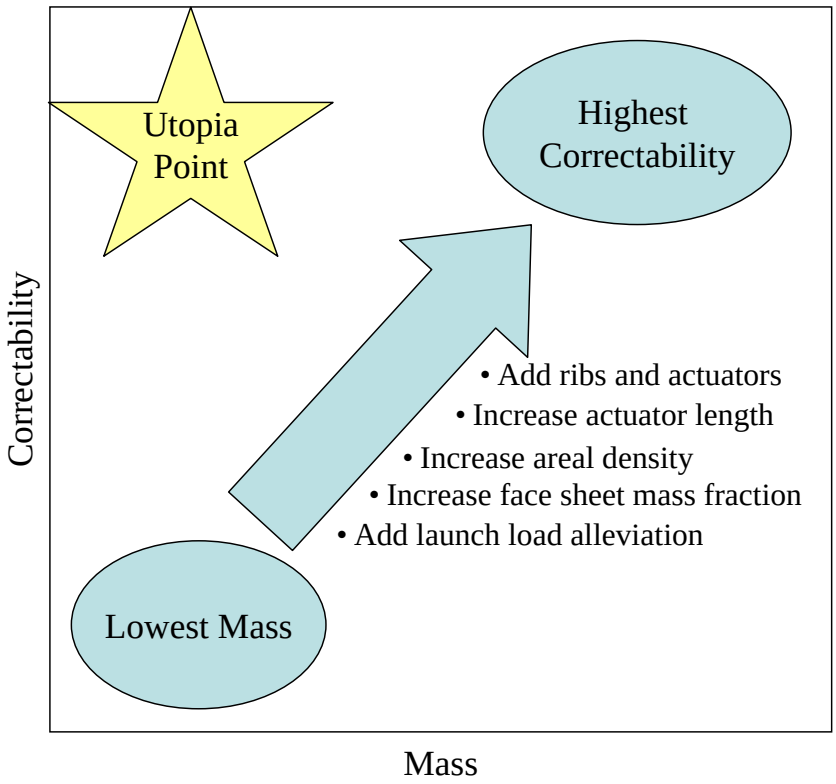

Figure 6-18: Illustration of How to Move Along Pareto Front

examining the effects of individual parameters will not capture the coupling between the parameters and metrics, and results in a sub-optimal design.

6.3.2 Next Steps in Active Mirror Development

As was discussed in Chapter 3, model-based technology development utilizes a model at the center of the design process, and that model is used to advance the technology. Specifically, integrated modeling should be used to find high performing designs and determine when prototypes or test data would be beneficial. This section suggests areas for further research and testing in the realm of lightweight mirror design.

Launch Stress As was shown in this chapter and in Chapter 5, the stresses due to launch are the most uncertain aspect of the analysis. This is due to a combination of the inherent uncertainties in damping, disturbance spectra, and modeling techniques (note that all acoustic modeling techniques have significant uncertainty). Since the

stress limit level has a significant effect on the Pareto optimal designs, it is desirable to further bound the uncertainty such that the system is not overly conservative. This can be accomplished through further acoustic and vibration testing of the mirrors, both to validate the model and to better estimate modal damping. Additionally, further research into the launch environment and the disturbance spectrum seen by the mirror would be useful. These tests could help to refine the necessary certainty level limits, thus refining the set of Pareto optimal designs.

Validation of Launch Load Alleviation Techniques Testing of the launch load alleviation techniques would be beneficial. The baseline mirror subjected to vibroacoustic launch loads has been validated. Additionally, the SoftRide isolator has been proven, shunting circuits have been implemented successfully on a variety of systems, and positive position feedback filtering for active damping has been tested and verified. However, these launch alleviation techniques have not been validated on a lightweight, active mirror. Given that the use of these launch load alleviation techniques is a deviation from traditional design, there is skepticism in using them on expensive systems. Therefore, it is important to prove and validate these techniques, increasing the probability that they will be used in future systems. Launch load alleviation is an example of a design solution that was first implemented in the model and found to be successful. The next step in the development is to test these techniques on a prototype to ensure that they perform as expected and to validate the model.

Simultaneous Variation of Parameters In addition to the aforementioned trends in the design variables that result in Pareto optimal designs, the importance of simultaneously varying the design parameters is also shown. As was discussed in Section 6.3.1, the design variables cannot be varied one at a time; finding the optimal designs requires concurrently varying many design parameters. This shows the advantage of the integrated modeling trade space effort, as those designs would not have been discovered by simply performing single-axis trades based on an existing baseline design. This practice should be continued as the technology development

effort progresses, so that the best designs are always found.

Iterative Design Finally, as was discussed in Chapter 3, model-based technology development is an iterative process. Given the results here, a new design iteration should begin. A new prototype should be built, based on one of the Pareto optimal designs to learn more information about the mirror system and mirror design, which is, as of yet, unknown. This information would then be incorporated back into the model, and the process would repeat itself. Since the integrated model already exists, the addition of the new test data and discoveries should involve significantly less effort than the initial model creation.

6.4 Integrated Mirror Design Summary

This chapter presents the integrated mirror design, simultaneously considering the launch and on-orbit environments. First, Section 6.1 discusses the model reduction efforts that make the large trade space analysis feasible without any extraordinary computational resources. A response surface approximation model is created for the on-orbit analysis, and the dynamic launch analysis computational expense is significantly reduced, leading to an overall model that has an acceptable computational expense, and making it feasible to examine a large trade space of designs.

As in previous chapters, a Latin Hypercube trade space exploration is performed in order to visualize the design space. This allows the constraints and limits to be imposed through post-processing. Then, the effects of different limits can be compared to one another using the same trade space. It also allows for visualization of the entire trade space, and avoids the concern of local minima and convergence issues that are present in optimization.

Initially, four performance metrics are considered: mass, peak stress, dimpling error under a prescribed RoC change, and maximum RoC change given the actuator limits. Assuming that the mirrors will be used in the visible spectrum, a $\lambda/20$ limit is applied to the wavefront error, resulting in a 30 nm requirement. Given this limit, the

natural on-orbit metric becomes the maximum radius of curvature change such that the dimpling error remains below the requirement, which is denoted as correctability. Additionally, one can impose launch stress limits on the designs. Once the stress is below the chosen limit and will confidently survive launch, the exact stress value is unimportant. However, difficulty arises due to disagreement in the community on the limit value. Therefore, the results are presented considering both the 3-σ and 6-σ certainty limit levels. This leaves two unconstrained performance metrics: mass and correctability. The two performance metrics can be easily compared using two-dimensional plots.

Minimizing mass and maximizing correctability are conflicting objectives, and result in a clear Pareto front. Therefore, the best design is dependent on which objective is favored. The lowest mass designs are shown to have low areal density, short actuators, and few thin ribs. The designs which perform best in terms of on-orbit performance have high areal density, many ribs, long actuators, and thick face sheets. In order to meet the launch load limits, many of the designs with high correctability necessitate launch load alleviation techniques, which add mass but reduce the launch stress to acceptable values. Changing the design parameters in the prescribed manner can move the design along the Pareto front. However, one should note that the correctability and mass Pareto front is dependent on the stress limit; less stringent stress limits allow higher performing designs to remain feasible, hence shifting the Pareto front to include overall higher performing designs.

Additionally, designs that minimize complexity, and consequently also minimize risk, are presented. These designs do not perform well in terms of the mass and correctability metrics, but they do offer a lower risk and likely less expensive alternative to the higher performing systems. Furthermore, a parametric uncertainty analysis is run on a few of the interesting designs for illustrative purposes. The uncertainty analysis considers the uncertainty in the modeled parameters, but not un-modeled effects, and demonstrates that the mass and correctability have low uncertainties, but the peak stress is more uncertain and can involve substantial variation in some circumstances.

Finally, guidelines for good mirror design, as well as future steps to continue the development of lightweight, active mirror systems are presented. The trade space suggests good designs, as well as areas where test data would be useful, such as validating the launch load alleviation techniques. Ideally, these observations will be used to develop future prototypes and tests to further the technology development effort.

Chapter 7

Conclusions

7.1 Thesis Summary

This thesis has explored the design of lightweight, active mirrors for use in future, space-based optical systems. Achieving better optical performance, in terms of resolution and sensitivity, can be obtained through the use of larger primary apertures. However, large primary apertures are challenging for a number of reasons, including launch mass, launch volume, and flexibility. Segmented apertures composed of lightweight, rib-stiffened, surface-parallel actuated silicon carbide mirror segments can solve many of the problems encountered in large aperture telescope systems. However, as they are a deviation from traditional design, there is very little knowledge on how to best design the lightweight mirrors. Hence, this thesis uses an integrated model to better understand the design space of lightweight, active mirrors, specifically with respect to launch and on-orbit correctability.

Chapter 3 presents an integrated modeling framework for use with technology development programs of complex, opto-mechanical systems. The key aspects of the integrated model are that it be: parametric, multidisciplinary, auto-generating, created in a modular modeling environment, and computationally efficient. This modeling implementation allows for trade space exploration or optimization to understand the design space. It also allows one to examine different design aspects in isolation or as a full system, and supports the adaptability required to evolve a model as data

becomes available and new insights are obtained. The integrated modeling proposed herein also supports model-based design, where a model is kept at the center of the design process. In model-based design, the model is used to guide the development of the technology, by using it to determine promising families of designs. The model also must be evolutionary, so that it changes to reflect the current state of the technology. Therefore, the model is used to determine tests and prototypes, which are in turn used to validate the model and suggest features and analyses that should be added to the model, resulting in an iterative design process. Furthermore, the test data that is generated can be directly stored in the model, and the model, as it changes in time, becomes an archive of knowledge about the technology.

This framework is particularly useful for technology development programs, where there is very little design heritage and high-performing designs are not known a priori. In these cases, choosing a point design can be fatal to the program since there is a significant probability that it will either not meet the requirements or not perform well enough to justify the risk in pursuing a new technology in an expensive system. Therefore, exploring the design space through integrated modeling and model-based design gives the technology the best chance of success through finding the best performing designs, and allowing the technology development path to adapt to new knowledge.

This process is demonstrated in this thesis in the case of lightweight, active mirrors. As was discussed in Chapter 3, the lightweight, active mirror modeling effort evolved from a model of the entire telescope that focused on disturbance sources that were found to be less important than those presented here. By using the modular modeling environment, the model evolved with the technology and is used here to suggest high performing designs with respect to metrics that have not been fully analyzed elsewhere. Though this thesis demonstrates the design for lightweight mirrors, a similar modeling effort and process could be used with any number of similar systems, with the model adapted for the specific case. However, this methodology will be most beneficial for multidisciplinary systems in the technology development phase.

After the presentation of the integrated modeling framework, Chapter 4 proceeds

with a discussion of the integrated model of the lightweight, active mirror. The mirrors of interest are low areal density, rib-stiffened, silicon carbide mirror segments. The ribbed back structure of the mirror contains embedded surface-parallel piezoelectric actuators to control the surface figure of the mirror. Additionally, though it is envisioned that multiple mirror segments would be used together in a larger, segmented aperture, only a single mirror segment is modeled here because it significantly simplifies the model without losing pertinent information about the system performance. The integrated mirror model is based in MATLAB and involves the creation of a structural finite element model. This finite element model is then used in two analyses: a quasi-static analysis for on-orbit optical performance and a dynamic model for launch load analysis. The pertinent design parameters in the structural model include: areal density, number of ribs and actuators, rib cross-sectional geometry, and mass distribution. The mirror structural model is validated using an existing prototype, and is used to perform the analyses throughout the thesis.

The on-orbit analysis focuses on changing the low spatial frequency shape of the mirror, as defined by the radius of curvature. Changing the low spatial frequency shape of the mirror solves a number of issues, including radius of curvature mismatch between mirror segments, thermal variations, and optical prescription changes. However, the finite length and spacing of the actuators limits the achievable shape change and causes a high spatial frequency dimpling error. The on-orbit analysis uses a quasi-static constrained least squares control algorithm to determine the dimpling wavefront error due to a prescribed curvature change and the maximum radius of curvature change due to the capability of the actuators. The best designs, in terms of both performance metrics, use many ribs and actuators, have long actuators, and have thick face sheets. Also, designs with low dimpling error tend to have high areal densities, though designs with high achievable shape changes tend to have low areal densities, since the actuators saturate less quickly in a less massive system.

Next, Chapter 5 discusses the launch environment, and the dynamic launch analysis. Typical launch analysis is performed either as a simple load factor application early in the design process, or as a detailed and computationally expensive coupled

loads analysis with the final spacecraft and launch vehicle design. Neither approach is appropriate for this case, so a dynamic launch model utilizing NASTRAN normal modes analysis and state-space modeling is developed. The frequencies and mode shapes of the system are used to create a state-space model with stress outputs. Then, vibroacoustic disturbances are applied to the state-space model, and a dynamic disturbance analysis is performed to obtain the stress outputs. The disturbance analysis provides a 1-σ certainty value, meaning that one expects the stress to be within that value about 68% of the time. Since launch survival is mission critical and there is inherent uncertainty in vibroacoustic modeling, 3-σ or 6-σ limits are used.

When designing a mirror specifically for launch survival, one is concerned with the peak stresses and the launch mass. The mirrors that minimize launch stress have high areal densities, few rib rings, and tall, thin ribs. However, mass-to-orbit is extremely expensive, so it is also desirable to minimize mass, and therefore areal density. The conflicting metrics result in a Pareto front, where improving one metric involves sacrificing performance in the other, and there is no single optimal design for launch. Also, while mirrors can be designed to survive launch, they are very close to the stress limits and the designs that are best for on-orbit performance have high launch stresses. Therefore, launch load alleviation techniques are also developed.

Three launch load alleviation techniques are presented: isolation, shunt circuits, and active damping. Isolation uses whole spacecraft isolation, and while it effectively reduces the vibrational disturbances, the more problematic, acousticly-induced stresses are unaffected. Therefore, isolation is not the best technique for mirror survival. Shunt circuits involve using the embedded piezoelectric actuators to passively damp the system. The piezos can convert mechanical energy to electrical energy, and a shunt circuit can be designed to dissipate that energy. Two types of shunt circuits are considered: a resistive shunt with low-level, broad frequency range damping, and a tuned resonant shunt with damping targeted at specific modal frequencies. The shunt circuits work well at reducing the stress in the mirror, but add both mass and complexity to the system. Finally, active damping is also implemented with the embedded piezos. In this case, a full active control system is used with individual

collocated single input-single output control loops for each actuator-sensor pair. This implementation with positive position feedback filters provides stability guarantees. The performance is better than all of the other techniques, but comes at the expense of adding an active system that operates during launch.

Another trade space is examined using the launch load alleviation techniques. In this case, many more designs meet the stress limits. However, since adding alleviation adds mass, the mass never decreases. The lowest mass designs, which have higher stresses, do not use any alleviation, but the lowest stress designs all use active damping or shunt circuits.

Since the launch and on-orbit environments drive the design in different directions, as is plainly illustrated by the optimal number of rib rings, a full, integrated design is performed, considering both environments. Again, a trade space exploration is performed to visualize the design space and the effect of the parameters on the performance metrics. However, the complexity of the model involves significant computational expense. Various steps are taken to improve the computational performance in both the quasi-static and dynamic analyses. Additionally, a response surface approximation model is created to provide an inexpensive surrogate for the full on-orbit model, greatly reducing the computational expense.

The full trade space is examined in terms of the four performance metrics. However, in order to effectively visualize the trade space, limits on the dimpling wavefront error and the stress are applied, resulting in a smaller feasible design space that can be examined in terms of mass and correctability. Unfortunately, the mass and correctability are conflicting metrics, so there is no single optimal design. Rather, one must decide which performance metric is valued more. Additionally, launch load alleviation is added, which can allow many more high performing designs, in terms of correctability, to meet the stress requirements. However, those designs tend to have high masses due to having many actuators and the addition of alleviation.

The best designs in terms of on-orbit performance have many ribs, long actuators, high areal densities, and include launch load alleviation, while the lowest mass designs have few thin ribs, short actuators, low areal density, and no alleviation. One can

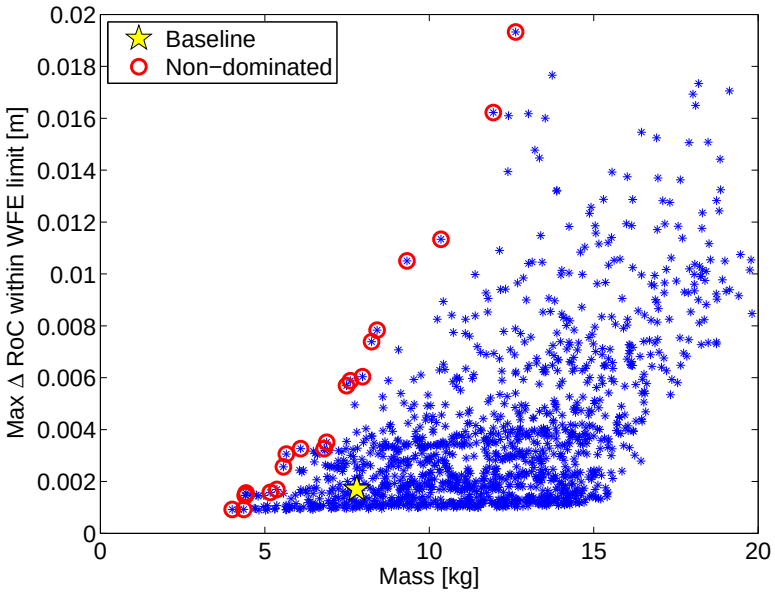

Figure 7-1: Mass versus Correctability Trade Space showing the Baseline Design

move along the Pareto front to find good designs by varying the design parameters in a specific way, though this must be done carefully to ensure non-dominance. If one varies the parameters in careless manner, then the design will end up away from the Pareto front, where one could obtain better performance in both metrics. The integrated modeling and trade space illustrate the importance of considering all of the parameters together. Consider Figure 7-1, which shows the mass versus correctability trade space with imposed stress and wavefront error requirements. Additionally, the baseline design is marked by a star. Notice that the baseline is far from the Pareto front, indicating that there are many other designs that would perform better. Furthermore, single-axis trades would not have allowed one to find the best designs, as the parameters must be varied concurrently to move along the Pareto front. Therefore, the integrated modeling has provided insights into the design of lightweight, active mirrors that would not otherwise have been discovered.

7.2 Contributions

The contributions made by this thesis can be summarized into five areas, which are described below.

Creation of an integrated modeling approach for lightweight, active mirror design This thesis presents the first integrated model of lightweight active mirrors in both the on-orbit and launch environments that can be used for design. This model considers the structural design, control systems, optics, and disturbance analysis. Additionally, it has been reduced such that the computational expense is low enough that it can be used for trade space exploration. Though there is not a suite of data encompassing all aspects of the model with which to validate it, the parametric nature of the model has allowed it to be validated against a number of data sets, resulting in a model in which all aspects are validated in some manner. Furthermore, this model has been built upon an adaptable and upgradeable framework, so it can be used to continue active mirror development by adding any additional components, performance metrics, or disturbance sources that arise.

As discussed in Section 2.5, a way in which to design lightweight, active mirrors, considering the performance implications of the structural and control system design, is lacking, and this model fills this gap. Furthermore, this model provides the first assessment of the effects and implications of launch loads on lightweight mirrors intended for use during the design process. The combination of the on-orbit and launch environments into a single model allows for the identification of previously unknown performance trade-offs in the design, and also enables the discovery of a set of best-performing designs. These designs offer significant performance improvement over previous baselines. The model is used to develop a set of design guidelines to be used in mirror development, and can continue to be used in the future so that the next set of lightweight active mirror designs achieve better performance than previous systems.

Development of a dynamic, state-space launch modeling technique A new dynamic, state-space modeling method for launch is presented. Typically, launch analysis is performed as simple load factors very early in the design process, or as a detailed, coupled loads analysis of the fully designed spacecraft-launch vehicle system. If launch analysis is done early in the design, it is typically implemented entirely within a finite element software package. Neither the simple load factors nor the detailed coupled loads analysis are appropriate for preliminary design or technology development of systems that may be close to launch stress limits, and analysis within a finite element software package does not allow for the addition of control systems or alleviation techniques.

The new state-space launch analysis method presented here provides a computationally efficient yet detailed way to analyze the response of a system to vibroacoustic launch disturbances early in the design process, and allows for the direct addition of control systems and alleviation techniques, thus filling the previous gap. This ability to directly add control systems to the launch analysis will continue to become important as launch load alleviation techniques are rendered necessary by the lightweight designs. A method such as this is lacking in the existing literature, and is useful for the lightweight mirror analysis, as well as the analysis of any lightweight, large surface area spacecraft component for which launch survival is a significant concern.

Formulation of launch load alleviation in mirrors using existing embedded actuators This thesis presents the first piece of literature analyzing the feasibility and performance of using existing embedded piezoelectric actuators to passively or actively add damping to lightweight, active mirrors during launch. Previous literature examines launch load alleviation using isolation or payload fairing control, but an analysis of the use of the existing embedded actuators to add damping is lacking. This thesis demonstrates that passively damping the mirror using both resistive and tuned resonant shunting circuits offers significant stress reductions. Additionally, active damping systems using single-input, single-output control loops with positive position feedback filters are found to perform extremely well, while imparting stability

guarantees.

Launch load alleviation using the existing embedded actuators can enable many mirrors to survive launch, thereby enhancing the potential on-orbit performance of lightweight, active mirrors. The ability to add damping directly to the mirror, rather than through structural paths such as isolation, will be come increasingly important as mirrors continue to become lighter due to dominance of the acoustic loads which cannot be isolated. Also, making use of the existing actuators minimizes the additional mass that must be added in order to add damping to the system. This thesis provides the first analysis showing that launch load alleviation using the existing embedded actuators is feasible and can provide significant improvement in the performance of lightweight, active mirrors, thereby improving performance of space telescopes that use such mirrors.

Synthesis of design guidelines for lightweight, active mirrors This thesis presents a unique set of guidelines for the design of lightweight, active mirrors considering launch stress, correctability, wavefront error, and mass. As discussed in Section 2.5, a trade space analysis and guidelines for the design of lightweight, active mirrors considering both on-orbit and launch performance is lacking from the literature.

The Pareto optimal designs identified using the integrated model offer significant performance improvement over previous baselines, which were thought to perform well, as was illustrated in Figure 7-1. Additionally, this thesis determined that launch survival and on-orbit performance lead to two different mirror designs, which was previously unknown and is a critical piece of information in lightweight mirror design. However, it was also shown that launch load alleviation can be used to enable designs that perform well on-orbit to survive launch.

Lightweight, active mirrors are complex systems that necessitate an integrated model and trade space. Therefore, the new design guidelines developed in this thesis provide a basis for the design of future lightweight, active mirrors. These guidelines will improve the performance of such mirrors and advance lightweight, active mirror

technology, leading to better performing space-based telescopes.

Development of an integrated modeling framework to support technology development programs This thesis presents a new integrated modeling framework for technology development of complex, opto-mechanical systems. Trade space exploration early in the design process has been used in other industries, and with very simple models. However, a method for technology development through trade space exploration of a high-precision opto-mechanical system early in the design process is lacking.

The methodology presented in this thesis supports the chronological nature of the design process, and demonstrates how to use the adaptability of integrated modeling to evolve a model as a technology progresses. Also, this methodology illustrates a procedure for capturing developmental experience, including test data, over the life cycle of the technology development program. Using this integrated modeling framework will result in better performing systems and will avoid the expense of redesign and repetition of work. This framework was used to identify superior lightweight, active mirror designs, and can also be used for similar, complex systems to maximize performance and guide future development.

7.3 Future Work

There are a number of ways this work could be built upon and extended. A few possible extensions are discussed below.

Multi-objective optimization for specific requirements This thesis presented trade spaces of designs in order to visualize the design space. Alternatively, multi-objective optimization could be used to find the true Pareto optimal points, once specific mission objectives are determined. Therefore, if one intends to use a lightweight, active mirror in an operational system, the system objectives and requirements could be used to define the relative weightings on the objectives, and a multi-objective optimization could be performed.

Prototype and test The creation of a prototype or test set-up with one of the high performing designs found here would be extremely beneficial. Also, it would be useful to validate the launch load alleviation techniques using embedded actuators on hardware. This prototype or test could be used to further validate the model, as well as find more lessons learned, and continue the iterative process of model-based technology development.

Add other design aspects into the model In order to feasibly scope this thesis, only the mirror design, as affected by the launch and on-orbit environments, was considered. However, there are many other aspects to mirror design, including manufacturing and wavefront sensing. Additionally, effects of other parameters, such as the translational direction in the vibration analysis, could be examined. These design aspects could be added to the integrated model to further its capabilities.

Appendix A

Uncertainty in Acoustic Analysis

Acoustic disturbances during launch can be extremely problematic for large surface area, lightweight structures, with launch survival often driving aspects of the design. The response of the system to the acoustic disturbance is also extremely uncertain, depending on a number of poorly understood variables. Therefore, systems are often over designed in an effort to ensure launch survival. A lightweight aluminum flat plate is used as a sample problem on which to quantify the uncertainty involved in the patch method of acoustic analysis. An experiment was performed on the plate in an acoustic test chamber with microphone data to characterize the input, and accelerometer data to determine the system response. This set up is modeled using a finite element model and the patch method for acoustic analysis.

Uncertainty Quantification (UQ) is the process by which one determines statistics on a system response quantity (SRQ) based on specified uncertainties in the input parameters. Here, accelerometer outputs on the flat plate are the system response quantities of interest. UQ can be performed using a variety of different methods, including sampling techniques, reliability methods, stochastic methods, and surrogate models [47, 144]. Here, sampling is used to quantify the uncertainty in the acoustic modeling. The accelerometer results can be extrapolated to suggest similar bounds and uncertainty trends in peak stresses.

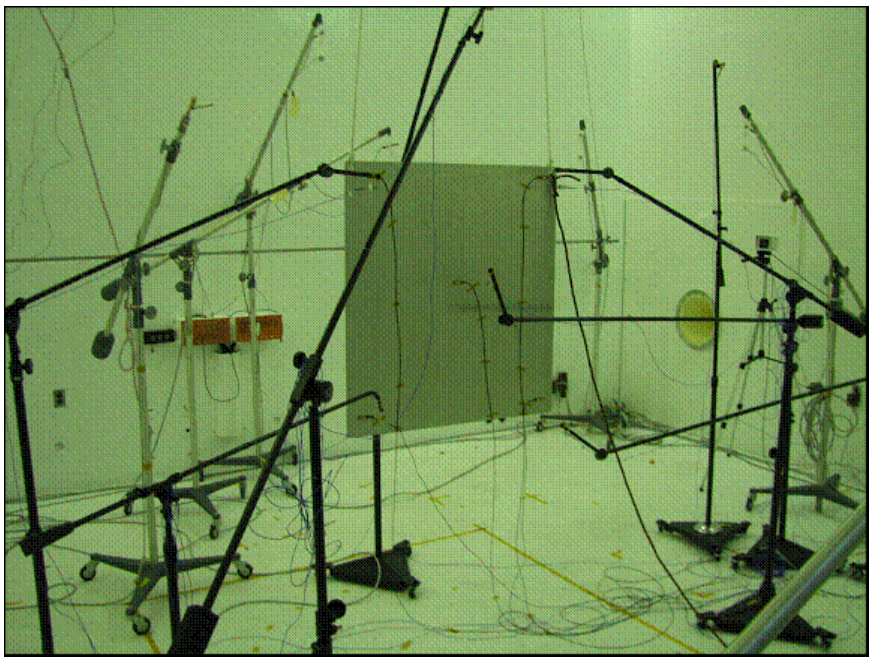

Figure A-1: Flat Plate Test Set Up

A.1 Flat Plate Sample Problem

A sample problem, on which there is available data, is used to quantify the uncertainty in the acoustic analysis. The system is a 0.95 x 1.04 m aluminum flat plate. It is suspended by bungee cords representing a free-free boundary condition in an acoustic test chamber. Eight control microphones are used to control the desired input sound pressure. Additionally, eight other response microphones are present to measure the acoustic conditions at various locations in the chamber. There are ten accelerometers mounted on the plate: two in the center and two located 6 inches from each corner, measuring accelerations in the x and z directions. A photograph of the test set up can be seen in Figure A-1. Power spectral density (PSD) data is available for the ten accelerometers, as well as the control and response microphones.

A finite element model of the test set up is created in MATLAB. The modeling method is the same as is used in the acoustic mirror model, as is described in Chapter 5. The acoustic input is the mean of the control microphones obtained from the test data, specified as a pressure power spectral density. The input spectrum can be seen in Figure A-2. An acoustic input factor is also included to account for the

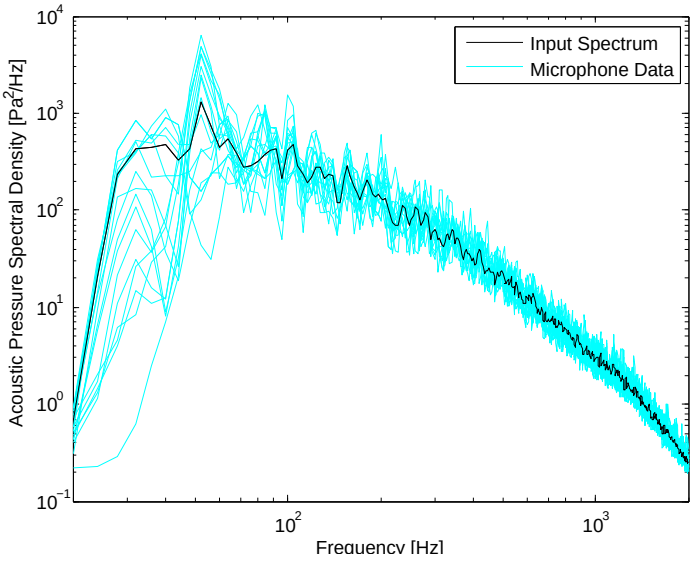

Figure A-2: Acoustic Input Spectrum

variation in the input pressure from the mean. This factor is obtained by bounding the control and response microphone test data. Figure A-2 also shows the spectra from the individual microphones, illustrating the difference between the input and the actual pressure levels around the room. Additionally, a correlation factor is added to the acoustic input, which takes into account the pressure loading on both sides of the panel. This varies between 1 and 2 with a most likely value of 1.4.

The outputs from the state-space model are accelerations, sensed by accelerometers. Using a dynamic disturbance analysis, the input PSD and the state-space model can be used to determine the PSD of the accelerometer outputs.

The baseline model and parameters can be compared to the test data to ensure that the model is functioning correctly. This comparison can be seen in Figure A-3. The total RMS acceleration of the model is 4.45 g, and the total RMS acceleration of the actual test data is 4.51 g. It is clear from Figure A-3 that the model overestimates the acceleration PSD at low frequencies, and underestimates it at high frequencies. Also, note that this test was specifically designed such that the acoustic test chamber would interfere with the response at certain frequencies due to standing waves in the test chamber. The frequencies of these expected deviations are calculated to be 35 Hz, 64 Hz and 106 Hz. These are the frequencies in which there are the greatest

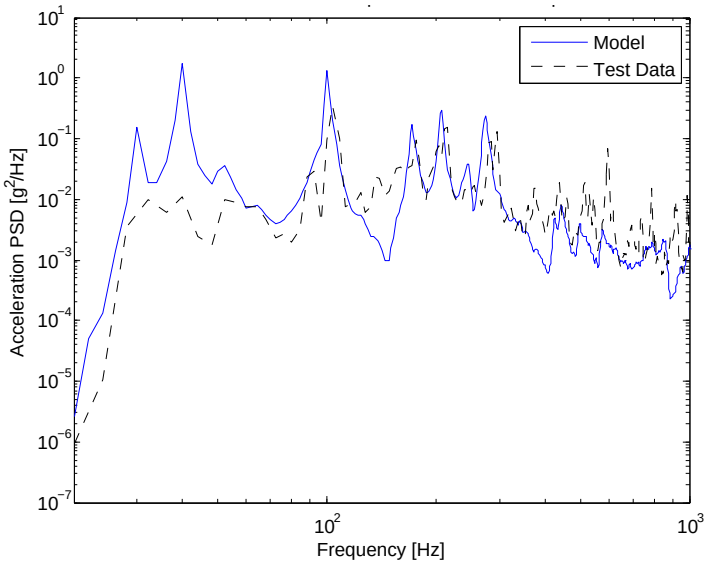

Figure A-3: Comparison Between the Model and Test Data

discrepancies between the initial model and test data.

The patch method has a number of known limitations. First, it is purely a pressure load, and does not include reverberant waves or air loading. Therefore, all forms of damping must be included in the modal damping, resulting in a much greater uncertainty in the damping than had it been purely structural damping. Similarly, the pressure is applied to one side of the plate, and a correlation factor is used to estimate the effects of the loading on both sides. This factor does account for some of the loading on both sides, but is an error factor rather than a description of physics. Also, the number of patches is a variable that must be chosen, and it is not a value that will converge. A typical choice is the number of patches that gives the worst case response. It is also common to choose a single patch to cover the entire surface. This is an issue with the method itself, and is a result of not modeling the physics of the acoustic waves through the air. Given these issues, it is understood that the patch method will typically slightly over-predict the response at low frequencies, and it will under-predict the response at high frequencies [23]. Despite these limitations, the patch method is a relatively easy method to implement and understand, and is compatible with finite element models and other analyses. Therefore, it is often used, and thus it is desirable to understand the uncertainties involved with the method.

A.2 Uncertainty Quantification

The uncertainty quantification in this work is done with the DAKOTA Software Package [47], which was developed at Sandia National Lab. DAKOTA, which stands for Design and Analysis toolKit for Optimization and Terascale Applications, provides an interface to the simulation code and allows the user to perform sensitivity analysis, optimization, uncertainty quantification, among other analyses on a "black box" simulation. A number of different uncertainty quantification methods were compared in terms of accuracy and efficiency on this problem; the results and descriptions of each method can be found in Reference [33]. Though the computational efficiency varies widely between methods, the results are all very similar. Therefore, only a single set of UQ results are presented here to describe the UQ for acoustic loading on lightweight structures.

The UQ results presented here are obtained using a sampling method, which is a very simple UQ technique. As indicated by the name, sampling methods use many sample runs of the simulation to compute the statistics of the output. With many simulation sample runs, the output statistics can be calculated quite accurately, but the drawback is that it may be computationally expensive or prohibitive to run enough samples. Specifically, Latin Hypercube sampling (LHS) is used. Latin Hypercube sampling is a technique that ensures uniform coverage of the probability space. The parameter distributions are divided into bins based on the specified uncertainty distributions. Then, the samples are chosen such that there is exactly one sample in each row or column of the n-dimensional hypercube, where n is the number of parameters. With the chosen parameters, the simulation is run and the results are used to calculate statistics on the output metrics [128]. In this case, computational resources were not a concern, and thus a 10,000 sample LHS uncertainty quantification was performed.

A.3 Parameter Distributions

In order to perform UQ, the pertinent variables in the model must be parameterized so that the parameter uncertainties can be propagated through the model to determine the system response. In order to proceed with such analyses, the uncertain input parameters need to be identified, and their distributions specified. The uncertain parameters and their distributions are summarized in Table A.1.

Table A.1: Uncertain Parameter Distributions

Gaussian Distributions		
Parameter	Mean	Standard Deviation
Plate thickness [mm]	6.35	0.05
Young's modulus [GPa]	71	0.5
Poisson ratio	0.31	0.005
Density [kg/m^3]	2711	8
Dimension (x) [m]	0.9525	0.005
Dimension (y) [m]	1.0439	0.005

Triangular Distributions			
Parameter	Median	Lower Bound	Upper Bound
Correlation factor	1.4	1.0	2.0
Damping ratio	0.015	0.001	0.02

Uniform Distributions		
Parameter	Lower Bound	Upper Bound
Number of patches (1 direction)	2	10
Acoustic input factor	0.5	2.5

The first set of Gaussian parameters are geometric or material properties. The correlation factor and number of patches are properties of the patch method. The acoustic input factor accounts for the input spectrum variation, as was seen in Figure A-2, and the damping is the modal damping factor. These uncertainty distributions are used to define the range of parameters that are propagated through the model so that the uncertainty distribution in the outputs can be determined.

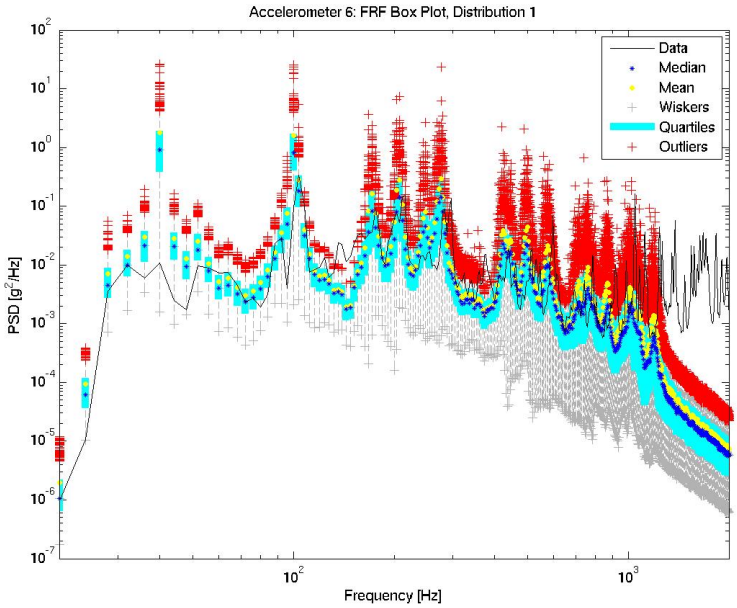

Figure A-4: Frequency Response Statistics

A.4 Uncertainty Quantification Results

The UQ results can be presented as either RMS comparisons, or as frequency response PSDs. First, PSDs of the frequency response outputs are shown. Figure A-4 shows the data as a box plot. Box plots are commonly used to quickly display statistical distributions. The black line is the test data. The median and mean are shown by blue and yellow dots respectively. The light blue bar extends from the first to the third quartile, and the gray bars extend to cover the expected range of data, about 2.7 standard deviations in each direction. The red + show the outliers. The mean is higher than the median, indicating the skew in the results toward higher values. Also, there are only outliers in the positive direction, again indicating the skew. Note that the log scale disguises some of the skewing at high values. The outliers are computed assuming a Gaussian distribution of the outputs, so shapes such as this appear when the data is not Gaussian. Also, note that the model only extends up to 1000 Hz, so the disagreement between model and test above 1000 Hz is expected.

These results can also be presented using the RMS value. The RMS acceleration results are presented graphically, as histograms, box plots, and cumulative distribu-

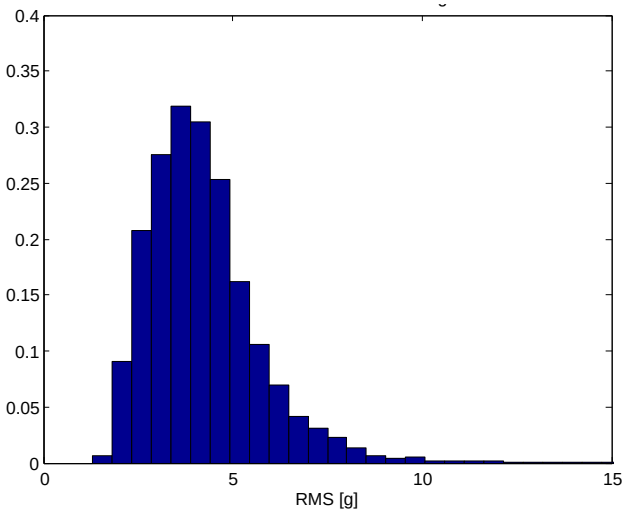

Figure A-5: RMS Acceleration Histogram

tion functions (CDFs). Figure A-5 shows the histogram, illustrating the distribution of the samples. Here, the RMS acceleration is on the x-axis, and the skew toward high values is clearly visible. Figure A-6 shows the box plot, which can present the statistics in such a way that the mean, median, quartiles, and outliers are displayed. Here, the RMS acceleration is on the y-axis. The red bar in the middle of the box plot represents the median data point. The box itself encloses the first through third quartiles, and the black lines extend out to the statistical extremes. The red points are outliers. Additionally, the + marks the mean of each point, and the $*$ marks the test data for comparison. The CDF plot in Figure A-7 shows the cumulative probability, along with the cumulative probability of a Gaussian with the mean and standard deviation of the results. These illustrate the tails and easily show the probability that the acceleration will be below a certain g-level.

All of the plots show the same trends in the output statistics. From the histogram, it is easy to see that the results are skewed upward toward higher g levels. The box plot shows the same data, with the additional overlay of the test data. The CDF, along with the Gaussian, shows the upper tail of the data. Using the CDF, it is easy to determine the probability that the acceleration will be below a given g-level, which is useful in launch survival calculations. The non-Gaussian nature of the data could degrade conservatism in launch survival calculations. The Gaussian assumption does

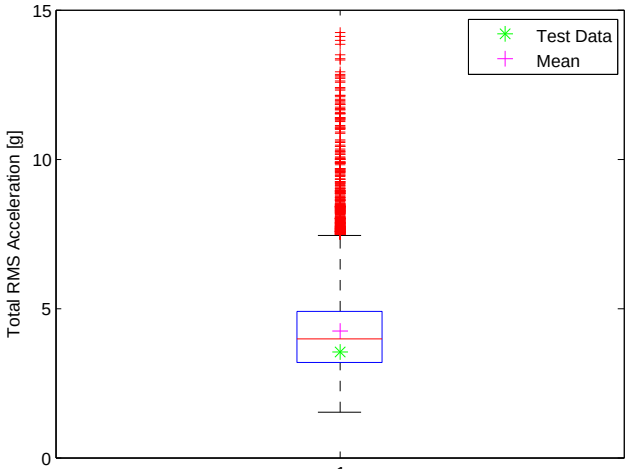

Figure A-6: RMS Acceleration Box Plot

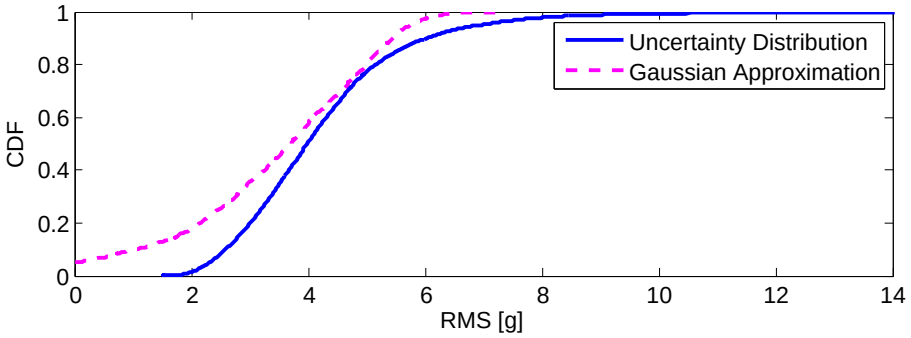

Figure A-7: RMS Acceleration CDF

not include the high outliers, which may matter in a 95% or 99% probability case. The CDF shows that the Gaussian assumption underestimates these low-probability, high-acceleration points.

A.5 Conclusions

The patch method is used for acoustic analysis on a flat plate example problem. The goal is to quantify the level of uncertainty that is involved with using this method. The patch method is relatively easy to implement with a finite element model. However, as a result of that simplicity, there are a number of uncertainties involved with the modeling process due to patch method limitations, as discussed in Section A.1. Namely, the correlation factor and number of patches are approximations to the true physics. Also, since the patch method is implemented purely as a pressure load, all damping and air loading is included as modal damping. This results in a wide range for the expected level of damping, and significantly influences the results, as damping is one of the most sensitive parameters.

The question remains as to whether or not the patch method can accurately be used to predict launch survival of a lightweight structure exposed to acoustic loading. The test data shows agreement at lower frequencies (the method is expected to deteriorate at higher frequencies), and the test data falls within the predicted statistical bounds. Also, the total RMS response from the test data is very close to the predicted RMS response. Therefore, the patch method is predicting the response. However, the uncertainty bands are very wide. This will require over designing of structures to ensure survival because of the wide expected range. Also, the non-Gaussian distribution (skewed upwards), indicates that higher limits may be necessary. If the resulting distribution is non-Gaussian, then 3-σ does not necessarily encompass 99.7% of the data as one would expect. The skewed nature indicates that there is significant probability of high RMS events, so one would need to design to accommodate survival under those conditions. Therefore, the patch method can be used for acoustic analysis, though it should be used cautiously, as there is uncertainty involved in the method, particularly

on the acoustic input, damping, and patch method parameters. The structure can be designed to survive within the probability range desired, resulting in some overdesign, but also a structure that will confidently survive launch.

Bibliography

[1] Electrical requirements for piezo operation. Technical report, Physik Instruments. http://www.physikinstrumente.com/en/products/prdetail.php?sortnr=400600.75.

[2] Softride launch environment mitigation. Technical report, CSA Engineering. http://www. csaengineering.com /spclnch/spacelaunch.asp.

[3] IEEE standard on piezoelectricity. Technical report, ANSI/IEEE, 1987. ANSI/IEEE Std 176-1987.

[4] Guide for the verification and validation of computational fluid dynamics simulations. Technical report, AIAA, 1998. G-077-1998.

[5] Delta iv payload planners guide. Technical report, Boeing, 2002. MDC 00H0043.

[6] Atlas launch system mission planners guide. Technical report, United Launch Alliance, 2004. CLSB-0409-1109.

[7] GeoEye-1. Technical report, GeoEye, 2008. http://launch.geoeye.com/ LaunchSite/about/.

[8] IKONOS. Technical report, GeoEye, 2008. http://www.geoeye.com/CorpSite /products/imagery-sources/Default.aspx.

[9] Worldview-1. Technical report, DigitalGlobe, Inc., 2008. http://www. digitalglobe.com/index.php/86/WorldView-1.

[10] Softride multiflex. Technical report, CSA Engineering, 2009. http://www.csaengineering.com /spclnch/CSAEngineering_multiflex.pdf.

[11] Brij N. Agrawal and Kirk E. Treanor. Shape control of a beam using piezoelectric actuation. *Smart Materials and Structures*, 8:729–740, 1999.

[12] George Angeli, Anna Segurson, Robert Upton, Brooke Gregory, and Myung Cho. Integrated modeling tools for large ground based optical telescopes. In *Proceedings of the SPIE, Volume 5178*, pages 49–63. SPIE, 2004.

[13] George Z. Angeli, Jennifer Dunn, Scott C. Roberts, Douglas G. MacMynowski, Anna Segurson, Konstantinos Vogiatzis, and Jeoleff Fitzsimmons. Modeling tools to estimate the performance of the Thirty Meter Telescope: an integrated approach. In *Proceedings of the SPIE, Volume 5497*, pages 237–250. SPIE, 2004.

[14] Koji Asari. Vibroacoustic modeling and control for launch vehicle shrouds. Master's thesis, Massachusetts Institute of Technology, June 1998.

[15] Vit Babuska, Delano Carter, and Steven Lane. Structural vibration modeling and validation: Modeling uncertainty and stochastic control for structural control. Technical report, Air Force Research Lab, 2005. AFRL-VS-PS-TR-2005-1174.

[16] Mark J. Balas. Direct velocity feedback control of large space structures. *Journal of Guidance, Control and Dynamics*, 2:252–253, 1979.

[17] Osman Balci. Validation, verification, and testing techniques throughout the life cycle of a simulation study. *Annals of Operations Research*, 53:121–173, 1994.

[18] J.-F.M. Barthelemy and R.T. Haftka. Approximation concepts for optimum structural design - a review. *Structural Optimization*, 5:129–144, 1993.

[19] Klaus-Jurgen Bathe. *Finite Element Procedures*. Prentice-Hall, 1996.

[20] Steven V. W. Beckwith. Space telescopes after the james webb space telescope. In *Proceedings of SPIE: UV/Optical/IR Space Telescopes: Innovative Technologies and Concepts*, volume 5166, pages 1–7. SPIE, 2004.

[21] Andrew S. Bicos, Conor Johnson, and L. Porter Davis. Need for and benefits of launch vibration isolation. In *Proceedings of the SPIE, Vol 3045*, 1997.

[22] C. Blaurock. Disturbance-Optics-Controls-Structures (DOCS). Technical report, Nightsky Systems, Inc., 2006. http://www.nightsky-systems.com/pdf/DOCS_Intro.pdf.

[23] Paul Blelloch. Fem based methods for vibro-acoustic response predictions. Technical report, Spacecraft and Launch Vehicle Dynamic Environments Workshop, 2006.

[24] Robert Grover Brown and Patrick Y. C. Hwang. *Introduction to Random Signals and Applied Kalman Filtering.* John Wiley and Sons, 3rd edition, 1997.

[25] Arthur E. Bryson and Yu Chi Ho. *Applied Optimal Control.* Hemisphere Publishing, 1975.

[26] J. Burge, S. DeRigne, R. Angel, B. Cuerden, S. Clapp, G. Rivlis, P. Woida, P. Gohman, S. Bell, and R. Kingston. NGST mirror system demonstrator from the University of Arizona. In *Proceedings of the SPIE, Volume 4013*, 2001.

[27] J. H. Burge, J. R. P. Ange, B. Cuerden, H. M. Martin, S. M. Miller, and D. G. Sandler. Lightweight mirror technology using a thin facesheet with active rigid support. In *Proceedings of the SPIE, Volume 3356, Space Telescopes and Instrumentation*, pages 690–701. SPIE, 1998.

[28] Mark E. Campbell. *Uncertainty Modeling for Structural Control Analysis and Synthesis.* PhD thesis, Massachusetts Institute of Technology, Cambridge, MA, 1996.

[29] Mark E. Campbell and Simon C. O. Grocott. Parametric uncertainty model for control design and analysis. *IEEE Transactions on Control Systems Technology*, 7(1):85–96, January 1999.

[30] W. G. Cochran. *Sampling Techniques*. John Wiley and Sons, New York, 1977.

[31] Lucy E Cohan. Control system architecture for space telescopes. In *AIAA Guidance, Navigation and Control Conference*, August 2007.

[32] Lucy E. Cohan. Integrated modeling to facilitate control architecture design for lightweight space telescopes. Master's thesis, Massachusetts Institute of Technology, June 2007.

[33] Lucy E. Cohan. Uncertainty quantification for acoustic loading on lightweight structures. Technical report, NASA Jet Propulsion Laboratory, 2009.

[34] Lucy E. Cohan, Elizabeth O. Jordan, and David W. Miller. Tradespace exploration for a parameterized modular optical space telescope (most). In 48^{th} *AIAA/ASME/ASCE/AHS/ASC Structures, Structural Dynamics & Materials Conference*. AIAA, 2007. AIAA-2007-2245.

[35] Edward Crawley, Mark Campbell, and Steve Hall. *High Performance Structures: Dynamics and Control*. Cambridge University Press - Draft, Cambridge, MA, 1998.

[36] Edward F. Crawley and Javier de Luis. Use of piezoelectric actuators as elements of intelligent structures. *AIAA Journal*, 25(10):1373–1385, 1987.

[37] Edward F. Crawley, Brett P. Masters, and T. Tupper Hyde. Conceptual design methodology for high performance dynamic structures. In *AIAA/ASME/ASCE/AHS/ASC Structures, Structural Dynamics, and Materials Conference and Exhibit*, 1995. AIAA-1995-1407.

[38] Noel Cressie. The origins of kriging. *Mathematical Geology*, 22(3):239–252, 1990.

[39] Noel Cressie. *Statistics for Spatial Data*. John Wiley and Sons, 1991.

[40] B. Cullimore, T. Panczak, J. Baumann, Victor Genberg, and Mark Kahan. Automated multidisciplinary optimization of a space-based telescope. *Society of Automotive Engineers*, July 2002. SAE-2002-01-2245.

[41] Olivier L. de Weck. Integrated modeling and dynamics simulation for the Next Generation Space Telescope. Master's thesis, Massachusetts Institute of Technology, Cambridge, MA, June 1999.

[42] Olivier L. de Weck. *Multivariable Isoperformance Methodology for Precision Opto-Mechanical Systems*. PhD thesis, Massachusetts Institute of Technology, 2001.

[43] Keith K. Denoyer and Conor Johnson. Recent achievements in vibration isolation systems for space launch and on-orbit applications. In *52nd International Astronautical Congress*, Toulouse, France, October 2001.

[44] Mark A. Ealey. Large optics in the 21st century: a transition from discrete manufacturing to highly integrated techniques. In *2003 IEEE Aerospace Conference*. IEEE, 2003.

[45] Mark A. Ealey. Fully active telescope. In *UV/Optical/IR Space Telescopes: Innovative Technologies and Concepts*, volume 5166, pages 19–26. SPIE, 2004.

[46] Mark A. Ealey and John A. Wellman. Polishabiity of CERAFORM silicon carbide. In *Proceedings of the SPIE, Volume 2857*, 1996.

[47] Michael S. Eldred et al. DAKOTA, a multilevel parallel object-oriented framework for design optimization, parameter estimation, uncertainty quantification, and sensitivity analysis. Technical report, Sandia National Laboratories, Livermore, CA, 2008.

[48] J. L. Fanson and T. K. Caughey. Positive position feedback control for large space structures. *AIAA Journal*, 28(4):717–724, 1990.

[49] A. J. Fleming, S. Belirens, and S.O.R. Moheimani. Synthetic impedance for implementation of piezoelectric shunt-damping circuits. *Electronic Letters*, 36:1525–1526, 2000.

[50] Brian D. Freed and Vit Babuska. Finite element modeling of composite piezoelectric structures with msc/nastran. In *Proceedings of the SPIE, Volume 3041*. SPIE, 1997.

[51] R. H. Freeman and J. E. Pearson. Deformable mirrors for all seasons and reasons. *Applied Optics*, 21:580–588, 1982.

[52] Mark E. Furber, David D. Blaszak, and Mario R. Pieri. Correctabilty modeling of a large deformable mirror. In *Proceedings of the SPIE, Vol 2201*, volume 2201. SPIE, 1994.

[53] Enrique Garcia. Advanced Mirror System Demonstrator (AMSD) progress update at Goodrich Electro-Optical Systems. Technical report, NASA Technology Days, 2002.

[54] Victor Genberg, Keith Doyle, and Gregory Michaels. Optical interface for MSC.Nastran. In *MSC 2004 VPD Conference*, 2004.

[55] Victor Genberg, Gregory Michaels, and Keith Doyle. Making FEA results useful in optical analysis. In *Proceedings of the SPIE, Volume 4769*. SPIE, 2002.

[56] James M. Gere. *Mechanics of Materials*. Brooks/Cole, 5 edition, 2001.

[57] P. E. Gill, W. Murray, and M. H. Wright. *Practical Optimization*. Academic Press, London, 1981.

[58] Anthony A. Giunta and Layne T. Watson. A comparison of approximation modeling techniques: Polynomial versus interpolating models. In *7th AIAA/USAF/NASA/ISSMO Symposium on Multidisciplinary Analysis and Optimization*, 1998. AIAA-98-4758.

[59] Roger M. Glaese. Development of zero-gravity structural control models from analysis and ground experimentation. Master's thesis, Massachusetts Institute of Technology, 1994.

[60] Roger M. Glaese. *Impedance Matching for Structural-Acoustic Control*. PhD thesis, Massachusetts Institute of Technology, April 1997.

[61] C Goh. and T. K. Caughey. On the stabilit problem caused by finite actuator dynamics in the control of large space structures. *International Jounal of Control*, 41:787–802, 1985.

[62] Thomas Gray. Minimizing high spatial frequency residual in active space telescope mirrors. Master's thesis, Massachusetts Institute of Technology, June 2008.

[63] Steven Griffin, Steven A. Lane, Colin Hansen, and Ben Cazzolato. Active structual-acoustic control of a rocket fairing using proof-mass actuators. *Journal of Spacecraft and Rockets*, 38:219–225, 2001.

[64] Simon O. Grocott. Comparison of control techniques for robust performance on uncertain structural systems. Master's thesis, Massachusetts Institute of Technology, Cambridge, MA, February 1994.

[65] Simon O. Grocott. *Dynamic Reconstruction and Multivariable Control for Force-Actuatued, Thin Facesheet Adaptive Optics*. PhD thesis, Massachusetts Institute of Technology, 1997.

[66] Homero L. Gutierrez and David W. Miller. *Performance Assessment and Enhancement of Precision Controlled Structures During Conceptual Design*. PhD thesis, Massachusetts Institute of Technology, Cambridge, MA, February 1999.

[67] Raphael T. Haftka. Integrated structure-control optimization of space structures. In *AIAA Dynamics Specialists Conference*, Long Beach, CA, 1990.

[68] N. W. Hagood and A. Von Flotow. Damping of structural vibrations with piezoelectric materials and passive electrical networks. *Journal of Sound and Vibration*, 146(2):243–268, 1991.

[69] John W. Hardy. Active optics: A new technology for the control of light. *Proceedings of IEEE*, 66(6):651–697, 1978.

[70] Jonathan How. *Robust Control Design with Real Parameter Uncertainty using Absolute Stability Theory*. PhD thesis, Massachusetts Institute of Technology, 1993.

[71] Jonathan P. How. Local control design methodologies for a hierarchic control architecture. Master's thesis, Massachusetts Institute of Technology, February 1990.

[72] Jonathan P. How, Steven R. Hall, and Wassim M. Haddad. Robust controllers for the Middeck Active Control Experiment using Popov controller synthesis. In *IEEE Transactions on Control System Technology*, volume 2, 1994.

[73] Deborah J. Howell. *Spatial Nyquist Fidelity Method for Structural Models of Opto-Mechanical Systems*. PhD thesis, Massachusetts Institute of Technology, 2007.

[74] T. Hyde, K. Ha, J. Johnston, J. Howard, and G. Mosier. Integrated modeling activities of the James Webb Space Telescope: Optical jitter analysis. In *Proceedings of the SPIE, Volume 5487*, pages 588–599. SPIE, 2004.

[75] H. Irschik. A review of static and dynamic shape control of structures by piezoelectric actuation. *Engineering Structures*, 24:5–11, 2005.

[76] Robert Jacques. *On-line System Identification and Control Design for Flexible Structures*. PhD thesis, Massachusetts Institute of Technology, 1994.

[77] Cyrus D. Jilla. *A Multiobjective, Multidisciplinary Design Optimization Methodology for the Conceptual Design of Distributed Satellite Systems*. PhD thesis, Massachusetts Institute of Technology, Cambridge, MA, May 2002.

[78] Conor D. Johnson and Paul S. Wilke. Protecting satellites from the dynamics of the launch environment. In *AIAA Space 2003*, Long Beach, CA, September 2003.

[79] John D. Johnston, Joseph M. Howard, Gary E. Mosier, Keith A. Parrish, Mark A. McGinnis, A. M. Bluth, Kevin Kim, and Kong Q. Ha. Integrated modeling activities for the James Webb Space Telescope: Structural-thermal-optical analysis. In *Proceedings of the SPIE, Volume 5487*, pages 600–610. SPIE, 2004.

[80] Elizabeth O. Jordan. Design and shape control of lightweight mirrors for dynamic performance and athermalization. Master's thesis, Massachusetts Institute of Technology, June 2007.

[81] Elizabeth O. Jordan and David W. Miller. Primary mirror shape control for athermalization using embedded sensors. In *Proceedings of the SPIE, Volume 6687*. SPIE, 2007.

[82] Elizabeth O. Jordan, Andrjez Stewart, Scott A. Uebelhart, Deborah Howell, and David W. Miller. Parametric modeling of space telescope architectures. In *2006 SPIE Astronomical Telescopes and Instrumentation Conference*, Orlando, FL, May 24-31, 2006.

[83] Alvar M. Kabe. Design and verification of launch and space vehicle structures. In *AIAA Structures, Dynamics and Materials Conference*, number AIAA-98-1718, 1998.

[84] Eldon P. Kasl and David A. Crowe. A critical review of ultralightweight composite mirror technology. In *American Institute of Physics Space technology and applications international forum*, volume 420, pages 173–178. AIP, 1998.

[85] Marty Kauchak. Eyes for a sharper image. *Military Geospatial Technology*, 4(5), November 2006. http://www.military- geospatial- technology.com/article.cfm?DocID=1787.

[86] Stephen E. Kendrick, David Chaney, and Robert J. Brown. Optical characterization of the beryllium semi-rigid AMSD mirror assembly. In *Proceedings of the SPIE, Volume 5180*, 2003.

[87] Dan Kerley, Scott Roberts, Jennifer Dunn, Nathan Stretch, Malcolm Smith, Simon Sun, John Pazder, and Joeleff Fitzsimmons. Validation and verification of integrated model simulations of a Thirty Meter Telescope. In *Proceedings of the SPIE, Volume 5867*, 2005.

[88] Witold Kowbel and J. C. Withers. SiC-SiC composites optics for UV applications. In *Proceedings of the SPIE, Volume 6666*. SPIE, 2007.

[89] Herbert J. Kramer. *Observation of the Earth and Its Environment: Survery of Missions and Sensors*. Springer, New York, 4th edition, 2002.

[90] Huibert Kwakernaak and Raphael Sivan. *Linear Optimal Control Systems*. John Wiley & Sons, New Yord, 1972.

[91] Donald J. Leo and Eric H. Anderson. Vibroacoustic modeling of a launch vehicle payload fairing for active acoustic control. In *AIAA Structures, Dynamics, and Materials Conference*, number AIAA-98-2086, pages 3212–3222. AIAA, 1998.

[92] Michael D. Lieber. Development of the ball integrated telescope model (ITM). In *Proeedings of SPIE*, volume 4757, 2002.

[93] Charles F. Lillie and Allen J. Bronowicki. Adaptation in space telescopes. In 45^{th} *AIAA/ASME/ASCE/AHS/ASC Structures, Structural Dynamics & Materials Conference*, Palm Springs, CA, April 19-22 2007. AIAA 2004-2064.

[94] Ketao Liu, Robert N. Jacques, and David W. Miller. Frequency domain structural system identification by observability range space extraction. In *Proceedings of the American Controls Conference*, pages 107–111, June 1994.

[95] David M. LoBosco. Integrated modeling of optical performance for the Terrestrial Planet Finder Structurally Connected Interferometer. Master's thesis, Massachusetts Institute of Technology, 2004.

[96] David M. LoBosco, Carl Blaurock, Soon-Jo Chung, and David W. Miller. Integrated modeling of optical performance for the Terrestrial Planet Finder Structurally Connected Interferometer. In *Proceedings of the SPIE*. SPIE, 2004.

[97] Howard A. MacEwen. Separation of functions as an approach to development of large space telescope mirrors. In *Proceedings of SPIE: UV/Optical/IR Space Telescopes: Innovative Technologies and Concepts*, volume 5166, pages 39–48. SPIE, 2004.

[98] Joseph R. Maly, Scott C. Pendleton, Steven J. Buckley, John E. Higgins, Eric J. Walsh, Ryan A. Hevner, Scott R. Schoneman, and Lt William A. Emmer. Caspar: Low-cost, dual-manifest payload adapter for minotaur iv. In *19th AIAA/USU Conference on Small Satellites*, 2005.

[99] Maggie Masetti and Anita Krishnamurthi. The James Webb Space Telescope. Technical report, NASA, 2008. http://www.jwst.nasa.gov/.

[100] Rebecca A. Masterson. *Dynamic Tailoring and Tuning for Space-Based Precision Optical Structures*. PhD thesis, Massachusetts Institute of Technology, February 2005.

[101] Rebecca A. Masterson and David W. Miller. Dynamic tailoring and tuning for precision optical space structures. In *45th AIAA/ASME/ASCE/AHS/ASC Structures, Structural Dynamics and Materials Conference*. AIAA, April 2004. AIAA-2004-1600.

[102] Lawrence E. Matson and David Mollenhauer. Advanced materials and processes for large, lightweight, space-based mirrors. In *IEEE Aerospace Conference*, March 2003.

[103] Gary Matthews, Frank Carbone, Pat Clark, and Devin Mack. Semirigid active mirror technology advancements. In *Proceedings of the SPIE, Volume 4451*. SPIE, 2001.

[104] Jim Mayo, Linda DeHainauta, Kevin Bell, Scott Smith, Don Kilipatrick, and Richard Dyer. Ultra-lightweight optics for space applications. In *Proceedings of the SPIE, Volume 4013*, 2000.

[105] D. W. Miller, E. F. Crawley, J. P. How, K. Liu, M. E. Campbell, S. C. O. Grocott, R. M. Glaese, and T. D. Tuttle. The Middeck Active Control Experiment (MACE): Summary report. Report 7-96, MIT Space Engineering Research Center, 1996.

[106] David W. Miller and Simon O. Grocott. Robust control of the Multiple Mirror Telescope adaptive secondary mirror. *Optical Engineering*, 38(8):1276–1287, 1999.

[107] Steve Miller, Roger Angel, Buddy Martin, John Kapp, Dean Ketelsen, and Lee Dettmann. Fabrication of ultra thin mirrors for adaptive and space optics. In *Proceedings of the SPIE, Volume 3126*, pages 391–396. SPIE, 2004.

[108] S. O. Reza Moheimani. A survey of recent innovations in vibration damping and control using shunted piezoelectric transducers. In *IEEE Transactions on Control Systems Technology*, volume 11, 2003.

[109] Bruce C. Moore. Principal component analysis in linear systems: Controllability, observability, and model reduction. In *IEEE Transactions on Automatic Control*, volume 26, 1981.

[110] Gary E. Mosier, Joseph M. Howard, John D. Johnston, Keith A. Parrish, T. Tupper Hyde, Mark A. McGinnis, Marcel Bluth, Kevin Kimb, and Kong Q. Hac. The role of integrated modeling in the design and verification of the James Webb Space Telescope. In *Proceedings of the SPIE, Volume 5528*. SPIE, 2004.

[111] MSC NASTRAN. *MSC/NASTRAN 102 Exercise Workbook*. Problem 10: Random Analysis.

[112] R. H. Myers and D. C. Montgomery. *Response Surface Methodology: Process and Product Optimization Using Designed Experiments*. John Wiley and Sons, 1995.

[113] Manfred Nader, Hubert Gattringer, Michael Krommer, and Hans Irschik. Shape control of flexural vibrations of circular plates by shaped piezoelectric actuation. In *Transactions of the ASME*, volume 125. ASME, January 2003.

[114] Junjiro Onoda and Raphael T. Haftka. An approach to structure/control simultaneous optimization for large flexible spacecraft. *AIAA Journal*, 25:1133–1138, 1987.

[115] Lars Pernebo and Leonard M. Silverman. Model reduction via balanced state space representations. In *IEEE Transactions on Automatic Control*, volume 27, 1982.

[116] Andre Preumont. *Vibration Control of Active Structures*. Solid Mechanics and its Applications. Kluwar Academic Publishers, 2, 2002.

[117] K. R. S. Riordan. Simulated inductors using differential amplifiers. *Electronic Letters*, 3:50–51, 1967.

[118] Hugh J Robertson. Development of an active optics concept using a thin deformable mirror. Technical report, NASA, August 1970.

[119] Theresa D Robinson. *Surrogate-Based Optimization using Multifidelity Models with Variable Parameterization*. PhD thesis, Massachusetts Institute of Technology, 2007.

[120] Thomas P. Sarafin, editor. *Spacecraft Structures and Mechanisms - From Concept to Launch*. Microcosm, Inc. and Kluwer Academic Publishers, 1995.

[121] Michael J. Shepherd, Gina A. Peterson, Richard G. Cobb, and Anthony N. Palazotto. Quasi-static optical control of in-plane actuated, deformable mirror: Experimental comparison with finite element analysis. In *47th*

AIAA/ASME/ASCE/AHS/ASC Structures, Structural Dynamics, and Materials Conference. AIAA, May 2006.

[122] Ryan Simmons. FEMCI: The book. Technical report, NASA Goddard Space Flight Center, 2008. URL: http://femci.gsfc.nasa.gov/femcibook.html.

[123] Sigurd Skogestad and Ian Postlethwaite. *Multivariable Feedback Control*. John Wiley & Sons, West Sussex, England, 2 edition, 2005.

[124] J. Sobieszczanski-Sobieski and R. T. Haftka. Multidisciplinary aerospace design optimization: survey of recent developments. *Structural Optimization*, 14:1–23, 1997.

[125] H. Philip Stahl. JWST lightweight mirror TRL-6 results. In *Aerospace Conference, 2007 IEEE*, 2007.

[126] H. Philip Stahl and Lee Feinberg. Summary of NASA advanced telescope and observatory capability roadmap. In *2007 IEEE Aerospace Conference*. IEEE, March 2007.

[127] Dongchang Sun, Liyong Tong, and Dajun Wang. An incremental algorithm for static shape control of smart structures with nonlinear piezoelectric actuators. *International Journal of Solids and Structures*, 41:2277–2292, 2004.

[128] L. P. Swiler and G. D. Wyss. A users guide to Sandias latin hypercube sampling software: LHS UNIX library and standalone version. Technical report, Sandia National Laboratory, Albuquerque, NM, 2003.

[129] Marc Trubert. Mass acceleration curve for spacecraft structural design. Technical report, NASA Jet Propulsion Lab, November 1989. JPL D-5882.

[130] Lori Tyahla. The Hubble Space Telescope. Technical report, NASA, 2008. http://hubble.nasa.gov/index.php.

[131] Robert K. Tyson. *Principles of Adaptive Optics*. Academic Press, Inc., San Diego, CA, 1991.

[132] Scott A. Uebelhart. Conditioning, reduction and disturbance analysis of large order integrated models for space telescope. Master's thesis, Massachusetts Institute of Technology, Cambridge, MA, February 2001.

[133] Scott A Uebelhart. *Non-Deterministic Design and Analysis of Parameterized Optical Structures during Conceptual Design*. PhD thesis, Massachusetts Institute of Technology, June 2006.

[134] Scott A. Uebelhart, Lucy E. Cohan, and David W. Miller. Design exploration for a modular optical space telescope architecture using parameterized integrated models. In 47^{th} *AIAA/ASME/ASCE/AHS/ASC Structures, Structural Dynamics & Materials Conference*, Newport, RI, May 1-4, 2006. AIAA 2006-2083.

[135] Scott A. Uebelhart, Deborah Howell, and David W. Miller. Evaluating alternative architectures for lightweight space telescopes using parameterized models. In *2006 IEEE Aerospace Conference*, Big Sky, Montana, March 4-11, 2006.

[136] Scott A. Uebelhart and David W. Miller. Uncertainty evaluation for parameterized spacecraft architectures in conceptual design. In 48^{th} *AIAA/ASME/ASCE/AHS/ASC Structures, Structural Dynamics & Materials Conference*. AIAA, May 2007.

[137] Joseph E. Wall. *Control and estimation for large-scale systems having spatial symmetry*. PhD thesis, Massachusetts Institute of Technology, 1978.

[138] James R. Wertz and Wiley J. Larson. *Space Mission Analysis and Design*. Microcosm, Inc, Torrance, CA, Kluwer Academic Publishers, Boston, 3^{rd} edition, 1999.

[139] Nicholas E. White. NASA strategic roadmap: Origin, evolution, structure, and destiny of the universe. In *Proceedings of the SPIE, Volume 5899*, 2005.

[140] Paul S. Wilke, Conor D. Johnson, and Eugene R. Fosness. Whole-spacecraft passive launch isolation. In *38th AIAA/ASME/ASCE/AHS/ASC Structures,*

Structural Dynamics, and Materials Conference and Exhibit, Kissimmee, FL, April 1997. AIAA-1997-1199.

[141] Karen Willcox and Jaime Peraire. Balanced model reduction via the proper orthogonal decomposition. *AIAA Journal*, 40(11):2323–2330, 2002.

[142] Darrel Williams. The Landsat program. Technical report, NASA, 2008. http://landsat.gsfc.nasa.gov/.

[143] S. E. Winters, J. H. Chung, and S. A. Velinsky. Modeling and control of a deformable mirror. *Journal of Dynamic Systems, Measurement, and Control*, 124:297–302, 2002.

[144] S. F. Wojtkiewicz, Jr. M. S. Eldred, R. V. Field, A. Urbina, and J. R. Red-Horse. Uncertainty quantification in large computational engineering models. In AIAA, editor, *42nd AIAA/ASME/ASCE/AHS/ASC Structures, Structural Dynamics, and Materials (SDM) Conference*, Seattle, 2001.

[145] Kemin Zhou and John C. Doyle. *Essentials of Robust Control*. Prentice Hall, New Jersey, 1998.